Ph.D. in Electronic and Computer Engineering
Dept. of Electrical and Electronic Engineering
University of Cagliari

CHEMO AND BIODETECTION IN LIQUID WITH ORGANIC TRANSISTOR

MONIA DEMELAS

Advisor: ANNALISA BONFIGLIO
Co-Advisor: MASSIMO BARBARO
Co-Advisor: ERIKA SCAVETTA

Curriculum: ING-INF/01 Electronics

XXIV Cycle
May 2013

Abstract

In the past, quality and quantity of the substances could be evaluated only in analytical chemistry laboratories, well-equipped with centralized and powerful data centres. The rising of miniaturized technology has made possible to conceive the realization of portable devices, i.e. chemical sensors capable to analyse small quantities in situ. Nowadays, the availability of portable devices allows to test those samples which are difficult or impossible to transport for long distances without degradation.

This work concerns the realization of two kinds of devices for detection of chemical and biological species in liquids by using organic transistor technology. One device, which is named Organic Charge Modulated Field Effect Transistor (OCMFET), is a charge sensor which was tested as pH and DNA sensor. The other device is an Organic Electrochemical Transistor (OECT) entirely made of poly(3,4-ethylenedioxythiophene):poly(styrene sulfonate) (PEDOT:PSS) which was realized by ink-jet printing. As these devices can be fabricated with low-cost processes, they can be considered portable and disposable.

A brief introduction on sensors, organic technology and the aim of this work is described in chapter one. In order to explain the reasons and the specific choices behind the development of these sensors, an overview of the most relevant sensing applications realized with Organic Thin Film Transistors and Organic Electrochemical Transistors is reported in chapter two. The working principle, the materials and methods and the recorded experimental results related to the OCMFET are treated in chapter three. A brief introduction on OECTs with a PEDOT:PSS channel and the study carried out to elucidate the operating regime of the OECT all made of PEDOT:PSS is treated in chapter four. The conclusions about this work are briefly summarized in chapter five. An overview on organic semiconductors and Organic Thin Film Transistors (OTFTs), the electrochemical techniques used in this work are treated in the appendixes.

Keywords: Organic Thin Film Transistors, pH sensors, DNA sensors, Organic Electrochemical Transistors, PEDOT:PSS, ink-jet printing.

Sommario

Sino a non molto tempo fa, lo svolgimento di analisi qualitative e quantitative delle sostanze chimiche poteva avvenire solo all'interno di laboratori di chimica analitica equipaggiati con sistemi di analisi su sistemi macroscopici. La miniaturizzazione delle tecnologie elettroniche ha reso possibile la realizzazione di dispositivi portatili, cioè di sensori chimici atti allo svolgimento di analisi in situ. La possibilità di trasportare gli strumenti di misurazione è particolarmente importante soprattutto per analizzare di quei campioni che sono difficili, se non impossibili, da trasportare per lunghe distanze senza degradarsi.

Questo lavoro riguarda la realizzazione di due diversi tipi di sensori per il rilevamento di specie chimiche o biologiche in ambiente liquido attraverso l'utilizzo della tecnologia basata su transistor organici. Un dispositivo, denominato Organic Charge Modulated Field Effect Transistor (OCMFET), è stato testato come sensore di pH e di DNA. L'altro dispositivo è un transistor elettrochimico interamente fabbricato in poly(3,4-ethylenedioxy-thiophene):poly(styrene sulfonate) (PEDOT:PSS) mediante l'uso di una stampante piezoelettrica a getto d'inchiostro.

Nel primo capitolo si riporta una breve introduzione sui sensori, la tecnologia organica e lo scopo di questo lavoro. Nel secondo capitolo si propone una panoramica sulle più importanti applicazioni sviluppate nell'ambito della sensoristica mediante l'uso di transistor organici a film sottile e di transistor organici elettrochimici. Il terzo capitolo dedicato allo sviluppo dell'OCMFET: se ne descrive il principio di funzionamento, i materiali e i metodi impiegati per la sua realizzazione e, infine, i risultati sperimentali conseguiti. Il quarto capitolo è dedicato al transistor elettrochimico realizzato in PEDOT:PSS: dopo una breve panoramica sui transistor elettrochimici a canale in PEDOT:PSS, si riporta lo studio effettuato per determinare la modalità di funzionamento

dei transistor elettrochimici interamente realizzati in PEDOT:PSS. I principali risultati ottenuti in questo lavoro, insieme ad alcune osservazioni per un ulteriore sviluppo dell'attività di ricerca, sono riepilogati nel quinto capitolo. Alcuni approfondimenti sono affrontati in appendici separate; in particolare, oltre ad una panoramica sui semiconductori organici e il principio di funzionamento dei transistor organici a film sottile, si riportano alcuni rudimenti sulle tecniche di elettrochimica impiegate per lo svolgimento di questo lavoro.

Parole chiave: transistor a film sottile, sensori di pH, sensori di DNA, transistor organici elettrochimici, PEDOT:PSS, stampa a getto di inchiostro.

List of related publications

Journal articles

- **Electrochemical characterization of self assembled monolayers on flexible electrodes**.
  E. Scavetta, A. G. Solito, **M. Demelas**, P. Cosseddu, and A. Bonfiglio.
  Electrochimica Acta, **65**:159-164, (2012).

- **An organic, charge-modulated field effect transistor for DNA detection**.
  M. Demelas, S. Lai, G. Casula, E. Scavetta, M. Barbaro, and A. Bonfiglio.
  Sensors and Actuators B: Chemical, **171**–**172**:198-203, (2012).

- **Ultra-Low Voltage, OTFT-Based Sensor for Label-Free DNA Detection**.
  S. Lai, **M. Demelas**, G. Casula, P. Cosseddu, M. Barbaro, and A. Bonfiglio.
  Advanced Materials, **25**:103-107, (2013).

- **Charge sensing by organic field effect devices: application to the detection of bio-related effects**.
  M. Demelas, S. Lai, A. Spanu, S. Martinoia, P. Cosseddu, M. Barbaro, and A. Bonfiglio.
  Accepted for publication on *Journal of Material Chemistry B*.

- **A deeper insight into the working regime of all-PEDOT:PSS Electro-Chemical Transistors**. *Applied Physics Letters*, (2013).
  M. Demelas, E. Scavetta, L. Basiricò, R. Rogani, and A. Bonfiglio.
  Accepted for publication on *Applied Physics Letters*, (2013).

Proceedings of international conferences with acceptance based on full paper submission

– **DNA Hybridization Detection based on an Organic Charge Modulated Field Effect Transistor**.
M. Demelas, S. Lai, M. Barbaro, and A. Bonfiglio.
IEEE Sensors 2011, (2011).

Proceedings of international conferences with acceptance based on abstract submission

– **Organic ThinFilm Transistors for pH detection**.
M. Demelas, A. Caboni, M. Barbaro, and A. Bonfiglio.
2010 MRS Spring Meeting, (2010).

Dedicated to my Dad

Contents

List of Figures

LIST OF FIGURES

LIST OF FIGURES

List of Tables

1

Introduction

This chapter provides a basic introduction to chemosensors and biosensors. Starting with a general definition, some basics informations related to sensor technology and the transistor structures used for chemical and biological sensors are shown. Then, the aim of this thesis is described.

1.1 Sensor and biosensor - Definition

According to the International Union of Pure and Applied Chemistry (IUPAC) (1991) [1], *a chemical sensor is a device that transforms chemical information, ranging from the concentration of a specific sample component to the total composition analysis, into an analytically useful signal.*

Usually, in a chemical sensor, a chemical information is converted into an electrical information. The device core consists of two basic components connected in series: a recognition system, the *receptor*, and a physicochemical *transducer* (see figure 1.1).

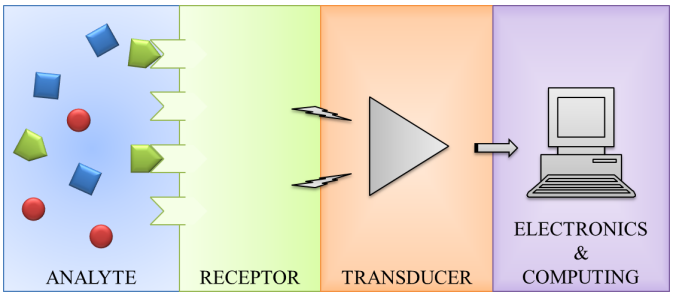

Figure 1.1: Scheme of a typical chemical sensor system.

As a general rule, the receptor is directly in contact with the analyte to be tested and transforms the chemical information into a form of energy which may be measured by the transducer. The interaction with the analyte affect a receptor's general property, whose change is translated by the transducer in an output signal, mostly electrical. In chemosensors, receptors are usually thin layers that can interact with the analyte by mechanisms such as surface adsorption, ion exchange and chemical reactions. Biosensors are a special class of chemical sensors, based on processes that are common to chemical sensors, but with a biological recognition system as receptor. Enzymes, antibodies, antigens, proteins and nucleic acids are typical biological systems used as receptors in biosensors. The selectivity towards the analyte of interest is the most important feature for the recognition system. A very common recognition mechanism is based on molecular steric hindrance, which means that molecules are recognized through their size and form. This mechanism also works in biological sensors. Enzymes, for example, are biocatalysts characterized by a specific three-dimensional configuration with a molecular cavity, including an active site, that is suitable for recognizing a special sort of molecule; oligonucleotides are extremely selective receptors as they can hybridize forming double strands only when interacting with their fully complementary strand.

The transducer transforms the energy that carries the chemical information about the sample into a useful analytical signal. Even if sometimes transducers are classified according to transducer output (current transducer, voltage transducer), a transducer classification system has not been developed yet.

Two additional elements, a unit for signal amplification and for signal conditioning, complete the systems.

1.2 Sensor technology

In literature, a few definitions for chemosensors and biosensors emphasize that a chemical sensor must have some pragmatic properties. According to Wolfbeis [2], a chemical sensor must be a *small-sized device capable of continuously and reversibly reporting a chemical concentration.* Moreover, nowadays a chemical sensor also needs to be cheap because of the high demand for chemical analysis in several fields such as medical diagnostics, forensic sciences, and so on.

Organic electronics is a branch of electronics that, compared to the traditional silicon technology, allows to realize electronic circuits and devices using relatively low-cost materials and processes. Moreover, with respect to the inorganic materials, many organic compounds have interesting properties such as good mechanical flexibility and biocompatibility. Flexibility makes them naturally compatible with low-cost substrate such as plastic or metal foils, while biocompatibility makes them integrable with biological systems. These reasons have contributed to push the research towards the realization of sensors base on this technology, and in fact, since the first discovery of the conductive properties of the organic molecules, organic electronics has made enormous progresses especially in biosensing applications. First examples of chemical sensors were small and transportable analytical probes, which could be stuck into a specimen, such as the ion-selective electrode used for pH detection. Nowadays, the integration between chemical and biological systems with electronic devices, and the development of biologically-inspired materials has led to the realization of devices for detecting and monitoring chemical and biological responses.

Apart from including an interface which is in direct contact with the sample, there is not a simple rule that describes how a sensor can be implemented. Its design strongly depends on the manufacturing technique. As they result from the integration of several technologies, during the last decade chemosensors and biosensors have been realized using different architectures and materials. Transistors are very attractive candidates for chemosensing and biosensing applications as they translate the chemical/biological information into a current, which can be detected with simple instrumentation and possibly amplified. In particular, the thin-film architecture used has proven to be especially adaptable to realize electronic devices with poorly conducting materials such as organic semiconductors. Organic molecules can be synthesized in a wide range of structures and morphologies, thus allowing to realize films with specific physical and chemical properties, and especially suitable for sensing applications. In particular, the organic semiconductors' chemical and physical properties can be adjusted in order to enhance a specific sensitivity and selectivity, and also to integrate recognition elements. Compared to transistors based on single-crystal inorganic semiconductors, organic semiconductors have charge carrier mobilities of three or more orders of magnitude lower. As a consequence, they are not suitable to be used in applications requiring very high switching speeds. In fact, organic electronics has captured its area of interest,

becoming extremely competitive, where the traditional silicon technology was lacking. Silicon technology requires high-temperature and sophisticated patterning methods; as a consequence it is quite expensive and not suitable for realizing flexible and large area applications. On the contrary, dealing with carbon-based compounds, organic electronics is easier to process and requires low-temperatures methods. As a consequence, it is resulting in a low-cost technique for large area coverage and structural flexibility applications.

Thin films of organic materials are deposited by techniques such as thermal evaporation [3] and chemical vapour deposition [4]. In thermal evaporation, the material is electrically heated to make it evaporate under under a high vacuum environment. In chemical vapour deposition, the material is firstly evaporated and thermally decomposed; a non-volatile film is then produced at the substrate surface at a relatively low temperature. Small molecules are usually deposited by thermal evaporation [5] or by chemical vapour deposition. On the other hand, polymers are usually dissolved in solutions and then drop-cast or printed onto the substrate [6]. Patterning of the metallic substrates can be obtained by means of a photolithographyc process [7]. A photosensitive material is deposited on the layer of interest; by illuminating and developing this photosensitive layer, the pattern is firstly transferred to it; then, an etching treatment allows to selectively remove the material of interest, and thus to transfer the pattern to the underlying film. Nowadays, inks made of metallic particles have been realized allowing to obtained patterned metallic surfaces by means of ink-jet printers, which are also widely used to deposit conductive polymers. As a matter of fact, ink-jet printing is one of the most promising techniques for large areas electronics.

In a few cases organic layers such as semiconductors or insulators directly interact with the analyte serving as receptors. More often, in order to make a surface sensitive towards a specific analyte, superficial properties are modified through functionalization. Functionalization consists in immobilizing functional groups, which can selectively interact with a group of substances, or even specifically with a single molecule. It can be performed by means of several methods. The most commonly used procedures are physioadsorption, covalent attachment and inclusion in a matrix. Fixation of molecules via covalent chemical bonding generally allows obtaining very well ordered and robust functional surfaces. Nevertheless, dense and well ordered layers can also be obtained by means of Self Assembled Monolayers (SAMs). SAMs are ordered molecular assemblies

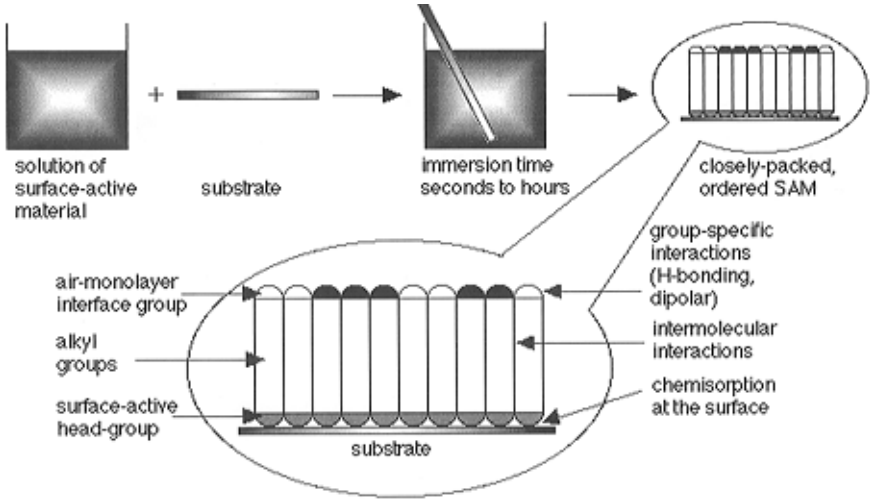

Figure 1.2: Schematic of the self assembly set up [8].

formed by the adsorption of an active surfactant on a solid surface [8] (see figure 1.2). Each constituent is made of three constitutive elements: a *head-group*, a *spacer-group* and a *terminal-group*. The terminal group is designed to allow the molecule attachment to the surface, therefore must have a strong preferential adsorption to the substrate. The functional group is responsible for the properties that the surface will acquire. The spacer group, is an alkyl or an aryl group which is used to connect the other two groups; the SAM arrangement depends on its form and length. In general, SAMs are easy to process: they spontaneously organize onto a substrate forming a two-dimensional assembly by means of chemical bonds' formation with the surface and intermolecular interactions.

1.3 OFET and OECT structures for chemical and biological sensors

Organic Field Effect Transistors (OFETs) and Organic Electrochemical Transistors (OECTs) are the devices most commonly used to realize sensing applications in organic electronics. A variety of configurations have been reported in the literature, nevertheless, the different devices can be grouped within the four approaches represented in figure 1.3 [9], [10]. Devices with the structure reported in figure1.3a are Organic Thin-Film Transistors (OTFTs) with a back gate. Source and drain are separated from gate

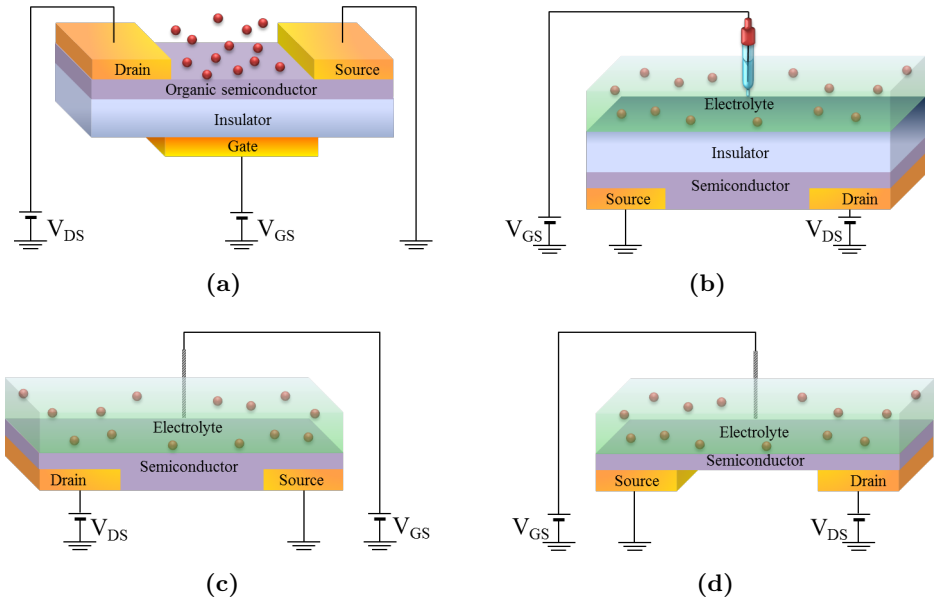

Figure 1.3: Configurations for sensing applications: OTFT (a), ISOFET (b), EGOFET (c) and OECT (d).

through an insulating layer. A conducting channel is established at the gate-insulator interface by applying a proper voltage to the gate. Majority carriers, injected/collected from source/drain by applying a potential between them, form a current flowing along the channel. Therefore, in the organic semiconductor the charge carrier density is controlled by the gate electrode via the electric field applied across an insulating layer; the source-drain current is modulated by the field-effect doping.

Devices structured as shown in figure 1.3b are Ion-Sensitive Organic Field-Effect Transistors (ISOFETs). The insulator is separated by the source and drain contacts through the organic semiconductor on one side, and by the gate contact through an electrolyte on the other. The metallic gate is replaced with a reference electrode, which is used to provide an electrical contact with the electrolyte solution. The reference electrode is characterized by a non polarizable interface, therefore it guarantees a constant potential drop at interface with the electrolyte. As a matter of fact, the electrolyte and the reference electrode forms an ionic gate. In fact, the arrangement of the ions in solution determines a potential drop on the electrolyte-dielectric interface, which is measured through the field-enhanced conductivity of the organic semiconductor. As OTFTs, the source-drain current is modulated by the field-effect doping,

but the electric field across the insulating gate dielectric depends on the charge at the electrolyte-insulator interface.

Device structured as in figure 1.3c are Electrolyte-Gated Organic Field-Effect Transistors (EGOFET(s)). Compared to OTFTs, an electrolyte separates the gate form the semiconductor. When the gate is biased, an electrical double layer is formed at the the interface metal-electrolyte and semiconductor-electrolyte. The source-drain current is modulated by electrostatic and electrolytic doping. As the double layer has a very high capacitance, EGOFET operates at very low voltages.

Finally, in figure 1.3d is reported the typical configuration of the Organic Electro-Chemical Transistors (OECTs). In OECTs the source and drain contacts are connected by a conductive polymer, which acts as channel; the gate electrode is separated from the active layer by the electrolyte, which in OECTs works as insulating gate-dielectric. When a proper bias is applied to gate contact, ions in the electrolyte penetrate the polymer bulk. The interaction between the active layer and the analyte may induce changes in charge carrier density, charge carrier mobility, trap density, charge injection, and other parameters that can alter the measured source-drain current and affect the sensor response. Therefore, conductivity changes of the organic semiconductor are mediated by ions from the adjacent electrolyte, and the current flowing between the source and drain contacts is modulated by the semiconductor electrochemical doping or de-doping. It is the ion conductivity which makes OECTs different from EGOFETs, despite they have similar structures.

OTFTs, ISOFETs, EGOFETs and OECTs, have different performances, which make them especially suitable to be used in a specific kind of application. Biological analytes and biologically derived recognition elements, for example, are only active in aqueous media. Because OTFTs work at high operating voltages, undesired redox reactions in water or biomolecules and de-lamination of the organic semiconductor may occur. Therefore, OTFTs are not especially suitable to be used in these sensing applications. In fact, in most of the published works OFETs operated in the dry state. ISOFETs were realized to overcome the degradation phenomena that generally occur in OTFTs when operating in liquids. Compared to all the other structures where the semiconductor works as active layer and receptor, the sensing function is played by the insulating layer, which also affects the operating voltages required for the sensing application. EGOFETs and OECTs are capable to work in liquid media at very low

voltages (below 1 V); this feature makes them especially suitable for performing analyte detection in liquids. On the other hand, because ions are involved in the sensing mechanism, their switching times are considerably slower those in OTFTs.

1.4 Aim of the project

The topic of this work concerns the realization of chemosensors and biosensors for detection in liquid media. Aiming at obtaining portable and disposable devices, they were realized using organic semiconductor technology, and in particular the OTFT architecture.

Two different kinds of devices suitable for detection of chemical species in liquid environments are under investigation. They are based on different structures, have different working mechanisms and require different techniques; however, both devices can be fabricated on flexible substrates and are potentially integrable in lab-on-chip micro-systems.

From an electronic point of view, the first device works as an OFET, even if it does not fall into the categories reported in section 1.3. The device structure has some original aspects which make it unique with respect to all the other OTFT-based sensors reported in the literature. It is an organic version of a CMOS (Complementary Metal-Oxide Semiconductor) device for charge detection that was previously realized to obtain a portable charge sensor [11], [12]. Compared to the CMOS device, the organic version realized in this work can be considered not only portable, but also disposable. Its architecture allows to overcome several typical drawbacks of the reported sensors for charged molecules detection in liquids media. It has been called Organic Charge-Modulated Field-Effect Transistor (OCMFET) as it is a charge sensor that turns into a chemosensor or biosensor, when the chemical analyte to detect causes a charge variation on the sensitive area of the transistor. A lot of chemical and biochemical analysis are based on charge detection of electrically-charged species, therefore there are many potential fields for employing OCMFET. In this work, it was tested as pH sensor and Deoxyribonucleic acid (DNA) recognition sensor. The choice to apply it for pH detection was driven by the fact that a wide range of chemical reactions heavily depends on acid-base equilibria. For instance, pH fluctuations can heavily influence the rates of biological reactions or even make them possible or not, by activating or deactivating

enzymes. The reason why it was also tested as DNA sensor is that there is an increasing demand for low-cost and portable DNA recognition systems in many fields such as genotyping, medical diagnostics and forensic science. DNA recognition is usually based on optical detection of the DNA double helix formation starting from two complementary strands (*hybridization*). This technique requires several time-consuming, bulky and expensive procedures. DNA probes must be immobilized on a solid substrate, while DNA targets must be labelled with a fluorescent dye. DNA hybridized strands are detected after targets' deposition into the substrate with the probes, and substrate rinsing. In fact the rinsing process removes only the non-complementary targets allowing the complementary DNA detection through fluorescence microscopy. Optical detection entails expensive equipments and laborious processes, therefore, it can hardly be used to realize portable and low-cost devices. Because both DNA probes and targets are charged molecules, the OCMFET can work as a low-cost, portable and label-free DNA sensor integrable in lab-on-chip micro-systems.

The second device is an OECT. Its feature is that all the electrodes are made of poly(3,4-ethylenedioxy-thiophene):poly(styrene sulfonate) (PEDOT:PSS) and realized by ink-jet printing. PEDOT:PSS, which is a commercially available polymer, is a prime candidate for manufacturing polymer-based bio-electronic devices, especially in medical applications, because of its biocompatibility. It has been proven to be a very good cell-culturing material and to be highly stable over a wide range of pH environments [13]. Moreover, ink-jet printing is one of the most appealing techniques as it is low-cost and based on a non-contact, additive approach. All made of PEDOT:PSS ECTs realized by ink-jet printing could be widely used as disposable devices in a wide range of applications. In general, OECTs working regime strongly depends on the device geometry and on the material used for the gate contact. In order to make the all made of PEDOT:PSS device usable in sensing applications, it is essential to know its regime of operation. This study has been done during this work. All made of PEDOT:PSS ECTs were realized and tested with a specific geometry which allows the combination of concurrent electrical and electrochemical measurements.

2

State of the art

In the last decades, driven from the increasing demand for chemosensors and biosensors in various applicative fields, research has produced many results in chemosensing and biosensing. In particular a lot has been done in organic electronics that, with the OTFT-based sensors, has especially met the need of disposable and low-cost devices.

In this chapter, a selection of the most relevant types of chemosensors and biosensors so far realized is reported. The selection was made by considering especially the type of applications addressed with the devices realized in this work. For this reason, as the OECTs realized in this work are made of PEDOT:PSS, only OECT sensors made of PEDOT:PSS are reported. Whenever possible it was chosen to report about applications that were realized by using alternative TFT structures in order to enhance the pros and cons of each architecture. Applications realized with the same structure are grouped into the same section, following, whenever possible, the historical evolution; devices with the same sensing function are grouped into the same subsection. Following this criterion, gas sensors, pH sensors, glucose sensors and DNA sensors are the applications reported in this chapter. Chemical sensors, such as gas and vapour sensors, are interesting for monitoring moisture-sensitive environments, such as glove-box, but can also be applied in food technology, gas-alarm and so on. pH monitoring is a basic application that, on the other hand, combined with the use of a specific recognition function, allows the detection of many chemical and biochemical compounds. The use of an enzyme able to react with glucose for example may convert a pH sensor into a glucose sensor. Glucose level monitoring is a topic of great interest because it is a vital need for millions people suffering of diabetes mellitus. Research has made a lot of efforts

in order to develop glucose sensing. As many glucose sensors have been realized using different TFT structures, thus allowing a comparison between their performances and characteristics, the most interesting applications are reported in this chapter. Finally, DNA sensors are reported with a special care, because they are one of the application studied in this work, and also because the demand for disposable and portable devices for DNA recognition is dramatically increased not only in genotype and medical diagnostics, but also in other fields such as forensic sciences.

2.1 OTFT-based sensors

OTFT-based sensors are generally implemented using bottom-gate structures, which consist of a thin film of an organic semiconductor deposited on top of a dielectric-coated conductor, acting as gate. Several examples are reported of both top-contact structures where source and drain contacts are deposited upon the semiconductor, and bottom-contact where the source and drain contacts are deposited upon the the gate-dielectric layer. The organic semiconductor works as sensing layer and gas detection is achieved through the direct interaction between the semiconductor and the analyte to be tested.

Except for the few examples reported in the literature, OTFTs are not suitable for operation in aqueous media: the high operating voltages needed to operate the device may cause electrochemical reactions and degradation processes which damage the device and affect the reproducibility of results. As a consequence, most of the reported results are related to sensors operating in the dry state. In the following subsections, applications with OTFT-based sensors operating in dry state and aqueous media are reported.

OTFT sensors operating in the dry state

In the following subsections, the most important achievements obtained during the last years with OTFT-based sensors operating in the dry state, such as gas sensors and DNA sensors, are reported .

2.1.1 Gas and vapour sensors

Organic semiconductors, and conducting polymers, are suitable as sensing materials for gas sensors and e-noises fabrication, as they may have a broad variety of interactions

with gases and vapours. Compared to vapour sensors based on metal-oxide active layers, such as Taguchi sensors, gas sensors based on organic semiconductors have proven to enhance chemical sensitivity and to have a lower power consumption.

A few years after the OTFTs were firstly reported in the mid-1980s, the chance to make gas sensing with organic based transistors was investigated. The further development of low-cost fabrication techniques such as ink-jet printing boosted the interest in this area since the year 2000. The most relevant results obtained in gas sensing starting from this date, are reported in the following subsection.

Working principle

As first reported in Torsi *et al.* [14], an OTFT-based sensor allows the unambiguous identification of a chemical species as it works as a multi-parameter sensor. In particular, in addition to the semiconductor bulk conductivity, which is a specific property of the organic thin-film, other three parameters may be derived from the experimental data: the two-dimensional field-induced conductivity, the transistor field effect mobility μ and the transistor threshold voltage V_{TH}. In [15] the authors realized a bottom-contact OTFT on a conductive silicon coated with a dielectric layer, and a thermally evaporated 1,4,5,8-naphthalene tetracarboxylic dianhydride (NTCDA) film as active layer (see figure 2.1a). In the off-state the OTFT works as a chemoresistor: the active

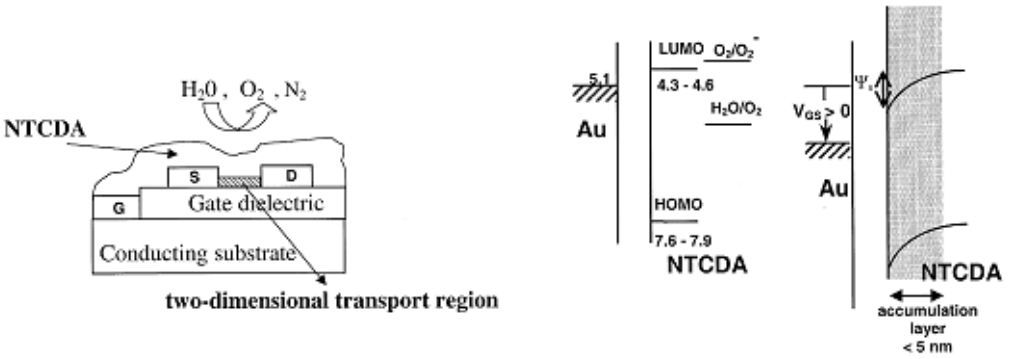

(a) **(b)**

Figure 2.1: Structure of the NTCDA-based gas sensor (a) and energy band diagram for the n-type NTCDA-based transistor: at open circuit left side and at positive gate bias right side (b) [14].

layer conductivity variation upon exposure to the chemical species under examination is derived from the drain current. When the gate is biased, the surface potential at the interface between the active layer and the gate causes the the HOMO (Highest Occupied Binding Orbital) and the LUMO (Lowest Unoccupied Antibinding Orbital) bending, which gives rise to a layer where two-dimensional transport occurs (see figure 2.1b).

In general, the transistor threshold voltage and mobility depend on the volume density of the trapped charges and on the potential barrier at the contacts; as several chemical species give rise to charge trapping-detrapping processes, the interaction of the transistor active layer with reactive molecules causes V_{TH} and μ variations and also changes in the corresponding drain currents. Therefore, molecular recognition is allowed by subtracting the device response, obtained by exposing the semiconductor to the analyte, to the one obtained without the analyte application.

The OTFT trans-characteristics are usually evaluated at a fixed drain potential, chosen in the saturation region. Conducting polymers, especially highly doped electrochemically grown films, are not very stable once a current has passed through them. In order to reduce potential damaging of the active layer, that can compromise the device reliability, performances are kept under control by measuring the currents with the device operating in pulsed mode, both when the analyte is absent (baseline current) and present [16]. In general, the signal does not return to the baseline once the analyte is removed, therefore responses are not spontaneously reversible. Nevertheless, a good response repeatability can be obtained by applying a reverse-gate-bias pulse after each forward pulse; this reverse pulse resets the device and the current is brought back to the original baseline.

Sensing mechanisms

The extent and nature of the response in an OTFT-based gas sensor depends on the mechanism associated with the semiconductor-analyte pair. There is a wide range of response mechanisms that can be used to design semiconductors specifically engineered for odour sensing, that is to realize combinatorial arrays of sensors able to respond differently to the components of an odour mixture.

In 2001 Crone *et al.* [17] reported that OTFT sensors, based on different types of organic semiconductor, are sensitive to different types of primary alcohols, starting

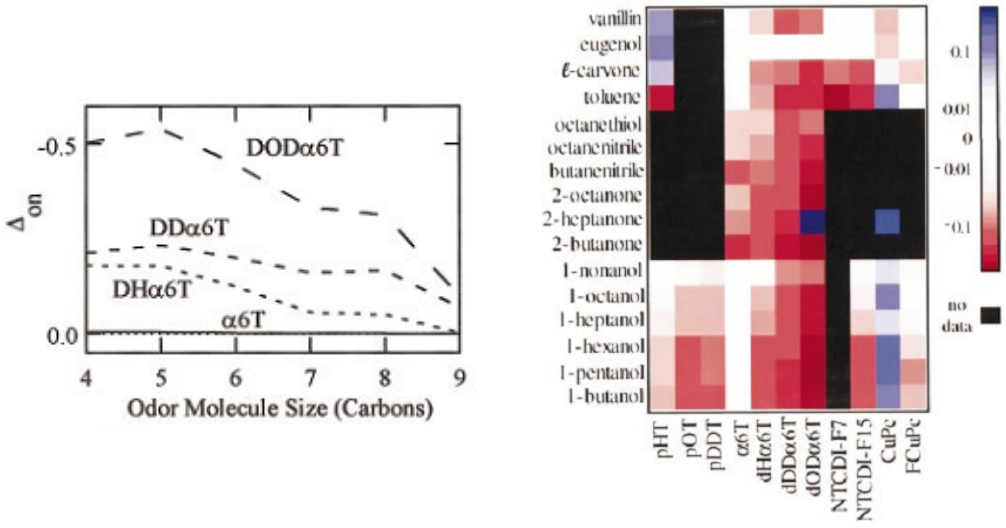

(a) **(b)**

Figure 2.2: Fractional current change in sensor current produced by different 1-alcohols (butanol through nonanol) on α-sexithiophene (α6T), di-hexyl α-sexithiophene (DHα6T), di-dodecyl α-sexithiophene (DDα6T), and di-octadecyl α-sexithiophene (DODα6T); map illustrating the effect of 16 analytes on 11 sensor materials: black indicates that data are not available, white indicates negligible response, blue shows positive changes in sensor current, while red shows decreases (b) [17].

from butanol to nonanol, and that the degree of odour response increases as the length of the semiconductor hydrocarbon end-group increases (see figure 2.2a).

On the contrary, ketones and nitriles, which have a strong dipole moment, results in a threshold shift and a change in mobility with gate bias. Figure 2.2b summarizes the responses of 11 organic semiconductors to 16 vapours.

As previously mentioned, the sensing mechanism in an OTFT-based gas sensor results form the interaction between the gas molecules and the organic semiconductor. Thus, the largest is the surface of interaction, the higher is the potential for device sensitivity. As a consequence, it was expected that the surface morphology of the active layer plays an important role in an organic gas sensor response. In order to highlight its influence several investigations were conducted during the last decade.

In 2001, Someya *et al.* [18] conducted a systematic study in order to define the role of the grain boundaries on the sensing mechanism. They realized OTFTs with

α,ω-dihexylquarterthiophene (DHα4T) as semiconductor. They compared the performances of devices having a DHα4T single crystal as semiconductor, and the ones of devices with polycrystalline DHα4T films as active layer. They gas-induced currents' variation are strongly correlated with the channel length. A very small response to vapour analyte was recorded in devices with no grain boundaries or having only a single grain boundary inside the active region, while higher current variations were measured in devices with polycrystalline films. These results demonstrate that the interaction between the organic semiconductor ad the gaseous analyte mainly occurs at the grain boundaries.

Correlations between the morphological structure of the active thin-film and responses to different kind of vapours were also investigated by Torsi *et al.* [19] by the combined use of electrical measurements of transient source-drain current under vapour flow and morphological characterization of the organic thin films by Transmission Electron Microscopy (TEM). They realized several DHα6T-based OTFTs on a highly conducting silicon wafer coated with silicon dioxide. TEM analyses revealed that DHα6T films, with the same nominal thickness, show a morphology which depends on the substrate temperature maintained during their deposition. Film morphology at room temperature and $T = 70$ °C (see figures 2.3a and 2.3b) consists of small and irregular nanodomains with diffuse grain boundaries, while at higher temperatures, the granular look is replaced with a lamellar one exhibiting a lower surface roughness (see figures 2.3c and 2.3d). When the DHα6T-based sensors are exposed to an alcohol such as 1-pentanol, the change in the square root of drain currents ($[Id^{1/2}(sig)1/2 - Id^{1/2}(bg)1/2]$) vs the gate potential V_g plots shows two distinct regimes (see figure 2.3e). The responses of samples grown at $T = 70$ °C or at lower temperatures are more intense than those of samples grown at higher temperatures. This result confirms that the OTFTs sensitivity to alcohol odours depends on its ability to adsorb on grain boundaries. In fact, the response is stronger for the low-temperature grown films, which have more grain boundaries, and weaker for those grown at high-temperature, as the elevated temperature promotes the formation of large, regular and flat grains, giving rise to a more compact morphology. On the other hand, the electrical responses recorded by the DHα6T-based sensors exposed to octanenitrile (see figure 2.3f) does not show any particular dependence on the substrate temperature and, as a consequence, on the film

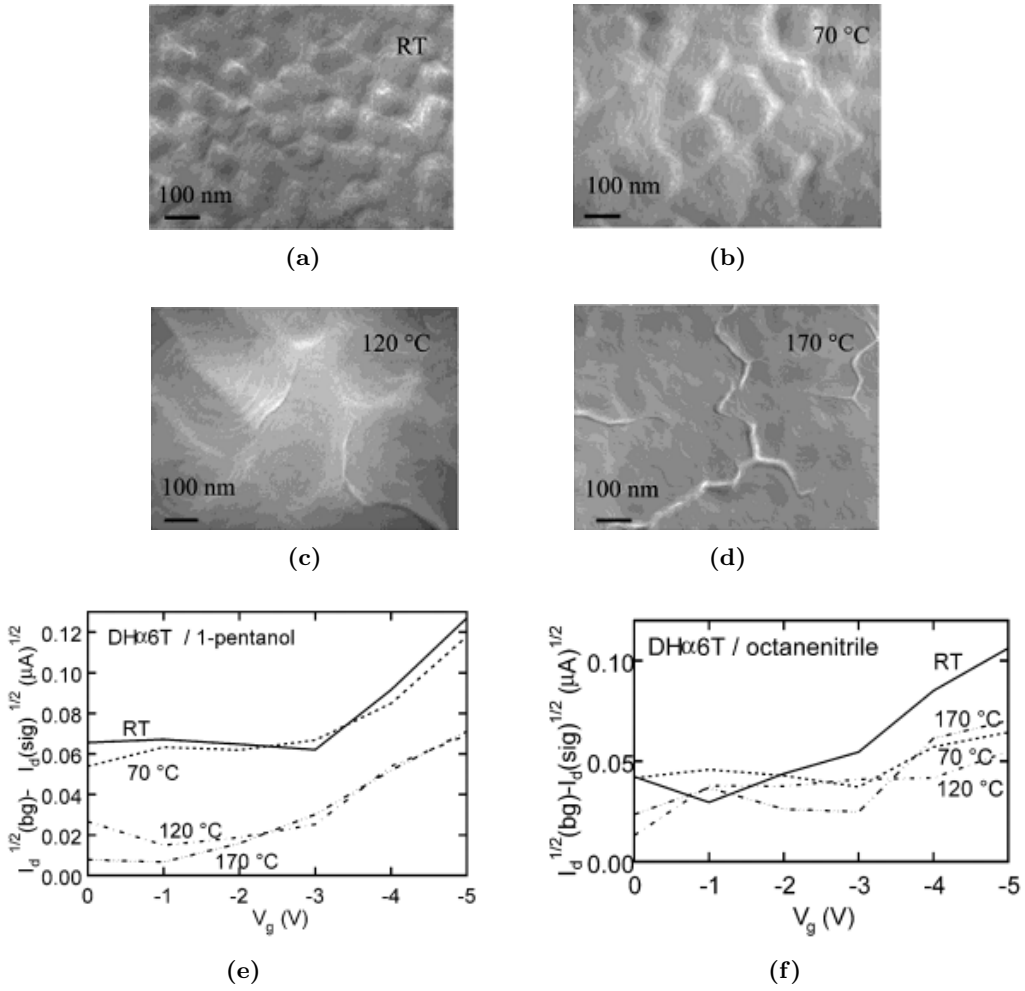

Figure 2.3: Transmission electron micrograph from a DHα6T film deposited by thermal evaporation keeping the substrate at nominally room temperature (a), T = 70 °C (b), T = 120 °C (c) and T = 170 °C (d); change in square root of drain current as a function of gate voltage, for sensors with DHα6T films deposited at different substrate temperatures exposed to 1-pentanol (e) and to octanenitrile (f) [19].

morphology. Therefore, the highly dipolar nitrile functional group might create an effective hole trap, which does not specifically occurs on the grain boundary.

As the film morphology depends on the film thickness, Torsi *et al.* [19] also investigated the relation between the film thickness and the sensor response. Figures from 2.4a to 2.4d show the morphology of DHα6T films with different thickness deposited at room temperature. The surface morphology appears more structured, contiguous with

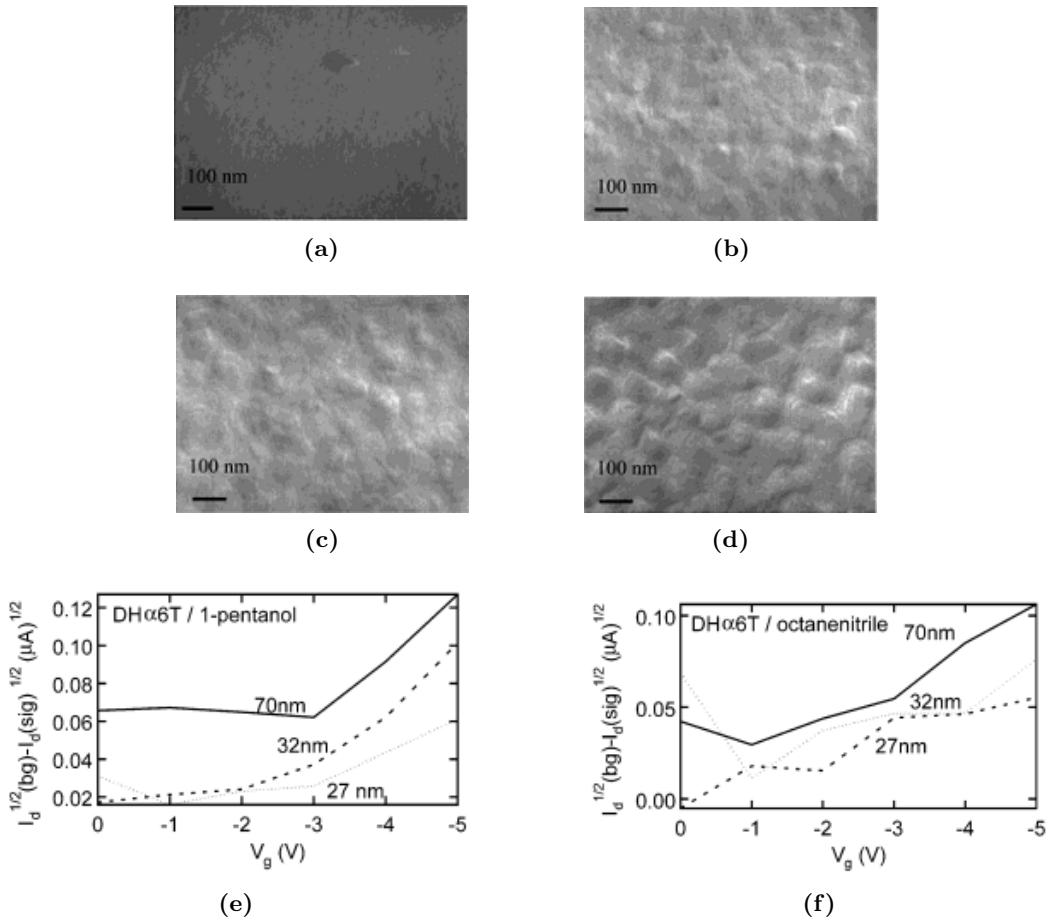

Figure 2.4: Transmission electron micrograph from a DHα6T film of different thickness: 27 nm (a), 53 nm (b); 61 nm (c) and 70 nm (d), deposited by thermal evaporation keeping the substrate nominally at room temperature; change in square root of drain current as a function of gate voltage, for sensors with DHα6T films of different thickness exposed to 1-pentanol (e) and to octanenitrile (f) [19].

higher and elongated grains in thicker specimens.

Figure 2.4e shows the electrical response recorded by several OTFTs, with a different thickness of the active layer, exposed to 1-pentanol. When increasing the semiconductor thickness, and as a consequence the grains' number and boundaries, the sensor response increases too. Accordingly with the results obtained on the temperature influence on the device fabrication, the semiconductor's interaction with 1-pentanol mainly occurs at grain boundaries. A less conclusive result was recorded from sensors exposed to

octanenitrile 2.4f. Because of the different interaction mechanism between the vapour and the active layer, grains and grain boundaries can not be considered preferential interaction sites. Finally, Torsi *et al.* [19] examined the effect on the sensor response due to the morphology of a series of alkyl-substituted hexathiophenes homologues such as α-sexithiophene (α6T), α,ω-dibutyl-α6T (DBα6T), α,ω-di-dodecyl-α6T (DDDα6T), α,ω-dioctadecyl-α6T (DODα6T), and α,ω-dihexyl-α-quaterthiophene. Their experimental results confirmed what already reported by Crone [17]. The larger alkyl substituents on the oligomers enhance the device response by changing the electronic or spacial barriers between grains, and by increasing the grain surface adsorption ability and accessibility.

Pentacene is a very commonly used p-type organic semiconductor because of high mobility. In 2002 Zhu *et al.* [20] demostrated that it is sensitive to H_2O vapour. They realized a bottom-contact transistor on a degenerate p-doped Si wafer coated with SiO_2 as a dielectric layer. the source and drain electrodes made of gold were photolithographically patterned to have a $W/L = 30$ ratio. Pentacene was grown by vacuum sublimation. A schematic representation of the device in shown in figure 2.5a; an experimental result is reported in figure 2.5b. The source-drain current was measured keeping gate and drain at –100 V. The OTFT was exposed to vacuum and N_2 gas with different levels of relative humidity (RH) alternatively. A saturation current change by as much as 80 % was recorded when the RH changes from 0 to 30%, thus proving

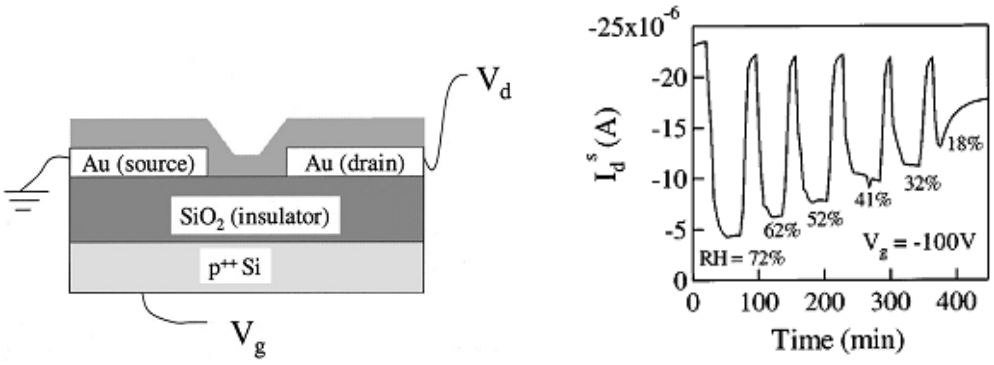

(a) **(b)**

Figure 2.5: Schematic of the Pentacene TFT (a) and experimental result: time dependence of the saturation current measured at a gate and drain voltage of –100 V after exposition to wet N_2 gas with different relative humidity and vacuum, alternatively (b) [20].

that the saturation current of a Pentacene is a good parameter to monitor RH changes in the atmosphere. The authors related the working mechanism to the semiconductor morphology. Even if Pentacene is highly hydrophobic, because its morphology is relatively open, H_2O molecules can easily diffuse into the large crevices between the grains thus reaching the first few monolayers on the substrate. A rate decrease of charge transport in organic materials as Pentacene is caused by polar molecules such as H_2O that, through charge-dipole interactions, cause an increase of the amount of energetic disorder.

In 2004 Wang *et al.* [21] extended to the nanoscale dimension the findings obtained by Someya *et al.* [18] and Torsi *et al.* [19]. Using Pentacene as active layer, they realized several bottom-contact transistors with different channel lengths from long to very short. By exposing Pentacene the devices to 1-pentanol, they found that the nanoscale and large-area sensors have different behaviours. The long-channel length devices exhibit a current decrease upon delivery of the analyte, while the small-channel length ones show an increase (see figure 2.6).

According to their exploitation, two different mechanisms influence the sensor behaviour: one is dominant in long-channel devices and is responsible for the current decrease; the other is dominant in small-channel devices causing the current increase. One the one hand, because of their dipole nature, the alcohol molecules deposited at the

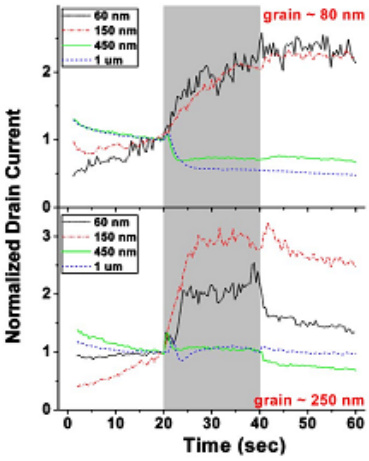

Figure 2.6: Drain current variation measured at gate and drain potential of 2.5 V and normalized to that measured just before the analyte delivery, for 80 nm Pentacene grain size and different nanoscale channel lengths ($W/L = 10$) [21].

grain boundaries, will trap the mobile charge carriers from the channel, thus decreasing the current. On the other hand, the analyte and the semiconductor inside grains will entail an excess of holes through a different chemical processes that are not completely understood. The first phenomenon is especially dominant in those devices which have enough grain boundaries inside the channel, that is, in devices with a longer channel relative to grain sizes. In those devices that have a very few number of grain boundaries inside channel, the chemical interaction predominates on the first phenomenon leading to the increase of currents.

Sensing enhancement

By employing different active layers, OTFT gas sensors have already been demonstrated to respond to a large variety of vapours with good stability and significant sensitivity. Nevertheless, improvements in selectivity and sensitivity are required in order to move this technology beyond the laboratory stage. To enhance gas sensors sensitivity and improve discrimination between vapours of small-molecule analytes, an interesting strategy was developed by Sokolov *et al.* [22]. They incorporated calixarene as container molecules onto the surface of an existing OTFT, so that the tunable nature of the container cavity serves to trap desired molecular shapes and functionalities with typically high selectivity. In particular, they deposited calix[8]arene (C[8]A) and C-methylcalix[4]-resorcinarene (CM[4]RA) on a 5,5′-bis-(7-dodecyl-9H-fluoren-2-yl)-2,2′-bithiophene (DDFTTF) layer used as organic semicondutor of a top-contact transistor. Figure 2.7 shows the C[8]A (a) and CM[4]RA (b) molecules, a cartoon of the OTFT device (c) and some experimental results. The sensor response after the analyte exposure was reported in terms of time variation of the drain current I_{DS} (dI_{DS}/dt). A good enhancement in the OTFT rate response was recorded for several calixarene-modified devices exposed to different types of analytes. For a C[8]A-modified device, a strong response was recorded after the exposure to ethyl acetate with a concentrations of 200 ppm, while an exposition to a concentration of 1000 ppm was required in order to obtain a corresponding signal in a bare DDFTTF device. Data also showed that calixarenes assist selective gas adsorption onto the semiconductor surface increasing the sensor selectivity, and passively prevent the interaction of undesired analytes through steric surface blocking.

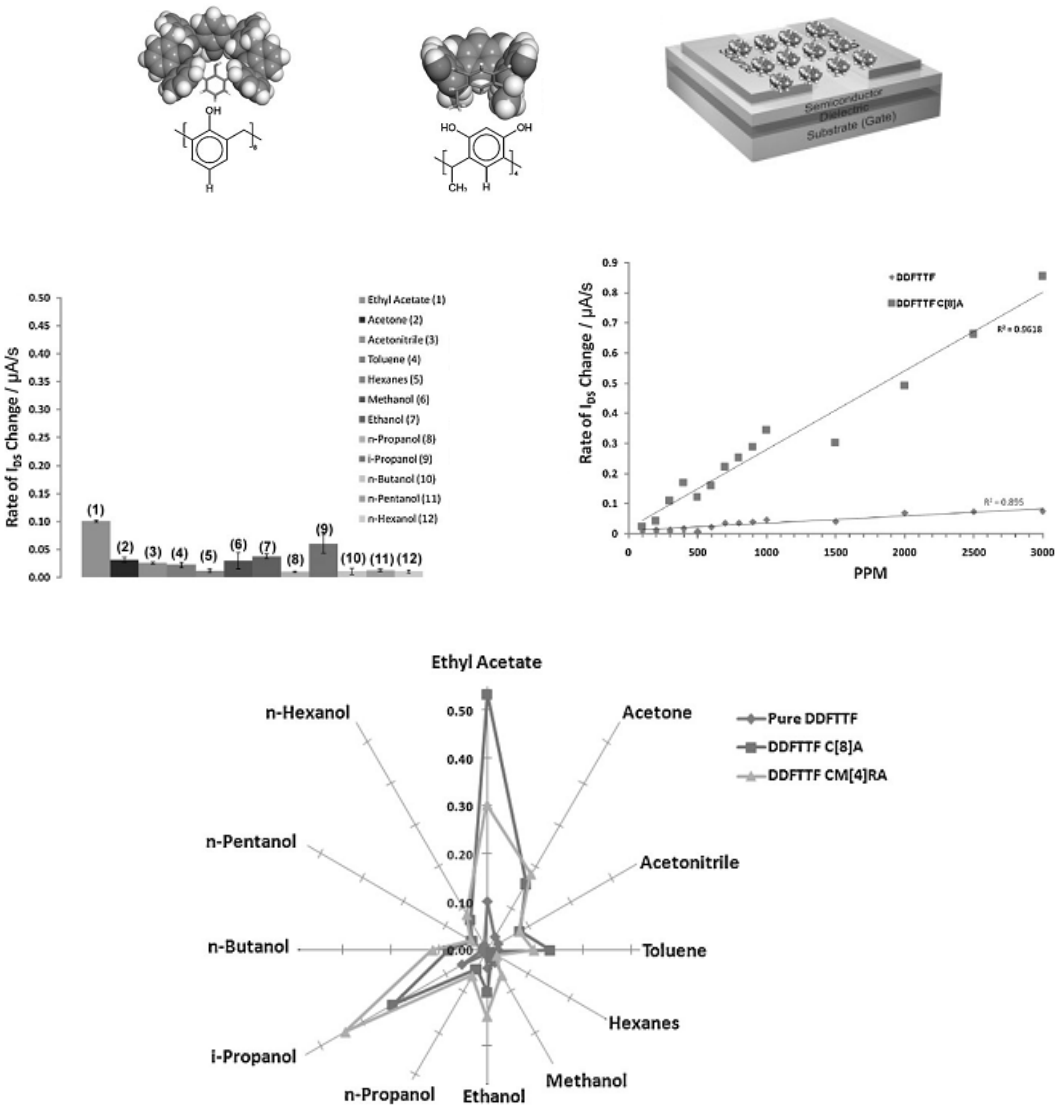

Figure 2.7: Representations of C[8]A (a) and CM[4]RA (b) molecules, cartoon of a calixarene-modified OTFT (c) and experimental results: average rate of response for a DDFTTF-based OTFT to series of analytes at a concentration of 3000 PPM (d), sensitivity enhancement between bare and C[8]A modified DDFTTF (e), and radial graph showing the enhancement of the calixarene-modified DDFTTF-based OTFT response to a series of volatile anlytes (f) [22].

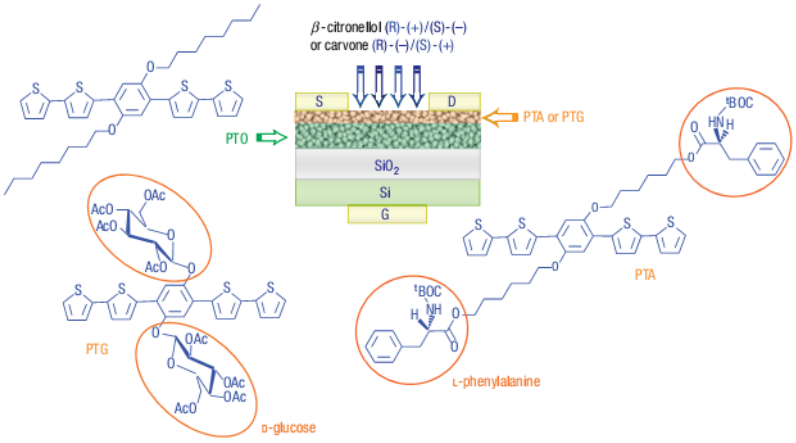

(a)

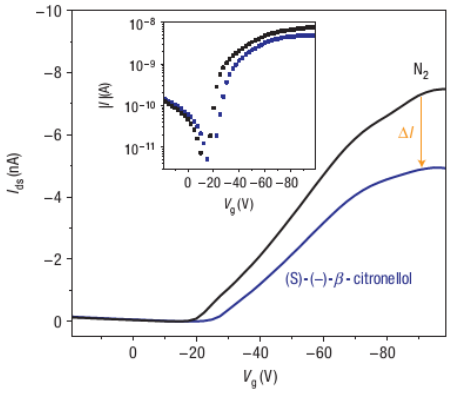

(b)

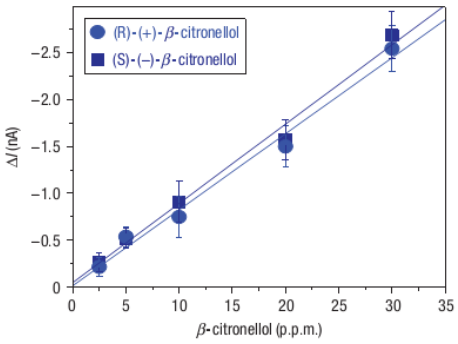

(c)

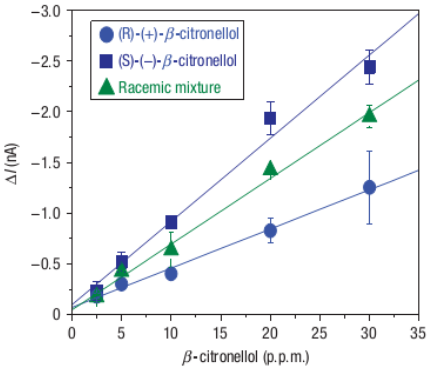

(d)

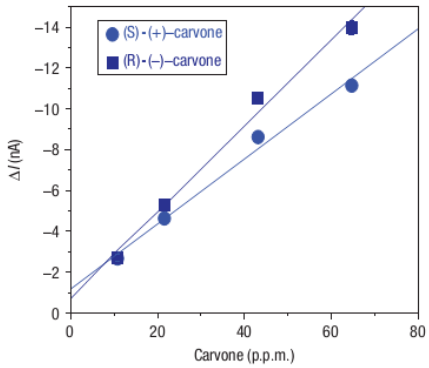

(e)

Figure 2.8: PTOPTA-bilayer OTFT transfer characteristics (drain potential $V_{ds} = -50V$) under a flux of nitrogen and of (S)-(−)-β-citronellol in N_2 (a); current variation ΔI (gate potential $V_g = 100$ V and drain potenial $V_{ds} = 50$ V) of a PTO achiral sensing transistor exposed to (S)-(−)-β-citronellol and (R)-(+)-β-citronellol (b); calibration curves of: PTO-PTA OTFTs exposed to (S)-(−)-β-citronellol and (R)-(+)-β-citronellol and to the racemic mixture (c), PTO-PTG OTFTs exposed to (R)-(−)- and (S)-(+)-carvone (c) [15].

Concerning selectivity to different type of gases, a challenging issue is represented by recognition of volatile chiral molecules. In order to obtain an OTFT sensor for chiral recognition, Torsi *et al.* [15] implemented a bilayer sensing OTFT able to combine field-effect and chiral-recognition properties. They realized bottom-gate transistors having two alkoxyphenylenethiophene oligomers, named PTO and PTA or PTG, as active layers (see figure 2.8a). The alkoxy-substituted phenylene ring is a structural unit, which enables the introduction of a wide variety of covalently bound substituents, while the L-phenylalanine amino acid and the β-D-glucosidic substituents, in PTA and PTG respectively, allow the chiral recognition. Therefore, while the PTA and PTG are chiral molecules, PTO is achiral. Plots in figure 2.8b show that the current decreases in the whole on-state regime when a PTO-PTA OTFT is exposed to a citronellol atmosphere. Picture 2.8c reports the calibration curve of an achiral single-layer PTO OTFT exposed to both the (S)-(–)-β-citronellol and (R)-(+)-β-citronellol vapours separately and at different concentrations; the slope of the calibration curves does not significantly differ for the two enantiomers as PTO is achiral. On the contrary, a current variation which linearly increases with concentration is recorded in the calibration curves of the PTO-PTA OTFT exposed to citronellol isomers (see figure 2.8d) and those of the PTO-PTG OTFT exposed to carvone enantiomers (see figure 2.8e). Interestingly, the sensitivity for the racemic mixture of citronellol (50% of each enantiomer) falls right between the previous two.

2.1.2 DNA sensors operating in the dry state

The first DNA sensor based on transistor was reported in 2007 by Zhang and Subramanian [23]: the DNA recognition occurred through electrical detection of DNA hybridization by measurements performed in the dry state. They realized bottom-gate transistors using a heavily doped silicon wafer as gate, coated with one hundred nanometers of SiO_2; gold source and drain contacts were realized by means of lithographic process and a thin layer of Pentacene was thermally evaporated to obtain the active layer. Pentacene was chosen for its good stability and also because it allows the physical immobilization of DNA molecules on the exposed channels: as both Pentacene and DNA molecules are hydrophobic, physioadsorption is made possible by their hydrophobic interactions (see inset in figure 2.9a). The sensing mechanism is based on the doping effect induced by the immobilized DNA molecules on the active layer, which

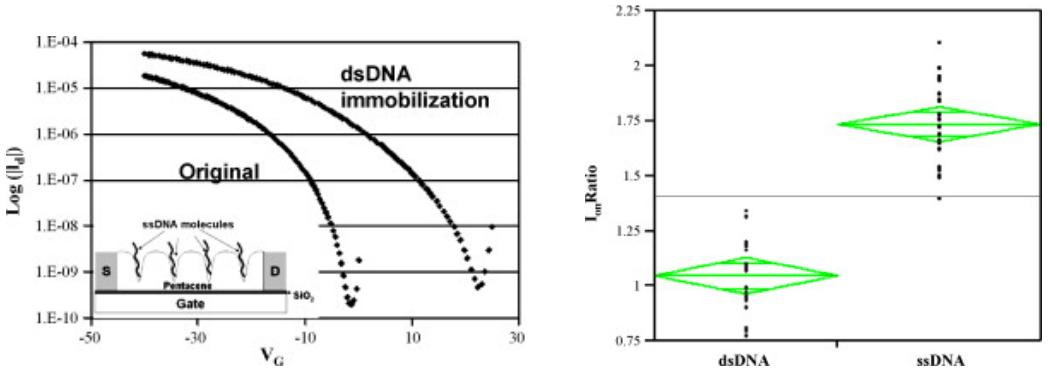

Figure 2.9: Schema of the OTFT-based DNA sensor ($W/L = 10$) (a) and experimental results obtained by Zhang [23]: transfer curves obtained with drain voltages at 45 V (b) and differential sensitivity of ssDNA and dsDNA obtained as ratio between the post-DNA-exposure drain saturation current to the original TFT one (c).

is a p-type semiconductor that works in accumulation mode: the negative phosphates groups in the DNA molecules attract holes in the transistor channel, thus causing a current increase and a positive shift of the threshold voltage. To maintain their activities, DNA molecules must be dissolved in specific buffer solutions. In order to establish a baseline, the authors studied the transistor performances under the effect of the pure buffer solution, following the same recipe as in the DNA experiments. The sensor response was then extracted by subtracting any current change caused by the buffer solution from the change recorded by the buffer containing the DNA. Figure 2.9a shows the transfer characteristic shift recorded after the exposure to double-stranded DNA (dsDNA). DNA molecules ranging from 125 to 23,130 base pairs, were tested and the thickness and roughness of the Pentacene layer was varied in order to optimize the sensor response; the maximum response point was estimated to be at a DNA concentration of 250 μg/ml and a Pentacene thickness of 100 Å. A statistical comparison between the sensor response obtained after single-stranded (ssDNA) immobilization and its hybridization is shown in figure 2.9b. After hybridization, negative charges in the DNA backbone will double and, as a result, an increase in the doping effect would have been expected. On the contrary, data reported in 2.9b shows that the doping effect recorded after hybridization was lower than the one measured after ssDNA immobilization. A possible explanation for this result was ascribed to the reduced immobilization

efficiency of dsDNA with respect to ssDNA. According to the authors, it is just the differential sensitivity with respect to ssDNA and dsDNA doping that would enable the unambiguous detection of DNA hybridization.

The working mechanism of ultra-thin film transistors based on Pentacene after the exposure to a poly-electrolyte environment, and, in particular, the effects induced on this kind of sensors from DNA was then studied by Stoliar *e al.* [24]. They investigated the relationship between the pinch-off voltage and the DNA concentration by performing both electrical characterization of OTFT based on Pentacene and Atomic Force Microscopy (AFM) characterizations of the active layer surface. Figure 2.10a shows the device schematic: it is a bottom-gate transistor with channel length L and width W ranging from 10 to 40 μm and 1 to 20 mm, respectively. Figure 2.10a shows that the Pentacene layer in the transistor channel is made of two stacked molecularly ordered monolayers with a height of 1.5 nm. Figures from 2.10c to 2.10f report the AFM images

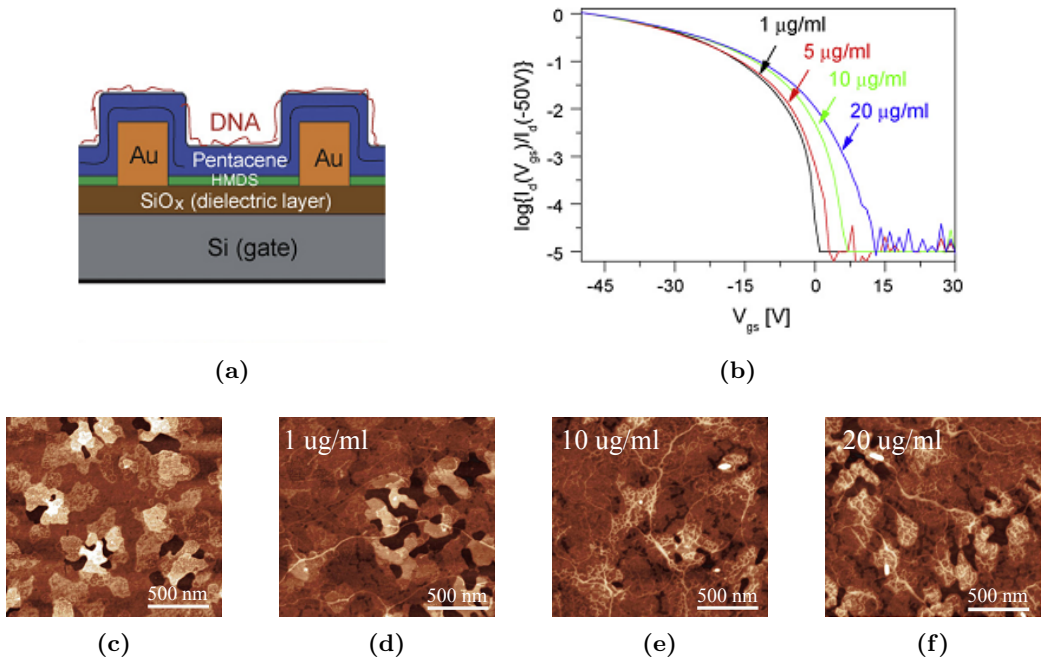

Figure 2.10: Schematic of the Pentacene-based OTFT (a) and AFM images of: Pentacene film in the transistor channel (b), Pentacene after the deposition of a DNA solution with a concentration of (c) 1 μg/ml, (d) 5μg/ml, (e) 10μg/ml and (f) 20μg/m; device transfer characteristics at different DNA concentrations (g) [24].

of DNA deposited on Pentacene at different concentrations: 1 μg/ml, 10 μ/ml and 20 μg/m. The adsorption of linear DNA give rise to the formation of bundles consisting of a few molecules (figure 2.10c); at higher concentrations (figures from 2.10d to 2.10f), a hierarchical DNA network is formed, where larger bundles are entangled with small DNA chains.

Finally, figure 2.10b reports the transfer characteristics of several sensors at different DNA concentrations. When the DNA concentration increases, the pinch-off voltage V_p, which is the gate value at which all the positive charge carriers are expelled from the channel, shifts towards more positive voltages. This result implies that the negatively charged DNA molecules induce an extra density of positive charges in the channel; and, as a consequence, an additional gate voltage is needed to deplete the transistor channel.

In a later work, Zhang *et al.* [25] further investigated the working mechanism of these DNA sensors. They used Kelvin Probe Microscopy (KPM) and Space Charge Limited Current (SCLC) techniques in order to study the physics of DNA sensitivity; moreover, they performed Time-of-Flight Secondary Ion Mass Spectrometry (ToF-SIMS) analysis in order to obtain a visual proof of DNA on the active surface layer and correlated images with electrical results. Finally, aiming at realizing a sensor for label-free readout of on-chip DNA hybridization, they presented a novel photolithography-based method which allows to build microfluidic systems on organic semiconductors. The microfluidic system implemented on the active layers permits to automatically deliver the DNA solution to the detection sites. They demonstrated that the data variation reduces when using the microfluidic system for DNA delivery, and when obtaining regular active surfaces by depositing the semiconductor films at low rate.

A similar approach was used by Kim *et al.* [26] that obtained DNA sensors using top-contact OTFTs built on a glass substrate. The gate-dielectric was made of a poly(4-vinylphenol) (PVP) layer, with a thickness of 480 nm, deposited over an aluminium gate; gold was used to realize source and drain contacts ($W/L = 10$) (see figure 2.11a). They also used Pentacene as organic semiconductor, because it allows the physioadsoption of DNA molecules on its surface through their hydrophobic interactions. Nevertheless, compared to the device realized by Zhang and Subramanian, this device has an opposite behaviour which can be ascribed to the different thickness of the organic semiconductor. In fact, as the DNA molecules were anchored on top of a much thicker layer (70 nm), DNA negative charges remove holes from the channel

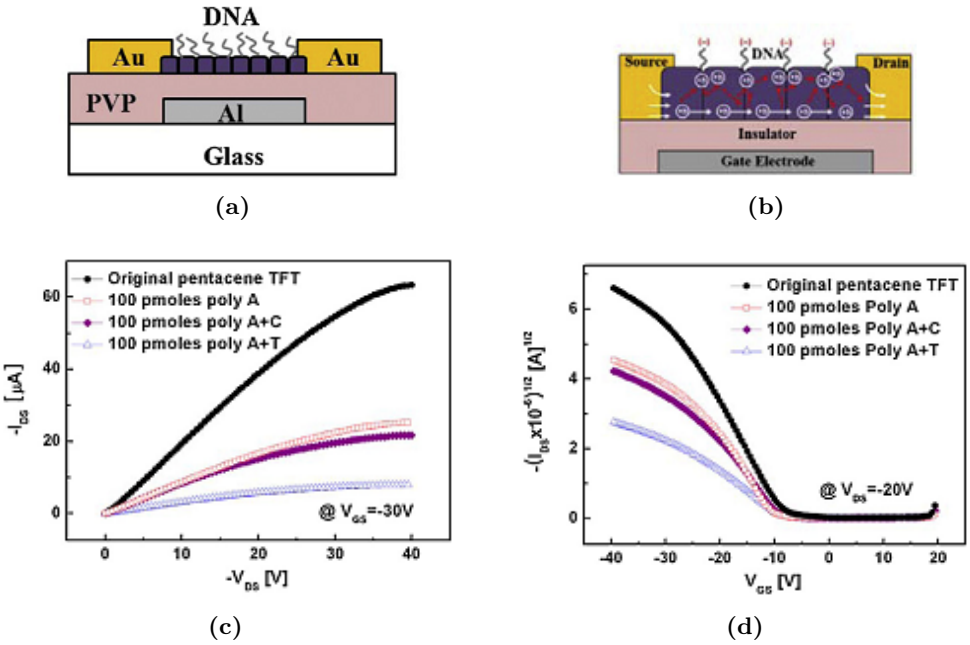

Figure 2.11: Sensor developed by Kim *et al.* [26]: schematic (a) and sensing mechanism (b); output (c) and transfer characteristics of the original device, after deposition of ssDNA (poly A), of a non-complementary (polyC) and complemenary target (polyT).

causing a decrease in the transistor current. Figures 2.11c and 2.11d show the output characteristics and the transfer characteristics, respectively, of a single sensor in the following conditions: original device, after a ssDNA (poly A) immobilization, after the deposition of a not complementary DNA (polyC) and a DNA complementary to ssDNA-polyA (polyT). According to the sensing mechanism previously described (see figure 2.11b), a lower current is detected after ssDNA immobilization and after the deposition of its complementary strands. No significant current variation is measured after the deposition of a not-complementary DNA (polyC); this result confirms that polyC does not immobilize on the Pentacene layer where polyA has been anchored, and that polyC does not hybridize to polyA.

Concerning DNA sensors based on the semiconductor functionalization, recently Liu *et al.* [27] demonstrated that the functionalization time can be reduced and the immobilization efficiency can be improved by attracting the negatively charged DNA molecules onto the Pentacene surface with a positive bias between source and gate contacts.

Approaches based on DNA probes immobilization on the active layer surface present an important drawback. Organic semiconductors are in general sensitive to the environmental conditions, and in particular Pentacene is sensitive to ionic solution exposure. Because the functionalization and hybridization procedures are generally realized in liquid, they can compromise the device stability and repeatability. Aiming at reducing the semiconductor degradation, a different approach was proposed by Yan *et al.* [28]. The DNA recognition is made by comparing the electrical response of a group made up with three bottom-gate transistors. Having the source and drain contacts functionalized by using ssDNA and dsDNA respectively, two of them were used as sensors, while the last one was used as control device. Each OTFTs was fabricated on a highly doped n-type silicon wafer with a 500 nm thick of SiO_2 as gate-insulator. Gold source and drain electrodes with $W/L = 10$ were deposited on top of the dielectric layer and then functionalized, with ssDNA in one device and dsDNA in another; no functionalization was applied to the source and drain electrodes of the control device. The sensor was finalized with the deposition of a regio-regular poly(3-hexiothiophene)(rr-P3HT) layer, which is a p-type organic semiconductor. Figure 2.12a shows the steps carried out to prepare one sensor. Figure 2.12b and 2.12c show the output characteristic and the transfer characteristic of a three devices' group: under the same bias, higher currents are recorded in the control device, intermediate currents in the device with ssDNA and lower currents in the device with dsDNA. Because of their intrinsic charge, the DNA molecules change the contact resistance and, because dsDNA molecules contain an almost double amount of negative charge, the effect in the dsDNA device is greater than the one observed in the device with ssDNA.

According to the authors, the negative DNA charge causes a decrease of the surface potential, and as a consequence, an increase of the potential barrier which limits the carriers movement across it; as a result, the injection current between source and channel decreases. The increase of the contact resistance due to the DNA molecule is considered small with respect to the previous phenomenon because DNA has been proven to be a good semiconductor.

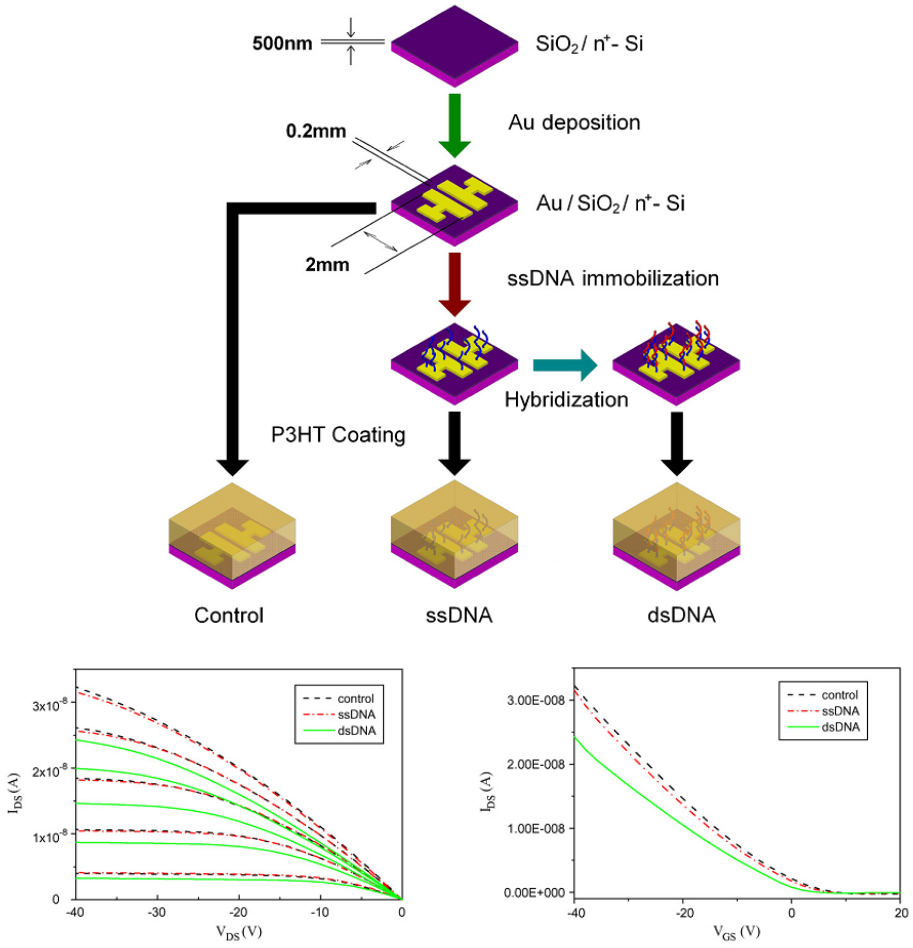

Figure 2.12: Schematic representation of the OTFT sensor fabrication incorporated with DNA layer (a) and experimental results: output characteristic measured at different gate potentials ranging from –40 to to 0 V (b) and transfer characteristic measured at drain potential of –40 V (c) [28].

OTFT operating in aqueous media

As a general rule, OTFTs are not suitable to operate with the active layer immersed in liquid, because the high electrical fields near the source and drain contacts may cause a water-mediated electrochemical reaction. As many reactions can only occur in a liquid environment, there is a great interest in developing potential solutions to overcome this limit. Some interesting approaches, especially for DNA detection, are reported in the following subsections.

2.1.3 Chemosensing in aqueous media

In 2002 Someya *et al.* [29] developed a microfluid flow channel in order to allow the analyte delivery only upon the channel region. They realized top-contact OTFTs on highly doped silicon wafers covered with silicon oxide, used as gate and gate-dielectric respectively. Source and drain with a $W/L = 3.125$ ratio were deposited upon the semiconductor layer. In order to confine the analyte to the central part of the active channel, above the organic semiconductor layer but away from the source and drain contacts, they coated the contacts with a fluorinated polymer, which is an hydrophobic material. This system allows driving the fluid in contact with the active region perpendicularly to the electronic current flow direction. Figure 2.13a and 2.13b show a section of the structure and a device top-view respectively. The OTFTs response was tested by measuring the drain current as a function of time and analyte after applying a source-drain voltage. Organic semiconductors such as Pentacene, R-sexithiophene (R6T), dihexylR6T (DHR6T) and copper phthalocyanine (CuPc) were able to operate under water, with and without analayte, for a few hours or dozens of cycles. They investigated several combinations of semiconductors and analytes: R6T was responsive to glucose, while CuPc was not; R6T and DHR6T responded to lactic acid CuPc was also sensitive to pyruvic acid. Nevertheless, the formation of ionic current channels between the electrodes and the de-lamination of the semiconductor from the dielectric layer are water-induced degradation mechanisms, that reduce the chance to obtain technologically valuable systems.

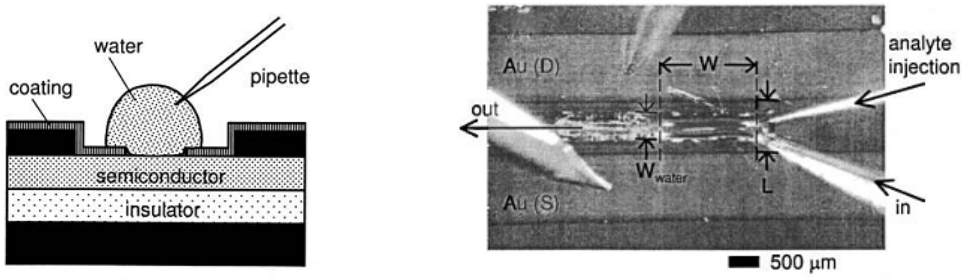

(a) **(b)**

Figure 2.13: Basic structure of the organic semiconductor device (a) and configuration of the analyte delivery system (b) [29].

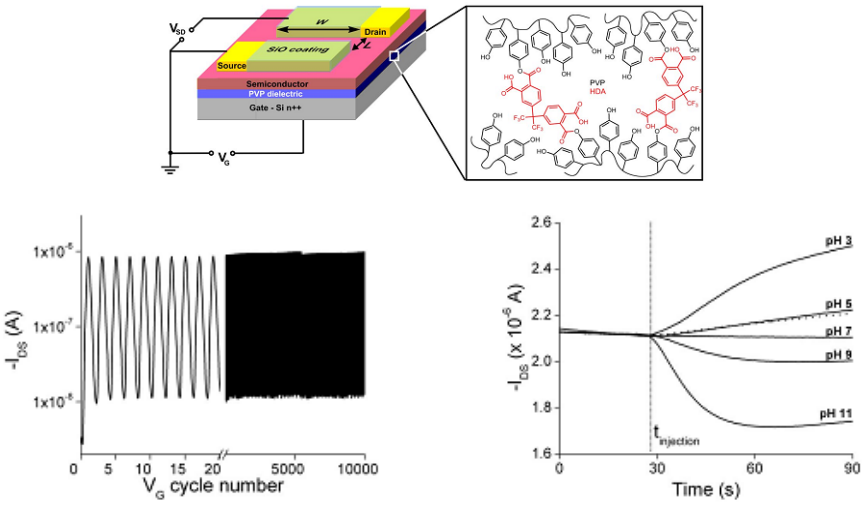

Figure 2.14: Structure of the top-contact sensor and chemical structure of cross-linked PVP with HDA (a); experimental results: drain current versus gate potential at a drain potential of 0.6 V measured over 10^4 cycles (b); drain current response at the pH 5 solution were measured before (solid) and after (dashed) the exposure to other pH solutions (c) [30].

In 2008 Roberts *et al.* [30] demonstrated that a low-voltage OTFT can work in aqueous media. They realized a top-contact transistor using a thin layer of poly(4-vinylphenol) (PVP) cross-linked with 4,4-(hexafluoroisopropylidene)diphthalic anhydride (HDA) as gate dielectric, in order to achieve the low-voltage behaviour. The device operation under aqueous conditions was characterized using 5,5′-bis-(7-dodecyl-9*H*-fluoren-2-yl)-2,2′-bithiophene (DDFTTF) as organic semiconductor. Figure 2.14a shows a scheme of the device and the experimental results. The device operational stability is shown in figure 2.14b: the drain current recorded with a source-drain voltage of 0.6 V remained constant by cycling the gate bias for more than 10^4 cycles. They tested the device sensitivity with respect to several analytes such as trinitrobenzene (TNB), glucose, cysteine, and methylphosphonic acid (MPA), and also with respect to H_3O^+ concentration. The device response as pH sensor is reported in figure 2.14c.

2.1.4 DNA sensors operating in aqueous media

In 2010 Khan *et al.* [31] reported another device for DNA detection in liquid environment. They deposited a protective layer upon the semiconductor which prevented its degradation and made possible DNA detection in liquids. The working principle

is based on the extraction of holes from the channel upon hybridization. Compared to all the previously reported devices, this device is the most sensitive and selective. In fact, it operates with low voltages, below 1 V, thus allowing stable OTFT performances even when operating in aqueous media. These performances were obtained by realizing a top-contact transistor with 22 nm of cross-linked poly(4-vinylphenol) PVP polymer as gate-dielectric and 15 nm of 5,5′-bis-(7-dodecyl-9H-fluoren-2-yl)-2,2′-bithiophene (DDFTTF) as organic p-type semiconductor. The source and drain electrodes ($W/L = 80$), made of gold, were coated with 50 nm of thermally evaporated silicon monoxide; this layer, which acts as electrical insulator and chemical barrier against the ions in solution, was deposited in order to reduce the influence of charge screening on the detection signal. By means of a Plasma-Enhanced Chemical Vapour Deposition (PE-CVD), an ultra-thin film (5 nm) of poly-maleic anhydride (pMA) was deposited upon the semiconductor in order to protect it during the functionalization, and to provide a contiguous functional layer for probes anchorage. Amine-terminated peptide nucleic acid (PNA) were covalently attached to the pMA layer as selective probe to target DNA. PNA is an artificially synthesized polymer having repeating N-(2-aminoethyl)-glycine units linked by peptide bonds rather than the deoxyribose sugar backbone of DNA. Compared to its DNA conterparts, which are negatively charged, PNA strands are neutral; this property allows hybridization with a greater selectivity, affinity and stability as it reduces the electrostatic repulsion between two complementary strands. Finally, a flow cell was laminated upon the OTFT surface in order to allow the solution delivery to the channel region of the interdigitated electrodes. Figure 2.15a summarize a schematic representation of the sensor fabrication while the experimental results recorded to highlight the sensor response to complement DNA-PNA and to mismatch PNA-DNA hybridization are shown in figures 2.15b and 2.15c respectively. In particular, figure 2.15b shows a comparison between the drain currents recorded in a sensor without target injection and with the injection of 1 nM of DNA target. Figure 2.15c shows the sensor response with time upon exposure to 1 nM of DNA sequences fully complementary to PNA (T2-MM0), with one mismatch (T1-MM1) and with three mismatches (T3-MM2) for an OTFT sensor operating at constant bias ($V_G = -1$ V, $V_{DS} = -0.5$ V); in this case, drain currents I_{DS} were normalized with respect to a baseline current $I_{DS-baseline}$ recorded after 100 s of constant bias prior to the analyte injection. The current initial-baseline restoring, recorded after rinsing the samples

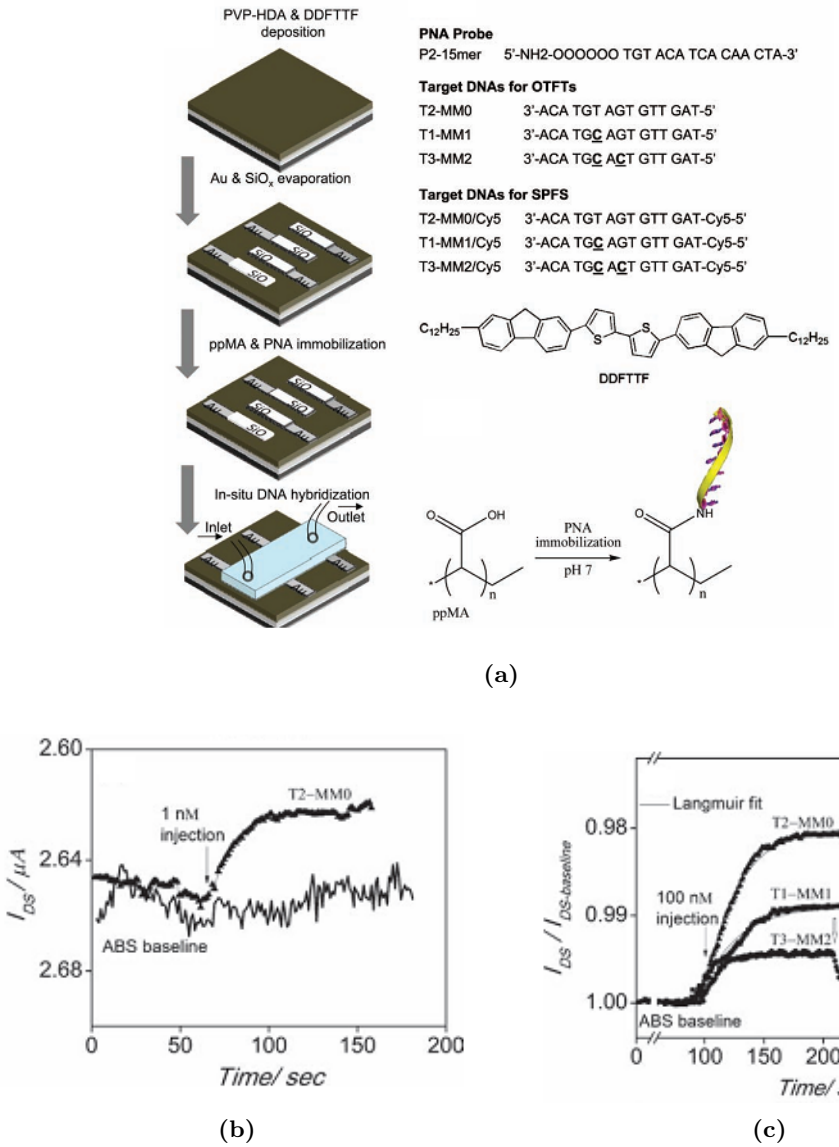

Figure 2.15: Schematic representation of the OTFT sensor fabrication (a) and experimental results: sensor response following the hybridization of complement DNA at minimum concentration (b) and to the mismatch dependent PNA-DNA hybridization (c) [31].

exposed to mismatched DNA, indicates that probes were non-specifically bounded or weakly hybridized with the PNA probe.

In a more recent work, Khan *et al.* [32] reported the electronic response of an OTFT, based on the same semiconductor and protective layer previously described, recorded in

buffer solutions with varying pH, target DNA concentration, and number of base mismatches in the target sequence. Their tests confirmed that DNA is negatively charged at pH 7, and that the equilibrium saturation requires a 10-fold increase in the solution concentration to detect a signal variation due to the single-mismatch DNA target, relative the complementary target. They also confirmed that the Debye length affects the sensitivity of sensors by competing with the capacitance effect at the functional layer surface.

2.1.5 Glucose detection

In 2008 Liu *et al.* [33] used an OTFT structure to realize a biosensor for glucose detection. They fabricated a top-contact OTFT with a silicon wafer as gate, a silicon dioxide layer as gate-dielectric, two gold electrodes as source and drain, poly(3,4-ethylenedioxythiophene):poly(styrene sulfonate) PEDOT:PSS as semiconductor channel and glucose oxidase (GOx) as sensitive layer (see figure 2.16a). GOx is an enzyme commonly used for glucose detection; it catalyses the reaction of glucose in the presence of oxygen producing hydrogen peroxide (H_2O_2) and gluconic acid according to the following reactions:

$$\text{Glucose} + \text{GOx(ox)} \rightarrow \text{Gluconolacton} + \text{GOx(red)} \tag{2.1}$$

$$\text{GOx(red)} + O_2 \rightarrow \text{GOx(ox)} + H_2O_2. \tag{2.2}$$

as shown in 2.16b. The sensor working mechanism is based on the redox property of PEDOT:PSS and the oxidation of H_2O_2. PEDOT:PSS works as a semiconductor when it is oxidized, while it behaves as an insulator when it is in the reduced state. H_2O_2 may work as a strong oxidant according to the following reaction

$$H_2O_2 \rightarrow O_2 + 2H^+ + 2e^-; \tag{2.3}$$

When the hydrogen peroxide is produced next to the channel, it oxidises causing the reduction of PEDOT:PSS, which in turn become less conductive. The de-doping effect produced by the H_2O_2 can be removed by applying a negative bias to the gate contact as the electrons are pushed away from the channel. As a general rule, PEDOT:PSS works as a p-type semiconductor, i.e., the transistor is switched on when the gate is negatively biased; in the presence of glucose, this behaviour is further enhanced because

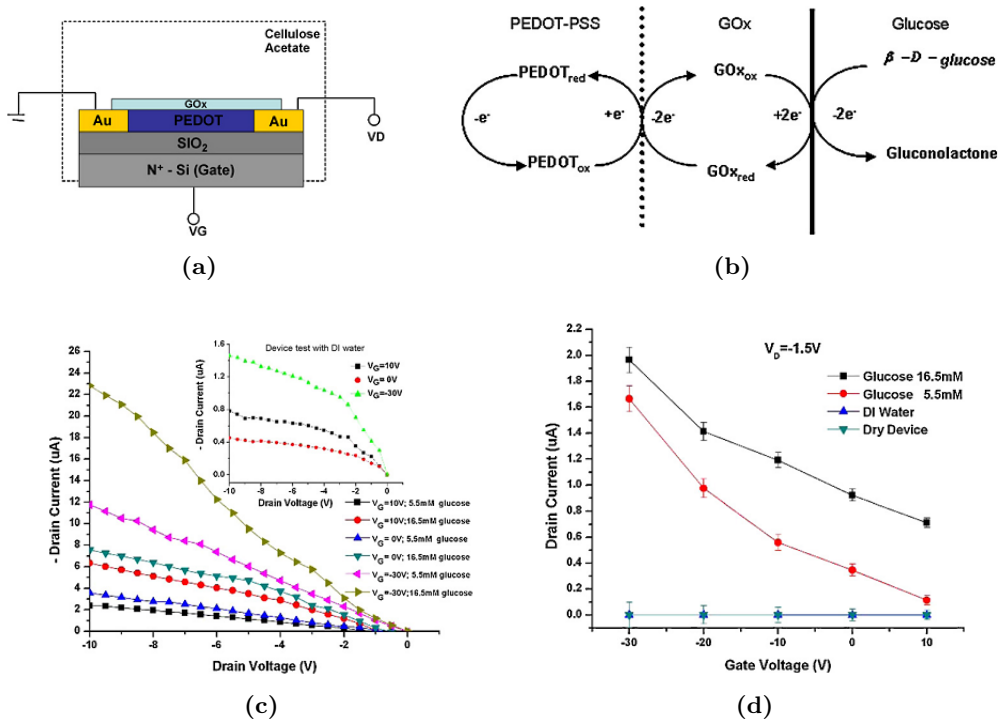

Figure 2.16: Schematic representation of the sensor (a) and working meachanism (b); experimental results: drain current versus drain potential (c) and gate potential (d) showing the sensor response recorded under different experimental conditions [33].

electrons are moved away form the channel. The experimental results shown in figures 2.16c and 2.16d confirmed that the drain current increased with negative biasing when the device was exposed to higher concentration of glucose solution.

2.2 ISOFET-based sensors

Inspired by the conventional ISFET devices, ISOFET-structured devices were implemented in order to realize sensors capable of detecting those chemical and biological species that are only active in aqueous media. The sensor specificity depends on the reactions occurring at the insulator-electrolyte surface, therefore the insulator surface properties determine the sensor specificity. The most important results obtained in pH and glucose sensing are reported in the following subsections.

2.2.1 pH sensors

Bartic *et al.* [34], [35] developed the first charge transducer based on an ISOFET structure. They used silicon nitride ($SiNH_4$) as dielectric layer, which is an oxide with an anphoteric character. $SiNH_4$ has two kind of H^+ specific binding sites: a silanol (SiOH) and a primary amine ($SiNH_2$); depending on the pH of the solution, these groups may be positively or negatively charged according to the following reactions:

$$\begin{aligned} SiOH &\rightleftharpoons SiO^- + H^+ \\ SiOH + H^+ &\rightleftharpoons SiOH_2^+ \\ SiNH_2 + H^+ &\rightleftharpoons SiNH_3^+. \end{aligned} \tag{2.4}$$

By postulating the charge neutrality for the whole electrolyte/insulator/semiconductor structure, the site-binding theory gives a relationship between the electrolyte-insulator interface potential and the charge that accumulates at the interface under a given pH of the electrolyte. Therefore, the gate voltage results from the sum of a constant term plus a further term associated with the chemistry-dependent potential drop at the solution-dielectric interface. When a pH change occurs in the electrolyte solution, the insulator surface charges and, as a consequence, the channel conductance changes as well. Figures 2.17a and 2.17b report a schematic representation of the device and of the experimental set-up, respectively. A silicon wafer was used as mechanical support for a membrane made of a silicon oxide and silicon nitride deposited upon both its sides. Silicon oxide is both the gate dielectric and the sensitive layer; it is exposed to the sample solution by means of a window anisotropically etched in the silicon substrate. Gold electrodes were patterned on the back side of the active layer as source and drain, and poly(3-hexiothiophene) P3HT was deposited as organic semiconductor. In order to allow it to work in liquids, the device was finally wire-bonded on a thick-film alumina substrate and encapsulated with a two-component epoxy resin. As shown in figure 2.17b, an Ag/AgCl reference electrode completes the sensor. Figures 2.17c and 2.17d show some experimental results. In particular, figure 2.17c shows the output characteristics recorded in buffer solutions with different pH values for the same reference bias: a change in the pH causes a change in the drain current, proving that the device is

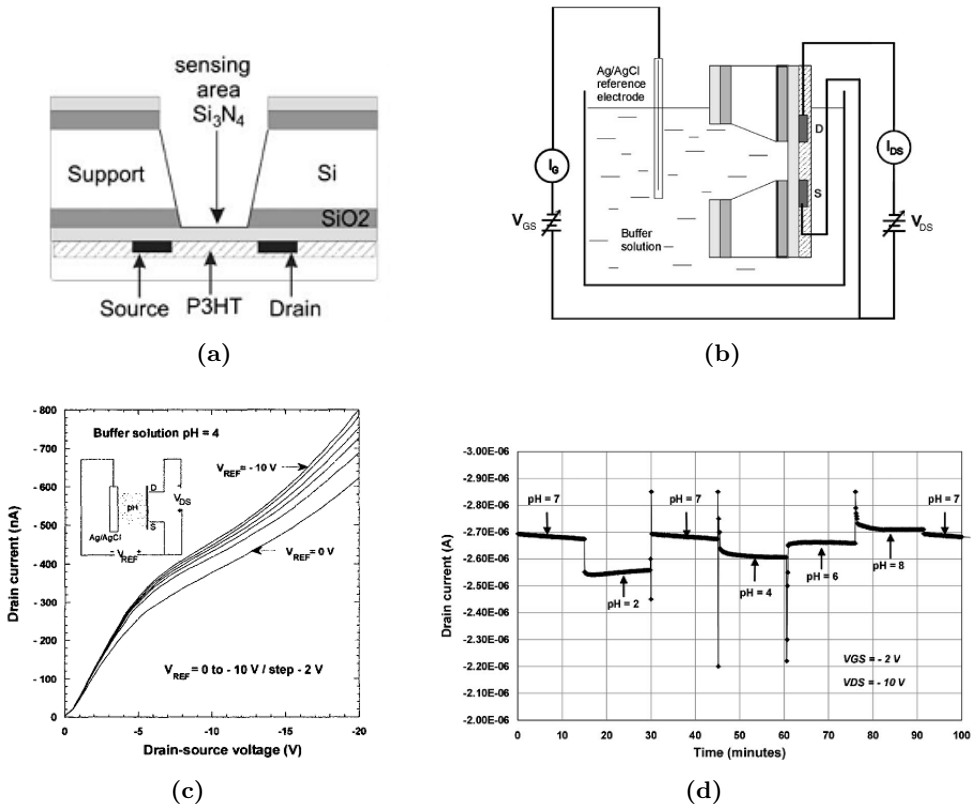

Figure 2.17: Schematic representation of the device [3] (a) and of the experimental set-up [35] (b); experimental results: output characteristics recorded in a buffer with constant pH under different reference bias (c), and in different pH buffer solutions using the same biasing condition (d) [34].

pH-sensitive [34]. Figure 2.17d reports about the stability and reproducibility of the current response in time, after successive immersions in different pH buffers [35].

The approach described by Bartic *et al.* has an important drawback: the structure is not flexible and cheap enough to realize disposable devices. A flexible and more cost-efficient ISOFET realized on a plastic substrate was reported from Gao *et al.* [36]. Gold source and drain were realized firstly, then P3HT was deposited as active layer and finally a tantalum pentoxide (Ta_2O_5) layer was deposited upon the semiconductor to form the insulator active layer. Ta_2O_5 is far away the most sensitive oxide to pH changes: it can induce a voltage drop of 59 mV per pH unit compared to the 25 mV induced by SiO_2 [37]. Because of its high dielectric constant ($\epsilon_r > 20$) it allows

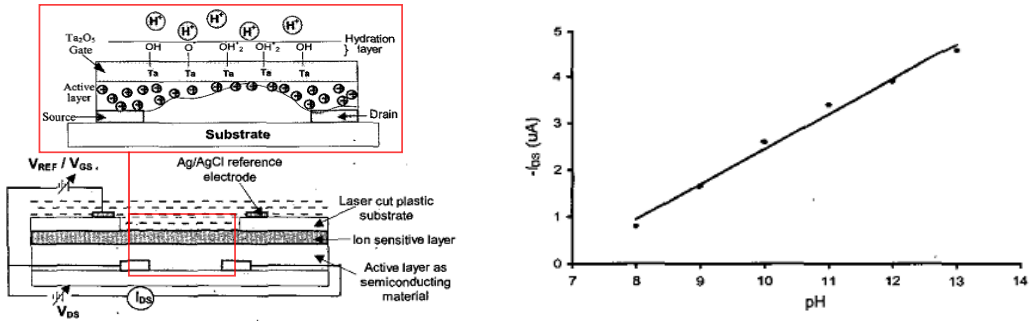

Figure 2.18: Schematic representation of the device and plot of the measured source-drain current with respect to pH value at a reference potential –2 V and drain potential of –7 V [36].

P3HT-based transistors working with external voltages below 3 V. Figure 2.18a shows a schematic of the device. The device is completed by an Ag/AgCl electrode fabricated using a laser micro-machining technology. The reference electrode integration in the sensing unit makes the device prone to be integrated with disposable lab-on-a-chip and *in vivo* applications. In figure 2.18b the source-drain current detected with respect to the pH sample value is reported. The device shows a good linearity in the source-drain current versus the pH concentration, and sensitivity of ΔI_{DS}/pH= 0.36 μA/pH. Despite the promising properties, the device processing requires UV exposure that can induce important changes, and eventually degrade the organic material properties.

Afterwards, further pH sensors with an ISOFET structure were proposed with the aim to overtake some limits of the previously reported sensors. Because Ta_2O_5 exhibits some hysteresis in the characteristics, and bias stress induces instabilities, Diallo *et al.* [38] realized a flexible device using a thin hydrogenated silicon nitride layer (SiN:H) as sensitive layer. The device is flexible as it is realized on a Kapton substrate. It has a top-gate bottom-contact structure with gold source and drain contacts, and Pentacene as organic semiconductor. A Parylene C layer deposited upon the semiconductor protects it from the liquid environment. Figure 2.19 shows the device structure (a) and the sensor response vs. the solution pH (b). The experimental results demonstrated that the device responded with a sensitivity which ranges between the ones recorded when using $SiNH_4$ and Ta_2O_5 as active layer. Moreover, they proved that Parylene C, which is a highly chemically inert material, provides a good passivation effect.

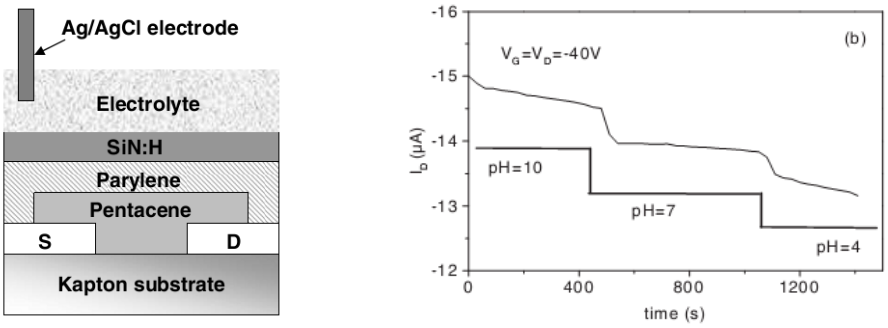

Figure 2.19: Schematic representation of the device (a) and sensor response for decreasing pH of the solution at reference and drain potential of –40 V (b) [38].

Finally, a full mechanical flexible ISOFET was proposed by Loi *et al.* [39]. A 900 nm thick Mylar^{TM} sheet was used as both dielectric and substrate. Gold source and drain electrodes, with a ratio of $W/L = 250$, were patterned on one side of the dielectric, and upon them, Pentacene was deposited as organic semiconductor. The other side of the Mylar film was exposed to the electrolytic solution and an Ag/AgCl reference electrode was was used to complete the device. Figure 2.20a shows a schematic of the device structure, while the experimental results are reported in figure 2.20b. Plot in figure 2.20b shows the sensor response at different pH of the electrolytic solution. This result demonstrates that Mylar is sensitive to pH and that the device responds to pH variation within the range of 50 - 100 mV/pH.

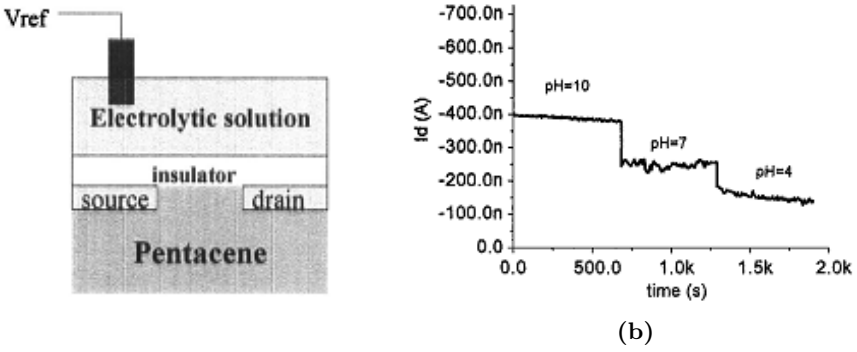

(b)

Figure 2.20: Schematic representation of the device (a) and sensor response at different pH value of the electrolytic solution (b) [39].

2.2.2 Glucose sensors

In 2003, Bartic et *et al.* [40] demonstrated that ISOFETs are suitable for biosensing by realizing a glucose sensor. They fabricated an ISOFET (see figure 2.21a) by depositing poly(3-hexiothiophene) P3HT as organic semiconductor upon two gold electrodes, which were patterned as source and drain contacts. In order to improve pH sensitivity and reduce the operational voltages, they deposited a Ta_2O_5 layer as dielectric. Ta_2O_5 was chosen as dielectric layer because it has a large number of proton-sensitive surface sites which ensure a good sensitivity to pH, and also because it has a high dielectric constant which allows working with low operating voltages. Glucose sensitivity was achieved by anchoring the glucose oxidase (GOx) enzyme onto the dielectric surface. By catalysing glucose, GOx converts glucose into gluconic acid and H_2O_2. Driven by the glucose concentration, a local pH variation is then produced: a gluconic acid increase causes a pH decrease. As a pH decrease in the insulating-layer interface causes a hole removal from the conducting channel of the p-type semiconductor, a decrease in the drain current is measured. Figure 2.21b shows a comparison between the drain current values recorded in a buffer phosphate solution with those obtained in the glucose solution at two different bias of the reference electrode.

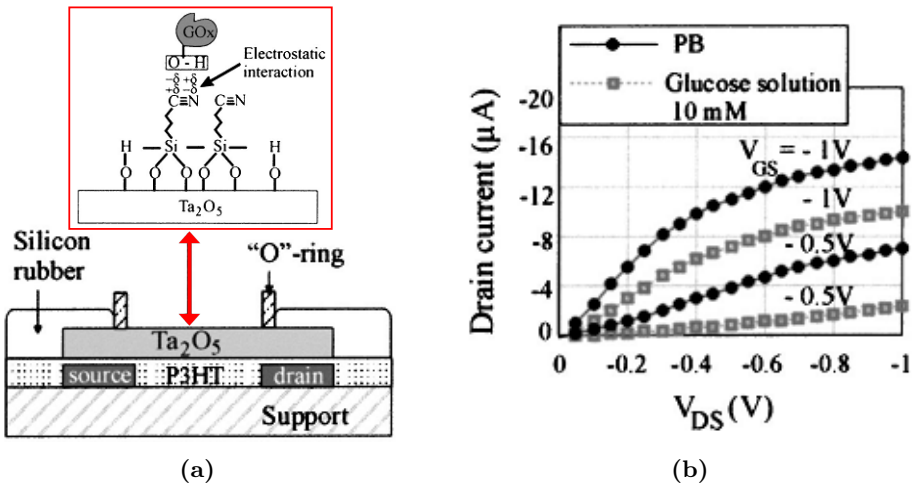

(a) (b)

Figure 2.21: Representation of the OTFT sensor (a) and effect of the biocatalytic reaction on the transistor characteristics at two different biases of the reference electrode (b) [40].

2.3 EGOFET-based sensors

As they operate in liquid media at very low voltages, EGOFETs are especially suitable to realize sensors for biological applications. A DNA sensor realized using this structure is reported in the following subsection.

2.3.1 DNA sensor

Recently, a DNA sensor with an EGOFET structure was realized by Kergoat *et al.*. [41]. Its special feature is that the device is operated in pure water and, for this reason, it works entirely in the field-effect mode. They called it Water-Gated OFET (WGOFET). As it works with voltages below 1 V, it allows biosensing applications in aqueous media. They called it Water-Gated OFET (WGOFET). The device, which has a bottom-contact top-gate structure, was built in a silicon wafer with 300 nm thermally grown oxide. A water droplet was deposited onto the semiconductor to form the gate-dielectric, and a platinum wire was dipped into the droplet to obtain the gate electrode. Figure 2.22a reports a schematic representation of the device. Figures from 2.22b to 2.22d show the transfer characteristics recorded at gate voltages of -0.5 V; a buffer phosphate solution (PBS) was used during the measurements reported in figures 2.22b and 2.22c, while a 18 MΩ deionized water was used for tests shown in figure 2.22c. Plots in figure 2.22c show that probes immobilization entails a current decrease and a shift towards negative voltages of the threshold voltage. This result is consistent with the fact that DNA molecules cause a shielding effect, which prevents the ions penetration into the semiconductor. In fact, in an electrolytic-gated transistor, when the gate is positively biased, cations penetrate into the semiconductor bulk from the solution. The adsorbed ions change the concentration of positive charges at the electrolyte-semiconductor interface; within this condition, fewer holes have to be injected to switch on the transistor, and the off current increases. The ion penetration is confirmed by the significant hysteresis observed in all the measurements taken in PBS. Because DNA molecules are negatively charged, they form an electrostatic barrier which partially impedes cations diffusion through the interface, thus reducing their doping effect. Figure 2.22b shows the experimental results obtained after DNA hybridization. DNA negative charge almost doubles after hybridization, nevertheless, curves show that the electrical screening is relatively weak with respect to the one

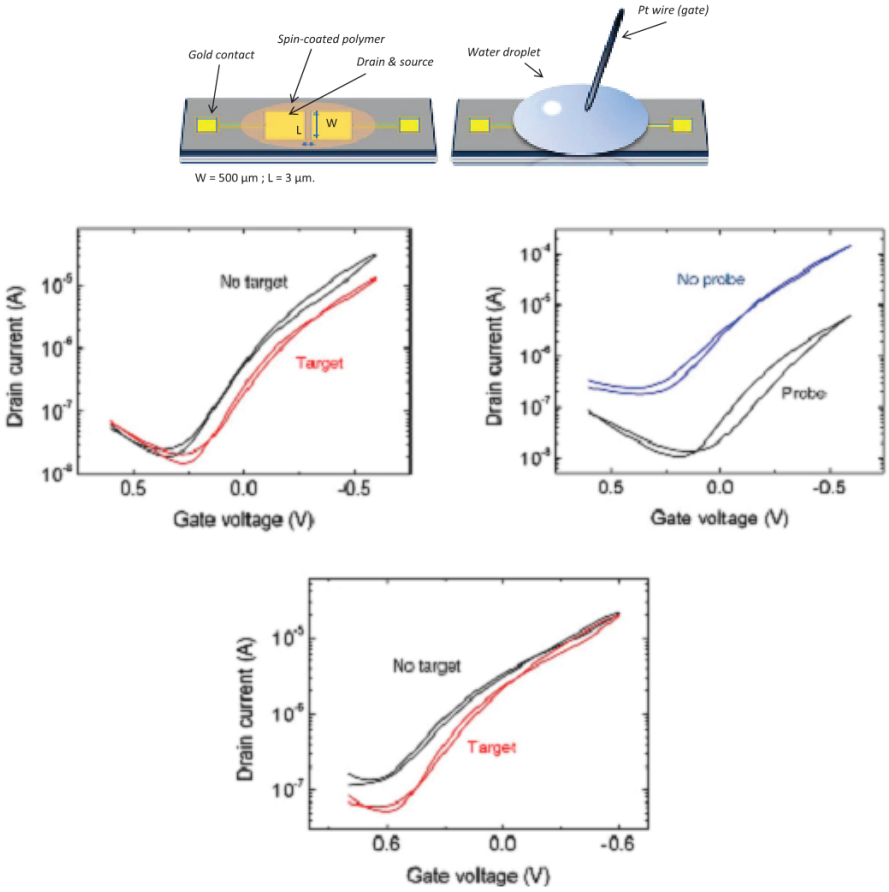

Figure 2.22: Schematic representation of the OTFT sensor (a); modification of the transfer characteristics taken after probes immobilization (b) and hybridization in PBS (c) and after hybridization in pure water (d) [41].

recorded under probe immobilization. Upon hybridization, DNA strands form a rigid double helix, that is, unfold assuming a shape which make more effective the electrical screening phenomenon due to the counterions contained in PBS. Only negative charges that lie within the Debye length can effectively be detected; therefore, the shift caused by the DNA electrical screening after hybridization is relatively weak compared to the one observed under probes immobilization. The counterions screening can be reduced by using solutions with a lower ionic strength. Figure 2.22d reports the sensor response upon hybridization using pure water as gate dielectric. Measurements taken in a relatively short time and at room temperature, in order to avoid possible significant denaturation, leads to comparable results but with lower off-currents.

2.4 OECT-based sensors

OECTs operate through the doping and de-doping process of a conducting polymer. First examples of OECTs were obtained through electropolymerization on microelectrodes; typical polymers were polypyrrole [42], polyaniline [43], [44] and polythiophene [45], [46]. The possibility to realize devices by printing conducting polymers has generated a renewed interest towards OECTs. The most common material used for realized printed device is PEDOT:PSS, which is nowadays investigated in various sensing applications. In the following subsections, some examples realized with OECTs made of poly(3,4-ethylenedioxythiophene):poly(styrene sulfonate) PEDOT:PSS are reported.

2.4.1 Gas and vapour sensors

One of the first applications with an all-organic ECT was obtained by Nilsson *et al.* [47] for humidity detection. The sensor was fabricated by combining an OECT based on PEDOT:PSS and Nafion, which is a proton conducting film. The OECT worked as transducer, while the Nafion film worked as receptor. The working mechanism is based on the different conductivities in the transistor channel, which can be electrochemically modulated. The PEDOT:PSS can be switched between different redox states by the mobile ions in the electrolyte, addressed by the potential applied to the gate electrode. Figure 2.23a shows a schematic representation of the device. PEDOT:PSS was printed onto flexible polyester foils or thin papers, which were tested as substrates, in order to

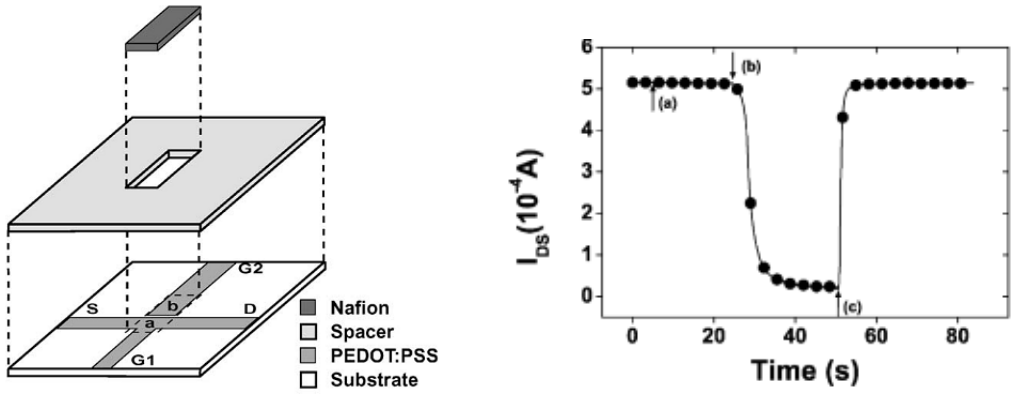

Figure 2.23: Schematic structure (a) and sensor response consecutively recorded under different gate bias and humidity conditions: 1.2 V and 30 % in (a), 1.2 V and 80% in (b) and 0 V an 80 % in (c) [47].

obtain flexible devices. Through an opening in a spacer, the Nafion film was deposited on top of the transistor channel and the gate contact. Figure 2.23b reports the drain-source current recorded upon applying a gate bias of 1.2 V for 15 s. The transistor channel and the gate electrode respectively switch to a reduced and oxidized state, depending on the ionic conductivity of the Nafion film, causing a current drop of two orders of magnitude when the relative air humidity changes from 40 to 90 %.

2.4.2 Glucose sensors

Zhu *et al.* [48] realized an OECT based on PEDOT:PSS in order to obtain a glucose sensor with a detection limit of 0.1 mM L^{-1}. They used a vertical transistor configuration. PEDOT:PSS was spin-coated ad then patterned on a glass substrate to form the active channel and the source and drain electrodes. A Pt wire was used as the top gate electrode of the transistor. Finally, an elastomeric well made of poly-(dimethyl siloxane) (PDMS) was placed in contact with the PEDOT:PSS layer in order to confine the phosphate buffer solution (PBS) (pH 7.14) solution which was used as electrolyte. In its pristine state, PEDOT:PSS is doped by PSS and positively charged ($PEDOT^+$). By applying of a negative bias to the gate electrode, positively charged ions penetrate into the channel from the solution; they bind to the PSS and cause the reduction of PEDOT. This de-doping effect leads to a conductivity decrease as shown in figure 2.24a. The current modulation did not change upon addiction of glucose oxidase (GOx) to

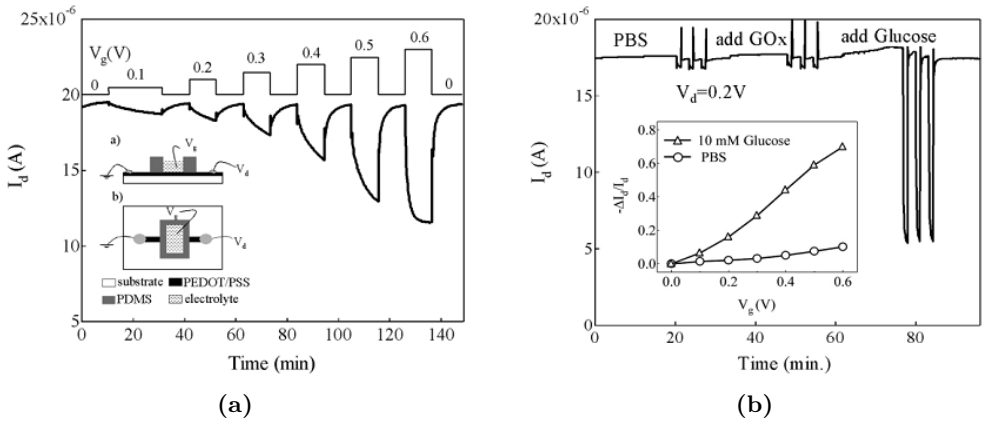

Figure 2.24: Current modulation in PBS of the device represented in the inset (a) and current changes obtained in the presence of GOx and glucose (b) [48].

the electrolyte, while a dramatic current decrease (70 %) was observed when glucose was added to the solution (see figure 2.24b). Because GOx catalyses the production of H_2O_2 and gluconic acid, the current change can be potentially attributed to both these products. Nevertheless, they proved that the current modulation was pH-independent in standard buffer solutions with pH ranging from 5 to 9. As a consequence, the sensing mechanism has to be attributed to the electrochemical mechanism of operation concerning H_2O_2. H_2O_2 oxidised at the Pt electrode, while, to maintain charge balance, $PEDOT^+$ of the active channel was reduced [49]. Compared to the glucose sensor based on an OTFT structure, the OECT structure allows decoupling the transducer from the recognition element, thus enabling simultaneous optimization of both. Moreover, the previous device has very low detection times because glucose does not have to diffuse inside the polymer to find the enzyme.

Detection times in this kind of sensor were investigated by Macaya *e al.* [50] as shown in figure 2.25b). In their work Macaya *e al.* realized a glucose sensor with a

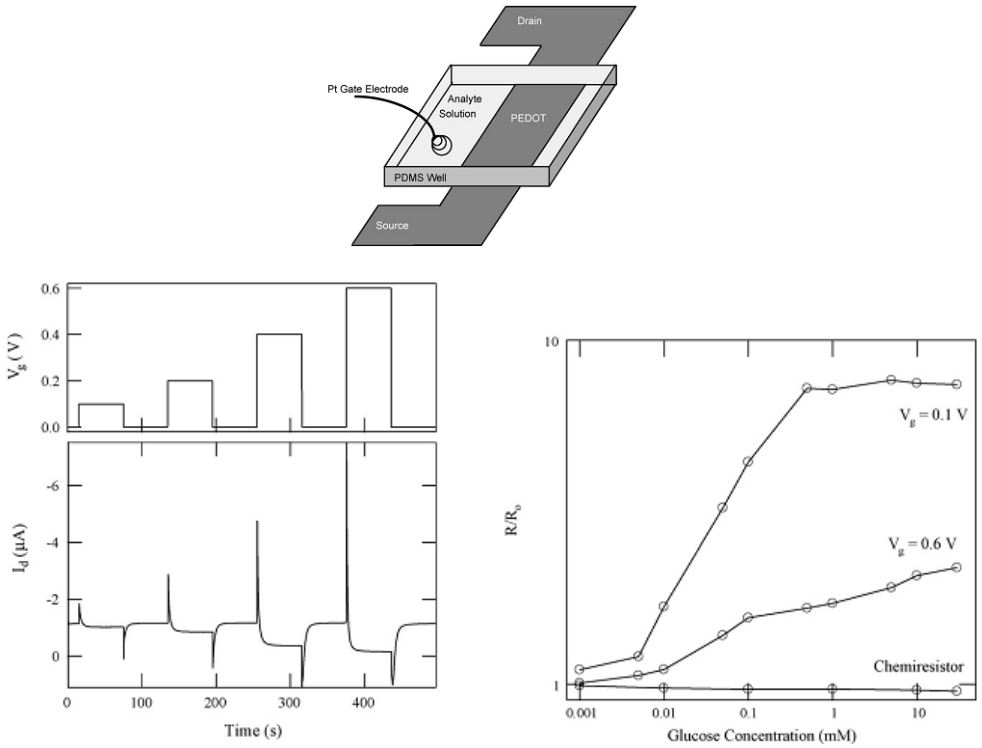

Figure 2.25: Schematic representation of the device (a) and experimental results: temporal response of drain current as a function of the gate voltage (b) and normalized transistor response at different gate bias to different glucose levels (c) [50].

structure similar to the one reported by Zhu *et al.*, but they also demonstrated that the lower and upper detection limits could be modulated by varying the gate voltage. The devices were fabricated on glass slides. A thick parylene layer was deposited on the glass and then patterned trough a standard photolithography and O_2 plasma etching. A solution made of PEDOT:PSS, ethylene glycol and dodecylbenzenesulfonic acid (DBSA) was then spin-coated upon the substrate and finally, the parylene film was peeled off leaving only the patterned PEDOT:PSS on top of the glass. Ethylene glicole and DBSA were added to the PEDOT:PSS solution to enhance its conductivity. A well made of PDMS was used to host the analyte solution. A Pt wire, which was used as gate, completed the device (see figure 2.25a). The device fastness to respond under a pulsed biased and its sensitivity are reported in figures 2.25b and 2.25c respectively. Drain current saturates within 60 s and glucose detection is obtained ranging from 1 μM to 0.5 mM, depending on the gate potential. Glucose detection with a micromolar sensitivity is an important result for detection in the range of glucose saliva, which ranges between 0.008 and 0.21 mM [51]. In figure 2.25c it is also reported the sensor response recorded when it is used as a chemoresistor, that is, without applying any gate bias. The gate role is therefore confirmed by the fact that the sensor response is negligible with respect to the one obtained with the device working as a transistor.

Afterwards, Bernards *et al.* [52] further investigated the study of this kind of sensors. They elucidated the underlying device physics and established a connection between sensor response and analyte concentration. Through appropriate scaling of the transfer characteristics at various glucose concentrations, they showed the universal curve that describes the device operation (see figure 2.26).

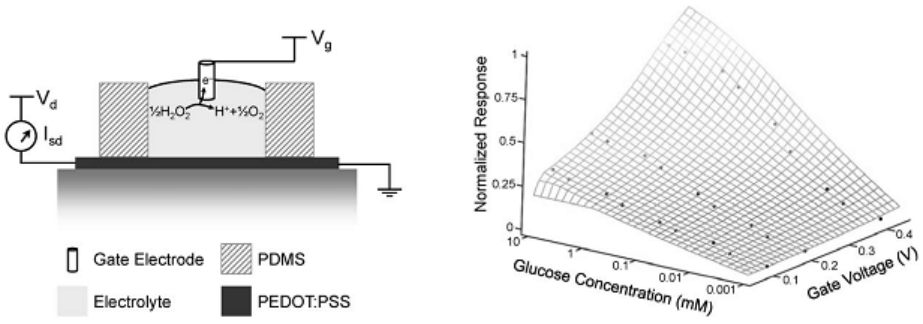

Figure 2.26: Schematic representation of the device (a) and normalized response of the drain current as a function of applied gate voltage and glucose concentration (b) [53].

Finally, Yang *et al.* [54] demonstrated that these sensors are promising candidates for system-on-a-chip applications. They obtained a system for multiple analyte detection by fabricating a surface-directed microfluidic system, which allows distributing the analyte in four separate measurement reservoirs, each containing a transistor that uses the analyte as an integral part of its device structure.

Glucose sensors consistent with levels present in human saliva are very interesting applications for common use. Nevertheless, to realize commercial devices, further improvements would be desirable, such as the Pt gate electrode replacement with a PEDOT:PSS electrode. In fact, Pt wire complicates the device fabrication and increases cost. To overcome this limit, Shim *et al.* [55] realized an ECT all made of PEDOT:PSS and replaced the O_2/H_2O_2 couple with the redox couple ferrocene [bis (^{5}-cyclopentandienyl)iron] (Fc)/ferricenium ion couple. The reaction cycles of the O_2/H_2O_2 and ferrocene/ferrocenium couples are shown in figures 2.27a and 2.27b. Because of its low redox potential, the ferrocene/ferrocenium couple can shuttle electrons from the reduced enzyme to the PEDOT:PSS electrode. Figure 2.27c shows a image of the sensor, while 2.27d reports the normalized response to glucose concentration. Consistently with the result obtained by Macaya *et al.*, when the transistor well

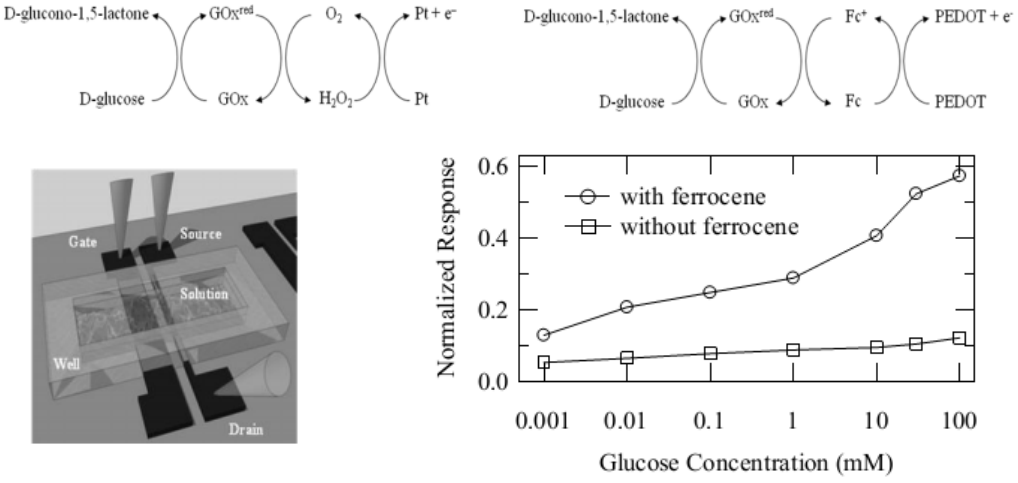

Figure 2.27: Reaction cycles for detection of glucose in devices with a Pt electrode (a) and with a PEDOT:PSS electrode and a ferrocene mediator (b); layout of a finished device and normalized response to glucose concentration for OECTs preloaded with a mixture with and without the ferrocene mediator (d) [55].

is preloaded with a mixture that does not contain ferrocene, the normalized response is small; this result confirms that the redox couple is essential for the transistor working with a PEDOT:PSS gate. On the other hand, when using ferrocene as mediator, the normalized response starts at 0.13 for the 1 μM solution and increases to 0.57 for the 100 mM one. This result confirms that ECTs all made of PEDOT:PSS are promising devices for glucose detection in human saliva.

3

Organic Charge Modulated Field Effect Transistor

In the present chapter, the Organic Charge Modulated Field Effect Transistor (OCMFET) which was realized for this project and the tested applications are presented. In the first sections, a brief introduction on the origin of the OCMFET, its structure and working principle are reported. Afterwards, the tested applications are described in chronological order they were developed. For each application, the layouts, the process and the materials employed in the device fabrication and functionalization are shown together with the experimental results.

3.1 Introduction

In 2006 Barbaro *et al.* [11] [12] proposed and realized a novel, solid-state sensor for charge detection in biomolecular processes. As the detection mechanism is based on the field-effect modulation induced by electric charge changes related to the bioprocess, they called the device Charge-Modulated Field-Effect Transistor (CMFET). This device was designed with the aim to realize an electronic label-free DNA detector for large-scale integration on a single chip. Charge detection is carried out without external electrodes.

A part of the work presented in this thesis started live from the idea to realize a portable and disposable device using the working principle developed by Barbaro *et al.*. As organic electronics is an electronic branch especially suitable to be used for

realizing disposable devices, the device presented in this thesis is an organic version of the CMFET, i.e., an OCMFET. Compared to the structures reported in chapter 2, the OCMFET represents an innovation: the sensing area is physically separated from the OFET and the sensing mechanism does not depend on the active layer. A previous OMFET version was realized and tested as pH sensor. The materials which were employed in its fabrication made it totally flexible, but also extremely fragile. Moreover, a fluidic system had to be integrated in order to deliver the analyte to the probe area. The present OCMFET version was designed with the aim to obtain a device which could be easier to test and use. As its shape allows immersing the probe area in the solution to be tested, it can work without using any fluidic system. Moreover, the employed materials allowed the realization of a device less than the previous one.

Several fabrication methods, materials and layouts were realized and tested. In particular, two kinds of devices were tested as sensors: a High-Voltage (HV) version, that is biased by applying tens of Volts, which is the typical polarization required to operate OFETs; a Low-Voltage (LV) version that can be operated by applying 1 V, which is considered a very low voltage polarization for OTFTs. This feature resulted from the use of a particular combination of materials which allowed realizing a very thin layer as gate dielectric. For each kind of device, electrodes with different dimensions were realized in order to reach a good compromise between electrical requirements and ease of use. Moreover, different electrical schemes were studied. In order to get rid of current drifts which are due to organic semiconductor degradation or bias stress, as a general rule, differential measurements were carried out. Aiming at using one device as reference and the other as sensor, some sensor layouts included two devices sharing a few electrical contacts.

The OCMFET was functionalized and tested as pH sensor and DNA sensor. Several functionalization procedures and materials were tested in order to achieve the device sensitivity and selectivity towards the analyte of interest. The procedure efficiency and accuracy were analysed by means of several investigation techniques, such as electrochemical measurements and Atomic Force Microscopy.

3.2 State of the art

An OCMFET was previously realized and tested as pH sensor by Caboni *et al.* [56], [57].

The device was fabricated starting from a Mylar sheet, that worked at the same time as insulator and support for the device. It was structured as a bottom-contact device with two electrodes as gates, one source and one drain ($W/L = 150$). All the electrodes were made of gold and Pentacene was used as organic semiconductor. The gate electrode, which was patterned on the opposite side of the insulating foil, was left floating; the transistor was biased by means of a fourth electrode, a control-gate, which was patterned on the same side of source and drain contacts. The floating-gate electrode was elongated in order to form a planar capacitor with the control-gate and also to host the probe area. In order to allow differential measurements, each device included two OFETs, each with its own floating-gate and probe area, which share the source and the control-gate contacts. To deliver the analyte on the probe area, the device was equipped with a a custom flow cell hosting two chambers, with inlet and outlet channels. Figure 3.1a shows a schematic representation of a single device, while figure 3.1c reports a picture of a device with and without the flow cell.

The sensitivity to pH was achieved by functionalizing the probe area with amino-terminated (NH_2) SAMs. According to the Henderson-Hasselbalch equation, amino groups immobilized on the sensing surface protonate/de-protonate depending on the H_3O^+ concentration. The conductance of the organic semiconductor in the channel region was switched on and off by the control-gate electrode, and modulated by the potential positive charge on the floating-gate. When the amino groups were protonated, they induced a charge separation inside the floating-gate, which contrasted the charge accumulation at the interface between the p-type semiconductor and the insulator (see figure 3.1c). In order to overcome this positive voltage offset and turn on the device a more negative threshold voltage was required; as a consequence, the sensitivity to pH could be expressed in terms of change in the effective threshold voltage of the transistor. Figure 3.1d shows threshold voltage measured on a device where one probe area was exposed to an analyte with a constant pH (reference), while the other was exposed to analytes with a different pH (sensor). While the threshold voltage of the reference

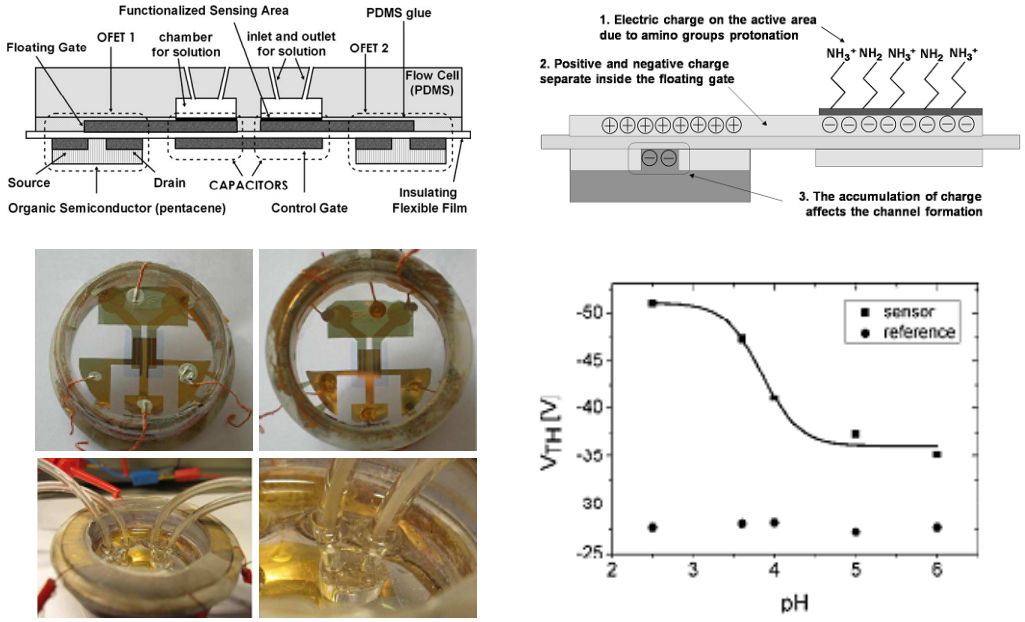

Figure 3.1: Schematic representation of the device realized by Caboni *et al.* [56] (a) and working principle [57] (b); images of a device with and without the fluidic system (c) and experimental result (d) [57] [56].

device remained almost unchanged, the sensor's changed with the sigmoid trend that is characteristic of the protonation reaction.

3.3 Design and model

In the following subsections, the OCMFET design and working principle is treated by illustrating its phenomenological behaviour and analytical model.

3.3.1 Structure

The core of the OCMFET is an OTFT. This particular implementation is a bottom-gate transistor. Compared to traditional OTFTs, the OCMFET has a second gate contact used to drive the transistor, while the primary gate is left floating. The most important feature is that the sensing function is not in relation with a specific property of the OTFT structure. In fact, the sensing area, which is located on the floating-gate, is physically separated from the OTFT. This result was obtained by realizing a proper shaped floating-gate contact.

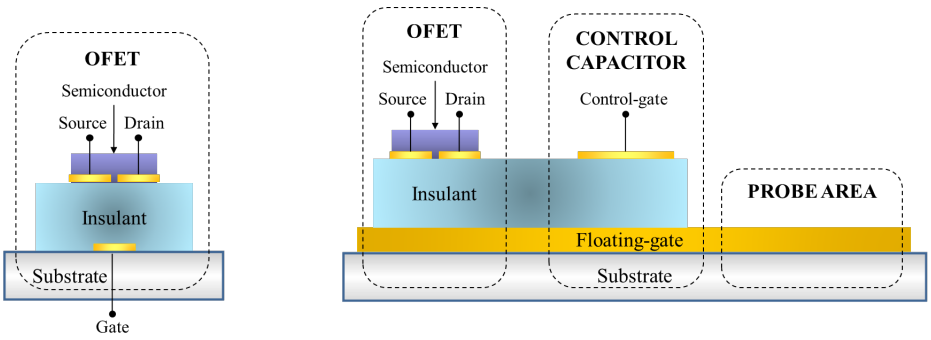

Figure 3.2: Vertical cross-section's representation of an OFET (a) and of the OCMFET.

The vertical cross-section of a conventional OFET and of the OCMFET are shown in figures 3.2a and 3.2b respectively. In the OCMFET, the bottom-gate contact is elongated and is only partially covered by a dielectric layer. On top of this layer, in addition to source and drain, there is a fourth electrode which is used as control-gate. It forms a planar capacitor with the bottom-gate contact that is left electrically floating. The portion of the floating-gate which is not covered by the dielectric layer is the probe area. This configuration allows the probe area to be immersed in the solution to be tested.

3.3.2 Working principle

When charges are immobilized on the probe area, they generate an electric field which induces a charge separation into the floating-gate. The induced charge causes in turn the dielectric layer polarization, setting a voltage drop on it. The dielectric polarization induced by positive superficial charges causes holes repulsion from the transistor channel and, as a consequence, a current decrease in the p-type semiconductor (see figure 3.3a);

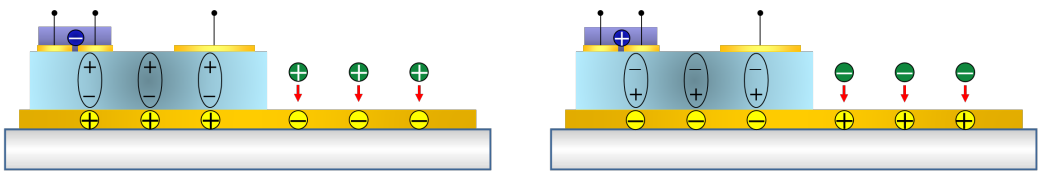

Figure 3.3: Charge induction operated by positive (a) and negative (b) superficial charges.

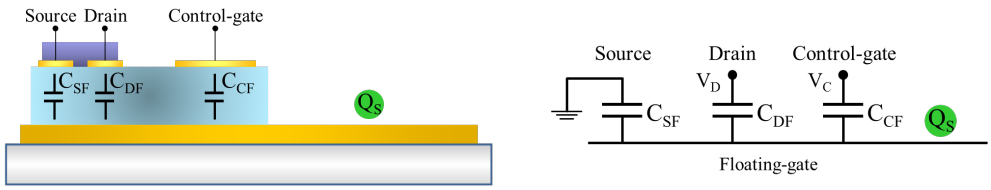

Figure 3.4: Representation of the vertical capacitances (a) and electrical scheme (b).

on the contrary, negative charges cause holes attraction and a current increase (see figure 3.3b).

The variation of the transistor current due to the anchored charges depends on the shift of the transistor threshold voltage. A relation between the surface charge and the OFET threshold voltage V_{TH} can be determined from the statement that the bottom-gate electrode is left electrically floating, therefore, its total charge Q_F is constant. In fact, Q_F can be expressed by means of the capacitances between the floating-gate and the other electrodes (see figure 3.4b) with the following equation:

$$Q_F = C_{CF}(V_F - V_C) + C_{SF}V_F + C_{DF}(V_F - V_D) + Q_I, \tag{3.1}$$

where C_{SF}, C_{DF} and C_{CF} are the capacitances between floating-gate on one side and source, drain and control-gate on the other respectively; Q_I represents the charge induced by the molecules anchored on the probe area; finally, V_F, V_C and V_D are the floating-gate, control-gate and drain potential.

As the gate is floating and the transistor is biased through the control-capacitor, the threshold voltage which is extracted from data is the one that is the one seen from the control-gate; it represents an *effective threshold voltage* and is expressed through the following equation:

$$V_C - V_{THF} = V_F - V_{TH} = \frac{C_{CF}}{C_{TOT}}V_C + \frac{C_{DF}}{C_{TOT}}V_D + \frac{Q_F - Q_I}{C_{TOT}} - V_{TH} \tag{3.2}$$

where C_{TOT} is the overall capacitance and is given by the sum of C_{CF}, C_{SF} and C_{DF}. The ratio C_{CF}/C_{TOT} depends on the device geometry and is approximated at 1. Within this approximation, equation 3.2 becomes:

$$V_C - V_{THF} \simeq V_C - \left(V_{TH} - \frac{C_{DF}}{C_{TOT}}V_D - \frac{Q_F - Q_I}{C_{TOT}}\right). \tag{3.3}$$

From equation 3.3 it results that the effective threshold voltage is given by

$$V_{THF} = V_{TH} - \frac{C_{DF}}{C_{TOT}}V_D - \frac{Q_F}{C_{TOT}} + \frac{Q_I}{C_{TOT}}. \tag{3.4}$$

During a series of measurements it is possible to consider constant the values related to the second and the third term. In fact, the capacitances and the drain potential do not vary when the measurements are performed by applying the same biasing. Q_I can also be considered a constant value as it expresses the charge that is stored in a electrode which is left electrically floating. The OTFTs threshold voltage may be affected by several elements such as environmental conditions and bias stress. Even if V_{TH} may vary during a series of measurements, it is reasonable to assume that the threshold voltage of two identical devices which are measured at the same time under the same conditions may vary in the same way. Therefore, the induced charge can be evaluated by using two devices which only differ in the charge immobilized on their floating-gates, i.e., by performing differential measurements between one device which is operated as *sensor* and the other as *reference*. By subtracting the reference V_{THF} from the sensor V_{THF}, it results that

$$\Delta V_{THF} = -\frac{Q_I}{C_{TOT}}. \tag{3.5}$$

As a consequence, the DNA charge can be determined by means of the following expression

$$\Delta Q_S = -C_{TOT} \cdot \Delta V_{THF}. \tag{3.6}$$

3.3.3 Strategies

According to the OCMFET model, both the amount of charge immobilized in the probe area and the all capacitances affect the device sensitivity. In order to detect small amounts of charge, small capacitances and operating voltages are required.

The total capacitance is given by the sum of the capacitances that the floating-gate electrode form with the other contacts. Two possible ways to reduce it are: reducing the overlapping area between the floating-gate and the other contacts, and/or increasing the thickness of the dielectric layer. As the control-gate is used to bias the transistor, its area has to be large enough to switch-on and off the transistor; on the contrary, source and drain capacitances are parasitic contributions, which must be reduced as much as possible. The achievement of self-aligned contacts would be the optimum solution, but it represents a technological improvement which was not investigated in this work, and can be obtained as a future development. Nevertheless, in order to optimize the overall capacitances and as a consequence the sensor response for pH sensing and DNA

recognition, several layouts were realized and tested both in the HV and in LV version. All of them were studied in order to find a compromise between the need to fulfil at the same time both electrical and practical requirements. The parasitic contributions were reduced, while the control-gate capacitance was kept large enough to ensure a good transistor biasing ($C_{CF}/C_{TOT} \simeq 1$) until a substantial sensitivity was obtained.

The second method to reduce the over-all capacitances is very disadvantageous as it implies high operating voltages which are not suitable for sensing applications in liquid media.

3.4 High-Voltage pH sensor

The HV pH sensor was the first application where the OCMFET studied in this work was realized and tested. Even if several layouts, material and methods were realized tested during the experimental activity, in the following subsections only the fabrication methods and experimental results which led to a relevant response are reported.

3.4.1 Layout

Several layouts were realized and tested for the HV pH sensors. Aiming at carrying out differential measurements, the first sensors were designed in order to include two devices, one working as *reference* and the other as *sensor*. Each sample consisted of two floating-gates, two drains, a common source and a common control-gate. Figure 3.5a shows a top-view scheme on the left and a vertical scheme on the right of such a configuration. Several HV devices were fabricated according to this scheme by adopting different shapes and dimension especially for the floating-gate contact.

In pH sensors, the floating-gate electrodes were elongated and the probe areas placed at a distance large enough to allow the probe area immersion into two different analytes. Figure 3.5b shows a tested layout. Aiming at depositing the semiconductor by thermal evaporation on both OFETs at the same time, the two channels were designed next to each other. According to the legend in 3.5b, the floating-gates, which represent the bottom-contacts, are in dark yellow, while the top-contacts, i.e., the source, drain and control-gate electrodes are in a lighter yellow. The choice of the colour reflects the material which was used to fabricate the electrodes, while a different colour gradation is used to make the bottom-contacts detectable from the top-contacts.

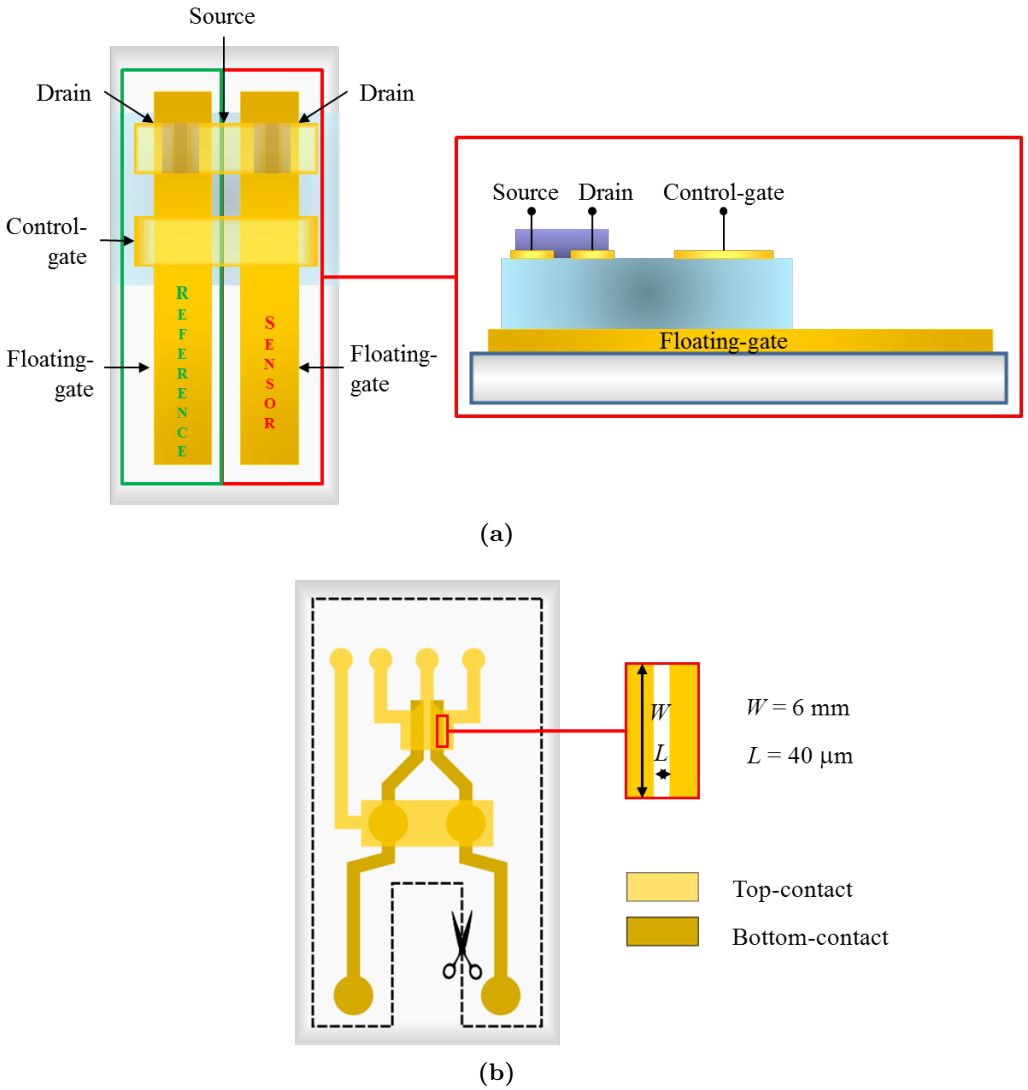

Figure 3.5: Top view and vertical section of the differential layout (a); layout of the HV pH sensor (b).

In this layout, the source and drain electrodes were designed to form a linear channel, wide $W = 6$ mm and long $L = 40$ μm, i.e with a W/L ratio of 150. The control capacitor is a circle with a diameter of 1.89 mm^2. These dimensions were chosen as they were proven to work in the OCMFET realized by Caboni *et al.* [56], [57]. A detail (not in scale) of the channel region is shown on the right in figure 3.5b. A circle with an area of ~ 28 mm^2 was designed as probe area.

3.4.2 Fabrication - Materials & methods

All the HV pH sensors were realized on a poly(ethyleneterephthalate) (PET) substrate (175 nm thick) which is a flexible and transparent material. Before use, it was sonicated in acetone first (15 min), 2-propanol (15 min) then, rinsed in bi-distilled water, and finally dried under a nitrogen flux.

Gold was used to realize the floating-gates and all the remaining electrodes, as its high work function (nominally 5.1 eV) allows to achieve good injecting contacts with p-type organic semiconductors. All the electrodes were obtained by thermal evaporation in a high-vacuum system (1×10^{-5} mbar); they were about 90 nm thick and were patterned through a standard photolithographic process.

As previously mentioned, the gold bottom-contact hosts the probe area where the receptor is immobilized. In order to obtain a good coverage of the probe area with the molecules of interest, its surface must be cleaned out from all the substances that naturally tend to adsorb onto gold. Several cleaning procedures were tested. Most of the effective procedures are extremely hard and cause the gold layer delamination. Gold showed a better tolerance to the chemical treatments when the PET substrate was covered with a Parylene layer (1.5 μm thick). Parylene is a chemically inert polymer and it was used as buffer layer because gold has good adhesion on it. As Parylene has very good electrical properties (dielectric constant of 3.15 at 60 Hz) and shows low hysteresis phenomena [58]), a thickness of 1.5 μm of Parylene was also deposited upon the floating-gate to form the gate dielectric. Both the buffer layer and the gate dielectric layer were obtained by CVD at room temperature, but for the gate dielectric deposition an adhesion promoter (A174) was used. Moreover, during this step, the probe area was protected with Parafilm.

Pentacene was used as organic semiconductor and it was deposited by thermal evaporation in a high-vacuum system (1×10^{-5} mbar). It is just to obtain a similar semiconductor layer in both devices used as reference and sensor that in these layouts the floating-gate electrodes under the OFET were designed very close together .

The semiconductor deposition was the final step for the HV pH sensors. Its frontal and vertical structure together with the material which was employed in its fabrication are shown in figure 3.6.

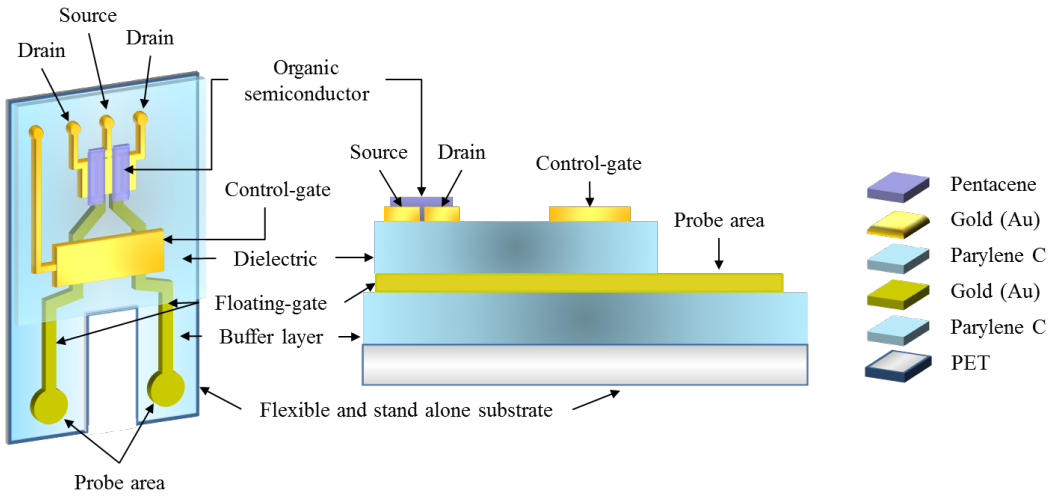

Figure 3.6: Fabrication steps of the HV pH sensor and employed materials.

3.4.3 Functionalization - Materials & methods

SAMs based on alkanethiols and probe area made of gold were chosen to realize the HV pH sensors. This choice was due to several reasons. First, alkanethiols on gold are widely used because gold can be easily deposited both as a thin film and a colloid, and it is also exceptionally easy to pattern by combining a lithography process with chemical etching. Secondly, alkanethiols on gold are by far the most extensively studied SAMs; therefore, many results, procedures and a number of existing results of spectroscopies and analytical techniques are available in the literature. Finally, functionalization through alkanethiolated SAMs is considered an easy procedure to apply. In fact, gold binds thiols with a very high affinity following the principle of soft-hard acids bases interaction [59] and the bond formation occurs spontaneously.

In the following subsections, after a brief introduction on Self Assembled Monoloayers (SAMs) based on alkanethiols, the molecules which were used as receptors in the sensor fabrication and the experimental procedure are described.

3.4.3.1 Alkanethiolated SAMs - General properties

Functionalization through alkanethiolated SAMs can be obtained by spontaneous adsorption from either the vapour phase or the liquid [60]. The vapour phase adsorption takes place in an ultra-high vacuum (UHV) system which allows to grow SAMs in

a clean environment. In order to obtain SAMs formation from the liquid phase, the thiolated molecules must be solved in a diluted solution where the substrate is then dipped. The second method is the most commonly used as it is a low-cost procedure; moreover, it is especially suitable for those applications that must be carried out from liquid phase, such as cell culture and wetting studies.

When functionalization occurs form the liquid phase, the head groups adsorb onto the substrate forming a disordered mass of molecules, in a time which ranges from milliseconds to minutes; then, in a period of few hours at room temperature, Van der Waals interactions among the tail groups give rise to the SAMs reorganization into a two dimensional layer. A tightly packed formation that reduces the monolayers free energy maximizes the SAMs density and minimizes the surface defects. Figure 3.7a shows a schematic diagram of an ideal SAMs of alkanethiolates supported on a Au(111) substrate.

Several experimental factors can affect the structure of the resulting SAMs and the rate of formation [61]: cleanliness of the substrate, solvent, temperature, concentration of the adsorbate, chain length, immersion time, purity of the adsorbate, concentration of oxygen in solution and surface structure are the most important.

Many molecules tend to adsorb onto gold surfaces which are exposed to the environments for a long time. Depending on the adsorbates, SAMs may not be suitable to displace the adventitious materials adsorbed onto the substrate. Therefore, in order to achieve a good functionalization, contaminants and impurities must be carefully removed from the gold surface.

Ethanol is the solvent most widely used in SAMs preparation as it solvates a variety of alkanethiols with varying degrees of polar character and chain length; nevertheless, depending on the SAM, also water and non-polar solvents can be used. The rate of SAM formation is small in non-polar solvents; moreover, the strong solvent-adsorbate interactions in these solutions can impede the organization of SAMs formed from alkanethiols.

The temperature is an important parameter which affects the SAMs formation especially during the first minutes. Elevated temperatures promote the removal of adventitious materials and solvent molecules physisorbed on the surface, and make it possible for the system to cross the activation barriers of processes such as chain reorganization and lateral rearrangements.

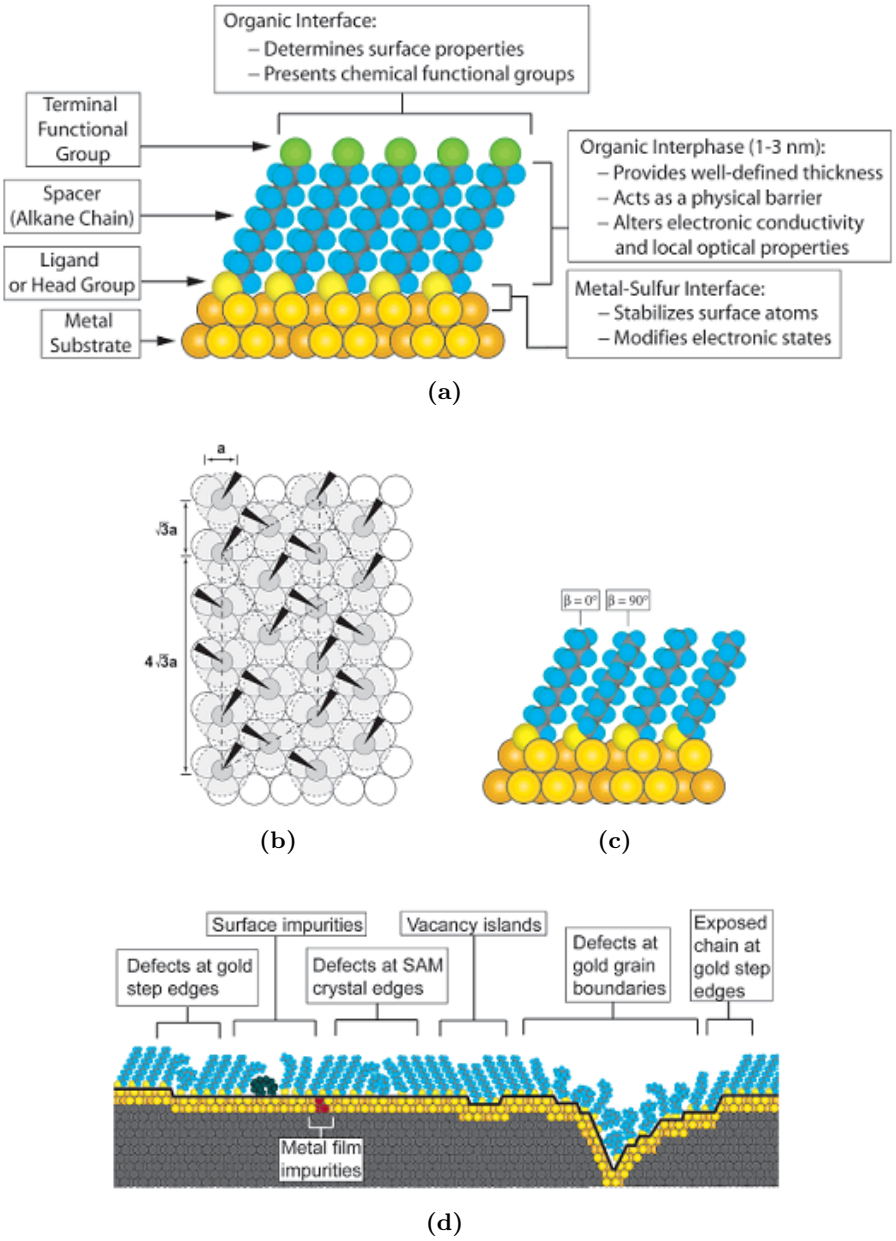

Figure 3.7: Schematic diagram of an ideal, single-crystalline SAM of alkanethiols supported on Au(111) (a); structural $(\sqrt{3} \times \sqrt{3})R30°$ arrangement with the sulphur atoms (dark gray circles) 3-fold hollows of the gold lattice (white circles a= 2.88 $\mathring{A}$); the light gray circles with the dashed lines indicate the approximate projected surface area occupied by each alkane chain, while the dark wedges indicate the projection of the CCC plane of the alkane chain onto the surface (b); SAM's cross-section showing the alternating rotations of the carbon chains (c); schematic illustration of some of the intrinsic and extrinsic defects found in SAMs formed on polycrystalline substrates (the dark line at the metal-sulphur interface indicates the changing topography of the substrate) (d) [61].

SAMs reorganization also depends on the chain length. Concerning alkanethiols with more than 6 carbons, the activation barrier of the dissociation process lies below the energy required for the molecular desorption. Therefore, with increasing chain length, the thermodynamic stability of the physisorbed state increases and the activation barrier for the S–H bond dissociation process decreases.

The solution concentration and the immersion time are two inversely related parameters. In order to obtain the maximum coverage with SAMs based on alkanethiols on gold ($\sim 4.5 \times 10^{14}$ molecules/cm^2), the minimum concentration is $\sim 1\mu$M or $\sim 6 \times 10^{14}$ molecules/cm^3. Thiols usually tend to oxidise forming disulfides. Disulfides are less soluble than their thiol precursors, therefore they tend to physioadsorb onto the substrate altering the physical properties of the SAM. Reducing the oxygen concentration in the solution limits the thiols oxidation. For this reason, degassing the solvent with an inert gas such as argon and maintaining the solution in an inert atmosphere can improve the SAMs' properties. The lattice orientation directly affect the quality of the SAMs. SAMs selectively form on Au(111), therefore, the substrate determines the orientation of the molecules. The alkanethiols tend to arrange following a $(\sqrt{3}\times\sqrt{3})$R30° structure with alternating rotations of the carbon chains, but intrinsic and extrinsic defect due to several factors are usually contained (see figures 3.7b and 3.7c).

Methods for preparing the substrates and purity of the solution of adsorbates are responsible for some defects in SAMs, but also the substrate structure has an important impact in the SAM structure and defect contents. Figure 3.7d schematizes a few typical defects which can be found on a polycrystalline substrate.

The thiols can be easily removed from the surface by means of several techniques. Chemical oxidants or reductants, acting as concentrated acids or bases, or plasma oxidation which is usually used to clean the substrates, perfectly remove thiols. A controlled removal can also be obtained by means of electrochemical techniques. When a negative potential is applied in an aqueous or ethanolic electrolyte solution with a neutral or basic pH, the following half-reaction takes place:

$$\text{RS–M} + e^- \longrightarrow \text{RS}^- + \text{M}^0. \tag{3.7}$$

As this process is reversible, thiols can be re-adsorbed by removing the applied negative potential onto the metal surface. Finally, thiols can be easily removed by means of photo-oxidation. When the thiolates are exposed to ultraviolet (UV) irradiation in air,

they convert to sulfonate groups; these oxidized SAMs can be removed from the surface by washing it with a polar solvent, such as ethanol or water.

3.4.3.2 Receptor

In order to make the probe area sensitive to pH, SAMs based on alkanethiols provided with a functional group that is able to change its charge status following the pH changes of the tested analyte was used. Amino-groups and carboxylic-groups are both functional groups which change their charge depending on the pH of the solution where they are immersed. They were chosen to study the OCMFET response to pH variations because of this property, and also because they can provide a good functional layer for future investigations in biological applications.

In aqueous solutions, the alkylamines behave as weak bases according to the following chemical reaction

$$\mathrm{NH_3^+ + H_2O \underset{k_2}{\overset{k_1}{\rightleftharpoons}} NH_2 + H_3O^+} \tag{3.8}$$

where k_1 e k_2 represent respectively the dissociation and association constant; therefore the equilibrium and the acid dissociation constants are given by:

$$K_{eq} = \frac{k_1}{k_2} = \frac{[\mathrm{NH_2}]\left[\mathrm{H_3O^+}\right]}{\left[\mathrm{NH_3^+}\right][\mathrm{H_2O}]} \tag{3.9}$$

and

$$K_A = K_{eq} \cdot [\mathrm{H_2O}] = \frac{[\mathrm{NH_2}]\left[\mathrm{H_3O^+}\right]}{\left[\mathrm{NH_3^+}\right]}. \tag{3.10}$$

From equation 3.10 it results that

$$\left[\mathrm{H_3O^+}\right] = K_A \frac{\left[\mathrm{NH_3^+}\right]}{[\mathrm{NH_2}]}, \tag{3.11}$$

and the following Henderson-Hasselbach equation

$$\mathrm{pH} = \mathrm{p}K_A - \log\frac{\left[\mathrm{NH_3^+}\right]}{[\mathrm{NH_2}]} = pK_A + \log\frac{[\mathrm{NH_2}]}{\left[\mathrm{NH_3^+}\right]} \tag{3.12}$$

that can also be expressed as

$$\frac{[\mathrm{NH_2}]}{\left[\mathrm{NH_3^+}\right]} = 10^{\mathrm{pH}-\mathrm{p}K_A} \tag{3.13}$$

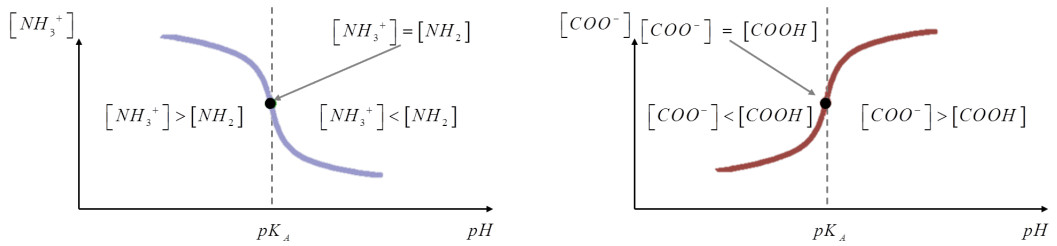

Figure 3.8: Graphic interpretation of the Henderson-Hasselbach equation for amino-groups protonation (a) and carboxylic acid deprotonation (b).

Equation 3.13 shows that there is a relation between the pH of the solution and the pK_A of the reaction. When the pH equals the pK_A, the amount of neutral amines equals the protonated amines; this equilibrium condition is called *isoelectric point* (P.I.). When the pH value is lower than the pK_A, the neutral amines will exceed the protonated form, and vice versa when pH > pK_A. Figure 3.8a provides a graphic representation of these relations. Therefore, these functional groups can work as receptor as they relate the pH of the solution to the amount of positive charges that are immobilized on the probe area surface. From figure 3.8a it results that the ratio between the concentration of the neutral and protonated amines has a large variation around the pK_A of the reaction. As a consequence, it is expected that the OCMFET is more sensitive to pH variation around the pK_A.

The carboxylic acid gives rise to the following chemical reaction

$$\mathrm{COOH} + \mathrm{H_2O} \underset{k_2}{\overset{k_1}{\rightleftharpoons}} \mathrm{COO^-} + \mathrm{H_3O^+} \tag{3.14}$$

which is expressed through the following equilibrium constant

$$K_{eq} = \frac{k_1}{k_2} = \frac{[\mathrm{COO^-}]\,[\mathrm{H_3O^+}]}{[\mathrm{COOH}]\,[\mathrm{H_2O}]} \tag{3.15}$$

and acid dissociation constant

$$K_A = K_{eq} \cdot [\mathrm{H_2O}] = \frac{[\mathrm{COO^-}]\,[\mathrm{H_3O^+}]}{[\mathrm{COOH}]}. \tag{3.16}$$

The Henderson-Hasselbach in this case is given by:

$$\mathrm{pH} = \mathrm{p}K_A - \log\frac{[\mathrm{COOH}]}{[\mathrm{COO^-}]} = \mathrm{p}K_A + \log\frac{[\mathrm{COO^-}]}{[\mathrm{COOH}]} \tag{3.17}$$

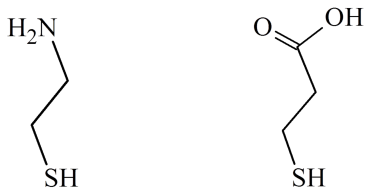

(a) **(b)**

Figure 3.9: Chemical formula of the 2-aminoethanethiol (a) and of the 3-mercaptopropionic acid (b).

or

$$\frac{[\mathrm{COO}^-]}{[\mathrm{COOH}]} = 10^{\mathrm{pH}-\mathrm{p}K_A}. \tag{3.18}$$

Figure 3.8b represents the graphic interpretation of the Henderson-Hasselbach equation the carboxylic acid.

As previously mentioned, the charges anchored on the probe area affect the transistor by inducing a charge separation into the floating-gate. In order to make their presence effective, they must be as close as possible to the floating-gate surface. As SAMs formed with long spacer-groups are not especially suitable to be used as receptors in the OCMFET, alkanethiols with a spacer consisting of only two saturated carbon atoms were employed: the 2-aminoethanethiol and the 3-mercaptopropionic acid molecules, both provided from Sigma Aldrich. Their chemical structure is reported in figure 3.9. This choice was also driven by the fact that their behaviour was successfully tested in the OCMFET developed by Caboni *et al.* [56], [57].

3.4.3.3 Functionalization procedure

The immobilization of SAMs was carried out as final step of the device fabrication, after a cleaning treatment of the probe area. From the literature it was reported [61] that gold surface can be effectively covered with alkanethiolated SAMs only if the adventitious materials which spontaneously tend to adsorb onto gold surface are removed. In order to develop a cleaning procedure which could effective and, at the same time, compatible with the materials employed for the sensors fabrication, electrochemical techniques were used. Several cleaning procedures were tested on gold electrodes, which were realized following the same procedures employed in the fabrication of the devices' probe area. As the electrochemical tests proved that a good coverage could be obtained by treating the

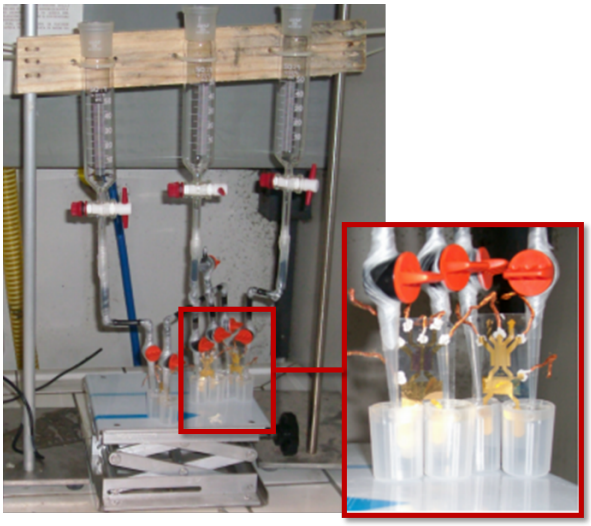

Figure 3.10: HV pH sensor - Experimental set-up for functionalization.

gold surface with sodium hypoclorite (NaClO), the probe areas were kept for 10 minutes in a NaClO solution (with 10 % of active Cl). Then, they were rinsed with ionized water and finally dried under a flux of Nitrogen. Functionalization was performed straight afterwards.

The solutions containing the SAMs to be anchored on the probe areas were solved in bidistilled water with the following concentration: 13 mM for the 2-aminoethanethiol (same recipe used by Caboni *et al.* [56], [57]) and 10 mM for the 3-mercaptopropionic acid. In order to reduce the thiols potential oxidation, the solution was de-aerated for at least 10 minutes by fluxing nitrogen in it. In order to reduce its exposition to air, the solution was prepared in a funnel and then poured through a small pipe into a specific container secured by a cover made of polydimethylsiloxane (PDMS). The portion of the floating-gate which hosted the probe area and had to be immersed into the solution was put into the container through a small slit which was created across the PDMS cover. Figure 3.10 shows the experimental set up used for functionalization. The probe areas were kept immersed into the solution for 15 hour. In order to prevent the thiols oxidation by UV exposition, the solution was prepared and kept in the dark during the whole procedure.

After functionalization, the probe areas were rinsed and then stored in bidistilled water.

3.4.4 Experimental results

The HV OCMFETs which had the probe area functionalized with the amine group or the carboxylic acid were tested as pH sensors by measuring the drain-source current using solutions with different pH values. AFM and electrochemical investigations were performed in order to validate the technique used for the molecules' immobilization. The experimental results carried out to study the SAM formation are presented first in the next subsection; afterwards, the capacitive characterization of the OCMFET and the electrical response of the sensor to pH changes are reported.

3.4.4.1 Receptor - Characterization

In order to set a proper functionalization procedure AFM analysis and electrochemical measurements were carried out on gold electrodes, which had the same dimensions and shape of the probe area, and which were prepared following the same process that was also used for the probe area's fabrication. Figure 3.11a shows the AFM images obtained for a 4 μm $\times$ 4 μm portion of the gold surface; the surface appears homogeneous with the presence of gold nanoparticles of about root mean square (RMS) roughness. The analysis was performed over different portions of the sample, obtaining an average value of 5.8 $\pm$ 0.8 nm (depending on the observed area which was varied from 4 μm^2 up to 140 μm^2). AFM was also employed to estimate the average thickness of the gold layer, which resulted to be 89 nm (see figure 3.11b).

In collaboration with the Inorganic and Physical Chemistry group of the University

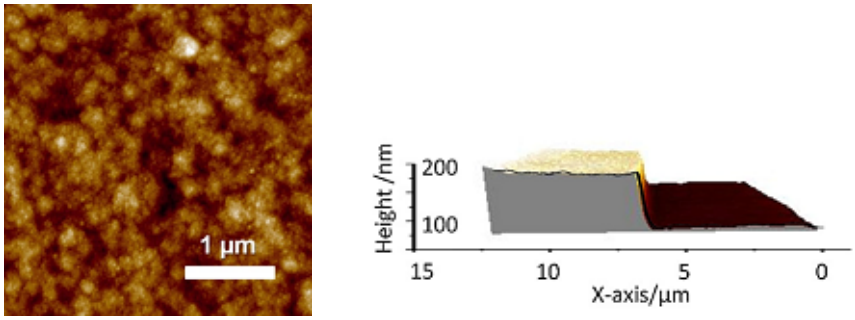

(a) **(b)**

Figure 3.11: AFM micrograph of the gold layer surface (a); three dimensional image of the substrate-Au interface cross section and corresponding profile (b).

of Bologna, Cyclic Voltammetry (CV) and Electrochemical Impedance Spectroscopy (EIS) were employed as surface characterization techniques. The charge of the acidic or basic terminal group of SAMs influences the amperometric response for the negatively charged electro-active probe $[Fe(CN)_6]^{3-}$, as the redox response of the probe molecule changes with the solution pH, as well as the extent of the attraction between the probe itself and the terminal group. All the electrochemical tests hereafter reported were carried out in a single compartment, three-electrode cell. Electrode potentials were measured with respect to an aqueous Saturated Calomel Electrode (SCE). A Pt wire was used as counter electrode and the working electrode was the PET-Au electrode under investigation. The tests were performed in 0.01 M buffer (phosphate or borate depending on the desired pH) solutions containing 5 mM $[Fe(CN)_6]^{3-}$ as a redox probe, at a potential of 0.17 V vs. SCE. The ionic strength was kept constant by adding 0.1 M KCl to all the buffered solutions. An Autolab PGSTAT100 equipped with px1000 modulus for pH control (Ecochemie, Utrecht, The Netherlands) potentiostat/galvanostat interfaced with a personal computer was used in all the CV measurements. EIS measurements were performed with a CHInstruments Mod. 660A, controlled by a personal computer via CHInstruments software. The temperature was kept constant using a thermostat HAAKE D8. The investigated frequency range was 100 mHz 10 kHz and the experimental data were fitted by using the software developed by Boukamp using Randles equivalent circuit. Figure 3.12a and figure 3.12b respectively show the CV and the EIS recorded on a electrode modified with the 2-aminoethanethiol SAM. The responses depended on the solution pH since the charge at the interface of the coated electrode changed once the solution pH was changed, due to the amino groups presence. In particular, when the measurements were taken in a more basic pH solutions, an increase of the charge transfer resistance and a corresponding decrease in the faradaic current (since a negative redox probe was employed) were recorded. CV and EIS measurements were also used to characterize gold surfaces modified with the 3-mercaptopropionic acid. Figure 3.12c and figure 3.12d summarize the plots of the measured mean values of Rct and ipc versus the pH of the solution. The amperometric measurements confirmed the effective immobilization of the molecules to the gold surface. All curves resulted sigmoidal in shape and showed a flex at different values depending on the pK_A of the amino or the carboxylic terminal groups. The Rct vs pH plots were therefore employed to evaluate the pK_A of the different molecules: 7.3 for

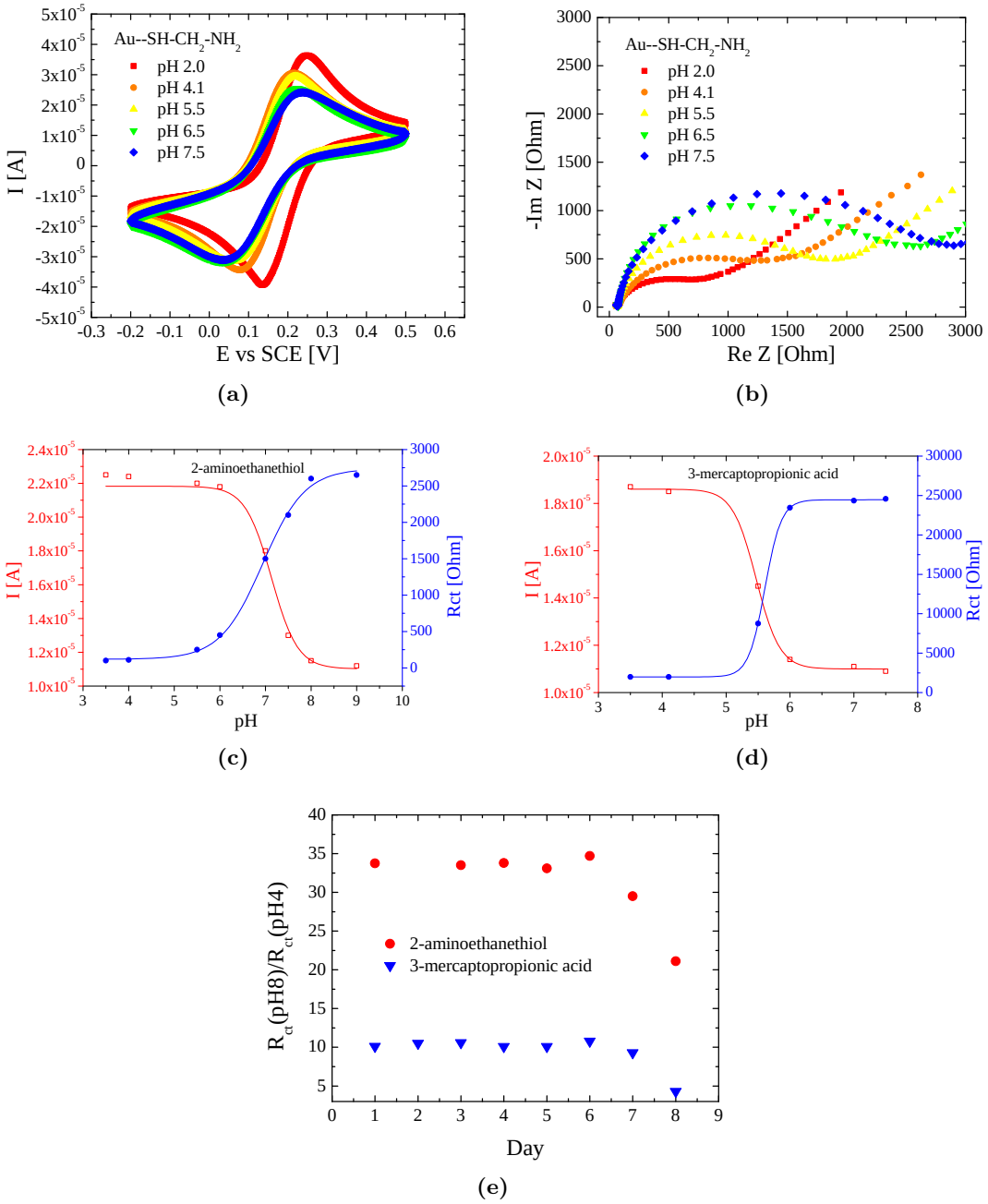

Figure 3.12: Electrochemical characterization of SAMs for pH detection: CV curves recorded at 0.05 V·s^{-1} (a) and Nyquist plots obtained at 0.17 V in the frequency range form 100 mHz to 10 kHz (b) for a gold electrode modified with 2-aminoethanethiol in a 0.5 mM $[Fe(CN)_6]^{3-}$ solution at the pH shown in the legend; plots of the faradaic current resulting from the CV (red line), and plot of the Rct resulting from EIS (blue line) as a function of the solution pH for a gold electrode modified with 2-aminoethanethiol (c) and 3-mercaptopropionic acid (d); plot of Rct(pH8)/Rct(pH4) as a function of the day of utilization of the electrode (e).

the molecules with the amino group and 5.6 for the molecules with the carboxylic acid. These values are in agreement with the literature data obtained by electrochemical techniques [62] or by other kinds of measurements such as contact angle measurements [63], chemical force titration using atomic force microscopy [64], or quartz crystal microbalance [65]. The stability of the SAMs was studied by repeating the EIS measurements at pH 4 and pH 8 for one week. Figure 3.12e shows the ratio of Rct at pH 8 to Rct at pH 4 which was plotted as a function of the utilization day. The electrode was stored at 4 °C in water solution when not in use. From the plot reported in Figure 3.12e it can be noticed that all the monolayers retained their properties for approximately 5 days.

3.4.4.2 Capacitances

Vertical capacitances of the device were evaluated by realizing a set of at least 10 capacitors. The capacitors had the same dimensions and shape of the electrodes fabricated in the device, and were prepared following the same process that was used for the device fabrication. C_{CF}, C_{SF} and C_{DF} were evaluated by means of an Agilent 4284A multimeter. Table 3.1 reports the recorded data.

	CAPACITANCE @60 Hz [pF]
C_{CF}	$(76 \pm 2)\cdot 10$
C_{SF}	21 ± 6
C_{DF}	26 ± 3
C_{TOT}	$(81 \pm 2)\cdot 10$

Table 3.1: Capacitances taken at 60 Hz; the average was calculated on ten devices and the error was estimated by doubling the standard deviation.

3.4.4.3 Electrical response

The experiment was carried out by characterizing the OCMFETs through current-voltage measurements. Output characteristics, were recorded at room temperature in air by means of two Keithley 2612 and 2636 source meters controlled by a Labview software. Figure 3.13 shows the output characteristics of a device with two OCMFETs sharing the control-gate and the source electrode.

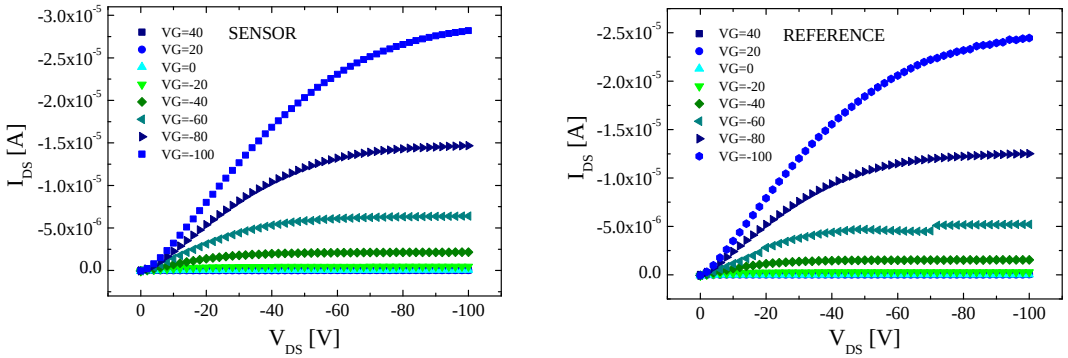

(a) **(b)**

Figure 3.13: HV OCMFET for pH sensing output characteristics recorded before functionalization in two devices sharing the source and control-gate contacts which were functionalized and used as sensor (a) and reference (b).

This device was functionalized with the 2-aminoethanethiol molecules and then tested as pH sensor. The two channels were referred to as *reference* and *sensor* because, during the measurements, the probe area of the OCMFET used as reference was kept in a solution with a constant pH, while the probe area of the sensor was soaked in electrolytic solutions with different pH values. Figure 3.14 shows the adopted experimental set-up.

Electrolytic solutions at different pH values were prepared by using aqueous solutions made of citric acid ($C_6H_8O_7$) and disodium phosphate (Na_2HPO_4) at different

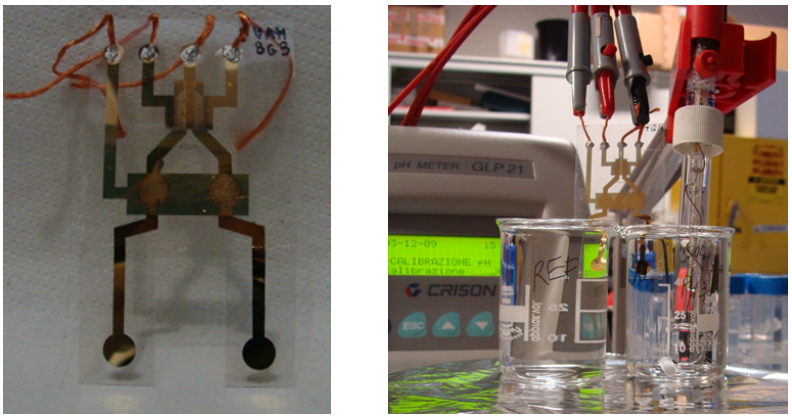

Figure 3.14: HV pH sensor (a) and experimental set-up (b).

concentrations.

The electrical response to solution pH of the device tested as pH sensor was measured by recording the OCMFETs output characteristics while the sensor and the reference had their probe area immersed in the solutions to be tested. A time of 10 minutes was waited in order to obtain a stable output drain current between the probe area soaking and each measurement recording. The working principle of the device was verified through the following experimental steps. Both probe areas were soaked in a pH 7.0 solution and, after 10 minutes, the output characteristics of both devices were recorded (step 1). After this measurement, the sensor solution was changed with a pH 2.5 solution, while the reference solution was left unchanged; the output characteristics were recorded same as in step 1. In step 3 the reversibility in the sensor output was tested by restoring also in the sensor the solution which was previously used in step 1. Finally, the sensor solution was changed with a 3.6 solution while, as in step 2, the reference solution was kept unchanged; currents were then recorded as in the previous steps.

Figures from 3.15a to 3.15d show the output characteristics recorded on the sensor. In order to allow a comparison between the source-drain currents taken using a different electrolytic solution, the currents which were measured during each step at a gate potential of –100 V are also reproduced in a single plot in figure 3.15e; the reference response is reported in figure 3.15f. Recorded data show that, while the reference currents held almost unchanged (see figure 3.15f), the sensor drain currents decreased significantly according to pH changes (see figure 3.15e). This experimental result agrees with the working principle of the device. Pentacene was used as organic semiconductor, therefore holes are the majority carriers which are driven by the source-drain polarization. When the amino groups are immersed in acidic solutions, they protonate and, as a consequence, drive holes back from the transistor channel through the dielectric polarization. As a result, they cause a decrease of the source-drain current, as shown in the recorded data.

The same kind of electrolytic solutions and experimental procedures were applied to test the working principle of the HV OCMFET by employing SAMs provided with the 3-mercaptopropionic acid. As this functional group de-protonate in basic solutions, it was expected that source-drain currents recorded using basic solutions should be higher than the one taken with acidic solutions. In fact, in basic solutions the negative charge

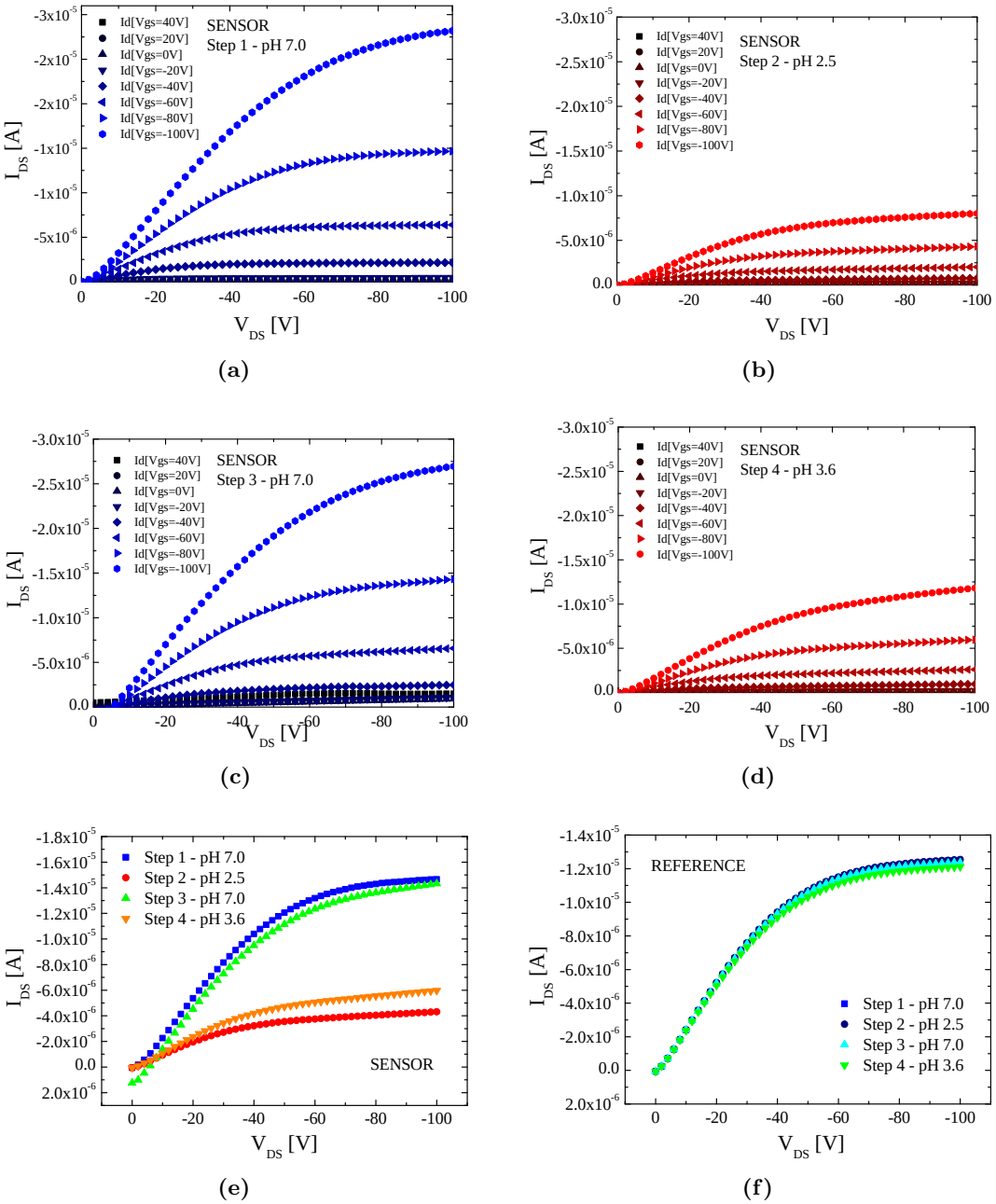

Figure 3.15: Experimental results for the HV pH sensor functionalized with the 2-aminoethanethiol: output characteristics of the sensor recorded with a pH 7.0 solution (step 1) (a), pH 2.5 solution (step 2), pH 7.0 solution (step 3) (c) and a pH 2.5 solution (step 4); output characteristics recorded during the four steps in the reference (e) and in the sensor (f).

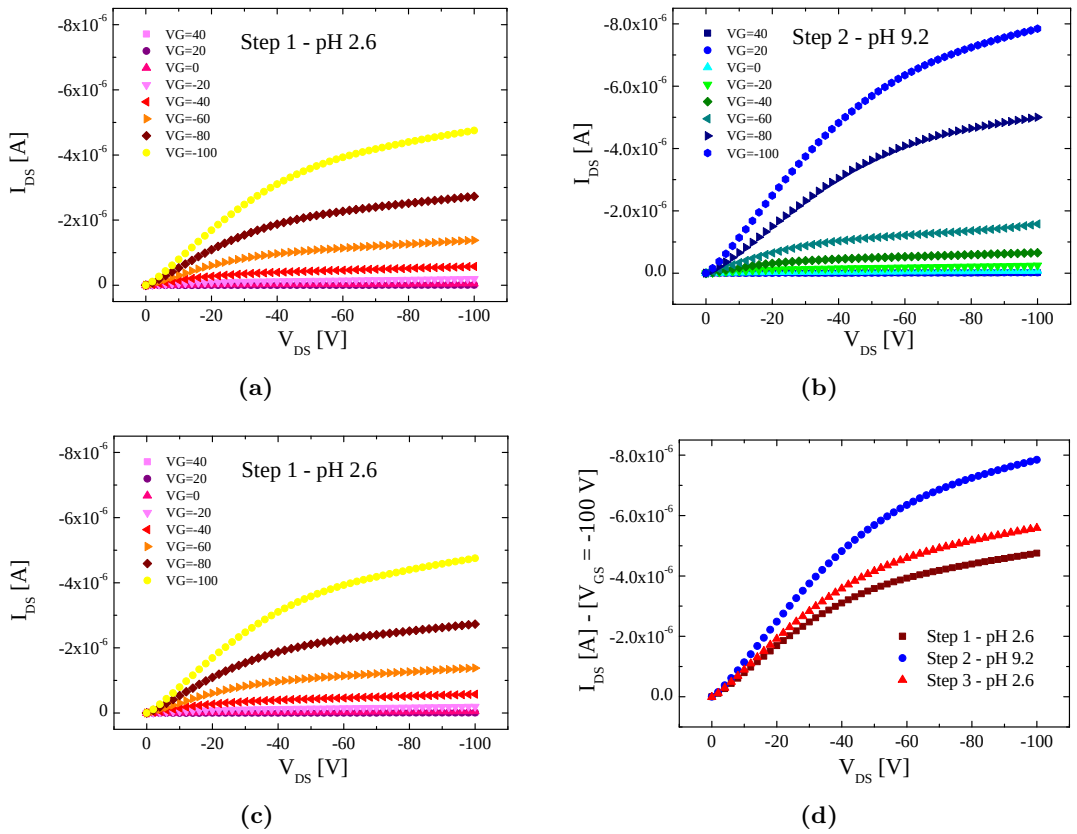

Figure 3.16: Experimental results for the HV device functionalized through the 3-mercaptopropionic acid which was tested as pH sensor: output characteristics recorded under a pH 2.6 solution (step 1) (a), under a pH 9.2 solution (step 2) (b), and under the same pH 2.6 solution used in step 1 (step 3) (c); output characteristics recorded at $V_G = -100$ V in steps from 1 to 3 (d).

of the carboxylic groups would attract holes in the transistor channel. The experimental results confirmed this behaviour. Figure figures from 3.16a to 3.16c report the recorded data. The sensor output characteristic was first recorded using a pH 2.6 solution (step 1); the measurement was then taken with a pH 9.2 solution (step 2). In order to verify the reversibility in the sensor output, currents were recorded again after restoring the same solution used in step 1 (step 3). A comparison between the source-drain currents taken at a gate potential of –100 V using a different electrolytic solution in steps from 1 to 3 are reported in the single chart shown in figure 3.16d.

3.4.5 Receptor - Efficiency investigation

The experimental results proved that the OCMFET works as charge detector and that it can be used to make pH sensing. However, the reproducibility of the experimental results was very low, when using both the SAM based on the 2-aminoethanethiol and the 3-mercaptopropionic acid. In order to establish if the low performances were due to the device layout or to a low efficiency of the receptor, further tests were carried out to investigate the properties of the sensing area.

In collaboration with the Department of Chemistry of the University of Bari, Xray Photoelectron Spectroscopy (XPS) were carried out on gold electrodes which were realized with the same process employed to fabricate and functionalize the probe area with the 2-aminoethanethiol. XPS experiments were performed using a Theta Probe Thermo VG Scientific spectrometer equipped with a microspot monochromatized AlKα source and a 180° spherical sector analyzer with a two-dimensional electron detector. All the spectra were recorded in Constant Analyzer Energy (CAE) mode using a pass energy of 150 eV for survey and 100 eV for high resolution regions (C1s, O1s, Au4f, N1s and S2p). Calibration of the binding energy (BE) scale was performed by taking a suitable signal as internal reference. In particular the reference peak was the $Au4f_{7/2}$ component of the Au4f signal (BE = 84.0 eV). Data analysis and curve-fit procedures were performed by means of *Avantage* 4.75 commercial software. The same peak lineshape parameters (Gaussian/Lorentzian ratio and full width at half maximum) values were employed for the curve fitting of components belonging to the same high-resolution spectrum. XPS peak intensities were obtained after a Shirley background removal, using *ChemState* sensitivity factors. Effective Attenuation Length (EAL) taken into account was calculated by the software on the basis of the TPP-2M formalism, allowing an automatically correction of the Kinetic Energies (KE) of the detected electrons.

SAMs with 2-aminoethanethiol on Au/Parylene-PET films were prepared and then analyzed by XPS. SAM formation was assessed by the acquisition of high resolution spectra of diagnostic regions (N1s, S2p, Au4f) and their deconvolution by curve-fitting procedures. $S2p_{1/2}$ component was automatically subtracted by a proper software algorithm before studying the S2p region, in order to perform signal deconvolution only on $S2p_{3/2}$. The same curve-fit parameters were used on analogue regions for all the samples.

The analysis of the elemental composition is reported in table 3.2. As expected, it resulted that the S/N ratio was close to 1.

Element	Surface atomic %	Standard deviation
C	38.3	1.5
Au	40.8	1.7
S	5.9	0.4
N	5.6	0.5
O	8.9	0.9

Table 3.2: Surface elemental composition of a SAM based on a Au/Parylene-PET chip; standard deviation is calculated on three replicates.

$S2p_{3/2}$ region (see figure 3.17) showed four components, whose attribution and relative abundance are reported in table 3.3. The most intense component, which is centred at (160.9 ± 0.3) eV, can be attributed to sulfur covalently bound to gold, as

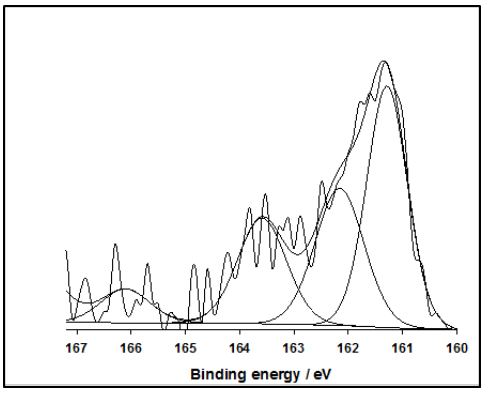

Figure 3.17: $S2p_3/2$ high resolution region of a SAM formed by 2-aminoethanethiol molecules.

Peaks	Position (eV)%	Relative surface %
S–Au	160.8 ± 0.4	51.3 ± 0.2
S–H	162.0 ± 0.5	18.2 ± 0.5
S–S	163.7 ± 0.7	17.1 ± 0.6
SO_x	166.2 ± 0.4	13.4 ± 0.5

Table 3.3: Sulfur chemical environments of an amino-terminated SAM on a Au/Parylene-PET chip; standard deviation is calculated on three replicates.

widely reported in the literature [66], [67], [68], [69]. Minority component at (162.0 ± 0.2) eV can be associated to unbound thiols. The two unexpected components at higher binding energies can be ascribed to the formation of disulfur and variously oxidized species, quite likely due to damaging induced by X-rays [70]. Nevertheless, the attribution of the two components centred around 164 and 166 eV is quite controversial in the literature. In fact, other hypothesis were presented [66], [68]. Wirde *et al.* [68] attributed the components at higher binding energy to the coexistence of anionic and zwitterionic forms of the 2-aminoethanethiol molecule, which are always present in aqueous solutions. Cossaro *et al.* [67], in agreement with Zhang *et al.* [69], observed that 2-aminoethanethiol can bond the gold surface in two different conformations: gauche and trans (more stable). These conformations depend on the preparation conditions and lead to the presence of undesired peaks on the left side of the $S2p_{3/2}$ spectrum, which are associated with the so-called *gauche defects*.

Concerning the nitrogen chemical states, the recorded data are shown in figure 3.18 and table 3.4. Two different environments were identified: a nitrogen lower binding energy component (399.7 ± 0.3) eV, which can be attributed to the neutral amine

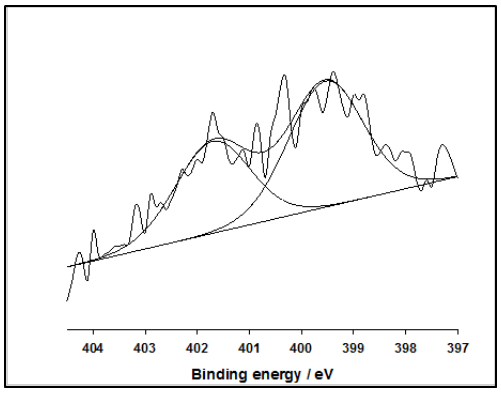

Figure 3.18: N1s high resolution region of a 2-aminoethanethiol SAM.

Peaks	Position (eV)%	Relative surface %
$–NH_2$	399.5 ± 0.4	58 ± 2
$–NH_3^+$	401.6 ± 0.5	42 ± 2

Table 3.4: Nitrogen chemical environments of a 2-aminoethanethiol SAM based on a Au/Parylene-PET chip; standard deviation on relative abundances is calculated on three replicates.

groups of the 2-aminoethanethiol molecules, and a second component (402.1 ± 0.5) eV, which suggests the presence of protonated amines [67]. The presence of two peaks could also be due to the formation of a multilayer, caused by the adsorption of other 2-aminoethanethiol molecules on those covalently bound to gold: in facts, amino end groups lead to the formation of a hydrophilic surface, and can be easily coordinated by thiolic groups [68].

The XPS analysis came out several important remarks which could explain the low reproducibility obtained in the experimental results. From table 3.3 it resulted that, in a freshly prepared surface (XPS analysis ws performed within 20 minutes from SAMs preparation), only the 51 % of the molecules bound the surface in a way which is suitable for the pH sensing; the remaining molecules interacting with the substrate can be considered as undesirable features of the SAM, which reduce the number of amino groups available for pH sensing. As SAMs further deteriorate because of the interaction with Oxygen, it is expected that the efficiency achievable in the sensor could be even lower because of the stress it is subjected during the electrical measurements. The XPS analysis showed that SAMs can also organize in multilayers. As the charge separation that the amino end groups can induce in the floating-gate surface depends on their distance form the surface, the multilayer formation can be considered another undesirable effect which can compromise the sensor performance.

Preliminary XPS tests carried out on electrodes modified with a SAM based on the 3-mercaptopropionic acid showed sulphur atomic percentage comparable with the amount recorded when the 2-aminoethanethiol molecules are used.

As a consequence, even if the working principle of the device was proven, it resulted that the use of a most efficient receptor is necessary in order to develop a sensor able to respond with accurate and reproducible results.

3.5 High-Voltage DNA sensor

An HV OCMFET implementation similar to the one employed for the HV pH sensor was used to fabricate and test the first HV OCMFET implementation for DNA detection. In the following subsections, the materials and the fabrication methods which were used to obtain the sensor are reported. Finally, the surface characterization of the sensing layer used as receptor and the electrical results are shown.

3.5.1 Layout

Same as for the HV pH sensors, a layout including two OCMFETs with a common source and control-gate was adopted to realize these HV DNA sensors. The channel and the control-gate were designed with the same shape and dimensions of the HV pH sensor (see figure 3.19), i.e., the transistor had a linear channel wide $W = 6$ mm and long $L = 40$ μm ($W/L = 150$) and a circle with a diameter of 1.89 mm^2 was used as control capacitor. A detail (not in scale) of the channel region is shown on the right-hand side in figure 3.19.

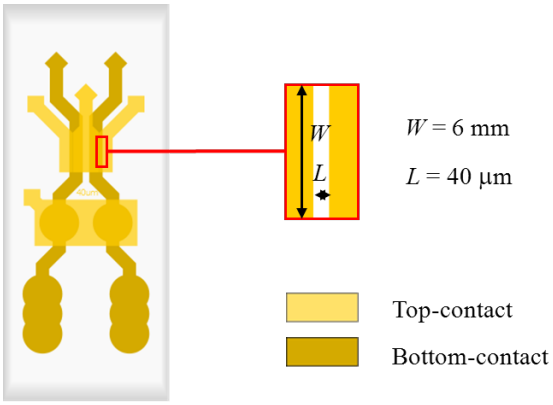

Figure 3.19: Layout of the HV DNA sensor.

Compared to HV pH sensors a few changes were introduced in the floating-gate. In order to have available a bigger surface as sensing area (~ 60 mm^2), the metal line with the probe area was enlarged. Moreover, its length was extended beyond the OFET in order to provide an electrical contact which could be used to allow electrochemical treatments on the probe area.

3.5.2 Fabrication - Materials & methods

This first implementation of the OCMFETs for DNA sensing were realized by using almost the same materials and procedures employed for the HV pH sensor up to the semiconductor deposition. All the electrodes were made of gold: they were deposited by thermal evaporation in a high-vacuum system (1×10^{-5} mbar) and patterned through a standard photolithographic process. Parylene was used as buffer layer and gate-dielectric as well: a 1.5 μm thick layer was deposited by CVD at room temperature.

Finally, Pentacene was used as organic semiconductor; it was deposited by thermal evaporation in a high-vacuum system (1×10^{-5} mbar).

Two further steps were carried out in order to finish the HV DNA sensors.

It is well known that the performances of the OTFTs which are based on Pentacene are highly affected by environmental conditions. In order to keep its electrical parameters stable in time, the OFETs were encapsulated by depositing a Parylene C layer with a thickness of 2 μm. Parylene C was chosen as it is a chemically inert and biocompatible material. Same as during the insulator deposition, a Parafilm protection was used to prevent Parylene from covering the probe areas.

Finally, a minichamber system was applied to protect each probe area. During functionalization, in fact, it is advisable to avoid that the solution which contains the DNA molecules completely evaporates; the minichamber system, together with a Parafilm protection, allowed to hold each probe area in a small close environment which delayed the evaporation of the DNA solution. The minichamber system was made of polydimethylsiloxane (PDMS, Sylgard 184, Downcorning). PDMS is an elastomer that, when mixed with a catalyst (a mixture of a platinum complex and copolymers of methylhydrosiloxane and dimethylsiloxane) and heated at elevated temperatures (100 °C), becomes a cross-linked solid in just a few hours.

Figure 3.20 schematizes the fabrication process of these DNA sensors.

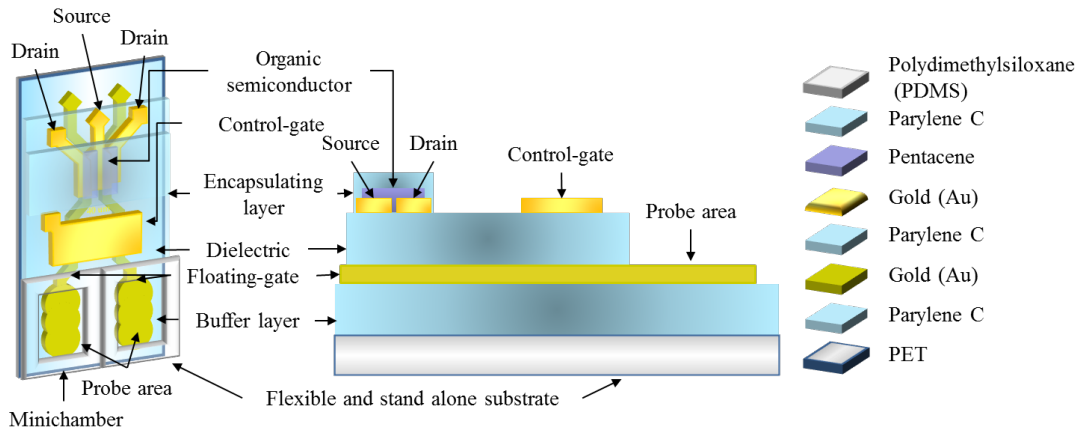

Figure 3.20: Fabrication steps of the HV DNA sensor and employed materials.

3.5.3 Functionalization - Materials & methods

The OCMFET was turned into a DNA sensor by immobilizing DNA molecules as probes on the sensing area. After a brief description of the DNA molecule and the mechanism used for its recognition, the materials and methods employed to functionalize the HV DNA sensor are described.

3.5.3.1 DNA molecule - Basics

The deoxyribonucleic acid (DNA) is the macromolecule that contains the genetic instructions for the development and functioning of most living organisms. This information is encoded as a sequence of four different units called *nucleotide*. Form a chemical point of view, the DNA molecules is a polymer made of repeating nucleotides, each containing a phosphate group (PO_4^-), a cyclic pentose sugar, *2-deoxyribose*, and a nitrogen-containing base. The nucleotides are covalently bounded together trough the sugar: the carbon atoms of adjacent sugar rings of the $5'$ (five prime) end which has a terminal phosphate group and the $3'$ (three prime) end which has a terminal hydroxyl group bound to the phosphates groups through phosphodiester bonds. They form a *backbone* which is known as *DNA-strand* or *DNA-chain*. In DNA there are only four different nucleotides as only four nitrogen-containing bases are found: *Adenine* (A), *Guanine* (G), *Cytosine* (C) and *Tymine* (T). They are classified into two different types following their chemical structure. A and G, named *purines*, are five- and six-membered fused heterocyclic compounds lying in the same plane. C and T, named *pyrimidines*, are six-membered ring atoms; same as same as for purines, all pyrimidine ring atoms lie in the same plane. Purines can form hydrogen bonds to pyrimidines, with adenine bonding only to thymine in two hydrogen bonds, and cytosine bonding only to guanine in three hydrogen bonds. Because of this selective bonding, that is called *base pairing*, A and T, together with the nucleotides that contains them, are considered complementary to each other, same as for G and C. In living organisms, DNA does not usually exist as a single molecule, but as a pair of molecules formed by two strands, which are made up by complementary nucleotides and have the shape of a double helix. As the alternating sugar-phosphate-bonds in the backbone have a direction, also DNA-strands have a direction, which is known as polarity: two complementary strands are anti-parallel as they have opposite orientations. Figure 3.21 shows

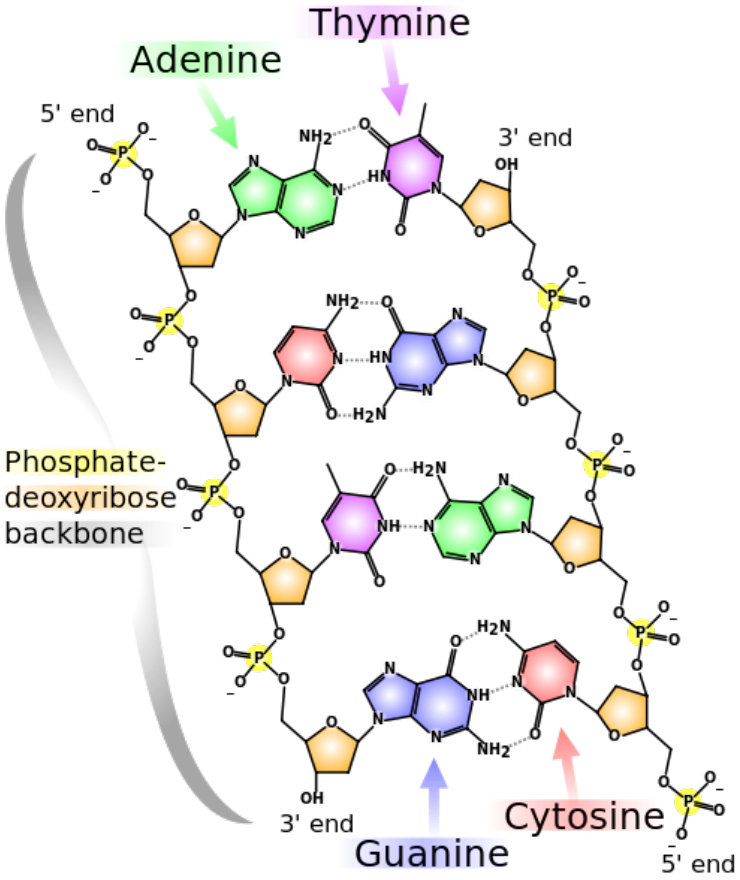

Figure 3.21: Chemical structure of the DNA molecule; hydrogen bonds are reported as dotted lines [71].

the chemical structure of the DNA molecule.

The hydrogen bondings which hold together two complementary strands are not particularly strong, therefore, two complementary strands can be easily broken and rejoined under specific conditions. The double helix can be separated into its single strands components by the action of a mechanical force, or by keeping it in strong acidic or alkaline solutions. Moreover, the double-stranded DNA (ds-DNA) abruptly dissociates at a temperature above the so called *melting temperature* (T_m), which value depends on the length of the DNA molecule and its specific nucleotide sequence. Separated complementary strands of nucleic acids spontaneously re-associate to form a double helix when the temperature is lowered below T_m. This process, also referred as *hybridization*, provides a powerful tool for investigating sequence similarity as well

as gene structure and expression. For instance, DNA molecules from two different organisms can be melted and allowed to hybridize in the presence of each other. If the sequences are similar, a DNA double helix is formed with the DNA contribution which can come from each organism. The degree of hybridization indicates the relatedness of the genomes and hence the organisms. Indeed, the most common techniques for DNA recognition are based on optical detection of DNA hybridization.

3.5.3.2 Receptor

In this first implementation of HV OCMFET as DNA sensor, two DNA sequences were used, both provided by Sigma Aldrich.

A ssDNA sequence formed by 31 bases (5′-$(T)_{13}$ GGT TTC CGC CCC TTA GTG-3′) modified with a spacer thiol ($HS(CH_2)_6$) in 5′ was used as probe. The thiol was collocated in order to allow the DNA binding to gold through acid-base interactions, same as for the alkanethiolated SAMs. With this sequence, two probes were used: one of them was provided with the Cyanine 3 (Cy3) in 3′ (HS-ssDNA-Cy3). Cy3 is a fluorescent dye with an absorption peak at 550 nm and an emission peak at 570 nm, which was applied in order to allow fluorescence detection of probes.

In order to test hybridization, a single strand formed by 18 nucleotides fully complementary to the probe sequence (5′-CAC TAA GGG GCG GAA ACC-3′) and provided with the Cy3 dye in 3′ was employed. The complementary strands did not include the bases complementary to the first 13 bases; these bases, which are closer the thiol, were introduced to work as spacer and promote hybridization.

The following list summarizes the DNA molecules used for each kind of test:

- 5′-$HS(CH_2)_6$-$(T)_{13}$GGT TTC CGC CCC TTA GTG-3′-Cy3 (HS-ssDNA-Cy3) for DNA immobilization tests;

- 5′-$HS(CH_2)_6$-$(T)_{13}$GGT TTC CGC CCC TTA GTG-3′(HS-ssDNA) together with 5′-CAC TAA GGG GCG GAA ACC-3′-Cy3 for DNA hybridization tests.

Herne and Tarlov [72] demonstrated that the hybridization yield of a surface-bound HS-ssDNA depends on surface coverage. In order to achieve a specific hybridization, the surface-bound HS-ssDNA must be accessible; to this aim they controlled the surface coverage by creating mixed monolayers of the thiol-derivatized probe and a spacer-thiol,

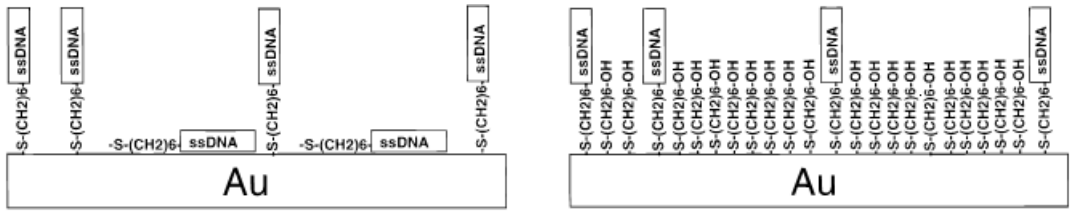

(a) **(b)**

Figure 3.22: Schematic of HS-ssDNA on Au (a) and with both HS-ssDNA and MCH adsorbed onto gold (b) [72]

the 6-mercapto-1-hexanol (MCH) molecule. By removing the non-specifically adsorbed DNA from the surface, this two-step functionalization technique makes the majority of the surface-bound probes accessible for specific hybridization with their complementary oligonucleotides, and facilitates the discrimination between complementary and non-complementary target molecules (see figure 3.22). Therefore, in view of their experimental results, in this work MCH molecules (provided by Sigma Aldrich) together with DNA oligonuecleotides were used as spacer.

3.5.3.3 Functionalization procedure

In order to obtain a good layer for DNA recognition, the probe surface requires a specific treatment. As the receptor is based on alkanethiols, cleaning the gold surface is necessary in order to allow the proper immobilization of the SAM onto the surface. Moreover, as the DNA strands can easily be damaged by bacteria, working with sterilized materials and surfaces is recommended. Before DNA immobilization, the gold surface is commonly treated by means of the piranha solution, which is a strong oxidant made of a 3:1 mixture of concentrated H_2SO_4 with H_2O_2. This solution is able to remove every kind of organic deposit and oxide from the surface; however, its use entailed a high risk of damaging the device. A freshly prepared piranha solution reaches the temperature of 120 °C, which is a temperature that the PET substrate is not able to sustain. The damage risk was reduced, but never eliminated, by keeping the solution temperature under 100 °C during its preparation.

The steps carried out in order to anchor the DNA molecules onto the probe areas followed the recipe reported by Herne and Tarlov [72]. The HS-ssDNA were solved in a 1 M buffer phosphate solution (pH 3.8) and a 3 μl drop was deposited on the probe

area straight after its cleaning; two hours later, a 3 μl drop of MCH (1.0 mM) was added. After the DNA and MCH deposition, the probe area was covered and kept for 15 hours at room temperature and in the dark in order to allow the self-organization of the DNA chains; then it was rinsed with bi-distilled water. After rinsing, the probe area was stored in a buffer phosphate solution (pH 7, 50 mM NaCl).

The target oligonucleotides were diluted in a 1 M TE, 1 M NaCl (10 mM Tris-HCl, 1 mM ethylenediaminetetraacetic acid (EDTA), 1 M NaCl, all reagents purchased from Sigma-Aldrich). Hybridization with the target oligonucleotides was performed by pipetting a 3 μl drop of the target solution on the functionalized probe area, which was previously rinsed by water and left dried in air. Same as for the functionalization process, when the probe area was exposed to the target solution, it was covered to reduce the solution's evaporation and kept in the dark for 24 hours. After hybridization, the probe area was rinsed by using the TE solution and then, same as after probe's immobilization, stored in the pH 7 (50 mM NaCl) buffer phosphate solution.

3.5.4 Experimental results

In the following subsections the experimental results recorded through this first implementation of the HV DNA sensor are reported. The data recorded on the electrically tested OTFTs were validated by using two different techniques: electrochemical surface characterization and fluorescence detection. The electrochemical characterization was used to investigate the surface properties of a few electrodes which were modified following the same procedure applied with the devices. Fluorescence optical detection was used to validate the hybridization process on working devices.

3.5.4.1 Receptor - Characterization

Three different electrochemical measurements were carried out to test the effectiveness of the functionalization and hybridization processes. In particular, Cyclic Voltammetry (CV) and Electrochemical Impedance Spectroscopy (EIS) were used to establish if the DNA was anchored to the surface by detecting the amperometric response in a solution containing a negatively charged electro-active probe, while Chronocoulometry (CC) were used to quantify the DNA density.

All the measurements were carried out in a three-electrode cell. Gold electrodes, which had the same dimensions and shape of the probe area, and which were fabricated

following the same process used for the probe area, served as Working Electrode (WE); a Pt wire was used as Counter Electrode (CE), while all potentials were reported in reference to the Ag|AgCl| 3 M KCl electrode (RE). An Autolab PGSTAT100 equipped with px1000 modulus for pH control (Ecochemie, Utrecht, The Netherlands) potentiostat/galvanostat interfaced with a personal computer and equipped with NOVA software package (Eco Chemie) was used in all the CV measurements.

In order to clean the gold surface before functionalization, three different solutions/procedures were applied: piranha solution, an electrochemical treatment in H_2SO_4 and NaClO. Among these solution/procedures, which were all proven to be efficient, the electrochemical cleaning was preferred to the other solutions because, in addition to clean the surface, it allows evaluating the active area of the electrodes which were then used to study the DNA coverage. In fact, this information was used to estimate the DNA charge that is usually immobilized during the anchoring of probes and the hybridization of targets. The electrochemical treatments consisted in cycling the potential from 0.0 V to 1.5 V at 1 $V \cdot s^{-1}$ in 0.5 M H_2SO_4 until cyclic voltammograms were reproducible (usually 400 cycles). Figure 3.23a shows the typical voltammograms recoded on five different electrodes in 0.5 M H_2SO_4. As the CVs resulted highly reproducible, they confirmed that the structure and the area of the gold layers were well controlled. The electrochemically induced deposition of an oxygen monolayer on gold and of the charge corresponding to the reduction of this monolayer was used to estimate the geometric surface area [73]. The charge obtained by integration of the cathodic peak on the voltammogram is proportional to the real area of the gold surface and, as a consequence, provides an indication of the surface roughness. The roughness factor result, which was calculated by the ratio between the real area and the geometric area, resulted of 2.26 $\pm$ 0.11.

The DNA molecules are negatively charged because of the presence of the phosphate groups. When the assembly is formed, it sets up a negatively charged interface which makes difficult the penetration of a negatively charge redox probe through the monolayer to undergo electron transfer at the gold surface. The phosphate groups form the DNA backbone, therefore a dsDNA contains a double amount of negative charge compared with respect to a ssDNA. As consequence, a further repulsion of the redox-probe and an increase in the electron transfer resistance at the electrode was expected when the amperometric response was recorded in presence of dsDNA.

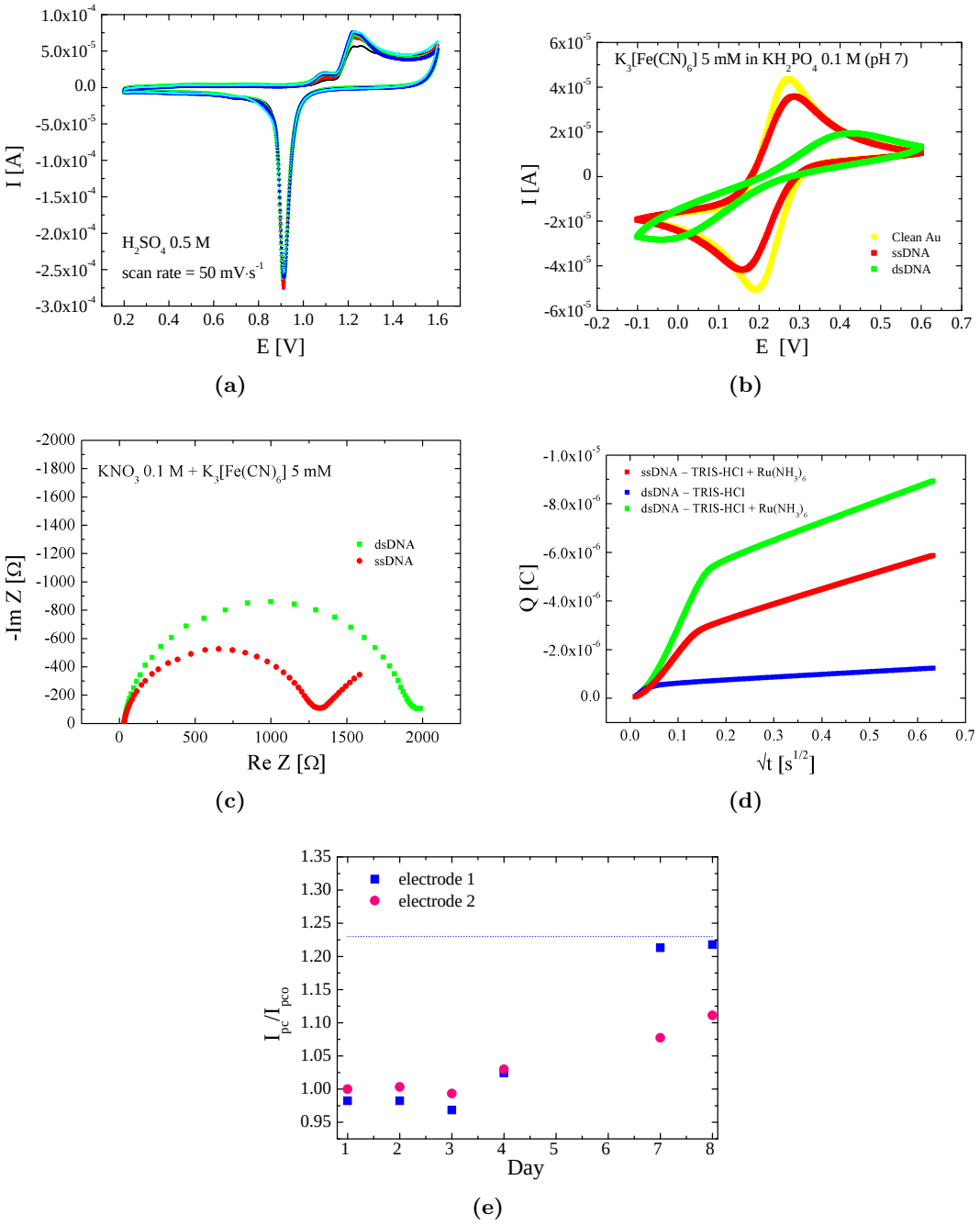

Figure 3.23: Electrochemical characterizations of gold surface for DNA detection: CV recorded in 0.5 M H_2SO_4 with 5 different PET-Au electrodes taken at a potential scan rate of 0.05 V·s^{-1} (a); CV taken from –0.1 V to 0.6 V at a scan rate of 0.05 V·s^{-1} (b) and EIS (c) recorded in a 5 mM $K_3[Fe(CN)_6]$; CC taken in 0.1 M Tris-HCl with and without $Ru(NH_3)_6^{3+/4+}$ of a DNA modified electrode (d); ratio between the cathodic peak current and the peak current (recorded performing CV in 5 mM $K_3[Fe(CN)_6]$ in buffer phosphate (pH 7)) measured on the first utilization day (I_{pc0}) vs. the utilization day for two different functionalized electrodes (e).

The CV curves confirmed that the functionalization procedure used for the electrodes and the devices allowed to immobilized the DNA on the surface. Figure 3.23b shows the CV recorded in a 5 mM $[Fe(CN)_6]^{3-}$ in buffer solution (pH 7). A reversible voltammogram for the redox couple was recorded when the bare gold electrode was used as WE, meaning that a diffusion-controlled process for the electron transfer reaction occurred at the surface. A decrease in the current for the oxidation/reduction peaks and an increase in the peak-to-peak separation value, compared to the voltammogram for bare gold, was detected after the thiolated DNA immobilization and its target deposition. The decrease in the current for the oxidation/reduction peaks indicates that repulsion between the $[Fe(CN)_6]^{3-}$ and the phosphate groups impeded the redox couple ferricyanide/ferrocyanide penetration through the monolayer [74]. As the DNA chain is a flexible molecule, the monolayer formed by ssDNA and dsDNA was not compact enough to completely prevent the redox couple penetration across it; nevertheless, the blocking effect recoded after the DNA hybridization was higher than that recoded after ssDNA because of the negative charge's doubling.

EIS was performed in a 0.1 PBS solution (pH 7) with a concentration of 5 mM $Fe(CN)_6^{3-}$, at the formal potential of the redox couple $Fe(CN)_6^{3-/4-}$ ($E = 0.22$ V vs. SCE). An AC amplitude of 0.005 V and a frequency range from 1 mHz to 1 MHz were applied. Figure 3.23d shows how the Nyquist plots of a ssDNA and dsDNA modified surface. According to what was already determined through the CV measurements, EIS measurements further confirmed the presence of a barrier for the interfacial electron transfer and that the resistance, which is proportional to the diameter of the semicircle to the electron-transfer recorded in the presence of dsDNA, was higher than that recorded in the presence of ssDNA.

The surface density of DNA immobilized after the anchoring of ssDNA and its complementary target was quantified following the method developed by Steel *et al.* [75], which is based on CC measurements. The technique takes advantage of the electrostatic attraction of specific redox cations with the nucleotide phosphate backbone. When the DNA is placed in a low ionic strength electrolyte containing a cationic redox marker, redox cations exchange for native counterions associated with the phosphate negative groups. CC determines the amount of redox marker which is electrostatically trapped at the DNA-modified electrode [75]; as a consequence, the measurement is insensitive to both the base composition and the chain order. The measured amount of redox marker

is directly proportional to the number of phosphate groups present at the surface. The surface density of the probe is calculated assuming that, at saturation coverage of the redox marker, redox cations charge completely compensate the DNA phosphate residues. In CC measurements the integrated current, or charge Q, as a function of time, is provided by the integrated Cottrell expression:

$$Q = \frac{2nFAD_0^{1/2}C_0^*}{\pi^{1/2}}t^{1/2} + Q_{dl} + nFA\Gamma_0; \tag{3.19}$$

where n is the number of electrons per molecule for reduction, F the Faraday constant (C/equiv), A the electrode area (cm^2), D_0 the diffusion coefficient (cm^2/s), C_0^* the bulk concentration (mol/cm^2), Q_{dl} the capacitive charge (C), and $nFA\Gamma_0$ the charge from the reduction of $nFA\Gamma_0$ (mol/cm^2) of adsorbed redox marker. The term $nFA\Gamma_0$ designates the surface excess and represents the amount of redox marker confined near the electrode surface. As the chronocoulometric intercept at $t = 0$ is given by the sum of the double-layer charging and the surface excess terms, the surface excess can be determined by the difference in chronocoulometric intercepts for the identical potential step experiment in the presence and absence of redox marker. The saturated surface excess of redox marker is converted to DNA probe surface density with the following relationship:

$$\Gamma_{DNA} = \Gamma_0 \frac{z}{m} N_A \tag{3.20}$$

where Γ_{DNA} is the probe surface density in molecules/cm^2, m is the number of bases in the probe DNA, z is the charge of the redox molecule, and N_A is Avogadro number. Measurements were carried out in a 10 mM TRIS-HCl (pH 7) with 100 μM $Ru(NH_3)_6^{3+}$. The potential was varied from 0 to -0.5 V for 0.4 s. The electrodes were modified by depositing a 8 μl drop of probes with a concentration of 10 μM. CC with and without the redox marker were carried out after DNA deposition. The Anson plot (Q vs. $t^{1/2}$) are reported in figure 3.23d. By elaborating the experimental data, resulted that the ssDNA density is $2.56 \cdot 10^{12}$ molecules/cm^2 which is in agreement with the literature data [75].

The chemical stability of the SAM was tested by recording CV curves in 5 mM potassium hexacyanoferrate (III) $K_3[Fe(CN)_6]$ in buffer phosphate (pH 7) of two different functionalized electrodes for one week. When not in use the electrodes were stored at 4 °C in buffer phosphate solution (pH 7). The test results are shown by reporting

the ratio of the recorded cathodic peak current to the peak current measured on the first utilization day (I_{pc0}) (see figure 3.23e). As the I_{pc}/I_{pc0} ratio is close to one, from the plots in figure 3.23e it can be deduced that the two monolayers retain their properties for approximately 4 days. After this period, the recorded peak currents for both electrodes increases and the ratio approaches the one obtained between the polished surface and the freshly functionalized surface (dash line in the graph); from this it can be deduced that the monolayers begin to detach from the electrode surface.

3.5.4.2 Capacitances

Vertical capacitances of this first implementation of HV OCMFETs were evaluated by realizing a set of at least ten capacitors. The capacitors had the same dimensions and shape of the devices electrodes and were prepared following the same process that was used for the device fabrication. C_{CF}, C_{SF} and C_{DF} were evaluated by means of an Agilent 4284A multimeter. Table 3.5 reports the recorded data.

CAPACITANCE @60 Hz [pF]	
C_{CF}	$(55 \pm 1)\cdot 10$
C_{SF}	27 ± 1
C_{DF}	41 ± 9
C_{TOT}	$(62 \pm 2)\cdot 10$

Table 3.5: Capacitances taken at 60 Hz; the average was calculated on at least ten devices and the error was estimated by doubling the standard deviation.

3.5.4.3 Electrical response

In this first HV OCMFET tested as DNA sensor, the double channel structure was used to separately verify the functionalization and the hybridization steps. One channel, later referred as *right*, was used to detect the sensor response to the DNA probe, while the channel referred as *left* was used to test the sensor response to the DNA target. The sensor response to DNA was evaluated by recording the output characteristics through a Keithley 2600 source meter controlled by a Labview software. Moreover, by means of a fluorescence microscope (Olympus BX60M), a fluorescence analysis was performed in order to check the immobilization of both probe and target. For this reason, the thiolated DNA provided with the Cy3 dye was immobilized in the right probe area; a

thiolated DNA without Cy3 and its complementary target provide with the Cy3 dye was deposited in the left probe area.

As the aim of this test was to verify that the OCMFET works as DNA sensor, very concentrated DNA solutions of both DNA probe and target (10 μM) were used. The non specifically bonded DNA was removed by rinsing the probe areas with a buffer phosphate solution (pH 7, 50 mM NaCl). The rinsing was performed immediately before carrying out the measurements. The target molecules were deposited straight after the measurements which were carried out to verify the sensor functionalization, and a relaxation time of 24 hour was waited before rinsing the non specifically bonded targets and measuring again the device. In order to make the electrical measurements comparable, all the measurements were conducted in the same experimental conditions; in particular, during the measurements, the probe areas were exposed to a buffer phosphate solution (pH 7, 50 mM NaCl).

The central picture in figure 3.24 shows a photo of the device, while the other photos are details of the fluorescence images recorded on the two probe areas: before and after the immobilization of probes on the right channel; after the immobilization of probes and before the deposition of targets on the left channel. The fluorescence analysis

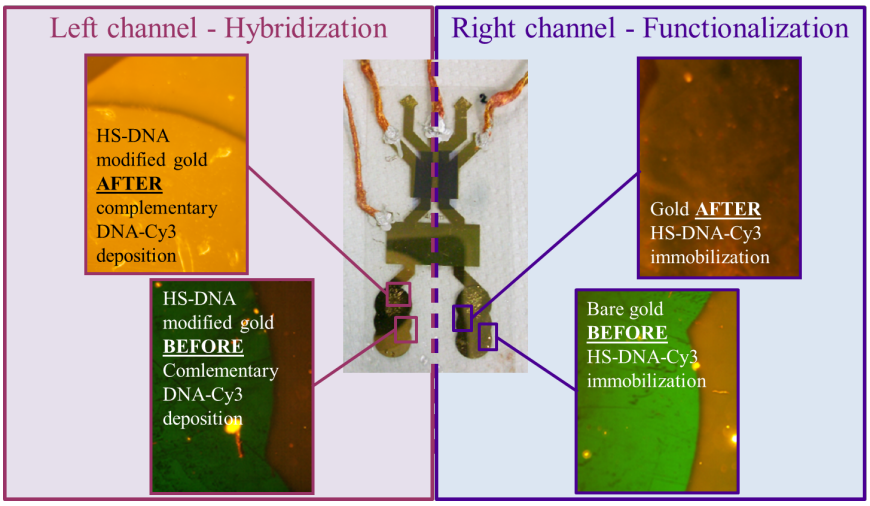

Figure 3.24: Photos of the HV OCMFET tested as DNA sensor (central picture) and fluorescent signals taken on the probe area: before and after the deposition of probes on the right channel (pictures on the right-hand side); after the immobilization of probes and before the deposition of targets on the left channel (pictures on the left-hand side).

confirmed the presence of the DNA through the detection of the Cy3 radiation. The bare gold surface, which looked green under the fluorescence radiation (bottom picture on the right-hand side), emitted a yellow radiation after the HS-DNA-Cy3 deposition (top picture on the right-hand side).

Figure 3.25 shows the electrical results recorded with this device. In particular, figure 3.25a shows the experimental results recorded on the right channel before and after the thiolated DNA immobilization. The source-drain current measured after the deposition of probe resulted higher than the one recorded before the immobilization of probe . Both measurements were taken at the same gate potential which was fixed at -100 Volt. This experimental result is coherent with the working principle of the device. As the DNA molecule is negatively charged, the charge separation induced in the floating-gate attracts holes in the transistor channel. As Pentacene is a p-type semiconductor, holes are the majority carriers and their increase will cause an increase in the source-drain current.

Figures from 3.25c to 3.25e reports the output characteristics recorded in the left channel at different gate potentials in the following steps: before the immobilization of probes, after immobilization of probes, and after hybridization of probes with their complementary target. In order to compare the source-drain currents taken in all the steps under the same bias, the currents recorded at $V_G = -100$ V are reported in a single chart in (figure 3.25b). Same as for the right channel, the current recorded after the thiolated DNA immobilization was higher than the current recorded before the its deposition. A further current increase was recorded after the target deposition. This result is coherent with the OCMFET model as, after hybridization, the phosphate groups density on the probe area roughly doubled and caused a further increase of the holes density in the transistor channel. Same as for the right channel, this experimental result was validated by means of the fluorescence analysis emitted form the probe area surface before and after the target deposition. The gold surface modified with a SH-DNA which did not not contain the Cy3 dye appeared green before the target deposition (bottom picture on the left-hand side) and emitted a yellow radiation after the fluorescent target deposition (top picture on the left-hand side).

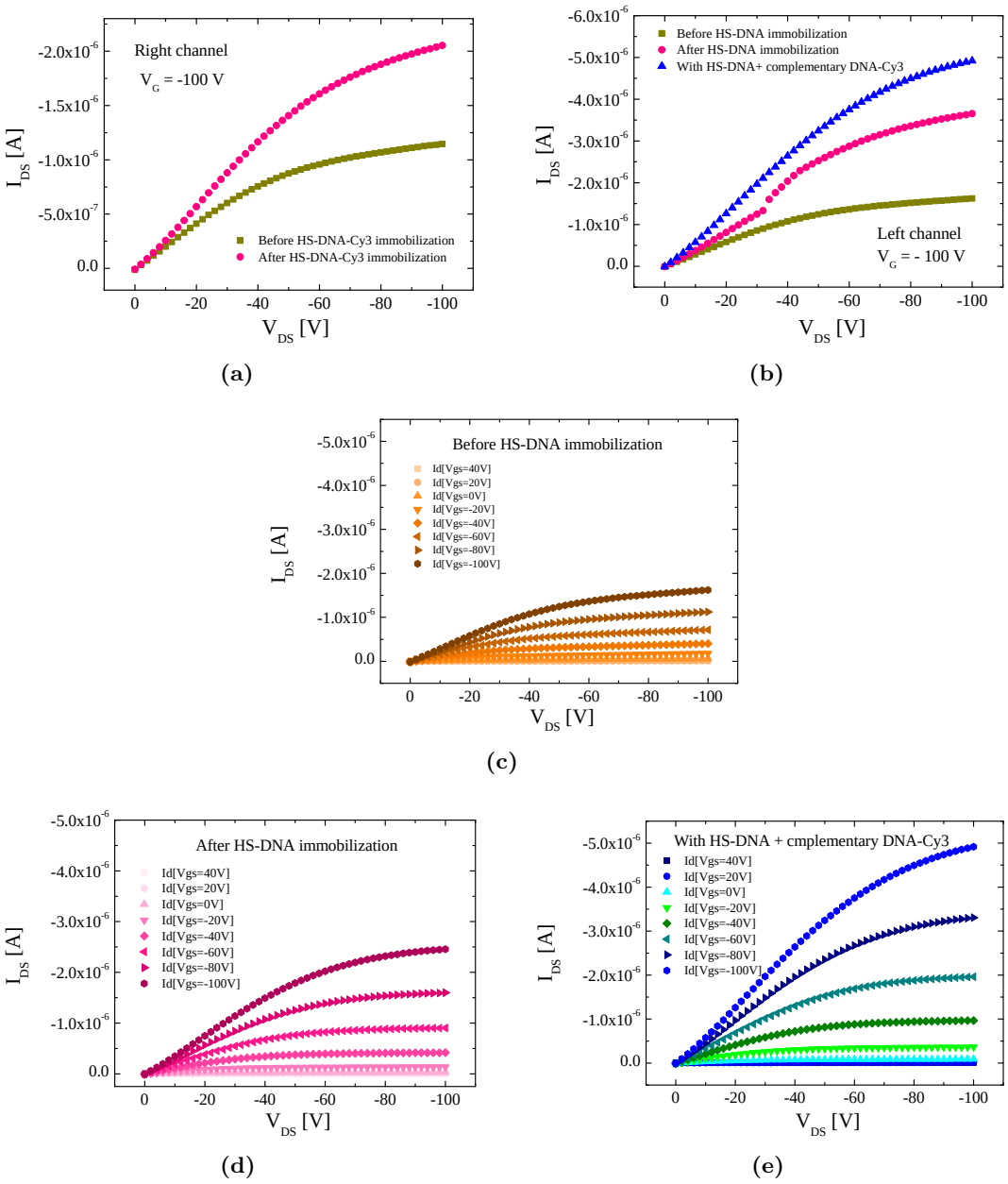

Figure 3.25: Electrical response to DNA: output characteristics recorded at $V_G = -100$ V before and after the DNA deposition in the right (a) and in the left channel (b); output characteristics recorded in the left channel at different V_G potentials before the deposition of probes (c), after the deposition of probe (d) and after the deposition of targets (e).

3.6 Optimized High-Voltage DNA sensor

The first HV OCMFET was proven sensitive to DNA charge when a very concentrated solution of DNA was used. According to the OCMFET model, a higher sensitivity can be obtained by reducing the parasitic capacitances. As a consequence, an optimized device was realized to test the OCMFET performances when low concentrated DNA solutions are used. In the following subsections, the layout, the material and fabrication methods employed to obtain an optimized HV DNA sensor are reported; finally the experimental results are shown.

3.6.1 Layout

Aiming at reducing the parasitic capacitances, a specific layout was designed and tested. Its scheme is shown in figure 3.26.

The parasitic contributions between the floating-gate on one side, and the source and drain on the other were decreased by narrowing the floating-gate and the source and drain contacts. The width and length of the channel were left unchanged; as a consequence, same as for the previous layouts, W/L was left equal to 150. The floating-gate length and the probe area were reduced ($\sim$ 7 mm^2) in order to decrease the electrode dimensions where charge separation must be induced.

Compared to the two previous layouts, the two floating-gates were designed more distant. This choice is closely related to the use of a different material and process during the semiconductor deposition.

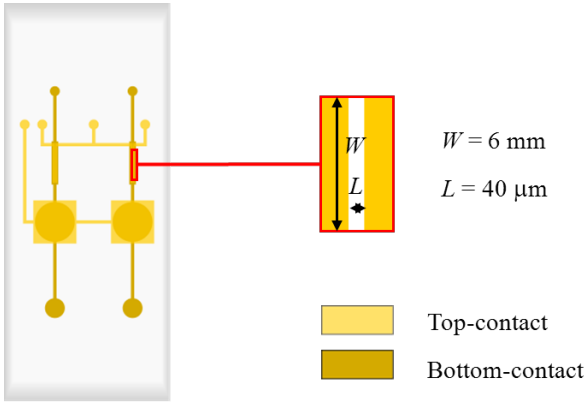

Figure 3.26: Layout of the optimized HV DNA sensor.

3.6.2 Fabrication - Materials & methods

Same as for the previous implementation of the OCMFET for DNA sensing, gold was used to realized all the electrodes: they were deposited by thermal evaporation in a high-vacuum system (1×10^{-5} mbar) and patterned through a standard photolithographic process. A 1.5 μm thick Parylene layer was deposited as buffer layer on the PET substrate and was also used as gate-dielectric. The polymer was deposited by CVD at room temperature. The materials and methods used to fabricate the optimized HV OCMFET for DNA detection were the same already described for the previous sensors except for the following two steps: the semiconductor deposition and the OFET encapsulation.

It was recently proven that OTFTs fabricated by using the solution-processed small molecule 6,13-bis(triisopropyl-silylethynyl) Pentacene (TIPS-Pentacene) as active layer showed good performances and environmental stability [76]. As TIPS-Pentacene remains stable in air for several weeks, it was used instead of Pentacene in the fabrication of this OCMFET. A volume of 2.5 μl was deposited by drop casting from a 0.5 wt% solution with toluene; after deposition, it was annealed for an hour at 90 °C over a hot plate in order to allow any residual solvent evaporation, and improve its film crystallization. This deposition technique does not require to have the floating-gate electrodes, that are below the source and the drain contacts, very close together. On the contrary, in order to have two separate OFETs working as reference and sensor, their floating-gate electrodes must be split up from each other by a proper distance. It is for this reason that in this layout the floating-gates were designed more distant than in the previously reported layouts.

TIPS-Pentacene can be considered air stable, therefore none encapsulating layer was deposited upon the OFET of these sensors. Moreover, it was also verified that TIPS-Pentacene can be easily removed from a device by rinsing the substrate with toluene, and deposited again with good results. This fact made possible to carry out again the semiconductor deposition when first attempt did not provide the expected results; moreover, as functionalization can be repeated as well, it contributed to make this kind of device reusable for more than one test, even if it was projected to be disposable.

Figure 3.27 shows the fabrication process of these optimized HV OCMFETs.

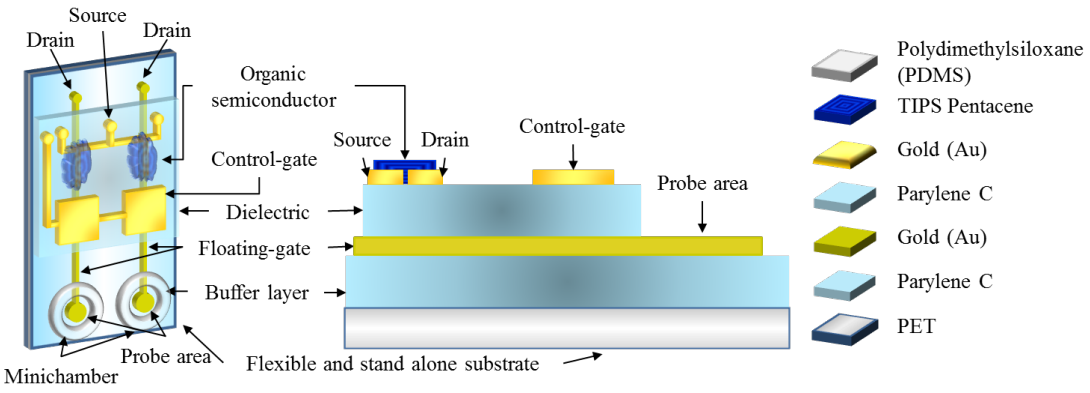

Figure 3.27: Fabrication steps of the optimized HV DNA sensor and employed materials.

3.6.3 Functionalization - Materials & methods

The same DNA sequences which were used in the first implementation of HV OCMFET for DNA sensing were also employed with these optimized devices. As the effectiveness of the immobilization of probes was already tested with the first implementation of HV DNA sensor, probes not containing the Cy3 were used; on the contrary, targets provided with this dye were still used in order to confirm by optical detection the DNA hybridization detected by the electrical measurements. Therefore, the following sequences were used: 5′-HS$(CH_2)_6$-$(T)_{13}$GGT TTC CGC CCC TTA GTG-3′(HS-ssDNA) together with 5′-CAC TAA GGG GCG GAA ACC-3′-Cy3.

As previously mentioned, piranha solution is not especially suitable to be used with these organic devices as its use entails a hight risk of damaging the device. To overcome this problem, several other cleaning procedures were investigated. Among these, good results in terms of probes immobilization was obtained by cleaning the probe surface through an electrochemical treatment. The gold surface was used as working electrode in a single compart three-electrode cell where the cleaning was obtained by cycling the potential from 0.0 V to 1.5 V at 1 V·s^{-1} in a 0.5 M H_2SO_4 solution. It is to apply this process that the floating-gate contact was extended beyond the OFET.

Concerning the immobilization of probes, the procedure adopted to carry out functionalization was almost the same already used with the DNA sensor previously reported, except for the buffer solution employed for the sample storage. A 3 μl drop of HS-DNA solved in a 1 M buffer phosphate solution (pH 3.8) was deposited in the

probe area immediately after its cleaning. Two hours later, a 3 μl drop of MCH (1.0 mM) was added. The probe area were then covered and stored at room temperature and in the dark. 15 hours later, the probe area was rinsed with bi-distilled water and then stored in the in the same buffer solution which was used to solve the DNA probe.

Concerning hybridization, in addition to the use of a different solution for the sample storage, the probe area was exposed to the complementary target for a time shorter than the one awaited for the previous device. Hybridization was obtained by depositing a 3 μl drop of the target solution on the functionalized probe area, which was previously rinsed by water and left dried in air. The probe area was then covered and kept in the dark for 1 hour before rinsing by using the same solution employed for target dilution.

3.6.4 Experimental results

In the following subsections the capacitances and the electrical results are reported. Same as for the first implementation of HV DNA sensor, electrical results related to hybridization were validated by fluorescence optical detection.

3.6.4.1 Capacitances

Vertical capacitances were evaluated by realizing the capacitances of a set of capacitors with the same dimensions and shape of the electrodes fabricated in the device; the electrodes were prepared following the same process that was used for the device fabrication. C_{CF}, C_{SF} and C_{DF} were evaluated by means of an Agilent 4284A multimeter. Table 3.6 reports the data which were recorded on seven samples.

CAPACITANCE @60 Hz [pF]	
C_{CF}	(76 ± 2)·10
C_{SF}	21 ± 6
C_{DF}	26 ± 3
C_{TOT}	(81 ± 3)·10

Table 3.6: Capacitances taken at 60 Hz; the average was calculated on at least seven devices and the error was estimated by doubling the standard deviation.

3.6.4.2 Electrical response

The HV OCMFET with the optimized layout was proven to work as DNA sensor when a DNA solution with a concentration lower than the one used in the first implementation of HV DNA sensor was deposited in the probe area. In order to evaluate the amount of DNA charge detected by the device, the two channels structure was used to perform differential measurements. One OFET worked as *sensor* while the other as *reference*. Same as for the sensor, the reference was subjected to all the processes which were carried out on the sensor, except for the presence of the DNA molecules in the solutions which were deposited on its probe area. This way, the effects which were induced by DNA were separated from those induced by other phenomena that usually affect the operating of the OFETs, such as temperature, Oxygen, bias stress, etc. In fact, even if in these devices the semiconductor is separated from the sensing area, it is exposed to the atmosphere and, as a consequence, a degradation of the semiconductor electrical properties may occur because of bias stress or humidity. During functionalization and hybridization, the threshold voltage of the reference OTFT might change, together with the sensor, for several reasons, of an amount which can be referred as $\Delta V_{TH,Step}$; in the sensor, the threshold voltage also changes because of the DNA immobilization and its overall threshold voltage is the sum of two contributions: one due to the process ($\Delta V_{TH,Step}$) and the other due to the DNA anchored charge ($\Delta V_{TH,DNA}$). By assuming that the uncontrolled effects on the threshold voltage shift are the same for both sensor and reference, the net effect due to the presence of the DNA molecule in the sensor ($\Delta V_{TH,DNA}$) can be properly highlighted only by considering the differences between the variations of threshold voltage shown by sensor and reference.

An HP 4155 Semiconductor Parameter Analyzer was used to electrically characterize these HV OCMFETs. Figure 3.28a shows the output characteristics of an HV optimized device, after the semiconductor deposition; transfer characteristics curves were taken in saturation regime in air, in order to detect their response to DNA. As the sensor is based on a p-type OTFT, when a negative voltage is applied between the control-gate and source contacts, holes are collected in the channel causing a current flow upon a V_{DS} negative bias. Negative charges due to the presence of DNA strands in the probe area will modify the charge configuration inside the floating-gate as they cause an increase of the holes' concentration in the channel. As a consequence, it is

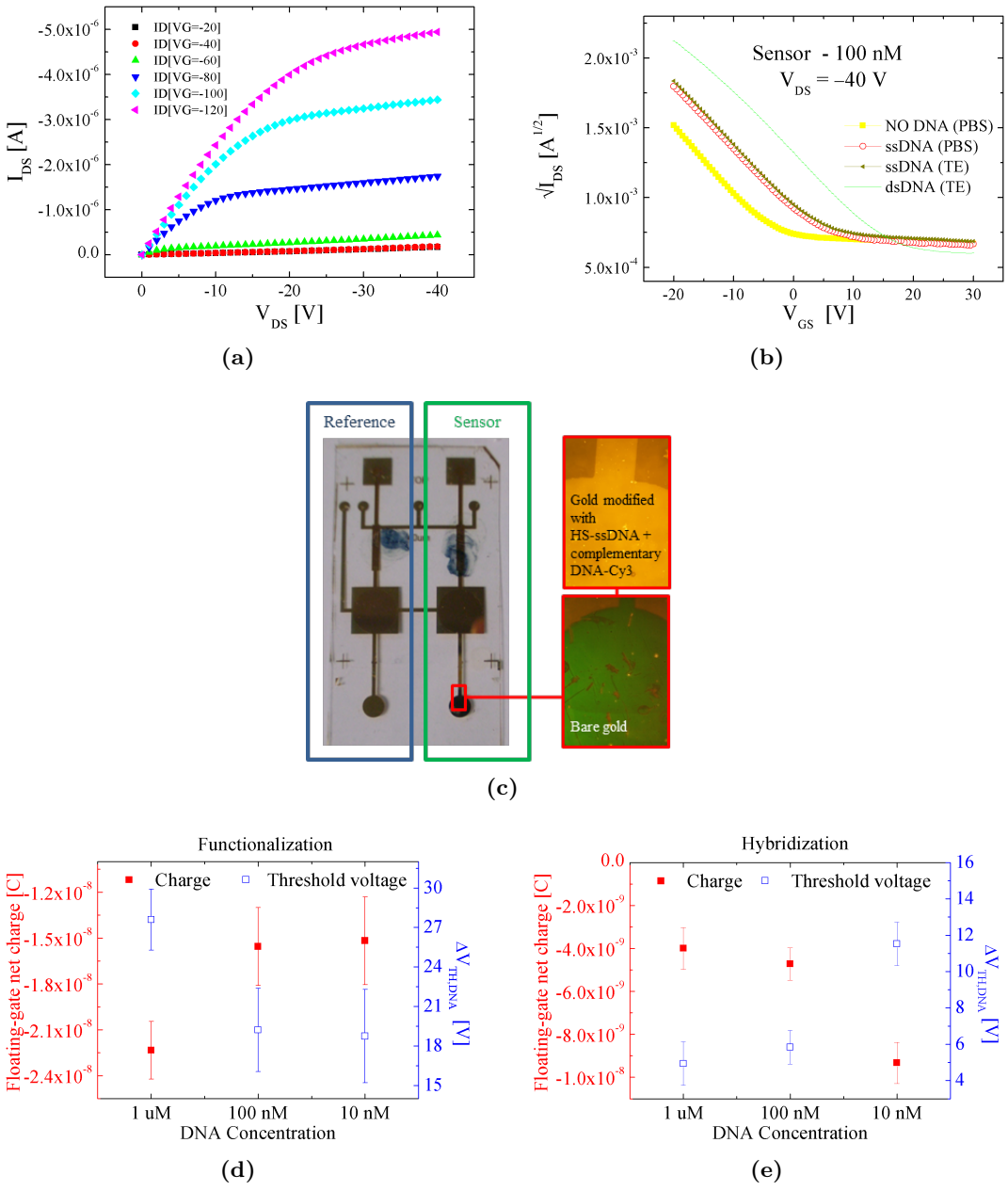

Figure 3.28: Output characteristic of a HV OCMFET optimized layout (a) square root of the transfer characteristics of a sensor taken before (NO DNA (PBS)) and after (ssDNA (PBS)) the immobilization of the ssDNA, and before (ssDNA (TE)) and after (dsDNA (TE)) the deposition of the fully complementary strands of the ssDNA (b); photos of the device and of the sensor probe area before and after the deposition of ssDNA and its Cy3-modified complementary target (c); net charge and net threshold voltage variation vs. DNA concentration detected after ssDNA immobilization (d) and hybridization (e).

expected that the transistor threshold voltage will change when they are immobilized in the probe area. Figure 3.28b reports the square root of the transfer characteristics of a sensor taken before and after its functionalization with a concentration of 100 nM of thiolated probes, and before and after the deposition of an equal concentration of their fully complementary targets.

Same as for the previous test, in order to remove the DNA molecules non specifically bounded to the probe area, the probe area was rinsed immediately before measuring. Compared to the previous tests, a different solution was employed to rinse the probe area after immobilization of the DNA probe and hybridization of the DNA target. The same buffer phosphate (PBS - pH 3.8) solution which was prepared for the thiolated ssDNA dilution was used to rinse the probe area after the immobilization of DNA probe. Moreover, in order to compare the electrical results which were made to test functionalization (NO DNA (PBS) and ssDNA (PBS)), the measurements were carried out while keeping the probe area exposed to the same PBS. The TE solution, which was prepared to dilute the target, was also used to rinse the probe area after the deposition of the DNA target. Same as for the tests of functionalization, in order to make the electrical results comparable, the devices were measured by keeping the probe area exposed to the TE solution (ssDNA (TE) and dsDNA (TE)). The experimental data were elaborated by means of the Origin 8.0 Software; in particular, the OTFT threshold voltages were extracted by fitting the linear part of $I_{DS}^{1/2}$ vs. V_{GS} and extrapolating the intercept with the x-axis. As expected, an increase of the transistor threshold voltage was detected both after probes immobilization and target deposition. Same as for the left channel in the previous reported HV sensor, the electrical results obtained after the complementary target deposition were validated by fluorescence detection. With this aim, thiolated DNA molecules not-containing any dye were employed as probe, while DNA strands provided with the Cy3 dye were used as target. The fluorescence detection was performed by means of the same apparatus previously reported, i.e., a fluorescence microscope (Olympus BX60M). Figure 3.28c shows a picture of a two channel device and the photos taken on the sensor probe area. The clear difference between the fluorescence signal emitted from the gold probe area before its functionalization (bottom picture on the right) and after its exposure to the complementary strands of the thiolated ssDNA modified with the Cy3 dye (top picture on the right) confirmed the presence of the DNA target modified with the Cy3 dye. The fluorescence signal

was only detected where the probes were anchored on the metallic surface; no relevant fluorescence was shown on the PET substrate. This leads to believe that fluorescent molecules were immobilized on the surface of the probe area. The device response to DNA immobilization and hybridization in terms of net floating-gate charge variation and net threshold voltage variation ($\Delta V_{TH,DNA}$) vs. DNA concentration was also investigated by depositing the same concentration of probes and targets. The experimental results are reported in figures 3.28d and 3.28e respectively. Two different sensors were measured for each point and the error bar was calculated by halving the difference between the maximum and the minimum measured values. Plot in figure 3.28d shows that the highest negative charge was detected after the deposition of a solution of probes with a concentration of 1 μM, while a lower charge was recorded at lower probes' concentration. Plots in 3.28e show the charge detected after hybridization. The highest response was detected on a surface which was functionalized by depositing a 10 nM solution of probes and then hybridized using the same concentration of targets. This result is consistent with the fact that, if the probe density is low, electrostatic repulsion and steric hindrance are minimized increasing the efficiency of hybridization, as also found in other hybridization simulations and experiments. This charge is related to the number of the DNA molecules anchored on the sensing surface, but to find an exact correspondence between the results of chemical measurements and those which can be detected by means of electrochemical techniques is extremely hard for several reasons. The distance between the charge and the floating-gate surface varies according to the orientation of the DNA molecules with respect to the sensing area and therefore it cannot be exactly defined; it is reasonable to assume that the DNA charge too far from the surface is not able to induce a charge separation in the floating-gate. Moreover, the ions in the buffer solutions might cause some screening effects affecting the charge induction in the floating-gate electrode.

3.7 Low-Voltage DNA sensor

The use of low operating voltages is particularly important when working with biological samples. As the LV OCMFET can be operated by applying 1 V, they seemed particularly suitable to be used for DNA detection. In the following subsections, the

layout, the fabrication methods which were used for the LV DNA sensor are reported; finally, the experimental results are shown.

3.7.1 Layout

The layout of the LV DNA sensor was designed by considering the specific needs related to the electrical measurements. Two steps were investigated for DNA recognition: the sensor response to DNA probes and to the anchoring of DNA targets. In order to make differential measurements after both steps, two references were designed: one was used to test the immobilization of DNA probes, while the other was used for the recognition of DNA targets. Therefore, a layout including three devices was designed (see figure 3.29). In this layout, only the control-gate electrode was shared by all the devices; the source contacts were split up. This configuration allowed to separate and make each device independent from the other ones by breaking up the control-gate contact. This choice was done in order to allow differential measurements by relating the responses of several sensors to more than one reference.

The detail on the right highlights that an interdigitated channel was designed for these devices. LV devices require a bias of about 1 V to switch on; within this potential range, in order to detect currents in the range of microamperes a higher W/L ratio was needed, therefore, interdigitated channels with a length of $L = 40$ μm and a width of $W = 3.8$ cm ($W/L = 950$) were used for the LV devices. A circle with an area of ~ 28 mm^2 was used as probe area.

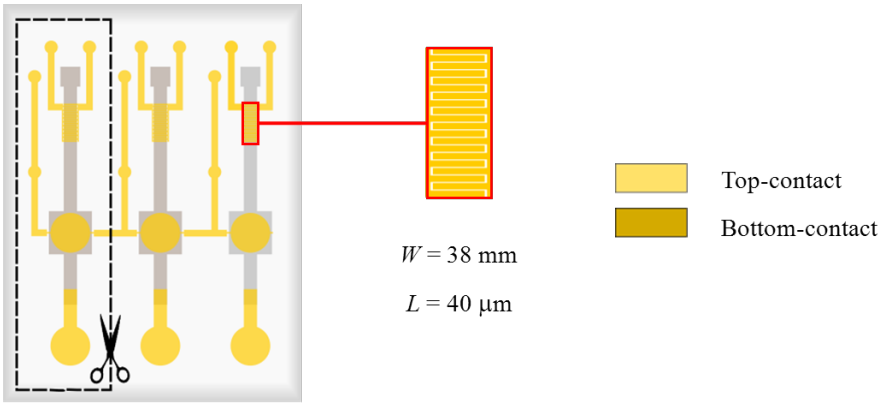

Figure 3.29: Layout of the LV DNA sensor.

Compared to the layout of HV OCMFET, the bottom-shape and the top-shape of the control-capacitors were exchanged. This choice was due to meet fabrication needs. All the devices were realized on plastic substrates which had a high superficial roughness. Because of this feature, when very thin layers are deposited to form the gate dielectric, the chance to have vertical shorts between the floating-gate and the other electrodes is rather high. As the presence of edges in the bottom-contact shapes also affected the chance to have vertical shorts, the bottom-contacts was made wider than the top-contacts in order to reduce this chance.

3.7.2 Fabrication - Materials & methods

The LV OCMFET is based on an OTFT which switches on at voltages below 1 V. Cosseddu *et al.* [77] fabricated an OTFT with this low voltage operating regime by combining two different dielectric materials as gate dielectric. They realized an aluminium gate. On it, an ultra-thin Al_2O_3 layer with a nominal thickness of 6 nm and a Parylene layer with a thickness of 25 nm were grown; this hybrid organic-inorganic dielectric layer was used as gate insulator. It has a high values of capacitance, creates an efficient barrier to gate leakage and provides an optimal interface with the organic semiconductor. The technology which was used to fabricate these ultra LV devices is low-cost, simple and easily up-scalable to industrial size. These features, together with the LV regime, make this technology particularly suitable to fabricate OCMFETs for DNA recognition. In fact, the DNA sensing was the first application where this fabrication technique was used.

The procedures which were applied to realize the LV OCMFET (see figure 3.30) are similar to the one used to fabricate the HV with a few exceptions. The LV DNA sensors were realized on a PET substrate which was cleaned with acetone, deionized water and finally dried under a nitrogen flux.

The portion of the floating-gate electrode which forms the bottom contact below the other contacts was fabricated by depositing an aluminium layer at room temperature in a high vacuum system (1×10^{-5} mbar), and was patterned by means of a standard photolithographic process.

Same as in the device proposed by Cosseddu *et al.* [77], the Al_2O_3 and Parylene C layers were used to obtain the gate dielectric. The oxide layer was realized at room temperature by means of UV-ozone oxidation; the aluminium surfaces were exposed

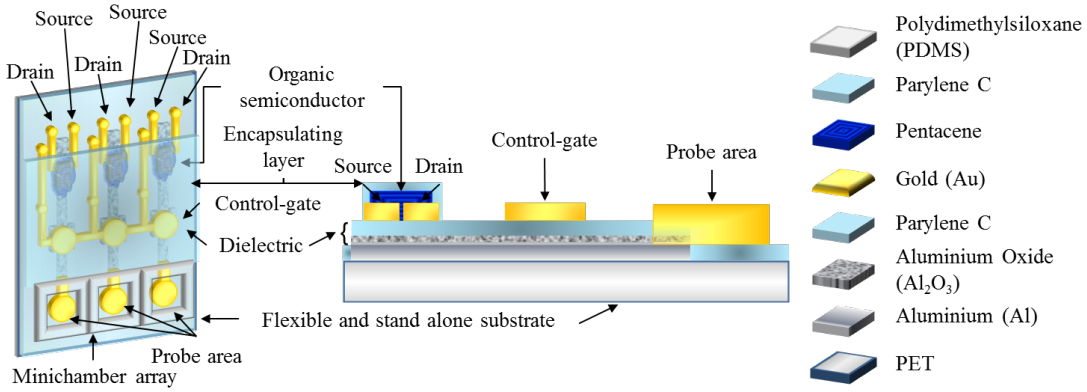

Figure 3.30: Fabrication steps of the LV DNA sensor and employed materials.

to a mercury lamp, UVP PenRay in ambient conditions for a maximum time of 1 hour. Parylene was deposited at room temperature by CVD using A174 as adhesion promoter.

The other contacts, i.e., the source, drain and control-gate electrodes which were made of gold, were deposited by thermal evaporation in a high vacuum system (1×10^{-5} mbar), and then patterned through a standard photolithographic process.

The probe area was made of the same material which was also used for the top electrodes. This choice allowed to functionalize the device by using the same kind of SAM which was employed in the fabrication of the HV sensors.

As the UV-ozone exposition causes the Parylene layer de-lamination, Parylene was not deposited to form a buffer layer; in these implementation, the Parylene layer which was deposited as gate-dielectric worked as buffer layer, even if it had an extremely small thickness. In fact, the probe area was realized together with the top electrodes, i.e., after the Parylene deposition. No protection was used to prevent that any part of the floating-gate would be coated during the insulator fabrication. The probe area was provided with a pad which could be superimposed to the end of the aluminium bottom-contact. As the dielectric layer is extremely thin, the short between these two contacts was created just applying a small pressure upon them. This step could have been avoided just protecting the floating-gate end during the insulator fabrication, but the described method was chosen because of a practical advantage. It was observed that the solution based on potassium iodide (KI) and iodine (I_2), which was used for

the gold etching, damaged the aluminium. The Parylene layer provided a protection from the etchant solution during the photolithographic process.

Same as for the optimized HV DNA sensors, TIPS-Pentacene was used as organic semiconductor. A volume of 2.5 μl was deposited by drop casting from a 0.5 wt% solution with toluene and annealed for an hour at 90 °C after the deposition over a hot plate.

The mini-chamber system was then applied to prevent the rapid evaporation of the DNA solution.

Finally, same as for the HV OCMFETs which was realized by first as DNA sensors, a Parylene layer was deposited to encapsulate the transistor and provide a protection from the environmental conditions.

On the whole, the materials which were used to fabricate the floating-gate contact and the gate dielectric represent the most important changes in the LV OCMFET fabrication procedure compared to the process adopted with the HV devices. The floating-gate was made of two materials, aluminium concerning the active part of the device and gold concerning the probe area, instead of being all made of gold. The gate dielectric results form combining aluminium oxide with Parylene, but the Parylene layer has a much smaller thickness value.

3.7.3 Functionalization - Materials & methods

Several DNA sequences were used to test the LV DNA sensors. In addition to the sequence of probe already used with the optimized HV DNA sensor and its fully complementary target, other two sequences formed by 18 nucleotides provided with the Cy3 dye in 3′ were used as targets: a fully non-complementary sequence (5′-AGA GCC TTT ACA CCG ACT-3′) and a sequence containing a single nucleotide polymorphism (SNP) in the middle of the chain (5′-CAC TAA GGG GCG GAA ACC-3′) which was used to test the OCMFET selectivity towards mismatches. Same as for the fully complementary target, these strands did not include the bases complementary to the first 13 bases close to the thiol. The following list summarizes the DNA molecules used for each kind of test:

– 5′-HS$(CH_2)_6$-$(T)_{13}$GGT TTC CGC CCC TTA GTG-3′(HS-ssDNA) together with 5′-CAC TAA GGG GCG GAA ACC-3′-Cy3 for DNA hybridization tests;

- 5′-HS$(CH_2)_6$-$(T)_{13}$GGT TTC CGC CCC TTA GTG-3′(HS-ssDNA) together with 5′-CAC TAA GGG GCG GAA ACC-3′-Cy3 for DNA selectivity tests;
- 5′-HS$(CH_2)_6$-$(T)_{13}$GGT TTC CGC CCC TTA GTG-3′(HS-ssDNA) together with 5′-AGA GCC TTT ACA CCG ACT-3′-Cy3 for DNA hybridization rebutting evidence tests.

Before anchoring the DNA probes, the probe area of the LV OCMFET was treated by using a sodium hypochlorite (NaClO) solution (10 % active Cl) for 10 minutes. It was proven that the surface coverage which could be obtained by using this cleaning procedure is slightly less efficient than the one achievable with electrochemical cleaning; however it was chosen because of its ease and speed of use.

Except for the cleaning procedure, the steps carried out in order to anchor the DNA molecules to the probe areas were the same for all the other OCMFETs used for DNA recognition. Functionalization was obtained by pipetting 3 μl of HS-ssDNA solved in a 1 M buffer phosphate solution (pH 3.8) straight after the cleaning procedure; two hours later, a 3 μl drop of MCH (1.0 mM) was added. After the DNA and MCH deposition, the probe area are covered and kept in the MCH solution for 15 h at room temperature, in the dark. After this time, same as for the firts HV DNA sensors, the probe area was rinsed with bi-distilled water and then stored in a buffer phosphate solution (pH 7, 50 mM NaCl).

Same as for the fully complementary target, the target with the single nucleotide polymorphism in the middle of the chain and the fully non-complementary sequence were diluted in a 1 M TE, 1 M NaCl (10 mM Tris-HCl, 1 mM ethylenediaminetetraacetic acid (EDTA), 1 M NaCl, all reagents purchased from Sigma-Aldrich). Hybridization with the target oligonucleotides was performed by pipetting a 3 μl drop of the target solution on the functionalized probe area, which was previously rinsed by water and left dried in air. Same as for functionalization, when the probe area was exposed to the target solution, it was covered to reduce the solution evaporation and kept in the dark. As a general rule, the duration of the exposition was long enough to allow a complete hybridization, therefore lasted at least one hour; nevertheless, in a few cases it was varied depending on the test and the oligonucleotides concentration. After hybridization, the probe area was rinsed by using the TE solution and then stored the buffer phosphate solution (pH 7, 50 mM NaCl).

3.7.4 Experimental results

In the following subsections the experimental results obtained are reported. In particular, recognition tests at different target concentration and selectivity tests are reported. Same as for all the other previous sensors, fluorescence optical detection was used to validate hybridization on working devices.

3.7.4.1 Capacitances

Vertical capacitances were evaluated by realizing a set of ten capacitors with the same dimensions and shape of the electrodes fabricated in the devices; the electrodes were prepared following the same process that was used for the device fabrication. C_{CF}, C_{SF} and C_{DF} were evaluated by means of an Agilent 4284A multimeter. Table 3.7 reports the data which were recorded on the samples.

CAPACITANCE @60 Hz [pF]	
C_{CF}	$(42 \pm 5)\cdot 10^3$
C_{SF}	$(10 \pm 1)\cdot 10^2$
C_{DF}	$(10 \pm 1)\cdot 10^2$
C_{TOT}	$(44 \pm 3)\cdot 10^3$

Table 3.7: Capacitances taken at 60 Hz; the average was calculated on at least ten devices and the error was estimated by doubling the standard deviation.

3.7.4.2 Electrical response

LV sensors for DNA detection were electrically characterized by means of an HP - Agilent 4155A Semiconductor Parameter Analyzer and two Keithley (2612 and 2636) controlled by a Labview software; data were elaborated by means of the Origin 8.0 Software. The experimental procedure carried out was the same already described for the optimized HV DNA sensors, except for the use of a different solution during the measurements execution. The TE solution which was used to solve the complementary ssDNA is a high ionic strength solution because this condition is essential to keep the oligonucleotides unfolded and favour hybridization with the DNA target. A high ionic strength solution as TE is not especially suitable to be employed during the measurements as the ions in the solution exert a screening effect of the immobilized charges.

Therefore, aiming at detecting as much DNA charge as possible, the measurements were taken in a buffer phosphate (pH 7, 50 mM NaCl) solution which was prepared by using Milli Q (18 Ω) deionized water.

Figure 3.31a shows the output characteristic of the sensor which was recorded before the thiolated DNA immobilization. Figure 3.31b reports the transfer characteristics obtained before the thiolated DNA immobilization (NO DNA), after the thiolated DNA immobilization (HS-ssDNA) and after hybridization with its complementary target (HS-DNA + complementary target). According to the working principle of the device, the transistor threshold voltage shifted towards positive values and an increase of the output current was recorded after probe immobilization and after hybridization with the complementary target. Same as for the other DNA sensors, fluorescence detection was used to validate the electrical results. Figure 3.31c shows a group of three LV OCMFETs tested as DNA sensors: one of them worked as reference and the other two as sensors; the other pictures report the fluorescent signals that was recorded on the right sensor after the thiolated DNA deposition (bottom picture on the right) and after the deposition of the DNA complementary target (top picture on the right).

The study of the OCMFET sensitivity towards the target concentration which was started with the HV devices was further investigated by using several LV OCMFETs. In addition to a reference, which was treated following the same process and solutions except for presence the DNA molecules, a group of three sensors for each target concentration was functionalized by depositing a solution of probes with a concentration of 100 nM. Hybridization was performed at room temperature and measurements were taken several hours after the target deposition in order to make sure that hybridization was complete, even when a very low target concentration was deposited. The calibration curve was obtained by averaging the difference between the threshold voltage shift recorded in each sensor with that detected on the reference (net threshold voltage shift). Figure 3.31d shows the calibration curve. The net threshold voltage shift has a linear dependence on the concentration of the targets which were solved in the solution. In the secondary axis, the charge density, which was estimated by using equation 3.6, was reported: the experimental results show that the LV OCMFET is able to detect very small amounts of immobilized charge (0.1 nM).

The capability of the sensor to distinguish between a fully complementary target sequence and a sequence containing a single nucleotide polymorphism was finally in-

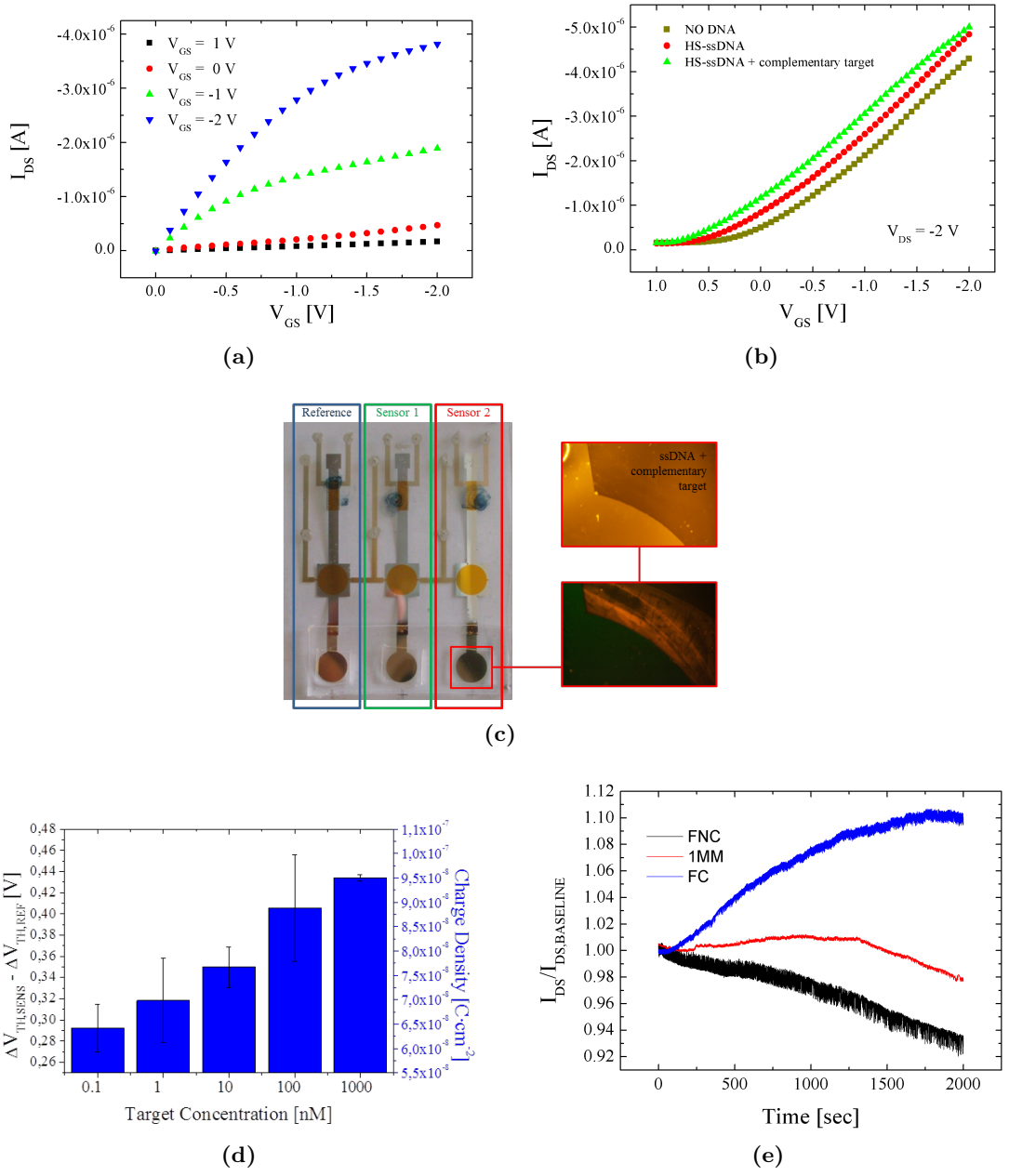

Figure 3.31: Output characteristic of a LV DNA sensor (a) and transfer transfer characteristic of a sensor taken before functionalization (bare gold), after the immobilization of the HSssDNA (HSssDNA), and after the deposition of its the fully complementary strand (HSssDNA + complementary target (b); photos of a group of three devices: on reference and two sensors and fluorescence images of the right-sensor probe area functionalized with HS-ssDNA (bottom picture on the right) and hybridized with its Cy3-modified complementary target (top picture on the right) (c); average shift of the net threshold voltage **vs.** the concentration of the target in solution (d); OCMFET output currents $I_{DS}/I_{DS,BASELINE}$ where $I_{DS,BASELINE}$ is the sensor output before the injection of the target sequence) during the hybridization process with fully not-complementary (FNC), single-mismatched (SNP) and fully complementary (FC) sequences (e).

vestigated. Figure 3.31e shows the real time current response of three sensors which had the probe functionalized by depositing the same solution of probes, but which were exposed to three different kinds of target. A fully not-complementary (FNC) sequence was deposited on the first, a fully complementary sequence (FC) on the second, and a sequence containing a SNP inserted in the middle of the chain was deposited on the third. Both the probes and target solution had a concentration of 100 nM. Hybridization tests were performed at room temperature. In order to reduce the bias stress of the structure during prolonged measurements, the sensors were biased with a pulsed gate signal (V_{GS} ranging from 0 V to –1 V, 50 Hz, duty cycle 25 %) and with a constant drain-source voltage drop ($V_{DS} = -1$ V). The experimental results were expressed by means of the normalized output current with respect to the baseline ($I_{DS,BASELINE}$) which was recorded before the injections. From plots in figure 3.31e it results that the current recorded in the sensor exposed to the FNC sequence had a monotonic decreasing trend, which can be ascribed to the effect of the residual bias stress. Concerning the response of the sensor which was exposed to the sequence with a single mismatch, its current had a very small increase, in the range of the 1 %, which was rapidly compensated by the effect of bias stress after around 1250 seconds. On the contrary, the output current recorded on the sensor which was exposed to the FC sequence, significantly increased (10 %) within a few tens of seconds from the injection of the target and reached a maximum value within 30 minutes; after this time, a slow reduction of the current, not shown in the plot, was noticed; same as for the other sensors, this current reduction can be ascribed due to the residual bias stress of the device. Even if bias stress affected these measurements, it does not represent a real limit for DNA recognition as, even if not strictly necessary, it can be further reduced by changing the gate voltage amplitude, frequency and duty cycle. By using a proper set up of these parameters, bias stress can completely compensate the detection-induced increase of current only after more than one hour of continuous operation, i.e., after a period of time which is beyond the requirements of any practical application.

3.8 Low-Voltage pH sensor

The experimental results obtained with the HV pH sensors were not very reproducible compared to the ones obtained in the DNA sensing. Even worse results were obtained

during a few preliminary tests made by using the same kind of LV OCMFET developed for the DNA sensing and the same SAMs used for the HV pH sensors. To overcome the low reproducibility, a LV OCMFET sensor for pH detection was realized by developing a specific structure with reduced parasitic capacitances and using tantalum oxide as sensitive layer. When SAMs were used as receptors, their immobilization was the final step after the device fabrication. In case of the LV pH sensor, preliminary tests demonstrated the it was better to deposit the sensing layer during the device fabrication. As a consequence, the sensor fabrication is described in a single subsection. The designed layout, the technique employed for the sensor fabrication are reported in separate subsections; finally, a description of the receptor's properties and the experimental results are shown.

3.8.1 Layout

An optimized layout was designed and tested in order to improve the sensor performance. Same as for the HV OCMFET, the layout was designed with the aim to reduce the parasitic capacitances between the source and drain contacts and the floating-gate electrode. The floating-gate electrode connecting the OFET to the probe area was reduced, while the probe area surface was extended; compared to the optimized LV DNA sensors the probe area was enlarged (~ 50 mm^2). Figure 3.32 shows the device layout. A good compromise between the need of currents in the range of hundreds of nA and reduced parasitic effects was found by designing an interdigitated channel with a length of $L = 40$ μm and a width of $W = 21$ mm ($W/L = 525$).

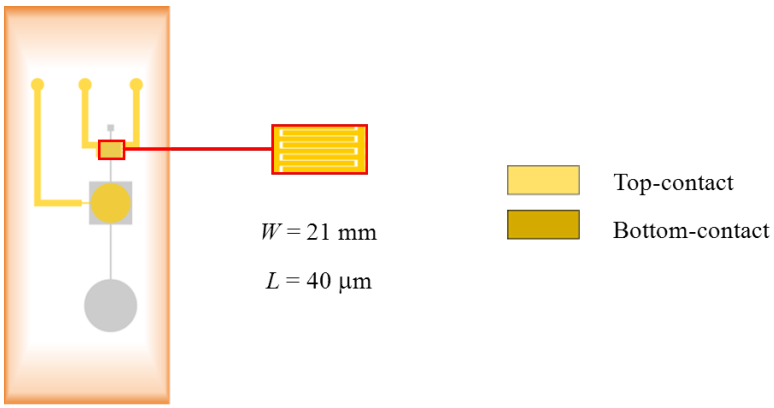

Figure 3.32: Optimized layout of the LV pH sensor.

As shown in the picture, the layout included a single device as the scheduled tests did not require to measure more sensors at the same time.

3.8.2 Fabrication - Materials & methods

The employment of a different sensitive material required the use of a different substrate and the introduction of a few changes in the fabrication procedure of the device.

As the sensitive layer need to be annealed at a temperature that the PET substrate could not sustain without damaging, a Kapton foil (200 nm thick) was used instead of the PET substrate. Kapton, which is a flexible and semitransparent plastic, was chosen as it is able to tolerate temperatures up to 200 °C. The Kapton substrate was cleaned by acetone, rinsed rinsed in bi-distilled water, and finally dried under a nitrogen flux before use.

The pH sensitivity, which was provided by the sensitive material deposited on the probe area, did not depend on the kind of metal employed in the probe area fabrication. Therefore, in this OCMFET implementation the whole floating-gate was made of aluminium which was deposited by thermal evaporation in a high-vacuum system (1×10^{-5} mbar) and patterned through a standard photolithographic process. A good adhesion of the aluminium layer to the substrate was obtained by exposing the substrate to a plasma oxygen for 1 minute, before the aluminium deposition.

Same as for LV DNA sensor, an Al_2O_3 layer (6 nm) was realized at room temperature by means of UV-ozone oxidation.

Preliminary tests showed that the technique employed for the oxide deposition caused the gate dielectric degradation. It is for that reason that, in these devices, functionalization was performed at this step of the fabrication process, i.e., after that the Al_2O_3 layer was grown.

A thickness of 100 nm of tantalum oxide was produced by rf magnetron sputtering in reactive atmosphere: an AJA ATC-1300 sputtering system was used with a rf power density of 7.4 W/cm^2, under a deposition pressure of 0.3 Pa and Ar/O2 flow ratio of 14/1. A shadow mask was used in order to deposit the Ta_2O_5 upon the probe area and a small portion of the metal line which connects the probe area to the bottom plate of the control capacitor.

A Parylene layer with a thickness of (25 nm) was then deposited at room temperature by CVD using A174 as adhesion promoter. A Parafilm coverage was used during

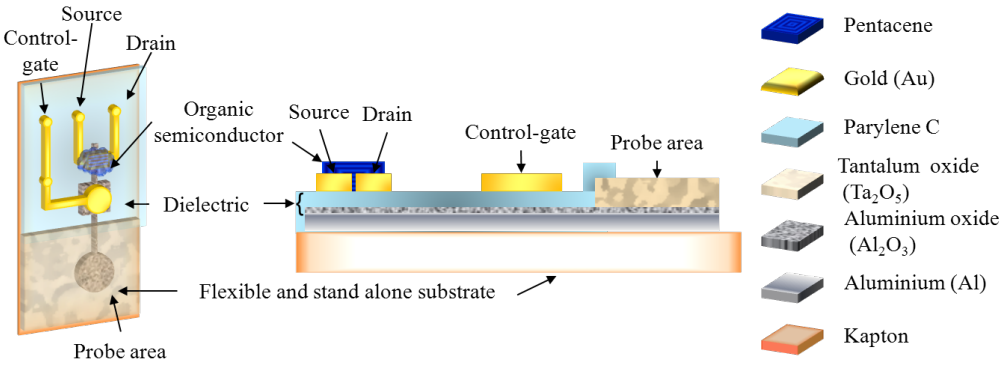

Figure 3.33: Fabrication steps of the LV pH sensor and employed materials.

the Parylene deposition in order to prevent the sensitive area to be covered form the insulator, but allow laying the Parylene layer upon the Ta_2O_5 deposited on the metal line; this solution allowed protecting the aluminium layer during both the chemical treatments in the later steps and the measurements.

Same as for the previous OCMFETs, the other contacts, which were made of gold, were deposited by thermal evaporation in a high-vacuum system (1×10^{-5} mbar) and patterned through a standard photolithographic process. A shadow musk was used to protect the probe area in order to prevent it to be covered during gold deposition.

Finally, TIPS-Pentacene was used as organic semiconductors. A volume of 2.5 μl was drop casted from a 0.5 wt% solution with toluene and, after the deposition, annealed for an hour at 90 °C over a hot plate.

Figure 3.33 shows the fabrication process and the materials employed for this LV pH sensor.

3.8.3 Receptor

In the following subsections an introduction on the processes occurring at the surface of metal oxides in the presence of aqueous solutions and the specific properties of the tantalum oxide employed in the LV pH sensor fabrication are reported.

3.8.3.1 Metal oxides - General properties

The chemical processes occurring at the interface between oxides and aqueous solutions are usually modelled through the *site binding* model developed by Yates *et al.* [78]. Ac-

cording to this model, an insulator such as a metal oxide, which contains a large amount of unsaturated bonds, may give rise to surface processes of dissociation-association of hydrogen atoms [37]. Therefore, the surface of any metal oxide covered with adsorbed water contains hydroxyl groups which may donate a proton to or accept a proton from the analyte; this phenomenon leaves negatively or positively charged sites, respectively, on the surface, according to the following reactions:

$$\mathrm{MOH} \overset{K_A}{\rightleftharpoons} \mathrm{MO^-} + \mathrm{H_S^+} \tag{3.21}$$

$$\mathrm{MOH} + \mathrm{H_S^+} \overset{K_B}{\rightleftharpoons} \mathrm{MOH_2^+} \tag{3.22}$$

where $\mathrm{MOH_2^+}$, MOH and $\mathrm{MO^-}$ represent positive, neutral and negative surface site respectively. At the equilibrium, the amphoteric dissociation constants are

$$K_A = \frac{[\mathrm{MO^-}][\mathrm{H^+}]_\mathrm{S}}{[\mathrm{MOH}]} \tag{3.23}$$

and

$$K_B = \frac{[\mathrm{MOH}][\mathrm{H^+}]_\mathrm{S}}{[\mathrm{MOH_2^+}]}, \tag{3.24}$$

where $[\mathrm{MOH_2^+}]$, [MOH] and $[\mathrm{MO^-}]$ are the number of sites per surface area.

The resulting surface charge, which depends on the excess of one type of charged sites over the other, varies with the solution pH because the ionizable OH surface groups can take up or release protons working as a buffer. By combining equations 3.23 and 3.24, the surface proton concentration can be expressed through

$$[\mathrm{H^+}]_\mathrm{S} = \sqrt{\frac{K_A}{K_B}\frac{[\mathrm{MOH_2^+}]}{[\mathrm{MO^-}]}}. \tag{3.25}$$

When the surface is neutral, the concentration of negative and positive groups are equal; in this condition, which corresponds to the zero point charge, it results

$$[\mathrm{H^+}]_\mathrm{S} = \sqrt{\frac{K_A}{K_B}} \qquad \text{that is} \qquad \mathrm{pH_S} = -\log\sqrt{\frac{K_A}{K_B}}. \tag{3.26}$$

Amongst the most commonly used dielectrics, tantalum pentoxide has the higher number of active hydroxyl surface groups and higher buffer capacity, therefore it has a sensitivity to pH next to the theoretical value of 59 mV/pH. Moreover, its short response time, high selectivity and long-term stability make it especially suitable to be used as receptor in pH sensors.

3.8.3.2 Tantalum oxide - Characterization

Recently, Pinto *et al.* [79] realized an ISFET based on Ta_2O_5 as active layer. They proved that it allows to obtain a sensitivity to pH changes of 40 mV/pH and small hysteresis. This response was obtained by depositing the tantalum oxide layer by sputtering and annealing it at 200°C.

The fabrication of the oxide layer and the post production technique influence the film properties. Branquinho *et al.* [80] studied the films structure and composition of RF sputtered Ta_2O_5 sensitive layers by carrying out X-ray diffraction (XRD) and Rutherford backscattering spectrometry (RBS); moreover they investigated the effect of post-annealing temperature on the pH sensitivity.

They fabricated electrolyte-insulator-semiconductor (EIS) capacitors with a Ta_2O_5 sensing membrane (90 nm) on p-type (100) silicon substrates (2.5×2.5 cm) coated with 100 nm thick thermally grown SiO in an AJA ATC-1300 radio frequency (RF) magnetron sputtering system. A 3-in-diameter TaO ceramic target from SCM 99.99% was used at a deposition pressure of 0.3 Pa with a ratio of 14/1 sccm and RF power of 150 W. The wafer backside was etched with a buffered HF solution to remove the silicon oxide film prior to the Al (200 nm) back-contact deposition by electron beam (e-beam) evaporation. The effect of the post-deposition temperature treatment was investigated on samples which were annealed from 200 °C up to 800 °C for one hour in air using a Thermolyne 21100 tubular furnace.

XRD is a technique which allows to determine the atomic and molecular structure of a crystal by analysing the diffraction pattern obtained when the sample is irradiated by means of a parallel beam of monochromatic X-rays. The angles and intensities of the diffracted beam provides informations related to the density of electrons within the crystal, and as a consequence, the mean position of the atoms in the crystal can be determined. A PANalytical X′Pert PRO in Bragg-Brentano geometry with Cu Kα line radiation (λ = 1.5406 Å) was used to perform the X-ray diffraction analysis. Figure 3.34a shows the collected experimental results. None diffraction peak was recorded after post-deposition annealing up to 600 °C, therefore, it reasonable to consider that also the sensing layer which was deposited on the LV OCMFETs probe area have an amorphous nature.

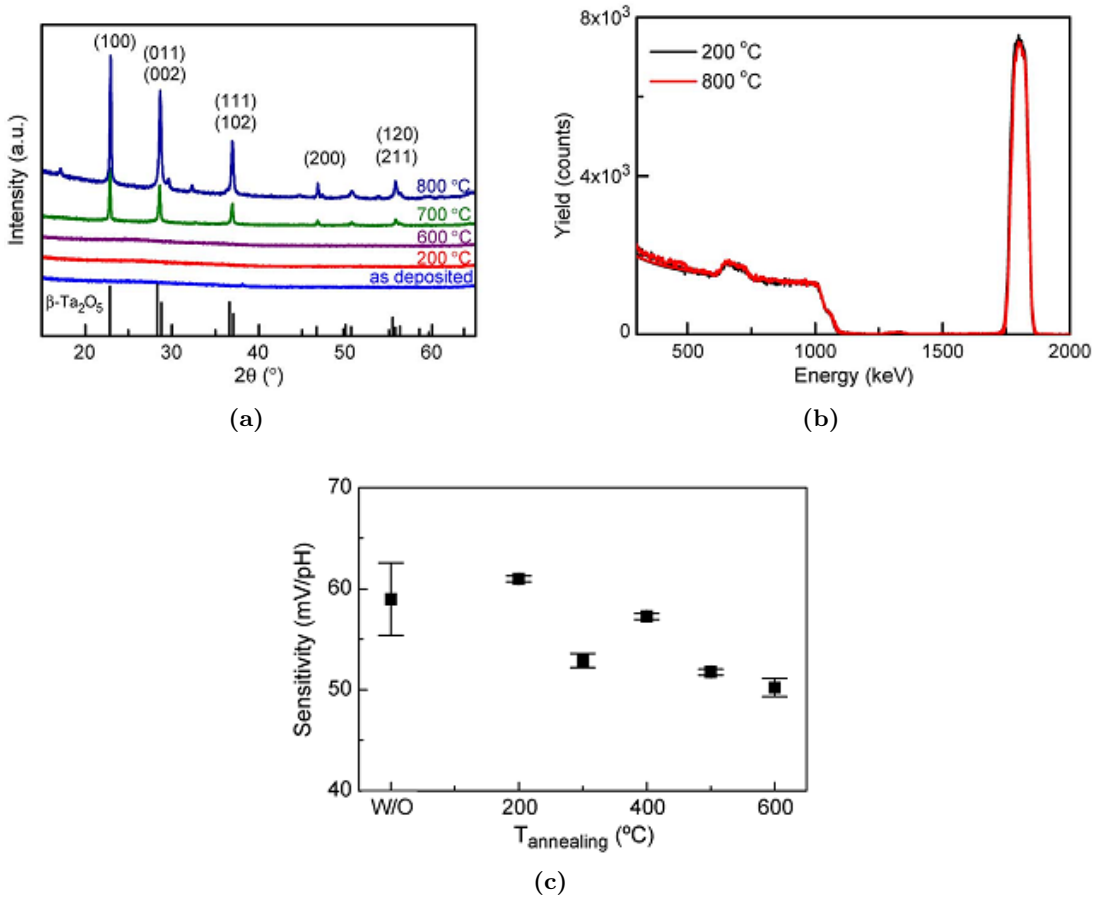

Figure 3.34: Characterization of the Ta_2O_5 layer deposited by rf sputtering: XRD diffractograms taken before and after post deposition annealing (vertical lines represent diffraction planes of orthorhombic Ta_2O_5 (a); RBS spectra of samples annealed at 200 °C and °800 C with respective fit curves (b); pH sensitivity of Ta_2O_5 EIS sensors with post-deposition annealing temperature (c) [80].

The RBS investigation confirmed the experimental results obtained with the X-ray analysis. RBS is an ion scattering technique commonly used to investigate the structure and composition of thin film materials. During an RBS analysis, high-energy (MeV) alpha particles are directed to the sample. As the backscattering cross section for each element is known, informations related to the quantitative compositional depth profile of films which are less than 1μm thick can be obtained by analysing the energy distribution of the backscattered ions at a given angle. Branquinho *et al.* used a 3.1 MV Van de Graff accelerator from High Voltage B.V., with a 2 MeV $^4He^+$ beam. The

depth profile of the sample constituents was extracted from spectra collected at a zero degrees incident angle. The backscattered particles were detected at 140 degrees with a silicon solid state detector of 13 keV energy resolution. The obtained spectra were fitted and analysed with the IBA Data-Furnace NDF software. Figure 3.34b reports the spectra of samples annealed at 200 °C and 800 °C. After fitting, the spectra show a negligible oxygen deficiency (4 %) that can be attributed to the reactive sputtering deposition process. Nonetheless, the oxide films present a quasi-stoichiometric oxygen proportion (2:4.8 vs. 2:5)-$Ta_2O_{4.8}$. No significant variation in stoichiometry with increasing annealing temperature was detected.

Branquinho *et al.* investigated the tantalum oxide films sensing performance by carrying out capacitance-voltage measurements in saline buffer solutions of varied pH. Figure 3.34c reports the results they obtained by performing electrochemical impedance measurements. The sensors with an amorphous tantalum oxide sensing layer show a sensitivity to pH above 50 mV/pH; in particular, the maximum sensitivity was obtained for an annealing temperature of 200 °C. It is for that reason that the tantalum oxide deposited on the HV pH sensors were subjected to an annealing at 200 °C.

3.8.4 Experimental results

The LV OCMFETs were tested as pH sensors by measuring the drain-source current with solutions having different pH values. In the following subsections the capacitance analysis of the device and the electrical response of the sensor to pH changes are reported.

3.8.4.1 Capacitances

Vertical capacitances were evaluated by means of an Agilent 4284A multimeter. Measurements were carried out on a set of three capacitors with the same dimensions and shape of the electrodes fabricated in the device; the electrodes were prepared by following the same process used for the LV pH sensor fabrication. Same as for the previous devices, C_{CF}, C_{SF} and C_{DF} were measured and the recorded data are reported in table 3.8.

CAPACITANCE @60 Hz [nF]	
C_{CF}	9 ± 1
C_{SF}	$(8 \pm 3) \cdot 10^{-1}$
C_{DF}	$(9 \pm 3) \cdot 10^{-1}$
C_{TOT}	11 ± 2

Table 3.8: Capacitances taken at 60 Hz; the average was calculated on three devices and the error was estimated by doubling the standard deviation.

3.8.4.2 Electrical response

The LV OCMFET for pH sensing was electrically characterized by means of an HP 4155 Semiconductor Parameter Analyzer.

Figure 3.35a and figure 3.35b respectively show the output characteristic and the transfer characteristic of a LV OCMFET for pH sensing recorded in air and at room temperature.

In order to test its sensitivity to pH changes, several solutions with different pH values were prepared by solving 0.1 M of KH_2PO_4 in 250 ml of Milli Q (18 MΩ) deionized water and by adding the necessary amount of H_2SO_4 or NaOH to change the solution pH.

The device sensitivity to pH changes was detected by recording the source-drain current changes while the sensing area was exposed to different solutions having a different pH value. Figure 3.35c shows the device and the experimental set-up.

A time of 5 minutes was waited in order to obtain a stable output drain current between the probe area soaking and each measurement recording. The output current was then measured by scanning the gate potential from 1 V to -1.5 V while the drain potential was fixed at -1 V. Figure 3.35d shows the maximum source-drain current recorded in a device at different pH conditions following the order they were taken. The solution pH was first increased and then decreased in order to show that the device response varies accordingly the pH variation. The same data were re-ordered following the pH values and reported in figure 3.35e. The experimental data reproduces a sigmoidal shape with a vertical flex. The curve trend is consistent the Henderson-Hasselbalch equation and allows concluding that isoelectric point is between 5.5 and 6 unit of pH.

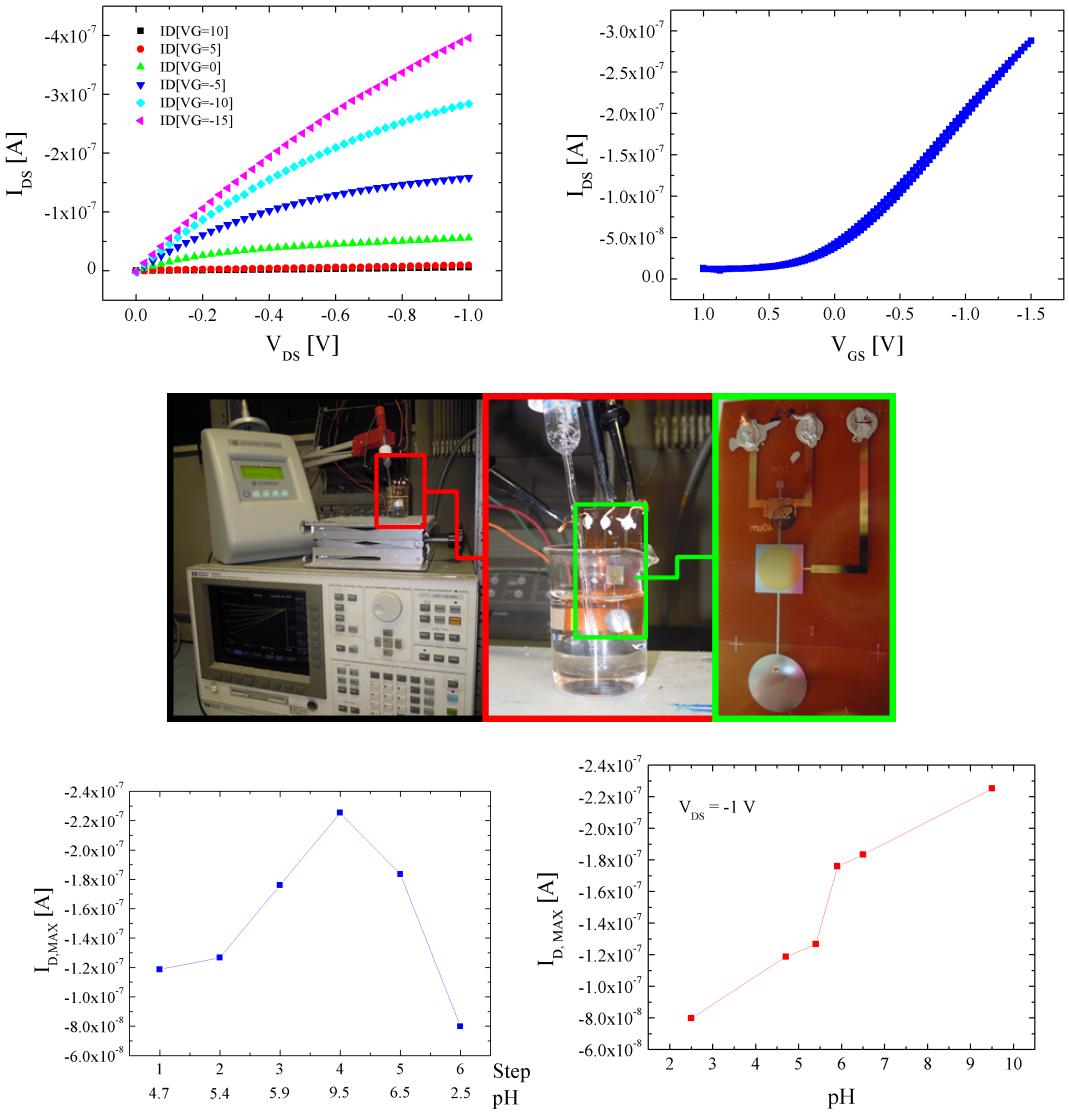

Figure 3.35: Output characteristic (a) and transfer characteristic (b) of a LV OCMFET for pH sensing; photos of the device and experimental set-up (c); electrical response to pH changes of the sensor: the maximum value of the output current (gate potential ranging form 1 V to −1.5 V and a drain potential fixed at −1 V) recorded at different pH value are order as they were taken (d) and versus the pH value (e).

3.9 Results - Analysis

The experimental results widely confirmed that the OCMFET can be used to detect charges in liquid media. The device responded to charges which varied according to the pH conditions of the electrolytic solutions, and so it worked as pH sensor. Moreover, it acted as a DNA sensor because it detected the charges borne by the DNA molecule. The experimental activity also demonstrated that several elements strongly affect the performances and sensitivity of the OCMFET.

The characteristics of the sensing layer affected the reproducibility of the experimental results. In fact, a large amount of tests were needed in order to obtain reasonable experimental results with the HV pH sensors. Still no reproducible results, not reported in this thesis, were obtained with the LV pH sensors functionalized with SAMs which were produced in smaller quantities compared to the HV sensors. Deeper investigations carried out on the sensing layer by means of XPS confirmed that less than the 50 % of the immobilized molecules efficiently worked as receptor. On the contrary, very good results were obtained when both the HV and LV implementations were tested as DNA sensors. Therefore, the SAMs employed for DNA recognition appeared sufficiently performing to this purpose. A possible reason could be that the SAMs based on the DNA molecule, having a longer chain, give rise to a more tightly packed and stable formation. Moreover, the SAMs formed by the DNA molecule contain more charges per area unit and as a consequence this can induce a higher response.

The device performances resulted strongly affected by the device structure as well. Sensitivity in DNA detection significantly increased when structures with reduced parasitic capacitances were used. The HV DNA sensors realized with the optimized layout showed better performances and reproducibility than the HV DNA sensors which were realized first, and had the same structure used for the pH sensors. In fact, the HV DNA sensors realized by using an optimized layout allowed DNA recognition also when low concentrated DNA solutions were used. These improvements must be ascribed to the increase of sensitivity which was obtained by reducing the parasitic capacitance effects. These results lead to believe that further improvements could be obtained by developing a technique to realize self-aligned contacts.

By working at very low operating voltages, the LV implementation of the DNA sensor allowed to obtain measurements in aqueous media which are more stable and

reliable than those obtained using the HV devices. In fact, this implementation proved that the device can work at very low DNA concentrations and that it has a good selectivity towards the single nucleotide polymorphism.

Very interesting results were obtained with the optimized implementation of the LV OCMFET which was tested as pH sensor by using tantalum oxide as sensitive layer. These results can be ascribed in part to the use of an effective stable and dense receptor, but also, same as for the HV DNA sensors, to the improvements obtained by reducing the parasitic capacitive effects.

4

Organic Electrochemical Transistor

In the present chapter, the investigation on the working regime of Organic Electrochemical Transitors (OECTs) all made of PEDOT:PSS is presented. After a brief introduction concerning the origin of the work and the state from where the investigation proceeded, the experimental activity is reported.

4.1 Introduction

OECTs have always been considered particularly interesting to use with sensing applications in liquid media for two reasons: they operate at very low voltage, and, compared to all OFET structures, they can be realized with a very simple geometry. In fact, OECTs are usually fabricated by realizing a planar, monolayer structure, composed by a channel, made of a conductive polymer, and a gate contact realized close to the channel, which can be fabricated by employing a variety of conductive materials.

Since Shirakawa *et al.* [81] discovered that polyacetylene has a high electrical conductivity, many interesting materials were synthesized and investigated over the past decades. Among them, PEDOT:PSS, which is a polythiophene derivative developed at the Bayer AG research laboratories in Germany during the second half of the 1980s, is one of the most successful conjugated polymer commercially available. In fact, PEDOT:PSS was used to fabricate the channel in many sensing applications based on OECTs, but it can also be used to fabricate the gate contact.

The working mechanism of OECTs based on PEDOT:PSS in devices with a metal gate contact is quite established. Indeed, the use of a metal as gate electrode makes the OECTs fabrication more complicated and increases costs, especially when using materials such as Pt. ECTs all made of PEDOT:PSS would be much more suitable to realize portable and disposable devices for sensing applications as they could be realized by means of low cost processes such as ink-jet printing. XXXXX ECTs all made of PEDOT:PSS by ink-jet printing were already reported, however, a closer examination of their working range is mandatory in order to make them use usable sensing applications. With regards to ECTs all made of PEDOT:PSS, the focus of this work was to determine their operative regime.

4.2 State of the art

In the following subsections an overview of the most important results on the working principle of ECTs with PEDOT:PSS as active layer is reported.

4.2.1 OECT - Model

Since White *et al.* [42] demonstrated that the conductivity of a poly(pyrrole) film is modulated by the application of a gate voltage through an electrolyte, several models were proposed in order to explain the working principle of OECTs. A model that reproduces the steady-state and the transient response of OECTs was recently reported by Bernards and Malliaras [82]. As the majority of organics used for OECTs are hole transporters, they referred to organic semiconductors with p-type doping; as a convention with p-type semiconductors, they assumed that the source contact was grounded and that a voltage was applied to the drain contact (V_d) relative to ground. When a positive voltage relative to ground is applied to gate (V_g), cations are injected from the electrolyte into the organic semiconductor film. Figures from 4.1a to 4.1c schematize the OECTs qualitative behaviour. They assumed that cations cause the organic semiconductor de-doping as each one of them compensates one acceptor; the charge of each cation which enters the organic semiconductor is neutralized by the extraction of a hole and is not replaced by a new injection at the source/drain contacts. As in OECTs the source-drain current is determined by the intrinsic conductance of

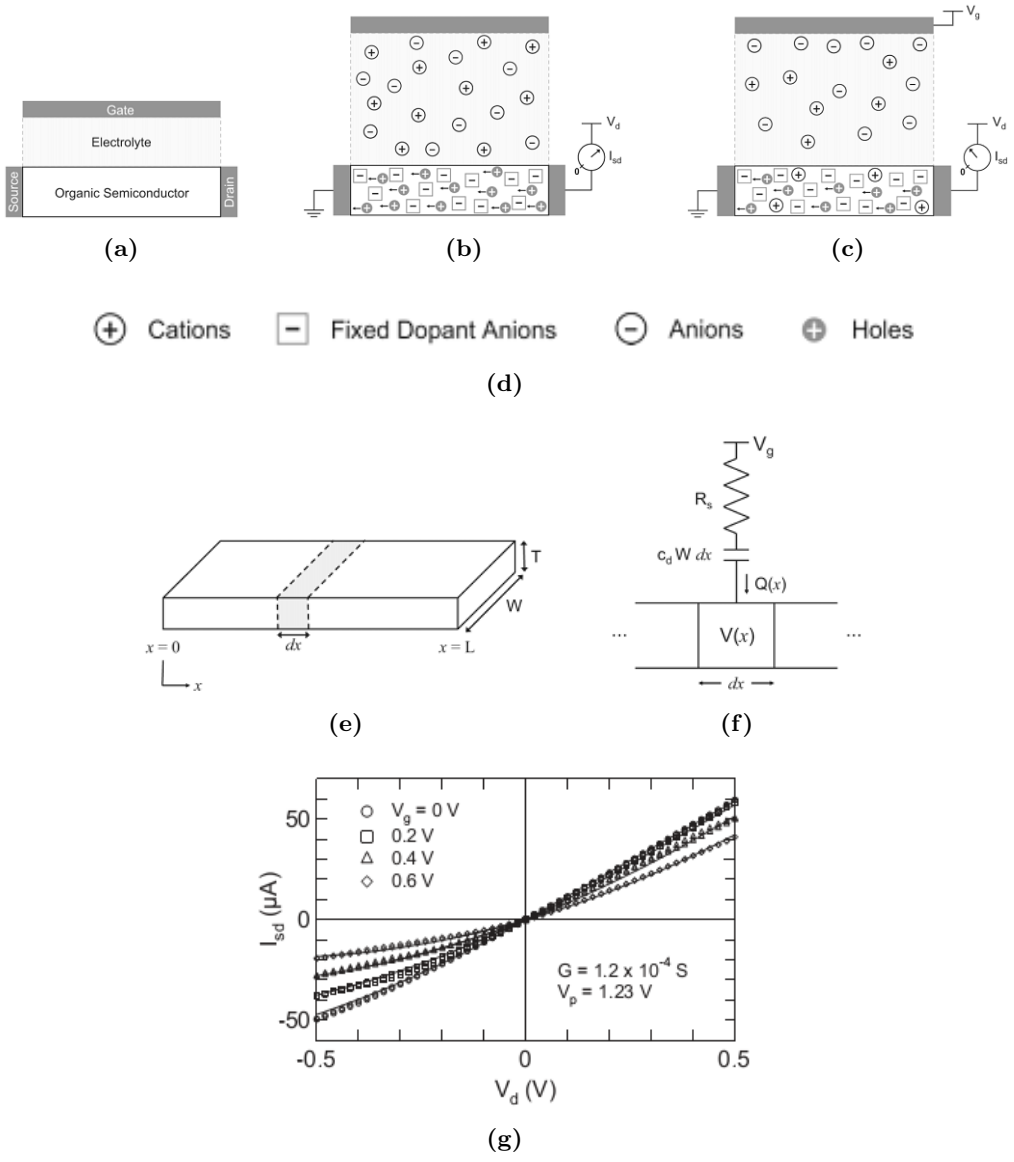

Figure 4.1: Qualitative representation of OECT labelling (a) and behaviour with an unbiased gate contact (b) and with a positively biased gate (c); ions legend (d); device geometry used in the model: organic semiconductor film with the source is located at $x = 0$ and the drain at $x = L$ (e); ionic circuit schematic: charge (Q) from the ionic circuit is coupled to the voltage in the electronic circuit at a position x along the organic semiconductor (f); experimental steady-state current-voltage characteristics (data points) for an OECT fitted to modelled stead-state current-voltage characteristics (solid lines) (g)[82].

the organic semiconductor, the source-drain current (I_{sd}) decreases because of the de-doping effect caused by cations entering in the semiconductor film. Moreover, they assumed that the negative ions did not cause any effect on the organic semiconductor.

Bernards and Malliaras described this behaviour by using an electronic circuit for hole transport in the organic semiconductor, and an ionic circuit for ion transport in the electrolyte. In the electronic circuit, the holes motion between the source and drain electrodes in the semiconductor was described by means of the Ohms law

$$J(x) = q\mu p(x)\frac{dV(x)}{dx} \tag{4.1}$$

where J is the current flux, q is elementary charge, μ is the hole mobility, p is the hole density and dV/dx is the electric field; the mobility was assumed as constant. They considered the conductivity of the undoped organic semiconductor as negligible. As a consequence, the effective dopant density in a volume v of semiconductor material was expressed as

$$p = p_0\Big(1 - \frac{Q}{qp_0v}\Big) \tag{4.2}$$

where p_0 is the initial hole density in the organic semiconductor before the application of a gate voltage and Q is the total charge of the cations injected in the organic film from the electrolyte. The transport of ionic charge in the electrolyte was described as a series of circuit elements. As a general rule, the electrode-electrolyte interface can be represented as a parallel between a resistance and a capacitor, while a pure capacitor can be used to model ideal polarizable interfaces. When an ideal polarizable electrode is used as metal gate, the transport of ionic charge in the electrolyte can be represented with the series of two capacitors and a resistor. The resistor describes the conductivity of the electrolyte; one capacitor accounts for polarization at the organic film-electrolyte, and the other represents the gate electrode-electrolyte interfaces. Bernards and Malliaras developed their model by considering a circuit formed by a series of a resistor (R_s) and a capacitor (C_d). The resistor, depending on the electrolyte conductivity, measured the solution's ionic strength; the capacitor, resulting from the series of the capacitance at the interface, measured the interface's polarization (see figures 4.1e and 4.1f). The transient behaviour of this circuit upon the application of a gate voltage has the characteristics of a charging capacitor:

$$Q(t) = Q_{ss}[1 - exp(-t/\tau_i)] \tag{4.3}$$

where $Q_{ss} = C_d \Delta V$ is the total charge that passes through the circuit, ΔV is the voltage applied across the electrolyte, and the ionic transit time is described by $\tau_i = C_d R_s$. C_d depends on the device area and can be expressed as $C_d = c_d A$, where c_d is the capacitance per unit area and A is the area of the device under consideration. In this model, the ion concentration and the ionic double layer capacitance's dependence from the potential were neglected and a constant value was assumed for c_d.

The steady-state behaviour for OECTs was determined by solving equation 4.1. As the effective dopant density throughout the organic film (equation 4.2) is known, they considered that for a differential slice, dx, in the vicinity of position x (figures 4.1e and 4.1f), the charge at steady-state is related to Q_{ss} from the following equation:

$$Q(x) = c_d \cdot W \cdot dx(V_g - V(x)) \tag{4.4}$$

where V_g is the gate voltage, $V(x)$ is the spatial voltage profile within the organic film and W is the width of the organic film. By combining equations 4.1-4.4 it results that the OECT characteristics at steady-state can be expressed by

$$J(x) = q\mu p_0 \Big[1 - \frac{V_g - V(x)}{V_p}\Big] \frac{dV(x)}{dx} \tag{4.5}$$

where V_p is the pinch-off voltage, defined as qp_0T/c_d and T is the depth of the channel. At steady-state, continuity requires the source-drain current density to be spatially constant. Equation 4.5 can be solved explicitly for various regimes of operation. Figure 4.1g shows the experimental steady-state current-voltage characteristics (data points) for an OECT fitted to model stead-state current-voltage characteristics (solid lines). Two regimes of behaviour were obtained in the first quadrant, for $V_d > 0$. When $V_d < V_g$, de-doping can occur everywhere in the organic film. Equation 4.5 was written in terms of current and explicitly solved by placing the source at $x = 0$ and the drain at $x = L$; in this case it resulted that

$$I = G\Big[1 - \frac{V_g - 1/2V_d}{V_p}\Big] V_d \tag{4.6}$$

where G is the conductance of the organic semiconductor film ($G = q\mu p_0 WT/L$). When $V_d > V_g$ de-doping only occurs in the region of the device where $V(x) < V_g$. This regime was described by:

$$I = G\Big[V_d - \frac{V_g^2}{2V_p}\Big] \tag{4.7}$$

where the current is linear with drain voltage, with the onset of linear behaviour occurring when $V_d = V_g$.

For $V_d < 0$, when the local density of injected cations becomes equal to the intrinsic dopant density of the semiconducting material, portions of the organic film can be completely de-doped. This condition, which is represented in the third quadrant, is mathematically reached when $V_g - V_d \geqslant V_p$, where the critical drain voltage for saturation can be written as $V_d^{sat} = V_g - V_p$. Same as for saturation in depletion-mode field effect transistors, the semiconductor will be locally depleted near the drain contact, but the holes which are injected into this region will still be transported to the drain contact. The depleted region moves towards the source contact for $V_d > V_d^{sat}$. In devices with a sufficiently long channel, the location of the depleted region closed to the source contact will not change noticeably with V_d, and the source-drain current will saturate; in devices with short channel, the extent of the depletion region moves significantly with variation in V_d and the current will not saturate but continue to increase. In devices with long channel, for $V_d \leqslant V_d^{sat}$, the current only depends on the drain voltage at saturation for a particular gate voltage and is given by:

$$I = -\frac{GV_d^{sat^2}}{2V_p} \tag{4.8}$$

Complete de-doping at $V_d > 0$ occurs when $V_g = V_p$. As high gate voltages are required to operate in this regime, the behaviour in this regime is not considered particularly interesting.

4.2.2 Gate electrode processes in OECTs

In the model proposed by Bernards and Malliaras it was assumed that no reaction occurs at the gate electrode; as a consequence the model can be considered accurate only for those devices where oxidation or reduction at the gate electrode is not significant and the device operates in the non-faradaic regime.

In 2006 Lin and Lonergan [83] investigated the significance of gate electrode processes to the transfer characteristics of electrochemical transistors where the active material is ion-permeable. They realized an electrolyte-gated transistor based on a polyacetylene (P_C) ionomer (see inset in figure 4.2a) with a sandwich geometry between two thermally evaporated gold electrodes; the top gold film was kept sufficiently

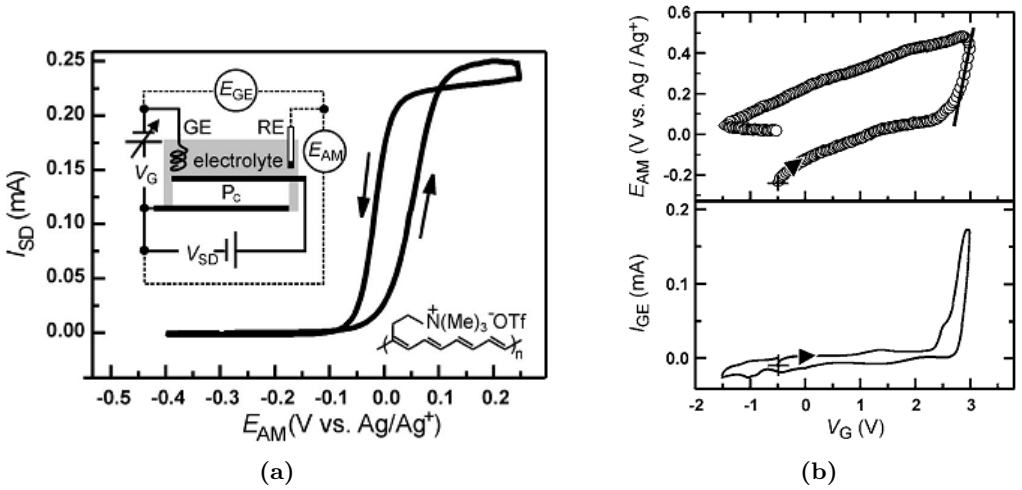

Figure 4.2: Source-drain current I_{SD} versus the electrode potential E_{AM} of the active material and insets showing a cross-sectional schematic of the ECT (a) [83].

thin to be porous to electrolyte permeation. They studied the device operation in 0.1 M tetrabutylammonium tetrafluoroborate (Bu_4NBF_4) in acetonitrile (CH_3CN) by using an Ag/Ag^+ as reference electrode in order to determine how the drop potential V_G distributes between the electrodes of the active material P_C and the gate electrode. Figure 4.2a and figure 4.2b show that two regimes of operation can be identified. In particular, from the bottom chart in figure 4.2b it results that the device operates in a non-faradaic regime when $V_G < 2.5$ V and in a faradaic regime when $V_G > 2.5$ V. These two regimes take their name from the process occurring at the gate electrode. The device works in a non-faradaic mode when the drop potential of the gate with respect to the reference electrode (E_{AM} vs. Ag/Ag^+) is kept within the stability window of the electrolyte. The polymer doping is coupled to the reversible charging of an ionic double layer - non-faradaic process - which occurs at the gate electrode. The level of charging depends on the quantity of active material, whereas the capacity of the gate electrode to modulate conductivity depends on the electrode's area. The faradaic regime involves the conventional redox process where two faradaic processes balance: oxidative doping of the polymer to modulate conductivity is coupled with the reduction at the gate electrode. The faradaic regime is characterized by the greatest possible sensitivity, but operates with the irreversible reduction of the electrolyte, as it results by the fact that E_{AM} does not return to its initial value in the return sweep of figure 4.2b.

The effect of the gate electrode material on the response of OECTs was further investigated by Tarabella *et al.* [84]. As most OECTs have a channel made of PEDOT:PSS, they studied the effect of the gate electrode material on the response of OECTs with a PEDOT:PSS channel when using a halide electrolyte (0.1 M $NaCl_{(aq)}$) and two different metal wires, Ag (Ag-OECTs) and Pt (Pt-OECTs), as gate contact. Figures 4.3a show the device structure and figures 4.3b and 4.3c schematize its working principle. As PEDOT:PSS is a hole conductor, when the drain is negatively biased with respect to the source contact, a drain-source hole current is generated (see figure 4.3b). Moreover, upon application of a positive bias to the gate contact, part of the ions from the electrolytic solution enters the PEDOT:PSS channel causing its de-doping (see figure 4.3c) according to the following chemical reaction:

$$\mathrm{PEDOT^+{:}PSS^-} + \mathrm{M^+} + e^- \leftrightarrows \mathrm{PEDOT} + \mathrm{M^+{:}PSS^-}. \tag{4.9}$$

Figures 4.3d and 4.3e show the different responses they recorded for Ag-OECTs and Pt-OECTs. In figure 4.3d the OECTs response was expressed as the current modulation of $\Delta I/I_0 = |I_{ds,off} I_{ds,0}|/I_{ds,0}$, where $I_{ds,off}$ is the off current ($V_{gs} > 0$) and $I_{ds,0}$ the on current ($V_{gs} = 0$). Ag-OECTs display a larger modulation throughout all the investigated V_{gs} range. This behaviour was ascribed to the different interaction between the metal gate and the electrolytic solution. Two operative regimes were identified. OECTs operates in a capacitive, or non-faradaic regime, when the application of V_{gs} induces a transient current in the electrolyte; they operate in faradaic regime when a steady-state current due to reduction/oxidation redox reactions was sustained in the electrolyte. A large steady-state gate-source current in Ag-OECTs indicates that a faradaic process at the gate electrode occurred when an Ag wire was used as gate; this process was ascribed to the oxidation of the Ag gate electrode in the halide environment according to the reaction:

$$\mathrm{Ag} + \mathrm{X^-} \leftrightarrows \mathrm{AgX} + e \tag{4.10}$$

On the contrary, Pt-OECTs showed a small gate-source current which is consistent with the polarizable nature of Pt electrodes. In Pt-OECTs, an electrical double layer forms at the $Pt/NaCl_{(aq)}$ interface so that $V_{sol} < V_{gs}$. As a consequence, OECTs employing a Pt gate electrode showed a response that depended on the area of the gate electrode [85]. No relevant change was recorded in the Ag-OECTs by varying the gate area; this result further confirmed that no drop potential at the $Ag/NaCl_{(aq)}$ interface occurs and,

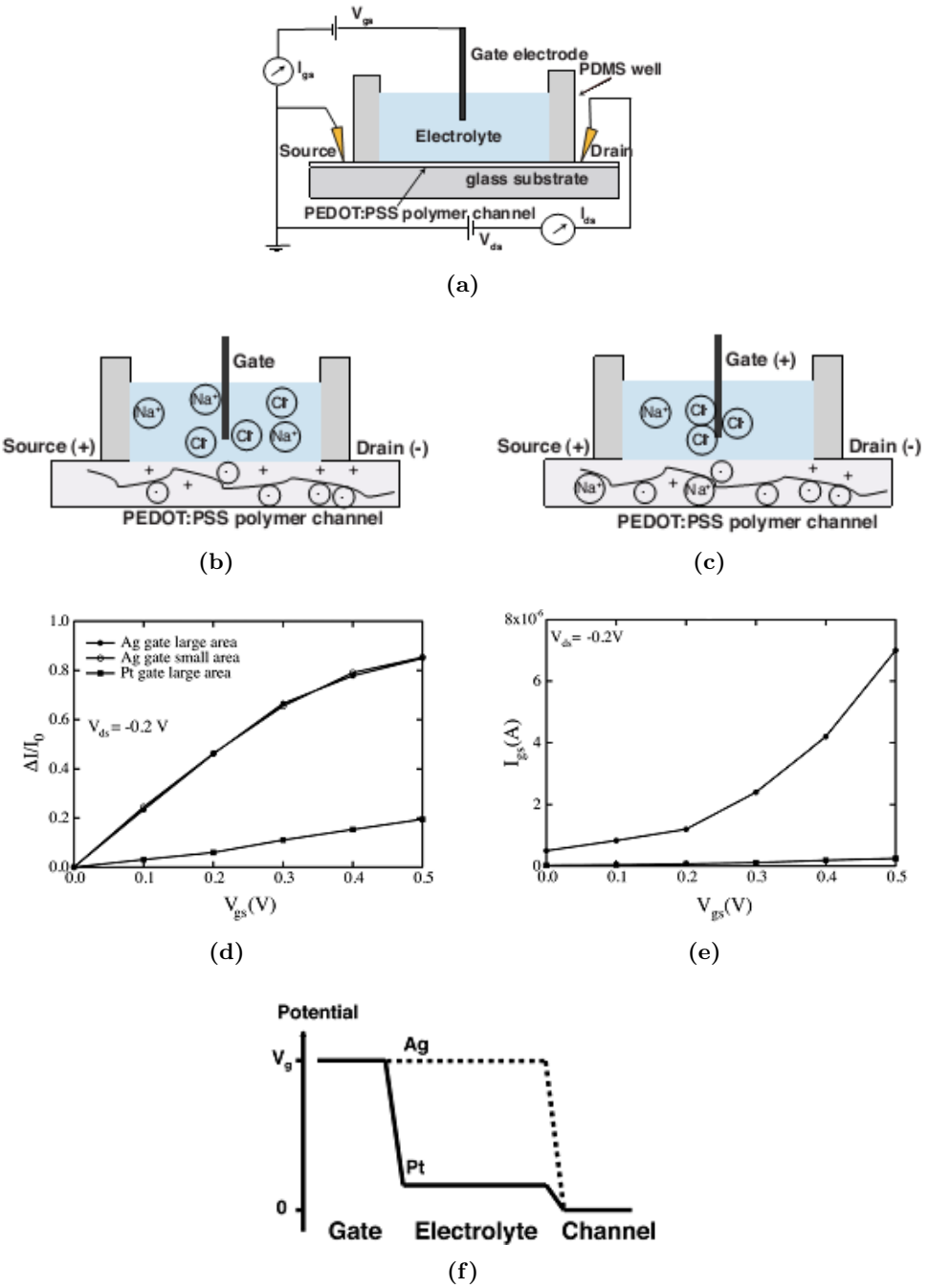

Figure 4.3: Device structure of a PEDOT:PSS ECT (a) and working principle with an unbiased gate electrode (b) and a positively biased gate (c) (circles filled with indicate PSS ions and + indicate mobile holes); $\Delta I/I_0$ vs. V_{gs} (d) and I_{gs} vs. V_{gs} in a 0.1 M $NaCl_{(aq)}$ electrolytic solution; distribution of the potential between the gate electrode and the channel for Ag and Pt gate electrodes (e) [84].

as a consequence, $V_{sol} \approx V_{gs}$. Figure 4.3f reports the distribution of potential between the gate electrode and the channel for Ag and Pt gate electrodes respectively.

4.2.3 OECT all made of PEDOT:PSS

As mentioned in the introduction, it is possible to fabricate ECTs with a gate contact made of a conductive polymer. The main advantage is that they can be fabricated with very low-cost techniques such as ink-jet printing.

In 2012 Basiricò *et al.* [86] realized an ECT entirely made of PEDOT:PSS by using a piezoelectric, drop-on-demand printer. The electrodes were fabricated on a PET substrate which was kept at a constant temperature of 60 °C and consisted of three superimposed printed layers. An annealing was performed after printing for 12 hours at 60 °C. Finally, an ethylene glycol (EG) treatment was carried out on the electrodes in order to increase PEDOT:PSS conductivity and to increase the robustness of the printed layers. Figures 4.4a and 4.4b show the AFM image of a double layer of PEDOT:PSS and the profile of a single layer of PEDOT:PSS stripe. Concerning the geometry, they realized two electrodes having the same length but different width. In the type 1 configuration (see left picture in figure 4.4c) the narrower electrode was used as channel

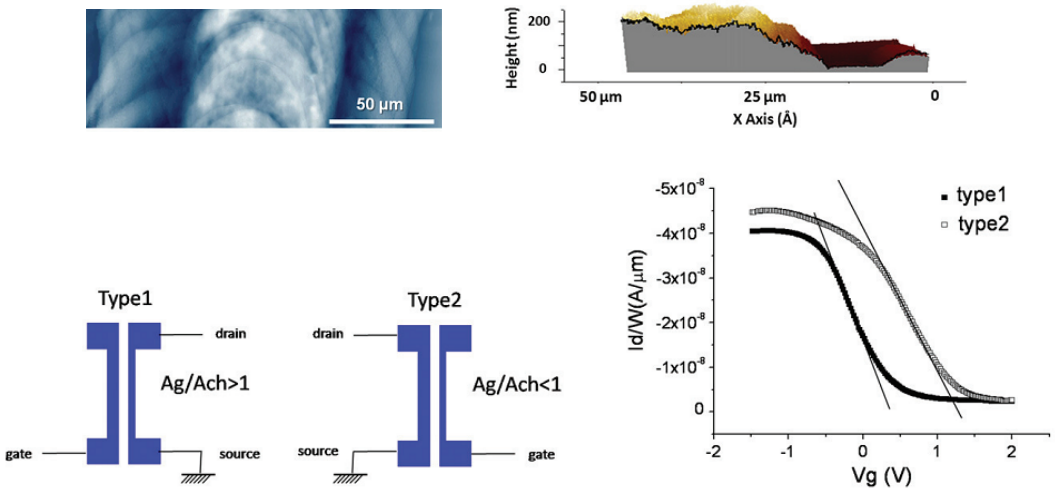

Figure 4.4: OECT Basiricò *et al.* [86]: AFM image of a double layer of PEDOT:PSS printed on top of a PET substrate (a), profile of a single layer of PEDOT:PSS stripe (b); schematic representation of the employed OECTs (c); I_{ds} vs. V_g curves recorded on a single device by exchanging the channel with the gate electrode (d).

while the largest worked as gate electrode, therefore the gate area was bigger that the channel area (Ag/Ach $>$ 1); in the type 2 configuration (see right picture in figure 4.4c) the electrodes were inverted, therefore the largest structure was taken as channel while the other worked as gate electrode (Ag/Ach $<$ 1). Figure 4.4d shows the transfer characteristics normalized with respect to the width that they recorded in a single device whose electrodes were used in the two configurations shown in figure 4.4c. As two different currents were measured, it was proven that the device working depends on the device geometry. Moreover, as their working range (i.e. the gate voltage range in which the device can operate) extends from negative to positive voltages, it is larger than the operation range of devices made with metal gate contact, which usually spans from zero (the on state) to a maximum positive voltage (the off state).

4.3 Dimatix Material Printer

The Dimatix Materials Printer 2800 (DMP2800), which is a piezoelectric drop on demand printer produced by FUJIFILM Dimatix, was used to realize the OECTs. The printer is provided by several components (see figure 4.5a) and an application software (*DMP Drop Manager software*) which allows managing the jetting process, performing the maintenance activities required to obtain optimal printing performance.

A *platen* allows hosting the substrate to be printed and a vacuum system allows blocking the substrate during the printing. The platen can be heated up to 60 °C in order to favour the ink-jetted droplets drying.

A *print carriage* (see figure 4.5b), which includes a *fiducial camera* and the *cartridge*, represents the core of the printer as it allows the printing actions. The fiducial camera, which is provided with two light sources for operating into three different light operation modes, allows setting the printing origin, carrying out alignment procedures, and evaluating the printed pattern quality. In particular, the visual feedback obtained through the camera can be used to change the settings of *firing voltage*, *jetting frequency* and *number of jetting nozzles*, which are some of the parameters which affect the jetting performances. The cartridge is formed by a *fluid module* (see figure 4.5c), which is provided with a plastic bag for the ink storage, and a *jetting module*, which is equipped of 16 aligned jetting nozzles which that are 254 μm apart and have an orifice size of about 21.5 μm (see figure 4.5d). A built-in heater allows heating the fluid

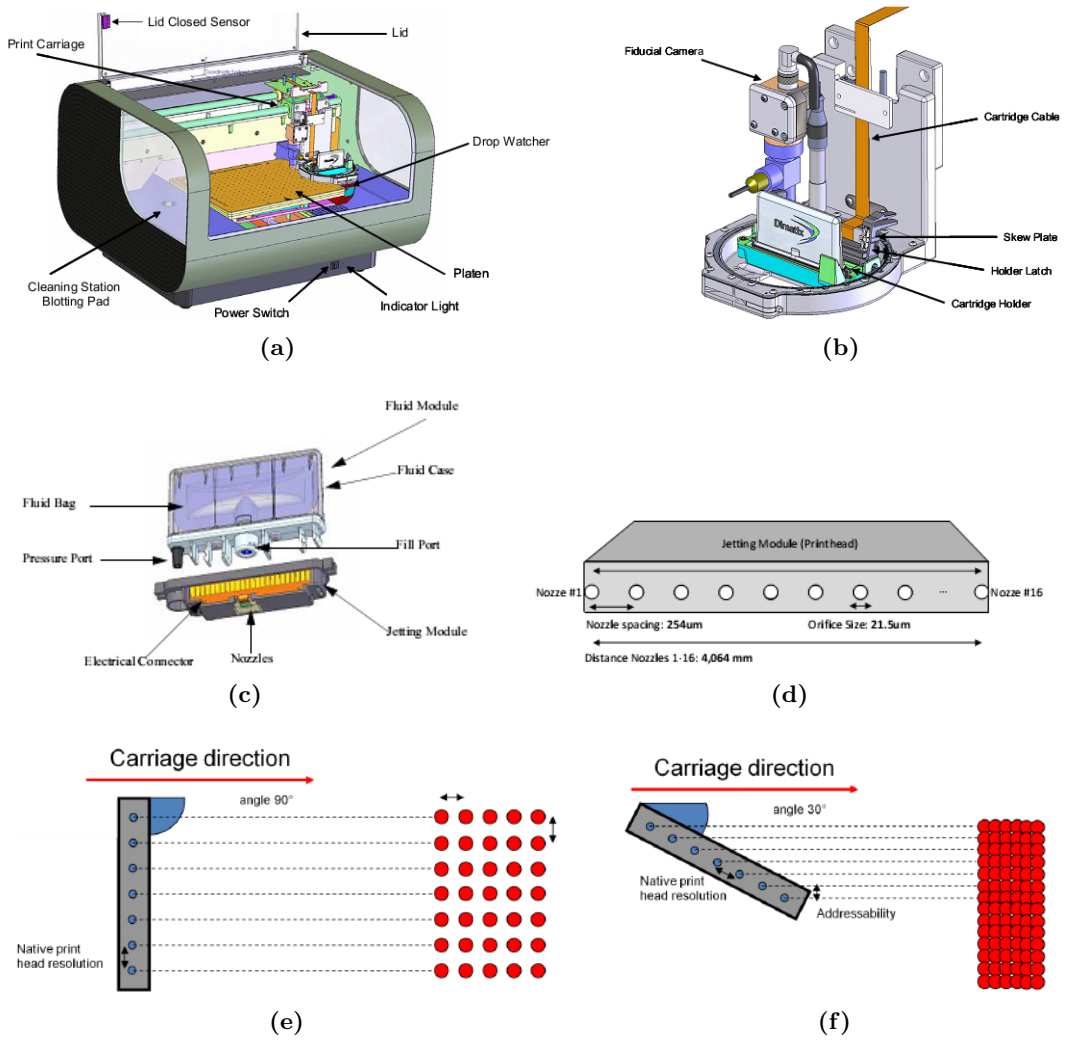

Figure 4.5: Schematic of: Dimatix Fujifilm printer (a), print carriage (b), cartridge components (c), carriage direction effect on printing resolution (d) and (e) [87]

to a maximum temperature of 70 °C in the jetting structure. When not in use, the cartridge is located upon a *cleaning station*: it consists of a replaceable and absorbent pad which allows drawing the fluid off of the nozzle plate when it is brought close to it. The quality of jets ejected from the nozzles can be monitored by using a *drop watcher camera system*, which includes a replaceable *drop watcher pad* for drops collecting, and a digital camera with a magnification of 150 × (image displayed resolution of 2.25 μm per pixel).

Both the carriage and the platen move and contribute to the pattern reproduction: the carriage move horizontally (x-direction) above the substrate, while the platen vertically shifts (y-direction).

Dimatix supplies two models of piezo-driven jetting cartridges which differ for the nominal drop volume they can eject: the DMC-11601 and the DMC-11610 model, which are able to eject drops with a nominal volume of 1 and 10 pL, respectively. As a matter of fact, the effective volume of jetted drops depends on the applied firing voltage and the jetting frequency, while the spot size and line width result form the interaction between the ink-jetted droplets and the specific substrate. The spot size of the ink affects the resolution achievable with the printing, as the resolution depends on the *drop spacing*, which is the distance in x and y, center to center, of the drops that the DMP deposit to create patterns (see figures 4.5e and 4.5f). The drop spacing may be setted between 5 and 254 microns in one micron increments. In the x direction, the printer triggers the ejection of a drop according to an encoder signal and image resolution; in the y direction, the drop spacing is determined by the cartridge mounting angle angle, which is the angle that the cartridge forms with the scan direction, and the print head resolution, which in turns depends on the distance between two subsequent nozzles in the nozzle plate. The cartridge mounting angle is set manually through a rotating system by means of two graduated scales. A continuous, uniform and smooth printed film can be obtained by setting the drop spacing to the half size of the deposited droplets. In order to accurately reproduce patterns, the dimensions and locations of the features should be divisible by the drop spacing for optimum placement match; moreover, the spatial density of the point to be printed, which is usually expressed in dots per inch (dpi, number of individual dots that can be placed in a line within the span of 1 inch 25400 μm), must equal the drop spacing. As a matter of fact, files with

the patterns to be printed must be saved with a resolution corresponding to following ratio:

$$\text{Resolution [dpi]} = \frac{25400}{\text{Drop spacing [dpi]}}. \tag{4.11}$$

4.4 Experimental activity

In the literature it was reported that the operative regime of OECTs depends not only on the material used as channel, but also on both size and material of the gate electrode [84]. From the transfer characteristics of OECTs it resulted that the off potential depends on the ratio between the gate and the channel area only in case of non-Faradaic behaviour of the gate-electrolyte; moreover, the gate current has a large steady-state value when a faradaic process occurs, while it is practically negligible in presence of non-Faradaic, capacitive behaviour.

Concerning the ECTs all made of PEDOT:PSS, it was demonstrated that their working range is larger than the operation range of devices made with a metal gate contact and that their behaviour depends on the device geometry [86]. Figure 4.6b reports the normalized transfer characteristics taken from data reported in figures 4.6c and 4.6d, which were measured in OECTs with the structure shown in figure 4.6a [88]. From the plots it results that the maximum (on) current was reached in both cases for negative values rather than for zero voltage; moreover, the more negative on-voltage was recorded in the device whose gate area was bigger than the channel's.

This data further confirmed that the device operation depends on its geometry and indicate that ECTs with a gate made of PEDOT:PSS behave like OECTs with a gate made of a polarizable metal electrode. Nevertheless, in these devices, as both channel and gate are made of PEDOT:PSS, they can both switch from the oxidized (doped) to the reduced form (de-doped) and vice versa by exchanging ions with the solution according to equation 4.9. As doping/de-doping can occurs in both of them, it is obvious to assume that there is a competitive behaviour of gate and channel in adsorbing ions from the solution. Further investigations are thus needed in order to determine the processes which occur at the gate-electrolyte interface during the operation of the device and its effective role.

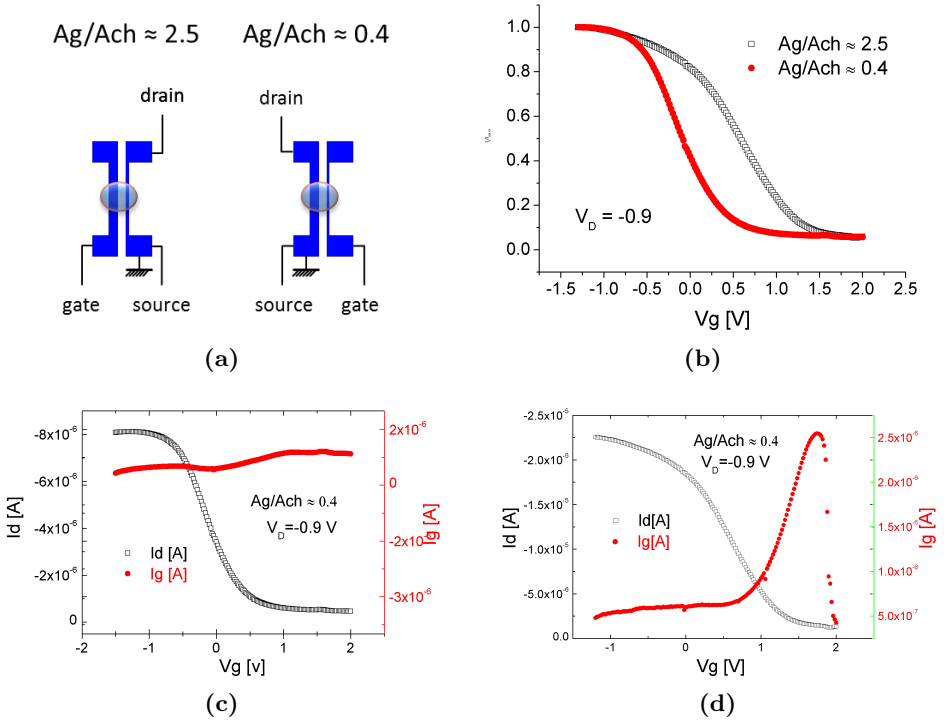

Figure 4.6: Structure of all made PEDOT:PSS ECTs (a) and experimental results: normalized drain-source current (b) obtained from drain-source curves measured for the two structures (c) and (d) [88].

This study represents the focus of this work and was carried out by performing both electrical characterization and a combination of contemporary electrical and electrochemical measurements.

From an electrochemical point of view, two kinds of processes can occur at the interface. One type is called *faradaic process* as it comprises redox reactions, which are governed by Faraday's law [89]. The other type is called *non-faradaic process* as charges do not cross the interface, and external currents can flow (at least transiently) when the potential, electrode area, or solution composition changes. As Cyclic Voltammetry (CV) measurements are electrochemical techniques commonly used to obtain information about electrode reactions, a specific experimental set-up was studied and realized in order to perform the electrochemical characterization of the device during its operation.

In the following subsections, after a description of the processes used for the device

design and fabrication, the experimental set-up and results are reported.

4.4.1 Design

Two different experimental set-ups were employed for the device characterization.

One set-up was used to carry out conductance measurements of the electrodes under a specific biasing and to make visible the processes occurring at the interface PEDOT:PSS/electrolyte. For these measurements, the devices were realized with the very simple linear geometry shown in figure 4.7a. The layout has an asymmetric shape and allows measuring the device in two possible configurations. By considering only the larger portion of the electrodes, when using the top electrode as gate contact, the ratio between its area and the channel area is equal to 2; when using the bottom electrode as gate, the ratio between the same areas is equal to 0.5.

The other layout was designed to allow combining electrical and electrochemical measurements. The experimental set-up which was used to carry out the measurements required that a part of the gate electrode and the channel could be kept immersed into the electrolyte. A solution was found by designing the electrodes with a horseshoe shape: the channel and the gate electrode, which had to be immersed in the electrolytic solution were designed in the central part of the area, while their extensions were used to wire them to the instruments.

In order to bring out the role of the ratio between the areas, the electrodes were designed with a very different area compared to the OECTs realized by Basiricò *et al.* [86]. Figure 4.7b reports the device geometry. The dotted line indicates the portion

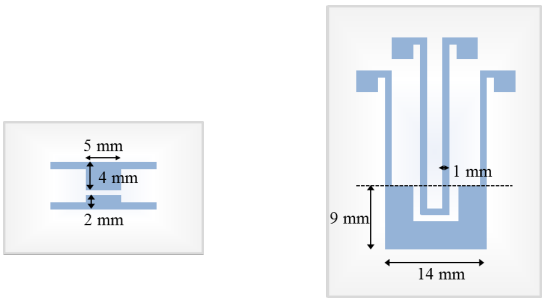

Figure 4.7: Layout of the OECTs used during the conductance measurements(a), during the electrochemical characterization (b).

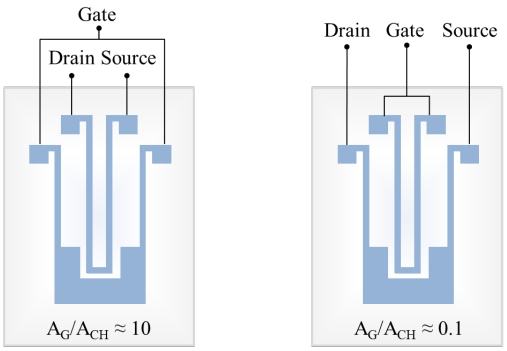

Figure 4.8: Scheme of the electrical configurations for OECT with $A_G/A_{CH} \approx 10$ (a) and $A_G/A_{CH} \approx 0.1$ (b).

of the device which must be exposed to the electrolytic solution in order to have a ratio of 9.6 between the external and the internal electrode. Both the external and the internal electrode were elongated and provided with two pads for the electrical connection. This solution allowed using both electrodes as gate contact or channel: when the external electrode was used as gate contact, the gate area was roughly one order of magnitude larger than the channel area; on the contrary, when the internal electrode was used as gate contact, the gate area was roughly one order of magnitude smaller than the channel area. Figure 4.8 shows the electrical connections for OECTs with $A_G/A_{CH} \approx 10$ and $A_G/A_{CH} \approx 0.1$.

4.4.2 Materials

A biaxially oriented PET (boPET) film with a thickness of 175 μm, purchased from Goodfellow, was used as substrate in the device fabrication. PET is a thermoplastic polymer resin of the polyester family. It consists of polymerized units of the monomer ethylene terephthalate, with repeating $C_{10}H_8O_4$ units arranged according to the chemical structure reported in figure 4.9. PET was chosen because, when in thin film, is a

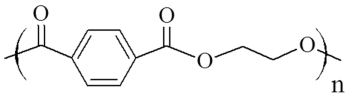

Figure 4.9: PET chemical structure.

highly transparent, flexible and dimensionally stable material; moreover it has a good chemical resistance, is stable to temperatures up to 100 °C and is biocompatible.

ECTs were entirely made of PEDOT:PSS. PEDOT is a polythiophene derivative based on 3,4-ethylenedioxythiophene (EDOT) monomer, which is made up of an aromatic thiophene ring with the carbon atoms in position 3 and 4 connected through a double ethereal bridge. Its chemical polymerization can be obtained by immersing EDOT in a polyelectrolytic solution in the presence of an oxidizing agent. Figure 4.10a shows its backbone structure. In its pristine state PEDOT is insoluble in all common solvents and very unstable in its neutral or undoped state as it quickly oxidises in air. It is for those reasons that it is usually produced in a doped state. By using standard oxidative chemical or electrochemical polymerization methods, PEDOT becomes a p-doped material. The most common electrolyte used is PSS (see figure 4.10b). The dispersion made of PEDOT and PSS, named PEDOT:PSS, is water-insoluble and in organic polar solvents has an excellent stability. It can easily be spin-coated giving rise to the formation of transparent films with electrical conductivity in the range of 0.0510 S/cm [90], i.e., with a very low resistance. The PEDOT:PSS dispersion gives

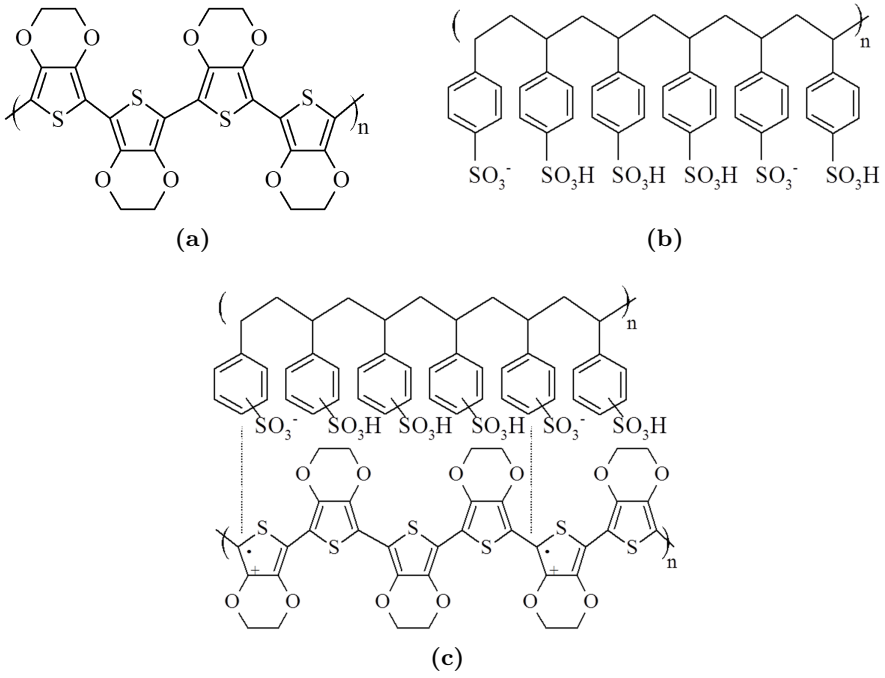

Figure 4.10: Chemical structure of PEDOT, PSS and PEDOT:PSS dispersion.

rise to the formation of grains with a coil conformation. As PSS chains consist of a few hundred monomer units, it is believed that the grains are defined by the PSS random coil with PEDOT chains ionically attached along them. In fact, PSS acts as an oxidant removing electrons from the thiophenic rings of the PEDOT chain (see figure 4.10c); as a consequence, PEDOT becomes positively charged, while PSS takes a negative charge.

In this work, it was decided to study the behaviour of ECTs all made of PEDOT:PSS when employing a water based solution as electrolyte. The measurements required that the channel and the gate electrode could be kept stably under the electrolyte for a long time (several hours) without damaging. In the literature it was reported that PEDOT:PSS solubility in water can be decreased by treating it with ethylene glycol (EG). It is for this reason that EG was deposited on the printed films. Ouyang *et al.* [91] investigated on the mechanism of conductivity enhancement in PEDOT:PSS film through solvent treatment by means of several experimental techniques. According to their experimental results they suggested that EG introduces some conformational changes on the PEDOT chains: PEDOT would transform from the benzoid to the quinoid structure (see figure 4.11), and its chains would change from the coil structure into an expanded-coil or linear structure.

They observed the conductivity enhancement only when using organic compounds which have two or more polar groups; as a consequence, they proposed that the conformal changes in the PEDOT chains resulted from the interaction between the dipole

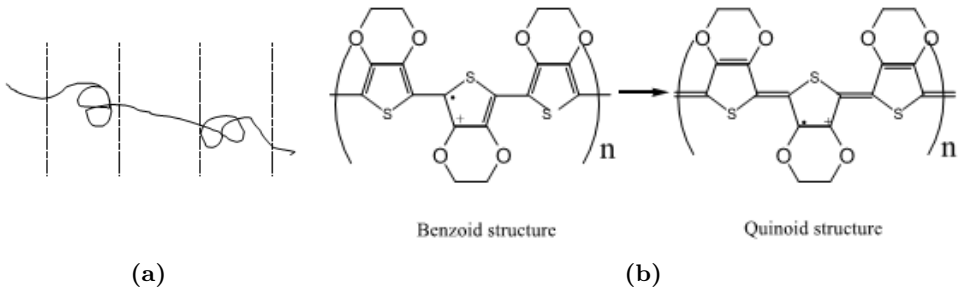

Figure 4.11: Schematic coil conformation of a PEDOT chain in PEDOT:PSS films treated with EG (central section) and in untreated PEDOT:PSS films (extreme sections) (a); scheme of transformation of the PEDOT chain from the benzoid to the quinoid structure: the dot and plus represents the unpaired electron and positive charge on the PEDOT chain, respectively (b) [91].

of one organic compound's polar group and the dipoles or the charges on the PEDOT chains.

4.4.3 Fabrication technology

The PET foils which were used as substrate were cleaned by subsequent 15 min ultrasonic baths in acetone and isopropyl alcohol, washed with deionized water and finally dried under nitrogen flow.

As the devices were realized by ink-jet printing, a waterborne dispersion of PEDOT:PSS sub-micrometer sized gel particles, optimized for ink-jet printing applications, was employed in the device fabrications. The ink, which is named *Clevios^{TM} P Jet HC*, was provided by H. C. Stark. Its solid content ranges from 0.6 and 1.2 %, conductivity may vary between 30 to 90 S/cm and viscosity between 5 to 20 mPa·s. Before filling the cartridge, the Clevios^{TM} P Jet HC formulation was sonicated for 15 min in an ultrasonic bath and then filtered with a 0.2 μm nylon filter. Both these procedures were made in order to re-disperse potential particles agglomerates that could cause the nozzles' clogging during the printing.

The devices were printed through the Dimatix Materials Printer 2800 (DMP2800). By using the DMC-11610 cartridge it resulted that spots with a 40 μm diameter were deposited when applying a firing voltage of 18 V. As a consequence, a drop spacing of 20 μm was set in order to minimize ink spreading on the substrate. Good printing performances were obtained by carrying out a cleaning cycle of the nozzles every 100 scans of the print carriage.

During printing, substrates were kept at a constant temperature of 45 °C to help fast solvent evaporation, while the cartridge was kept at room temperature. The electrodes were fabricated by superimposing 3 printed layers and waiting at least for 60 s between the printing of two subsequent layers. Figure 4.12a shows a photo of a complete device with details of the printed PEDOT:PSS layer taken by the camera of the printer.

After printing, samples were annealed on a oven at 60 °C for 8 h. After annealing, EG was deposited on the structure by means of spin coating (see figure 4.12b), then the devices were dried in a oven at 60 °C for 12 hours.

When using the layout in figure 4.7a, in order to contain the electrolytic solution only on top of a portion of the electrodes, a well made of PDMS Sylgard 184, provided by Downcorning, was used. The PDMS well was prepared by mixing the elastomer with a

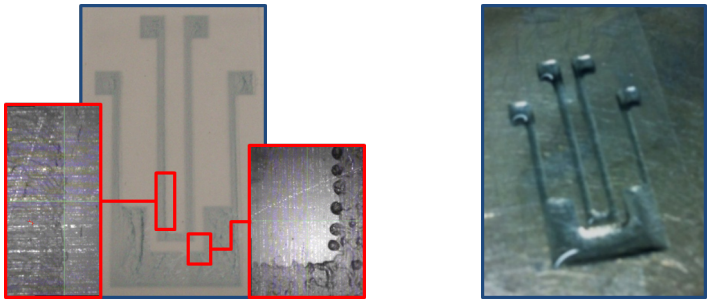

Figure 4.12: Photo of a complete device with details of the printed PEDOT:PSS layer taken by the camera of the printer (a) and immediately after the glicole deposition (b).

curing agent (a mixture of a platinum complex and copolymers of methylhydrosiloxane and dimethylsiloxane) and then heating it at 100 °C for one hour; after heating, as it becomes a cross-linked solid, it can be cut in the wanted shape, pealed off the master (a slide) and applied on the device.

4.4.4 Experimental set-up

Two kind of measurements were carried out: conductance measurements and contemporary electrical and electrochemical characterization.

The first kinds of measurements were carried out by means of a Keithley 2612 and 2636 source meters controlled by a Labview software.

The second kind of measurements were recorded by using an HP 4155 Semiconductor Parameter Analyzer (SPA) and an Autolab PGSTAT 101 potentiostat/galvanostat electrochemical analysis system with NOVA software package (Eco Chemie). The 4155 SPA was used to bias the transistor; the potentiostat was used to determine the drop potential at the PEDOT:PSS interface during the device biasing, by performing an Open Circuit Potential (OCP) measurement. Figure 4.13a shows the experimental set-up employed when the internal electrode was used as gate contact. As reported in the picture, the source contact was put at the same ground for both the SPA and the potentiostat, and worked as Working Electrode (WE) during the OCP measurement; a Pt wire was used as Counter Electrode (CE) and an Ag/AgCl as Reference Electrode (RE). The same experimental set-up was used when measuring those devices where the external electrode was used as gate: the source contact always worked as WE. With this arrangement, the OCP allowed obtaining the drop potential at the interface between

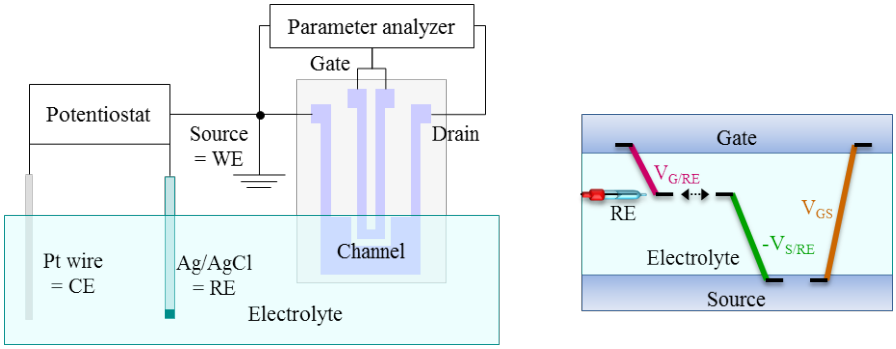

Figure 4.13: Experimental set-up used during the electrical and electrochemical characterization of the all made PEDOT:PSS ECTs (a) and drop potential at the PEDOT:PSS interface (b).

the source and the RE ($V_{S/RE}$); the drop potential at the interface between the source and the RE, named ($V_{G/RE}$), was extracted from data.

All the measurements were carried out in air at room temperature by using a 0.01 M PBS (pH 7) as electrolytic solution.

4.4.5 Experimental results

PEDOT:PSS is an electrochromic material as its colour depends on its oxidation state: it is light blue when oxidized and dark blu when reduced. The absorbance of a PEDOT:PSS electrode, which was fabricated with the same process used to realize the OECTs, was measured in collaboration with the Inorganic and Physical Chemistry group of the University of Bologna. Figure 4.14 shows the recorded measurements. In agreement with data reported in the literature [91], a peak was observed around 600 nm and the absorbance of the reduced PEDOT:PSS (E = –1 V vs. Ag/AgCl) is higher than that of the oxidized PEDOT:PSS E = 1 V vs. Ag/AgCl)

In the OECTs under investigation both the channel and the gate contact were made of PEDOT:PSS and it was expected that doping/de-doping would occur in both of them, even if at different voltages. This assumption was demonstrated by taking a sequence of pictures of OECTs during operation. In order to clearly show the change of colour, a device with a ratio between the biggest and the smallest electrodes equal to 2 (see figure 4.7a) was used. All photos were taken on a single device: the biggest electrode was used as gate in the picture reported in the first row, and worked as

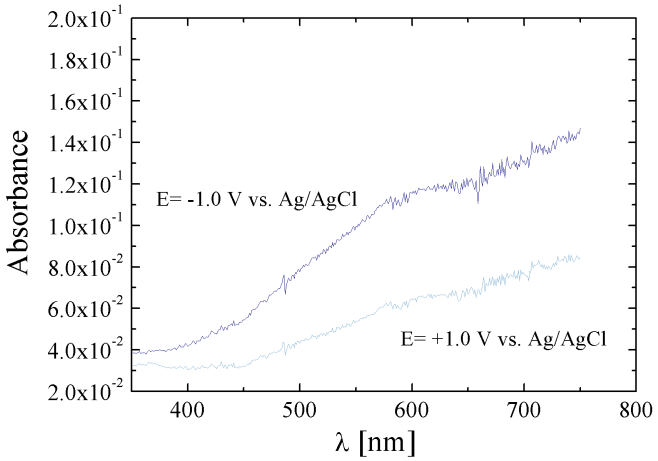

Figure 4.14: Absorbance of a PEDOT:PSS electrode.

channel in the pictures reported in the second row. The OECT was measured in air, at room temperature, and the photos were taken under the same light conditions. The pictures clearly show that both the channel and the gate electrode become light blu when oxidized and dark blu when reduced. As a consequence, it was confirmed that doping/de-doping occurs in both channel and gate electrode, even if at different gate voltage values: at positive gate voltages the gate is fully doped while the channel is fully de-doped, at negative voltages the opposite occurs. These results were further confirmed by conductance measurements, which were recorded immediately after the electrolytic solution evaporation, by applying a potential ranging form –1 V to +1 V. The conductance variations are reported next to the corresponding pictures in figure 4.15. The results are expressed in the form of percentage variation with respect to

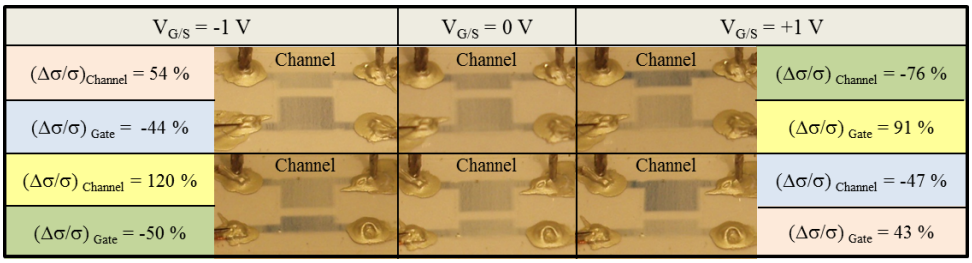

Figure 4.15: OECTs electrochromic behaviour and percentage of the conductance variation of channel and gate contact with respect to the conductance recorded on the PEDOT:PSS electrode in its pristine state.

the value recorded on the PEDOT:PSS electrode in its pristine state. The percentage variations obtained in the small electrode in its oxidized state when it was used as channel (gate-source potential of –1 V) corresponded to the value recorded when it was used as gate contact (gate-source potential of 1 V). The same correspondence was found when the small electrode was in its reduced state. With regards to the big electrode same results were detected in both states oxidized and reduced. These correspondences are highlighted by the use of the same background in boxes. Therefore, the conductance measurements confirmed that there is a competitive behaviour of gate and channel in adsorbing ions from the solution.

The role of the gate contact in the device operation was further investigated by recording transfer characteristic of OECTs and OCP at the same time. The gate potential was spanned between –1 and +1 V, while the drain potential was maintained at –1 V. Figures 4.16a and 4.16c show the gate-source ($I_{G/S}$) current recorded in two different devices: in one device the external electrode was used as gate ($A_G/A_{CH} \approx 10$), while in the other it was used as channel ($A_G/A_{CH} \approx 0.1$). In the first chart, currents were plotted vs. the gate to source potential and represent the ionic current which flows between the gate and the source contact through the electrolytic solution. In the second chart, currents were plotted vs. the gate to RE potential $V_{S/RE}$, which was derived by summing the OCP measured by means of the potentiostat, and the potential of the gate with respect to source $V_{G/S}$. No significant differences were noticed between plots in figure 4.16a; on the contrary, from plots in figure 4.16b it resulted that currents were recorded in a different range of potential in those devices which have a very different ratio between the gate electrode's area and the channel's.

In a standard CV, the potentiostat imposes a linear variation with time of the WE potential vs. the RE, whilst the electrolytic cell is closed on a CE whose area is much bigger than the area of the WE. Plots in figure 4.16c show that in the device with a gate smaller than the channel ($A_G/A_{CH} \approx 0.1$), $V_{G/RE}$ varied linearly with time (effective scan rate 0.07 V/s). This result can be ascribed to the fact that, in the I_G vs. $V_{G/RE}$ measurements, the channel worked as CE and only when the channel is bigger than the gate ($A_G/A_{CH} \approx 0.1$) a minimal voltage drop at the channel/electrolyte interface is guaranteed. As a consequence, the I_G vs. $V_{G/RE}$ measurement of the device with $A_G/A_{CH} \approx 0.1$ corresponded quite exactly to a CV measurement carried out on the gate electrode during the OECTs working.

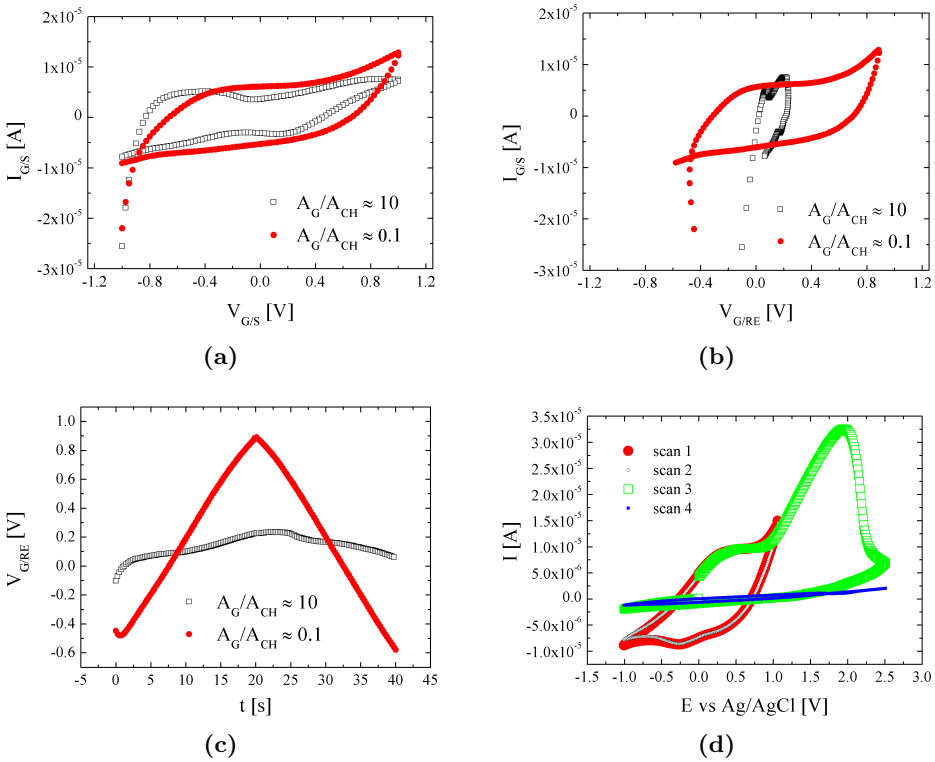

Figure 4.16: Experimental results for all made PEDOT:PSS ECTs with a ratio between the area of the gate contact and the channel roughly equal to 10 and 0.1: gate-source current vs. gate-source potential (a) and vs. gate-Ag/AgCl potential (b); gate-source potential vs. time (c); CV of an all made of PEDOT:PSS electrode (d).

This experimental result, and especially what it represents, agrees with the electrochemical characterization obtained for PEDOT:PSS electrodes which were realized with the same process used for the device fabrication. Figure 4.16d shows 4 CV cycles. In the first two cycles, the potential was varied between –1 V and +1 V vs. Ag/AgCl; up to a potential of –0.80 V, a highly reversible, capacitive response, typical of conductive polymers is observed [92]. In this potential range, the system was stable since successive cycles were performed with no observable degradation in the signal. In particular, two broad cathodic and anodic processes can be noticed in the potential range between –0.25 V and +0.35 V, which can be associated with the uptake of cations by the polymer. Since the polymer blend contained an immobilized polyanion which compensated the charge of PEDOT, electroneutrality during the charging and discharging

of PEDOT was maintained by the movement of the supporting electrolyte's cations in and out of the polymer layer (see equation 4.9). Figure 4.16b reproduces quite faithfully the trend of the first two cycles shown in figure 4.16d between –0.5 V and +1 V, which is the $V_{G/RE}$ variation range; the reason why $V_{G/RE}$ spans a smaller range than V_G is due to the fact that, in the OECT, V_G is the sum of $V_{G/RE}$ and $V_{S/RE}$. Only when the upper anodic potential was extended to +2.5 V, the response was dominated by an intense oxidation peak at a potential of about +1.8 V, which can be associated to the polymer overoxidation [93], [94]. This process is irreversible since no corresponding reduction peak was observed, and brought to the loss of the polymer conductivity as confirmed by the current drop in the fourth cycle. This behaviour was also observed in the all made of PEDOT:PSS, realized by Basiricò, with a ratio of 0.4 between the area of gate electrode and the channel. From figure 4.6d it results that for positive, relatively high voltages, the gate-source current presented a peak which, in agreement with the CV signals of figure 4.16d, can be attributed to the polymer over-oxidation. The over-oxidation effect was also confirmed by the fact that ECTs all made of PEDOT:PSS completely degraded and did not work anymore after a cycle within this extended gate voltage range. Therefore, it can be deduced that below $1.5 \div 2$ V all made of PEDOT:PSS ECTs have a capacitive behaviour, while a faradaic process due to the polymer over-oxidation, is observed for higher positive voltages.

4.5 Results - Analysis

Bernards and Malliaras [82] proposed that OECTs can be modelled as a combination of an electronic and an ionic circuit: the ionic circuit has been used to describe the transport of ionic charge through the electrolyte and was formed by the series of one capacitor and one resistor. The resistor was used to account for the resistance of the electrolyte, while the capacitance globally included the contribution of the interfaces gate/electrolyte and channel/electrolyte, combined in series. In standard OECTs, it is normally assumed that the capacitance per unit area at the interface between the electrolyte and the channel is much bigger than that one at the other interface. As a consequence, since the two capacitances are combined in series, the total capacitance is dominated by the capacitance at the gate/electrolyte interface, which determines the device behaviour. In the OECTs all made of PEDOT:PSS, as the material exposed

to the electrolyte is the same for the gate electrode and the channel, the capacitance per unit area is the same at each interface and the differences between them are only related to their areas.

Conductance measurements and optical observations confirmed that there is a faradaic electron-transfer process at both gate/electrolyte and channel/electrolyte interfaces, corresponding to the doping/de-doping of the polymer. However, the CVs demonstrated that the PEDOT:PSS/electrolyte interface behaves as a supercapacitor or pseudo-capacitor, i.e. , as an electrode which is able to accept or deliver charge from/to the electrolytic solution by means of a faradaic process, and at the same time to charge and discharge the electrical double-layer at the interface with the electrolyte. In fact, the doping/de-doping occuring at the polymer/electrolyte interface is a faradaic electron-transfer process which involves a potential-dependent change of the oxidation state, that, in turn, originates a capacitive effect. With this assumption, it results that the size of the exposed area determines whether the gate/electrolyte or the channel/electrolyte prevails in the ionic circuit contribution to the device behaviour. If the gate area is much bigger than the channel area, the global capacitance is dominated by the channel/electrolyte interface; if the channel area is bigger than the gate, the gate/electrolyte equivalent capacitance prevails. Thus, in an all-PEDOT:PSS device, it is the size of the smallest area exposed to the electrolyte to dictate the behaviour of the ionic component of the transistor, i.e. of the gate-source current. This is true in the whole voltage window in which the behaviour of the polymer is supercapacitive. When the faradaic peak occurs, a large current flows and, at the same time, the polymer is over-oxidized and irreversibly degraded. This situation is normally obtained outside of the voltage range of the transistor action. As a consequence, in the whole working range of the transistor, the device regime can be assimilated to that of a device with a capacitive gate, even if the mechanism under this effect is rather different and could be definite as *pseudocapacitive*, because the interface between the electrolyte and the polymer (at the gate side or at the channel) is a supercapacitor which can exchange ions with the solution and give rise to a non negligible variation of immobilized charge with voltage.

5

Conclusions

Organic semiconductor technology was used to realize and test two different kinds of devices for detection of chemical species in liquids.

The first device, the OCMFET, is a charge sensor based on a OTFT structure. Its sensing area is physically separated from the OFET and as a consequence the sensing mechanism does not depend on the active layer. Two different implementations of the OCMFET, one working in the range of tens of Volts (HV) and the other in the range of Volts (LV) were realized. Positive results were obtained with both the HV and LV sensors. Nevertheless, the LV OCMFETs resulted particularly suitable for the detection of chemical species in liquids. In fact, as they can be operated at very low voltages, they allow to obtain more stable and reliable results than the HV OCMFETs. The experimental results also demonstrated that the OCMFET performances improve when structures with reduced parasitic capacitances are used. As a consequence, it can be assumed that best performances could be obtained by realizing LV OCMFETs with self aligned contacts. OCMFETs were tested as pH and DNA sensors. Concerning pH detection, alkanethiolated SAMs and tantalum oxide were used as receptors. Tantalum oxide resulted more stable and as a consequence provided better results than SAMs. Aiming at using organic molecules as receptor, other processes, such as electrochemical techniques, should be considered in order to form stable covalent bonds between the molecules of interest and the atoms of the probe area. It is noticeably that the results obtained with the devices presented in this work are, in terms of sensitivity and selectivity, the world record for the organic technology and have shown the same behaviour of a recently explored silicon-based device. This result is particularly promising be-

cause it demonstrates that organic technology may successfully compete with silicon technology not only for costs and simplicity of the fabrication procedures, but also in terms of performances. Concerning DNA recognition further investigations could be carried out in order to study the OCMFET response with respect to the length of the DNA molecule, the ionic strength of the solution used for the measurements etc.

The second device is an OECT entirely made of PEDOT:PSS realized by ink-jet printing. The experimental activity allowed to elucidate that in the working regime of the transistor, the ECT all made of PEDOT:PSS can be assimilated to ECTs with a capacitive gate. Knowing their operative regime, the ECT all made of PEDOT:PSS can be used to obtain all printed PEDOT:PSS sensors.

In conclusion, the experimental activity allowed to obtain two different kinds of devices both suitable for detecting chemical species in liquids as both can be operated at low voltage. They were realized by using low-cost techniques and can be considered portable and disposable devices easily integrable in lab-on-chip micro-systems.

Appendix A

Organic semiconductors and OTFTs - Overview

In general, electronic devices manufacturing entails several functional materials such as conductors, insulators and semiconductors. In particular, semiconductors are the active layer that allows the transistors' action. In this appendix an overview of organic materials, with special care to organic semiconductors and their electrical properties, is presented. Moreover, the working principle and an analytical model of organic semiconductors based on thin film transistors are described.

A.1 Organic chemistry - Basics

Organic semiconductors are mainly made of carbon atoms, hydrogen and oxygen. Carbon is the first element in the fourth column of the periodic table, therefore, according to the Aufbau and Pauli exclusion principle, its most stable electronic configuration is $1s^2 2s^2 2p^2$. This configuration does not account for the specific bonding of many molecules which contains carbon atoms [95].

Covalent bonding in molecules is generally described by means of the *molecular orbital* (MO) model. According to to this model, electrons occupy molecular orbitals (MOs), which, in the simplest approximate method, are calculated as a combination of atomic orbitals (*linear combination of atomic orbitals* LCAO-MO). In case of the H_2 molecule, two MOs with rotational symmetry around the internuclear axis (σ *symmetry*) are predicted: a bonding orbital σ obtained by the sum of the two atomic orbitals,

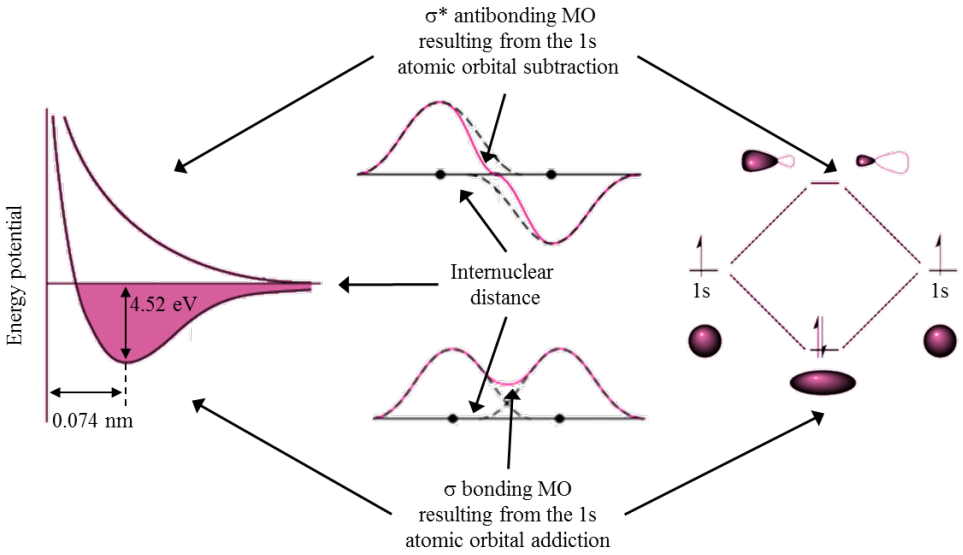

Figure A.1: Potential energy vs. distances of the bonding (σ) and antibonding (σ^*) molecular orbital for the H_2 molecule.

and an anti-bonding orbital σ^* obtained by their subtraction (see figure A.1). These molecular bondings have a different electronic distribution. In σ bonds the atomic orbitals' overlap is maximum and the electron density is mostly concentrated along the internuclear axis. The antibonding orbital has a nodal surface between the two atoms, meaning that the probability of finding electrons between the nuclei is minimum. The electrons in the σ^* orbital do not contribute to stabilize the molecule, therefore, the antibonding molecular orbital has a higher energy than the bonding molecular orbital. Because stable covalent bonds are formed when the electrons fill the molecular orbitals following the increasing energy, in the ground state the σ orbital is filled with two opposite spin electrons, while no electrons are in the σ^* orbital.

In the MO model, the number of molecular orbitals and of the atomic orbitals, which are combined to produce them, are identical. Moreover, covalent bonding requires the overlap of two half-filled orbitals. The electronic configuration of the carbon atom provides only two half-filled orbitals, therefore, this model can not explain the existence of the molecules such as methane (CH_4). In 1930 Linus Pauling explained the possible carbon-bonding by assuming that one electron is "promoted" from the $2s$ orbital to the vacant $2p$ orbital and that the $2p$ orbitals form chemical bonds with different geometries. The $2s$ and the $2p$ orbitals mix together, i.e. *hybridize*, forming the following geometries:

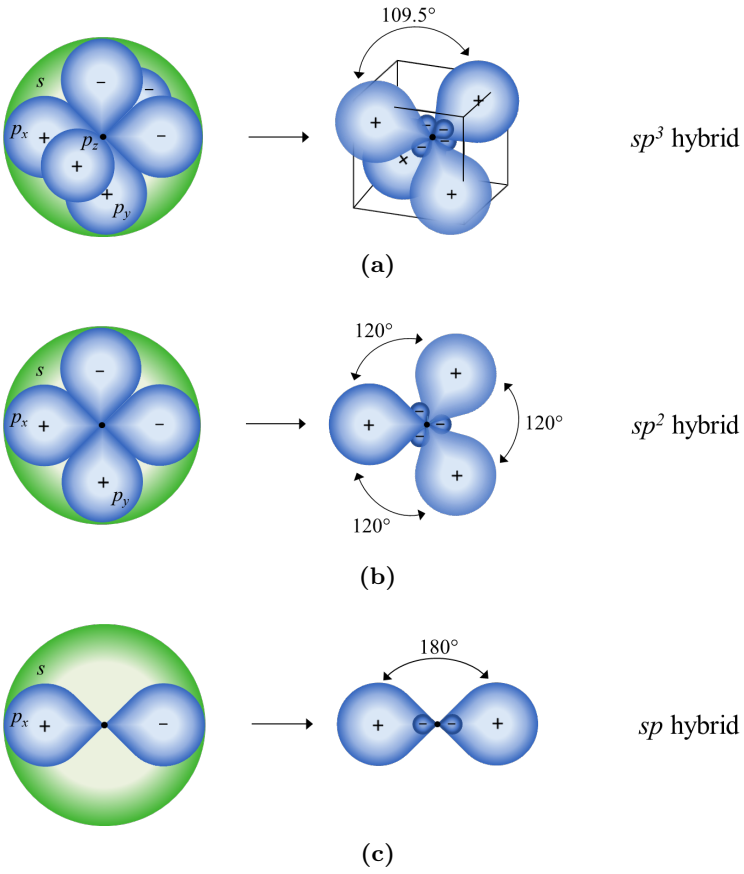

Figure A.2: Atomic orbitals combination and probability distribution in sp^3, sp^3 and sp^3 hybrid orbitals.

sp^3, sp^2 and sp.

In the sp^3 configuration the four valence orbitals of the carbon atom ($2s, 2p_x, 2p_y$ and $2p_z$) combine to give four half-filled orbitals of equal energy (see figure A.2a). The electron density on one side of the nucleus is greater than on the other, therefore, each hybrid orbital has two lobes of different size. These hybridized orbitals have a tetrahedral arrangement and an sp^3 hybridized carbon generally forms σ bonds along the internuclear axis.

Three equivalent hybrid orbitals are generated by mixing the carbon $2s$ orbital with two of the $2p$ orbitals in the sp^2 geometry (see figure A.2b). The remaining $2p$ orbital is left unhybridized. The hybrid orbitals form a trigonal planar structure and are involved in σ bonds. The two half-filled $2p$ unhybridized orbitals are perpendicular to the plane

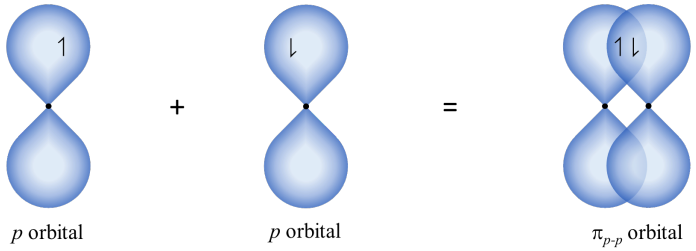

Figure A.3: Covalent bond formed along the internuclear axis trough the overlapping of two p atomic orbitals π_{p-p}.

of the sp^2 hybrid orbitals. By means of a side-by-side overlapping they give rise to a *pi* bonding (π) (see figure A.3), which can be considered as a standing wave with a single node in the plane of the molecule. π bonds are weaker than σ bonds as they result from parallel orbital overlap: the two combined orbitals meet lengthwise and create more diffuse bonds than the σ bonds. As a consequence, the electrons involved in π bonds, referred to as π *electrons*, are delocalized and can move across the molecule with a special freedom degree. Molecular fragments joined by a π bond can not rotate around that bond without breaking it, as the rotation would involve the destruction of the parallel orientation of the constituent p orbitals. Combinations of a σ bond and a π bond are possible and give rise to the formation of double bonds, which are in general both stronger and shorter than single bonds.

Finally, in sp hybridization (see figure A.2c), the carbon $2s$ orbital and one of the $2p$ orbitals combine to generate a pair of two equivalent sp hybrid orbitals. The hybridized orbitals share a common axis and have their major lobes oriented at an angle of 180° to each other. The others two original $2p$ orbitals remain unhybridized keeping their axis perpendicular to each other and to the common axis of the pair of sp hybrid orbitals. They are available to form π bonding.

A.2 Charge transport in organic semiconductors

Organic materials are carbon-rich compounds generally classified into three categories: *small molecules*, *polymers* and *biological materials* [6]. Small molecules have a well-defined molecular weight, while polymers are macromolecules consisting of repeating structural units, which are usually connected by covalent chemical bonds forming a chain.

The electronic properties of the organic molecules depend on the specific characteristics of the individual molecules, such as bonding, chain length and nature of substituents, but also on the processing conditions that determine the structural order of the molecules in the film.

Molecules made of sp^3 hybridized carbon atoms have backbones mainly consisting of σ bonds. The energy band gap E_g between the bonding and the antibonding orbital is quite large, therefore these materials are electrically insulating. Molecules which present an alternating of single and double bonds between the carbon atoms, named conjugated molecules, have chains containing adjacent unsaturated carbon atoms, sp^2 or sp hybridized, which form additional π bonds with the remaining unhybridized valence electrons. Because the π bondings in their chain reduce the electronic band gap between the highest occupied binding orbital (HOMO) and the lowest unoccupied antibinding orbital (LUMO) in the range between 1.5 and 3 eV, these molecules usually show semiconducting properties.

As previously mentioned, the electronic properties of the organic compounds also depend on the morphological characteristics which are developed during the deposition process. Pentacene, which is a polycyclic benzenoid aromatic hydrocarbon molecule ($C_{22}H_{14}$) consisting of five linearly fused benzene rings (see figure A.5a), shows insulating or semiconducting properties depending on the specific morphology obtained during its deposition. In fact, an amorphous and practically insulating film is obtained

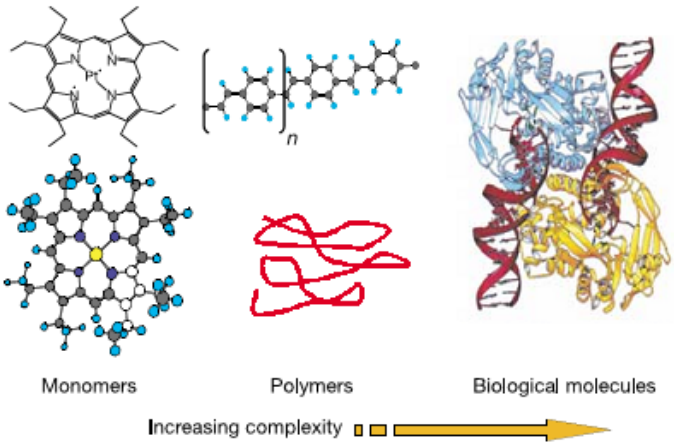

Figure A.4: Various types of organic electronic materials ranged in order of increasing complexity from left to right [6].

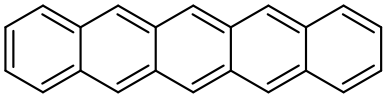

(a)

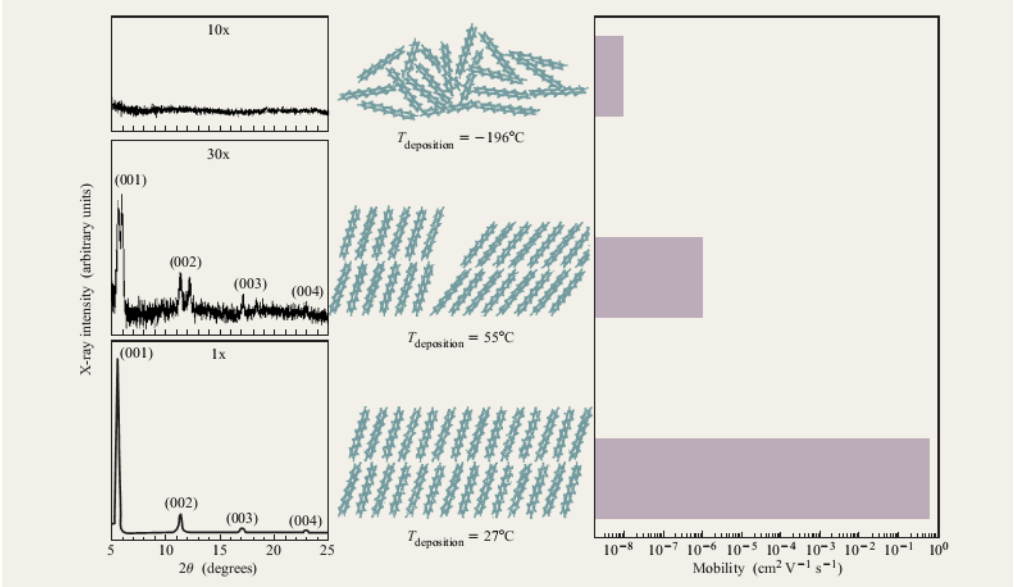

(b)

Figure A.5: Molecular structure of pentacene (a) and experimental results obtained for three different phases of thin-film pentacene (b) [96].

by keeping the substrate temperature low during the layer growth; on the contrary, a well-ordered film with semiconducting properties is achieved when operating at room temperature [96]. Figure A.5b shows the experimental results related to the structural order for a pentacene layer obtained at three different deposition temperatures and the related mobility μ, which is the parameter that describes how easily charge carriers can move within the layer under the influence of an electric field. Therefore, under specific conditions, highly ordered films can be grown with chain-like or rod-like molecules that, having one molecular axis much longer than the other, can develop large π-conjugation length along the longer axis and close molecular packing. When a large number of stacked molecules interacts, the delocalization increases and, as a consequence, the gap between the HOMO and the LUMO becomes smaller.

Because the electrical properties of solids based on organic compounds depend on both the material and the film structure, several models have been developed in order

to explain how charge transport occurs. The experimental results suggest that, in highly ordered materials, charge transport occurs by a band-like motion. Nevertheless, in both polymers and small molecules, charge transport is ruled by the formation of an excitonic state, which is a molecular excited state that, until it recombines, can hop along the polymer backbone, and also from chain to chain in polymers [6]. The excited electron-hole pair localized on the same molecule (Frenkel exciton) is tightly bound ($\sim$ 1 eV binding energy) and is the most dominant species; nevertheless, in highly ordered molecular crystals more weakly bound charge-transfer (CT) excitons over different molecules (Wannier exciton) are formed as well [6], [97].

In a solid based on organic compounds, charge transporting elements, named sites, can either be molecules or segments of a main chain that are separated by topological defects (see figure A.6). The elementary transport consists in the transfer of a charge carrier among adjacent transporting sites and requires a concomitant-activated transfer of deformation [98]. Its activation energy is the the sum of an inter-molecular and an intra-molecular contribution. The former arises from statistical variations due to some local disorder: the energy of two chemically identical hopping sites of a molecule can be made physically non-equivalent because of the lattice contribution. The latter is due to a redox reaction process: the molecular conformation can be changed upon removal or addition of an electron from/to the transport molecules. Because the optical spectra of molecular solids are controlled by excitonic transitions, there is no direct and easy way to measure the inter-molecular and intra-molecular contributions to the transfer activation energy. Therefore, it is assumed that the hole/electron energy in a site has a

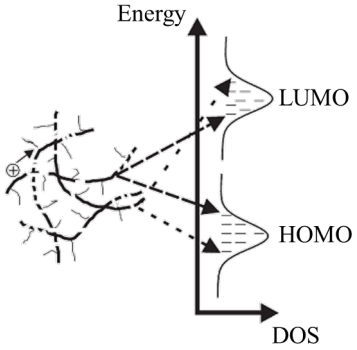

Figure A.6: Schematic view of a disorder organic solid and Gaussian distribution for the localized states.

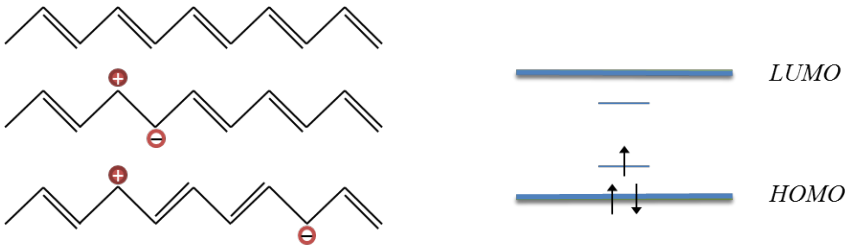

Figure A.7: Schematic view of a polaron in a polymer chain (a) and corresponding energy diagram (b).

distribution of localized energies, usually shaped as a Gaussian (see figure A.6), because the excitonic absorption band has a Gaussian profile, and because the polarization energy is determined by a large number of internal coordinates, each varying randomly by small amounts.

When a charge is formed or injected in a conjugated chain, it deforms the chain [5]. The charge with its accompanying self-consistent polarization field is named *polaron* and can be treated as a quasi-particle with its peculiar characteristics such as effective mass and total momentum energy (see figure A.7a). The polaron produces some atom displacement, which reduces its energy giving rise to a potential well formation; the charge is in a tied state and is self-trapped by the deformation it has induced. Therefore, in terms of energy diagrams, this local distortion can be described as a localized state in the energy gap between the HOMO and the LUMO (see figure A.7b).

The *variable range hopping* (VRH) model [99] provides a good theory for charge transport in disordered solids such as polymers. According to this model, the charge transport is thermally activated by tunneling of carriers between localized states. A carrier may either hop over a small distance with a high activation energy, or hop over a long distance with a low activation energy. Hopping between two sites depends on the overlap of the site's electronic wave function and is phonon assisted, i. e., the difference in energy between the sites is accommodated by the absorption or emission of a phonon.

Upon the application of an electrical field , highly ordered molecular solids have charge mobility close to the limit of 1 $cm^2/(Vs)$, which is almost temperature independent at low temperatures in single-crystals [100]. These experimental proofs are usual in solids where charge transport occurs in delocalized states and is limited by

phonon scattering. As a consequence, it is believed that in organic based solids, within specific conditions, the charge localization-delocalization boundary can be approached and charge transport occurs in a band-like motion. The *multiple trapping and release* (MTR) model, developed by Horowitz *et al.* [101], provide a theory to explain the conductivity properties of these structured materials. In this model it is assumed that a high concentration of localized levels forms a narrow delocalized band and that lattice defects or impurities give rise to levels near the band. Crystal grains and the grain boundaries are characterized by different conducting properties. By assuming that traps are mainly localized at grain boundaries, because grains and grain boundaries are connected in series, the effective mobility of the medium is given by the harmonic mean of the mobility in each region (see equation A.1)

$$\frac{1}{\mu} = \frac{1}{\mu_g} + \frac{1}{\mu_b}. \tag{A.1}$$

When grains are large enough, charge transfer from one grain to the next can occur via tunneling, leading to a temperature-independent mobility; the charge carriers trapped in these localized level are released through a thermally activated process only at high temperature.

A.3 TFT - Working principle

A field-effect transistor (FET) is a three electrodes device which basically operates as a current source modulated by the gate voltage. One plate is a conducting channel between two ohmic contacts, namely source and drain electrodes; the conductivity of this channel is modulated by the capacitor's second plate, the gate, which is the third electrode of the device. In 1987 Koezuka [102] reported a field-effect transistor on a structure based on an electrochemically polymerized polythiophene. From then on, several structures to realize TFT using organic semiconductor technology were investigated; among these, the thin-film structure was proven especially suitable to be used with low conductivity materials [103].

The OTFT architecture consists of a thin organic semiconducting layer, two ohmic contacts, which act as source and drain, and a gate contact which is separated from the semiconductor film by an insulating layer. They can be fabricated with several

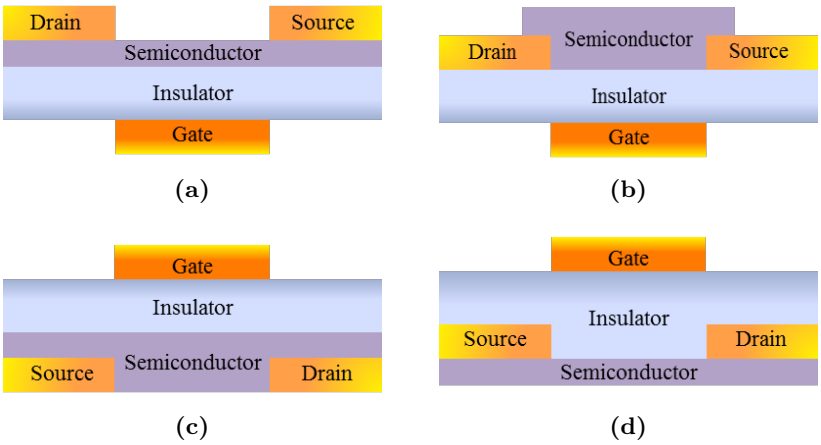

Figure A.8: OTFT sections of bottom gate with top (a) and bottom-contact (b), and to gate with bottom-contact (c) and top-contact (b.)

configurations, which are named according to the position of the electrodes; in particular the source and drain contacts position is related to the organic layer. Figure A.8 shows all the possible geometries: bottom gate with top-contact (a) and bottom-contact (b), which are the most commonly used, and top gate with bottom-contact (c) and top-contact (d).

Usually organic semiconductors are intrinsically undoped, therefore there are no free charge carries available for conduction. In order to develop semiconducting or metallic properties polymers need to be doped [97]. A doping effect can be achieved by several ways, such as:

- charge transfer from a donor (n-type) or acceptor (p-type) dopant,
- unipolar injection of charges by an electrode,
- electric field effect through an organic, metal-insulator-semiconductor (MIS) or semiconductor structure,
- photogeneration of electronhole pairs under the influence of light excitation,
- bipolar injection of opposed charges (electrons from cathode and holes from anode) forming quasi-particles,
- doping/de-doping using acidbase equilibria (polyaniline) in a process yielding metallic.

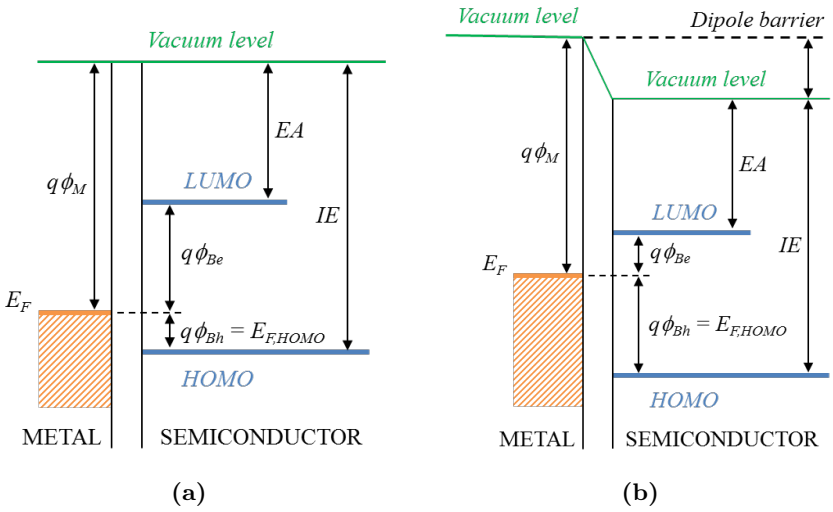

Figure A.9: Energy diagram of a metal-organic semiconductor interface without (a) and with (b) a dipole barrier. ϕ_e and ϕ_h are the electron and the hole barriers respectively.

In OTFTs the current flowing is assured by the direct injection of charges into the the source and drain electrodes. The charge injection strongly depends on the matching between the Fermi level of the metal electrodes and HOMO and LUMO of the organic semiconductor. In the first models it was assumed that the vacuum levels of the molecular orbitals at the metal-semiconductor interface were aligned according to the Schottky-Mott model which was developed for the inorganic semiconductors [104]. The hole injection barrier (ϕ_h) was defined through the difference between the ionization energy of the semiconductor (IE) and the metal work function (ϕ_M); the electron injection barrier (ϕ_e) was defined trough the difference between the electrode work function (ϕ_M) and the organic electron affinity (EA) (see figure A.9) [105]. Afterwards, further studies demonstrated that when atoms and molecules are adsorbed or deposited on the metal surface, there is a breakdown of the vacuum levels alignment [106]. The shift of the metal work function entails the change of the hole and electron injection barriers and, as a consequence, it establishes the type of charge carriers in the organic semiconductor.

In a device with the Fermi level of the source and drain metal close to the HOMO of the semiconductor, holes can be injected/extracted [107]. When the gate is positively biased with respect to the source (see figure A.10a), holes are attracted in the channel

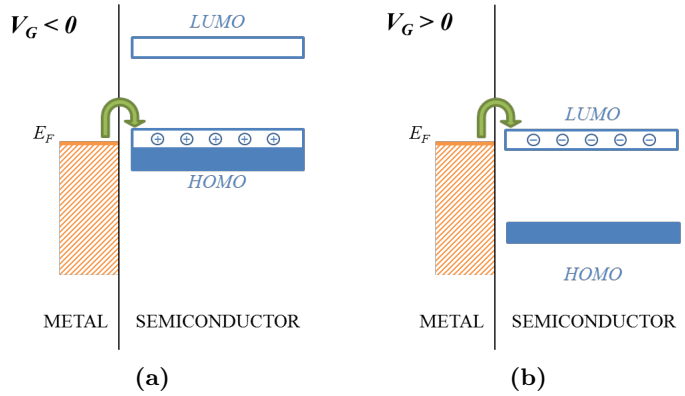

Figure A.10: Charge injection with respect to the applied voltage in a p-type semiconductor (a) and in a n-type semiconductor (b).

within few angstroms from the insulator-semiconductor interface and can be driven from source to drain by applying a negative voltage between drain and the source. On the contrary, when the gate voltage is reversed, electrons are induced in the channel. As the Fermi level of the metal is far from the LUMO of the semiconductor, the electron injection/extraction is very unlikely, therefore, no current flows through the semiconductor except for leaks through the insulating layer. In this case, the organic material is named *p-type* as holes are the majority charge carriers, and the device is named *p-channel* as it is activated upon the application of a negative gate potential. OTFT with the Fermi level of the source and drain metal close to the LUMO of the semiconductor has a symmetrical behaviour. As electrons can be extracted from the source and drain contacts, the current flows when negative charges are induced in the channel, that is, when the gate is positively biased (see figure A.10b). In this case the semiconductor is called *n-type*, because electrons are the majority carriers, and the device is named *n-channel*.

Figure A.11 shows a comparison between the metal work function of some standard metals, and the HOMO and the LUMO of some organic materials. In particular, it reports that gold has a low hole injection barrier with the most common organic semiconductors such as pentacene. In fact, gold is usually used to realize p-type organic transistors.

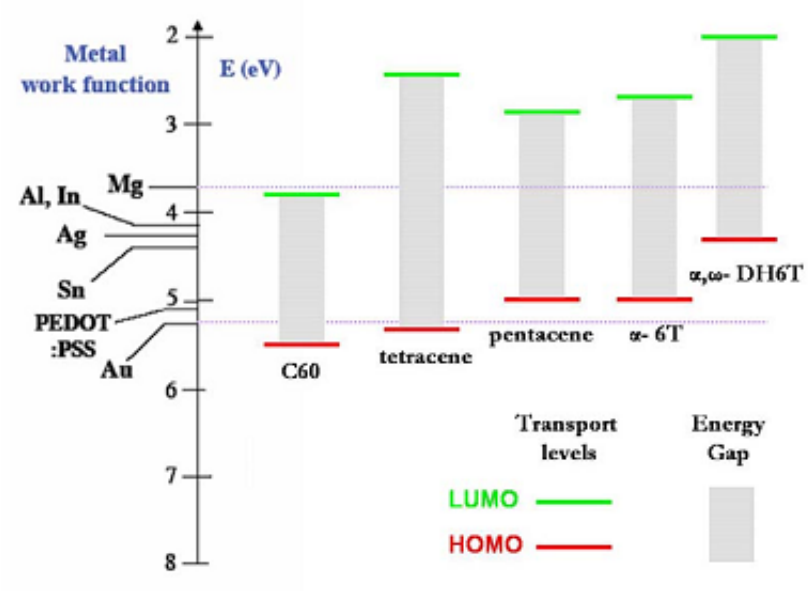

Figure A.11: Comparison between the metal work functions of some standard metals and the HOMO and the LUMO of some organic materials [105].

A.4 OTFT - Analytical model

Compared to inorganic devices, OTFTs present two important differences. First, the source and drain electrodes form ohmic contacts with the conducting channel. Second, it works in the *accumulation* regime [5]. Despite these differences, in first approximation, the characteristic equations of the OTFT can can be derived by applying the same approach that is used to describe the metal-oxide-semiconductor FET (MOSFET) operation [104].

Figure A.12 reports the schematic view of an OTFT and its fundamental parameters: the channel length L and the channel width W. As shown in the picture, the source contact is assumed as connected to the ground. The current-voltage characteristics are calculated in the gradual channel or Shockley approximation, that is, the electric charge density related to a variation of the electric field along the channel is considered much smaller than that related to a variation across the channel. This condition is generally fulfilled when the channel length L is much larger than the insulator thickness d_i. Moreover, the charge mobility μ in the channel is assumed to be constant. Within these approximations, the elemental resistance dR of an elemental segment dx

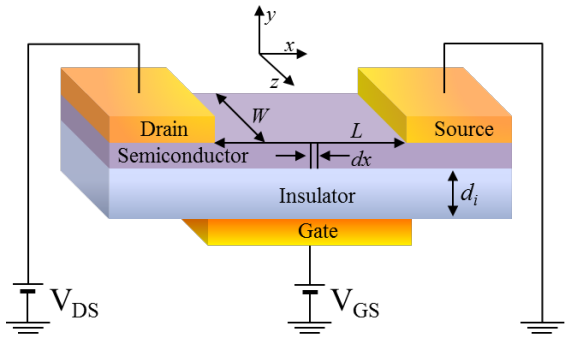

Figure A.12: Perspective view of an OTFT.

of the conducting channel is

$$dR = \frac{dx}{W\mu|Q(x)|}, \tag{A.2}$$

where $|Q(x)|$ is the surface charge at x and includes the bulk charge Q_0 and the superficial charge Q_S. Q_0 is a constant and is related to the semiconductor charge carriers at the equilibrium, while Q_S varies along the channel and can be expressed as

$$Q_S = -C_i \left[V_G - V_{FB} - V_S(x) - V(x)\right]. \tag{A.3}$$

In equation A.3 C_i is the insulator capacitance per unit area and V_G is the gate potential. V_{FB} is the so called flat-band potential and it is introduced to account for any difference between the semiconductor and the gate contact work-function. $V_S(x)$ is the ohmic drop through the semiconductor; its contribution can generally be neglected for gate voltages higher than few voltages as most of this ohmic drop occurs trough the insulator. Finally, $V(x)$ accounts for the drain bias. In the gradual channel approximation $|\partial F_x/\partial x| \lll |\partial F_y/\partial y|$, where F is the electric field, and x and y the directions parallel and perpendicular to the insulator-semiconductor interface, respectively (see figure A.12); therefore $V(x)$ only depends on the drain voltage and gradually increases from 0, at the source contact, to V_D, at the drain contact. As OTFTs work in accumulation mode, Q_0 and Q_S have identical sign. The drain current does not depend on x, therefore the drop voltage through the elemental segment dx is

$$dV = I_D dR = \frac{I_D dx}{W\mu|Q(x)|}, \tag{A.4}$$

By integrating equation A.4 from source ($x = 0$, $V = 0$) to drain ($x = L$, $V = V_D$) results the following expression for the drain current may be derived:

$$I_D = \frac{W}{L}\mu C_i \left[(V_G - V_{TH})\, V_D - \frac{V_D^2}{2} \right]. \tag{A.5}$$

The term V_{TH} in equation A.5 is the gate voltage for which the channel conductance, at low drain voltages, is equal to that of the whole semiconducting layer. It is a threshold voltage that, under assumptions that all doping centres are ionized, can be expressed as

$$V_{TH} = \pm \frac{qNd_s}{C_i} + V_{FB}, \tag{A.6}$$

where N is the density of doping centres, donors or acceptors, depending on whether the semiconductor is n-type or p-type, and d_s is the semiconductor thickness.

For small drain-source bias, equation A.5 can be approximated by

$$I_D \approx \frac{W}{L}\mu C_i \,(V_G - V_{TH})\, V_D. \tag{A.7}$$

In this regime, the channel conductance g_d and trasconductance g_m are given by:

$$g_d = \left| \frac{\partial I_D}{\partial V_D} \right|_{V_G \equiv cost} = \frac{W}{L}\mu C_i \,(V_G - V_{TH}) \tag{A.8}$$

$$g_m = \left| \frac{\partial I_D}{\partial V_G} \right|_{V_D \equiv cost} = \frac{W}{L}\mu C_i V_D. \tag{A.9}$$

Assuming that V_{TH} is small, when the drain voltage becomes comparable to the gate voltage, the channel is pinched off at the drain contact, thus, I_D ceases to increase and the transistor enters the saturation regime. Within this approximation equation A.5 reduces to

$$I_{D,sat} = \frac{W}{2L}\mu C_i \,(V_G - V_{TH})^2 \qquad \text{for} \qquad V_D \geqslant (V_G - V_{TH}). \tag{A.10}$$

In this regime g_d is

$$g_m = \left| \frac{\partial I_{D,sat}}{\partial V_G} \right| = \frac{W}{L}\mu C_i \,(V_G - V_{TH}) \tag{A.11}$$

while the $g_d = 0$.

A.5 OTFT - Parameters

In order to electrically characterize devices, the drain current with respect to the drain potential (output characteristic) and to the gate potential (transfer characteristic) are detected. The model described in A.4 involves only two parameters, the charge mobility μ and the threshold voltage V_{TH}, which can be easily extracted by fitting the the square root of the drain current measured versus the gate potential. As the square root of equation A.10

$$\sqrt{I_{D,sat}} = \sqrt{\frac{1}{2}\mu C_i \frac{W}{L}}\,(V_G - V_{TH})\,. \tag{A.12}$$

linearly varies with the gate potential, considering it in the straight-line form $y = mx+q$ with

$$y = \sqrt{I_{D,sat}} \qquad x = V_{GS} \qquad m = \sqrt{\frac{1}{2}\mu C_i \frac{W}{L}} \qquad q = -\sqrt{\frac{1}{2}\mu C_i \frac{W}{L} V_{TH}},$$

m and q can be obtained by fitting the experimental curve corresponding to equation A.12. As a consequence, μ and V_{TH} can be extracted through the following expressions:

$$V_{TH} = -\frac{q}{m} \qquad \mu = \frac{m^2}{\frac{1}{2}C_i\frac{W}{L}}. \tag{A.13}$$

The validity of the extracted values is restricted within the limits of the taken approximations, that in organic devices are not always fulfilled. In particular, mobility has been proven to be voltage dependent [108]. Under a specific gate potential, the Fermi level at the insulator-semiconductor interface moves towards the band edge, where most of the traps that limit charge transport are localized. When the gate biasing starts, traps start to fill until trapping becomes less efficient, thus causing a consequent increase in the charge mobility. Moreover, as charges are moved along the channel by means of the voltage drop between source and drain, the mobility changes along the channel as well. An accurate evaluation of the charge mobility that considers the effect of the electric transversal field is usually obtained by using the following semi-empirical power law

$$\mu = \kappa\,(V_G - V_{TH})^{\gamma} \tag{A.14}$$

where κ and α are two empirical parameters [99], [108]. On the other hand, the dependence of mobility on the drain voltage can be considered very small when the measurements are carried out under the lowest possible value of the drain potential.

Appendix B

Electrochemical techniques

Electrochemistry is a branch of chemistry concerning with the interrelation of electrical and chemical effects, which deals with the study of chemical changes caused by the passage of an electric current and the production of electrical energy by chemical reactions. It is widely used to study the chemical reactions which take place in a solution at the interface between an electrode and an ionic conductor. In the following subsections a brief introduction on the fundamentals of electrochemistry is reported.

B.1 Electrode processes and electrochemical cells

Electrochemistry involves chemical phenomena associated with charge transport across the interface of an electrode, conductor or semiconductor, and an electrolyte. It is not possible to experimentally deal with events occurring at a single interface, but only to study the properties of collections of interfaces which are called *electrochemical cells*, i.e., systems formed by two electrodes separated by at least one electrolyte phase.

The chemical processes occurring in a cell can be represented by means of two independent half-reactions. Each half reaction describes the chemical reaction occurring at one of two electrodes and is related to the interfacial potential difference at the corresponding electrode. Usually, only one of these reactions is under investigation, and the electrode at which it occurs is called *working electrode*, while the other electrode is used as *reference electrode*. Electrode made up of phases having essentially a constant composition and a fixed potential are often used as reference, as this choice allows to

control the energy of the electrons within the working electrode through the potential of the working electrode with respect to the reference.

When electrode reactions take place, two types of processes occur at electrodes.

One kind of processes includes charge transfer across the electrode-solution interface. For example, a flow of electrons from electrode to solution may be obtained by driving an electrode to more negative potentials: if their energy is increased enough, the electrons transfer into vacant electronic states on species in the electrolyte giving rise to a *reduction current* (see figure B.1a). Likewise, by imposing a more positive potential, the energy of the electrons can be lowered; the electrons will transfer in the electrolyte if there is a more favorable energy on the electrode and generate an *oxidation current* (see figure B.1b). These reactions are governed by Faraday's law: the amount of chemical reaction caused by the flow of current is proportional to the amount of electricity passed. As a consequence, these reactions are called *faradaic processes* and the electrodes at where the faradaic processes occur are called charge-transfer electrodes.

Some electrode-solution systems can possibly show, under some conditions, a range of potentials where charge-transfer reactions does not occur because they are thermodynamically or kinetically unfavorable. At these interfaces, *nonfaradaic processes* can occur, such as adsorption and desorption, which alter the structure of the electrode-solution interface with changing potential or solution composition. In nonfaradiac processes, there is not a charge transfer across the interface; a flow of transient external currents may be obtained by changing the potential, the electrode area, or the solution composition.

An electrode where no charge transfer occurs across its interface with the electrolyte for any value of potential applied by an outside source is called an *ideal polarized* or *ideal polarizable* electrode (IPE) (see figure B.1c). Real electrodes which can be considered as IPEs over the whole potential range available in a solution do not exit; however, there are some electrode-solution systems that behave as IPEs over limited potential ranges. These systems are usually modelled as a capacitor because charges can not flow across the IPE by applying a different potential across the electrode-solution interface. A surface charge will be produced on the electrode surface, while an excess of cations o anions, depending on the sign of the electrode charge, will approach the electrode surface; all the charges and the oriented dipoles which move in the proximity of the electrode-solution interface form the so called emphelectrical double layer, even if it

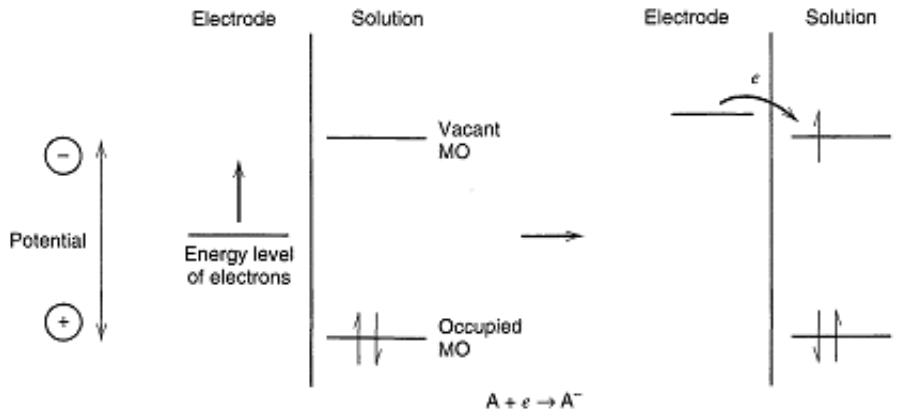

(a)

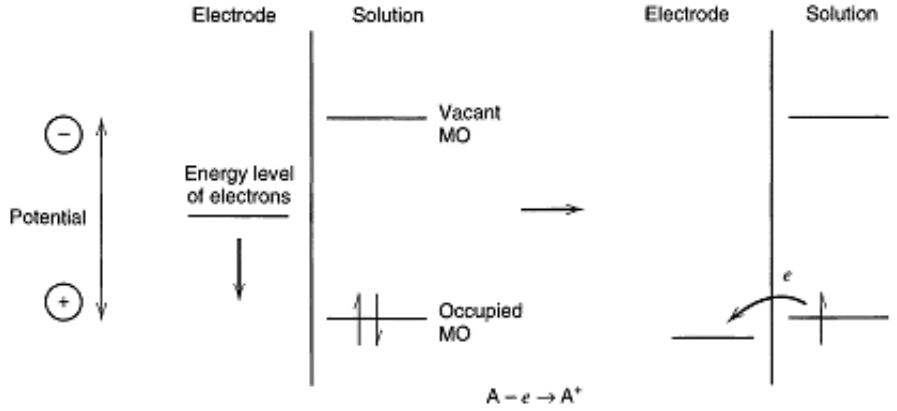

(b)

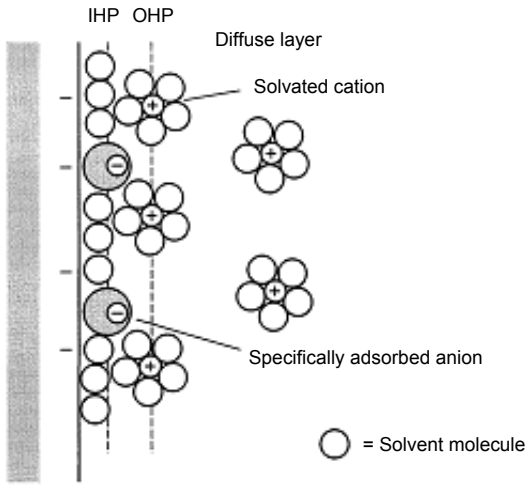

(c)

Figure B.1: Representation of a reduction (a) and oxidation (b) process of a species, A, in solution; double-layer region with anions specifically adsorbed (c) [89].

is thought to be made up of several layers. The inner layer closest to the electrode, also called the compact Helmholtz or Stern layer (IHP), contains solvent molecules and sometimes other species (ions or molecules) that are said to be specifically adsorbed. Solvated ions can approach the metal only to a certain distance and the locus of their centres is called the outer Helmholtz plane (OHP). As long-range electrostatic forces are involved in the interaction between solvated ions with the charged metal, their interaction is essentially independent of the chemical properties of the ions, which are said to be non specifically adsorbed. The thermal agitation in the solution entails that the non specifically adsorbed ions distribute in a three dimensional region, called the diffuse layer, which extends from the OHP in the bulk of the solution.

Electrochemical cells are systems formed by two electrodes immersed in an electrolytic solution. If faradaic currents spontaneously flow by a conductor which is used to externally connect the electrodes, the cell is named *galvanic*. A cell where reactions at the electrode occur by applying an external voltage greater than the open-circuit potential of the cell are called *electrolytic*.

An experimental cell must includes the electrode system of interest (working electrode) and an electrode of known potential that approaches ideal nonpolarizability (reference electrode). Figure B.2a shows the scheme of an electrochemical cell composed by a working electrode and a reference electrode, which is named *two-electrode cell*. This systems allows to determine the current flowing in the working electrode only if the passage of current does not affect the potential of the reference electrode. When

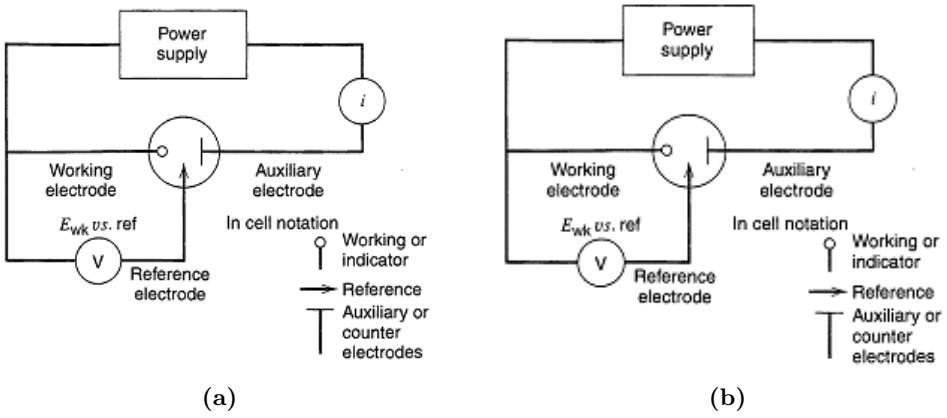

Figure B.2: Scheme of an electrochemical cell with two (a) and three-electrodes (b) [89].

using highly resistive solutions, an arrangements with three electrodes is preferable. In a *three-electrode cell* (see figure B.2b), the current is passed between the working electrode and a counter electrode, while the potential of the working electrode is monitored relative to a separate reference electrode, through a device with a high input impedance.

B.2 Electrochemical methods

Based on the Faraday's law, electrochemistry allows performing the quantitative and qualitative chemical analysis of various substances and media. In the following subsections, a brief description of the electrochemical methods which where used in this work is reported.

B.2.1 Cyclic Voltammetry

Voltammetry is one of the techniques which are commonly used to investigate electrochemical processes in an electrochemical cell. Among all the voltammetry techniques, Cyclic Voltammetry (CV) is most widely used and it allows to obtain informations on the thermodynamics of redox processes, on the kinetic of heterogeneous electron-transfer reactions, on chemical reactions and adsorptions processes [109]. In a CV, a potential is applied to the working electrode and the resulting current is monitored. The potential is ramped linearly versus time, starting from a value where no electrode reaction occurs and moving to potentials where reduction or oxidation of a the material being studied occurs (see figure B.3a). When the set potential is reached, the direction of the working electrode's potential is inverted. Depending on the investigation, the inversion can be repeated multiple times during a single experiment. The plot of the current at the working electrode versus the applied voltage is called *cyclic voltammogram*. Figure B.3b shows the typical voltammogram of a reversible redox couple during a single potential cycle. It is assumed that a negative-going potential is applied during the first half-cycle and that at the beginning only the oxidized form O is present. As the voltage is swept further from its initial value, the reduction of reactants occur; during the reverse scan, the reduced molecules R which where generated in the forward half cycle are re-oxidized. Both the cathodic and the anodic current reflect the change of the concentration gradient of the reactants with the time, in proximity of the electrode

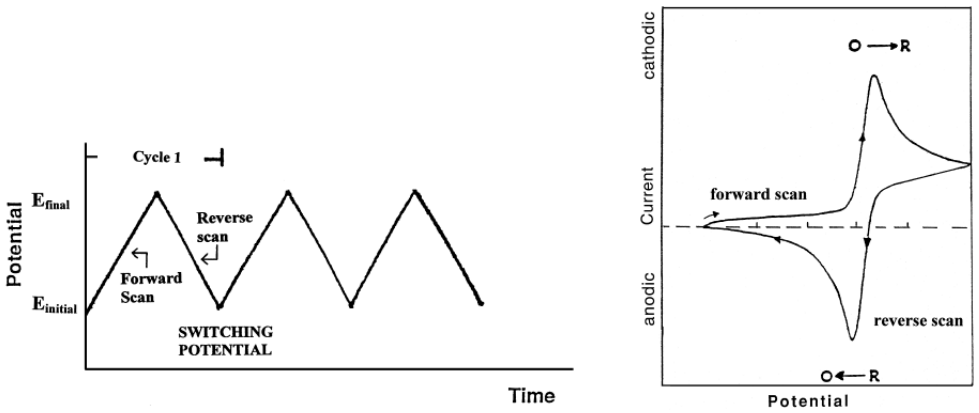

Figure B.3: Cyclic potential sweep (a) and resulting cyclic voltammogram (b) [109].

surface. As a consequence, in a ideal reversible system, the cathodic current increases up to reaching a peak and then decreases, and a symmetric behaviour results for the anodic current.

B.2.2 Chronocoulometry

Chronocoulometry is an electrochemical technique frequently used to measure the electrode surface areas, diffusion coefficients, adsorption of electroactive species, and the mechanisms and rate constants for chemical reactions coupled to electron transfer reactions. It involves the measurement of the charge vs. time response to an applied potential step waveform.

The potential of working electrode, which is initially set at a potential value where no current flows, is then set to a value which lead to oxidation or reduction of some species in solution and is held at this potential for a user-defined time period. During a measurement where a faradaic process occurs, the total charge includes the amount of charge which is needed to charge the electrical double layer Q_{dl}, the charge of adsorbed species Q_{ads} and of diffusing species Q_{ads} [110].

$$Q_{total} = Q_{dl} + Q_{ads} + Q_{diff} \tag{B.1}$$

The charging of the double layer and the charge passage due to adsorbed material take place almost instantaneously; as a consequence, Q_{dl} and Q_{ads} can be considered

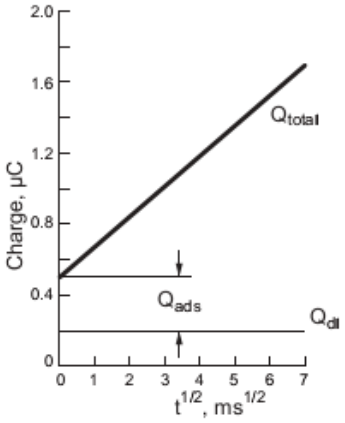

Figure B.4: Plot of charge vs. time after a chronocoulometry [110].

as time-independent. The charge Q_{diff} due to diffusion-current contribution linearly varies with $t^{1/2}$ as it results form the integration of following Cottrell equation [89]

$$i(t) = \frac{nFAC_0D0^{1/2}}{1/2}t^{1/2}. \tag{B.2}$$

As a consequence, Q_{ads} can be obtained by subtracting Q_{dl} from the intercept of the Anson plot, which is obtained by representing the total charge charge vs. time (see figure B.4). By assuming that Q_{dl} is the same in the presence and in the absence of the adsorbed species, its contribution can be obtained by performing the experiment on the supporting electrolyte alone.

B.2.3 Electrochemical Impedance Spectroscopy

Electrochemical impedance is usually measured by applying an alternating potential to an electrochemical cell and measuring the current through the cell in a quasi steady system, i.e., its average state is time invariant: a monochromatic signal $v(t) = V_m sin(\omega t)$, involving the single frequency $v \equiv \omega/2p$, is applied to a cell and the resulting steady state current $i(t) = I_m \sin(\omega t + q\theta)$ (θ is the phase difference between the voltage and the current) is measured. The voltage-current relations, which are very complex in the time domain, can be rearranged to a form similar to Ohms law for dc current in the frequency domain. As a consequence, the response of real electrodes is usually studied as an impedance $Z(\omega)$ to a small sinusoidal excitation and the data of real electrodes can be analysed by fitting them to an equivalent electric circuit model. The

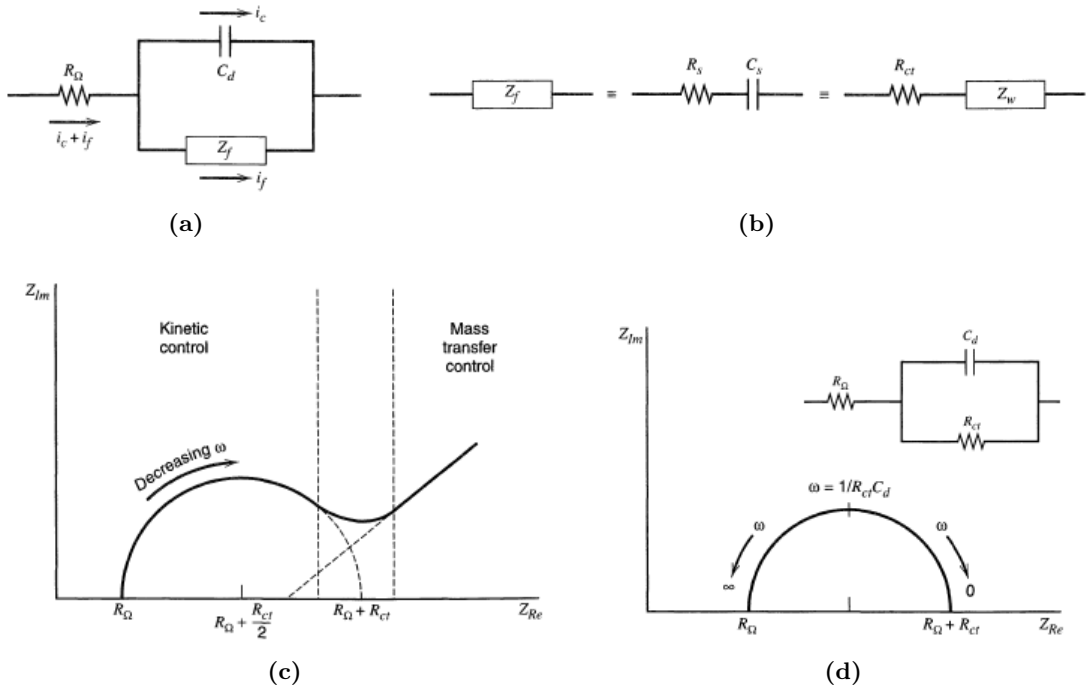

Figure B.5: Equivalent circuit of an electrochemical cell (a) and two possible representations of the faradaic working resistance (b); impedance plot for an electrochemical system: the regions of mass-transfer and kinetic control are found at low and high frequencies, respectively (c) and impedance plane plot for an equivalent circuit with a negligible Warburg impedance (d) [89].

most commonly used is the *Randles equivalent circuit* shown in figure B.5a. As all of the current passes through the resistance and the working interface, it consists of a series between the solution resistance R_Ω and the working electrode impedance. The last term results from two distinct contributions: the double-layer charging, which can be considered as a nearly pure capacitance C_d, and the faradaic process occurring at the interface, which is usually expressed as an impedance Z_f. Figure B.5b shows that the faradaic impedance can be represented as a series which includes the polarization resistance R_s and a pseudocapacity[1] C_s, or as a series between the pure resistance R_{ct} to the charge-transfer and the Z_w, the *Warburg impedance* resulting from the diffusion of ions.

The impedance spectra can be plotted in the form of complex plane diagrams

[1]Pseudocapacitance of an electrode is recognized when the accepted or delivered charge is Faradaic and is a function of potential [111].

(Nyquist plots): the real part of the impedance is reported on the X-axis and the imaginary part on the Y-axis; each point represents the impedance at a specific frequency. For a reversible reaction at a solid interface, two regions can be identified (see figure B.5c): a semicircle at high frequencies, which describes the faradaic electron transfer process, and a straight region at lower frequencies, which depicts the diffusion-limited transport of the redox species from the electrolyte to the electrode interface. The imaginary component to the impedance for a system where the Warburg impedance can be neglected (see figure B.5d) is only due the double layer C_d; its contribution falls to zero at high frequencies; therefore, all of the current is charging current and the impedance correspond to the ohmic resistance. At very low frequencies, the current flow passes mostly through R_{ct} and R_Ω; as a consequence, the finite impedance of C_d manifests a high impedance which causes the imaginary impedance component falling off.

B.2.4 Ultraviolet and visible spectroelectrochemistry

Spectroelectrochemistry is a techniques which combines electrochemistry and spectroscopy. The product of the chemical reaction involving a redox active compound are monitored in a specially designed electrochemical cell by spectroscopic techniques.

Figure B.6 shows a typical experimental set-up. A cuvette, which is used to contain the working electrode, the reference electrode and the counter electrode work as electrochemical cell. This apparatus allows to measure the color changes occurring in

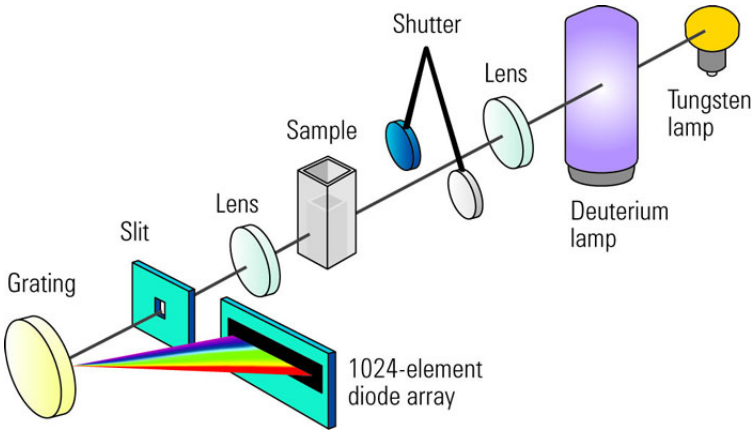

Figure B.6: Scheme of a diode array spectrophotometer; a cuvette is used as three electrode cell (picture taken from [112]).

the solution or at the electrode surface when an *optically transparent electrode* (OTE) is used as working electrode. Examples of OTEs are thin films or organic semiconductors (e.g., SnO_2 or In_2O_3) or metals (e.g., Au or Pt) deposited on glass, quartz, or plastic substrate. By directing a light beam through the working electrode surface, the absorbance can be measured as a function of the wavelenght at different times. Transmission experiments may involve the study of absorbance vs. time as the electrode potential is stepped or scanned, or they may involve wavelength scans to provide spectra of electrogenerated species. Either of these experimental goals can be attained with cells fitting into conventional spectral evolution over comparatively short time scales; as a consequence, a rapid scanning system is needed. Usually, a spectrophotometr equipped with a fotodiode array, providing a fast acquisition speed, is used.

This experimental set-up can be employed to perform any electrochemical experiment and, from an electrochemical standpoint, the response at the working electrode is the same achievable when the experiment is performed in a conventional cell. When a CV experiment is performed the potential scan rate and the absorbance acquisition time must be settled in order to allow the acquisition of the spectra at the desired potential values; usually it is preferable to perform the CV experiment at low potential scan rates.

References

[1] A. Hulanicki, S. Glab, and F. Ingman. **Chemical sesnors definitions and classification**. *International union of pure and applied chemistry*, **63**(9):1247–1250, 1991. 1

[2] O. S. Wolfbeis. **Chemical sensors survey and trends**. *Fresenius' Journal of Analytical Chemistry*, **337**(5):522–527, 1990. 2

[3] C. Bartic and G. Borghs. **Organic thin-film transistors as transducers for (bio)analytical applications**. *Analytical and Bioanalytical Chemistry*, **384**(2):354–365, 2006. 4, 38

[4] G. Ozaydin-Ince, A. M. Coclite, and K. K. Gleason. **CVD of polymeric thin films: applications in sensors, biotechnology, microelectronics/organic electronics, microfluidics, MEMS, composites and membranes**. *Reports on Progress in Physics*, **402**(1):1–40, 2012. 4

[5] G. Horowitz. **Organic Field-Effect Transistors**. *Advanced Materials*, **10**(5):365–377, 1998. 4, 162, 167

[6] S. R. Forrest. **The path to ubiquitous and low-cost organic electronic appliances on plastic**. *Nature*, **428**:911–918, 2004. 4, 158, 159, 161

[7] E. Menard, M. A. Meitl, Y. Sun, J.-U. Park, D. J.-L. Shir, Y.-S. Nam, S. Jeon, and J. A. Rogers. **Micro- and Nanopatterning Techniques for Organic Electronic and Optoelectronic Systems**. *American Chemical Society*, **107**(4):1117–1160, 2007. 4

[8] A. Ulman. **Formation and Structure of Self-Assembled Monolayers**. *Chemical Reviews*, **96**(4):1533–1554, 1996. 5

[9] J. Mabeck and G. G. Malliaras. **Chemical and biological sensors based on organic thin-film transistors**. *Analytical and Bioanalytical Chemistry*, **384**(2):343–353, 2006. 5

[10] L. Kergoat, B. Piro, M. Berggren, G. Horowitz, and M.-C. Pham. **Advances in organic transistor-based biosensors: from organic electrochemical transistors to electrolyte-gated organic field-effect transistors**. *Analytical and Bioanalytical Chemistry*, **402**(5):1813–1826, 2011. 5

[11] M. Barbaro, A. Bonfiglio, and L. Raffo. **A Charge-Modulated FET for Detection of Biomolecular Processes: Conception, Modeling, and Simulation**. *IEEE Transactions on Electron Devices*, **53**(1):158–166, 2006. 8, 51

[12] M. Barbaro, A. Bonfiglio, L. Raffo, A. Alessandrini, P. Facci, and I. Barák. **A CMOS, Fully Integrated Sensor for Electronic Detection of DNA Hybridization**. *IEEE Electron Device Letters*, **27**(7):595–597, 2006. 8, 51

[13] M. Berggren and A. Richter-Dahlfors. **Organic Bioelectronics**. *Advanced Materials*, **19**(20):3201–3213, 2007. 9

[14] L. Torsi, A. Dodabalapur, L. Sabbatini, and P. G. Zambonin. **Multi-parameter gas sensors based on organic thin-film-transistors**. *Sensors and Actuators B: Chemical*, **67**(3):312–316, 2000. 13

[15] L. Torsi, G. M. Farinola, F. Marinelli, M. C. Tanese, O. H. Omar, L. Valli et al. and F. Babudri, F. Palmisano, P. G. Zambonin, and F. Naso. **A sensitivity-enhanced field-effect chiral sensor**. *Nature Materials*, **7**:412–417, 2008. 13, 23, 24

[16] L. Torsi and A. Dodabalapur. **Organic Thin-Film Transistors as Plastic Analytical Sensors**. *Analytical Chemistry*, **75**(19):380–387, 2005. 14

[17] B. Crone, A. Dodabalapur, A. Gelperin, L. Torsi, H. E. Katz, A. J. Lovinger, and Z. Bao. **Electronic sensing of vapors with organic transistors**. *Applied Physics Letters*, **78**(15):2229–2231, 2001. 14, 15, 19

[18] T. Someya, H. E. Katz, A. Gelperin, A. J. Lovinger, and A. Dodabalapur. **Electronic sensing of vapors with organic transistors**. *Applied Physics Letters*, **81**(16):3079–3081, 2002. 15, 20

REFERENCES

[19] L. Torsi, A. J. Lovinger, B. Crone, T. Someya, A. Dodabalapur, H. E. Katz, and A. Gelperin. **Correlation between Oligothiophene Thin Film Transistor Morphology and Vapor Responses**. *Journal of Physical Chemistry B*, **106**(48):12563–12568, 2002. 16, 17, 18, 19, 20

[20] Z.-T. Zhu, J. T. Mason, R. Dieckmann, and G. G. Malliaras. **Humidity sensors based on pentacene thin-film transistors**. *Applied Physics Letters*, **81**(24):4643–4645, 2002. 19

[21] L. Wang, D. Fine, and A. Dodabalapur. **Nanoscale chemical sensor based on organic thin-film transistors**. *Applied Physics Letters*, **85**(26):6386–6388, 2004. 20

[22] A. N. Sokolov, M. E. Roberts, B. O. Johnson, Y. Cao, and Z. Bao. **Induced Sensitivity and Selectivity in Thin-Film Transistor Sensors via Calixarene Layers**. *Advanced Materials*, **22**(21):2349–2353, 2010. 21, 22

[23] Q. Zhang and V. Subramanian. **DNA hybridization detection with organic thin film transistors: toward fast and disposable DNA microarray chips**. *Biosensors & bioelectronics*, **22**(12):3182–3187, 2007. 24, 25

[24] P. Stoliar, E. Bystrenova, S. D. Quiroga, P. Annibale, M. Facchini, M. Spijkman, S. Setayesh, D. de Leeuw, and F. Biscarini. **DNA adsorption measured with ultra-thin film organic field effect transistors**. *Biosensors & bioelectronics*, **24**(9):2935–2938, 2009. 26, 27

[25] Q. Zhang, L. Jagannathan, and V. Subramanian. **Label-free low-cost disposable DNA hybridization detection systems using organic TFTs**. *Biosensors & bioelectronics*, **25**(5):972–977, 2010. 26

[26] J. Kim, S. K. Jha, R. Chand, D. Lee, and Y. Kim. **DNA hybridization sensor based on pentacene thin film transistor**. *Biosensors & bioelectronics*, **26**(5):2264–2269, 2011. 27, 28

[27] N. Liu, Y. Hu, J. Zhang, J. Cao, Y. Liu, and J. Wang. **A label-free, organic transistor-based biosensor by introducing electric bias during DNA immobilization**. *Organic Electronics*, 2012. 29

[28] F. Yan, S. M. Mok, J. Yu, H. L. W. Chan, and M. Yang. **Label-free DNA sensor based on organic thin film transistors**. *Biosensors & bioelectronics*, **24**(5):1241–1245, 2009. 29, 30

[29] T. Someya, A. Dodabalapur, A. Gelperin, H. Katz, and Z. Bao. **Integration and Response of Organic Electronics with Aqueous Microfluidics**. *Langmuir*, **18**(13):5299–5302, 2002. 31

[30] M. E. Roberts, S. C. B. Mannsfeld, N. Queraltó, C. Reese, J. Locklin, W. Knoll, and Z. Bao. **Water-stable organic transistors and their application in chemical and biological sensors**. *Proceedings of National Academy Of Sciences of the United States of America*, **105**(34):12134–12139, 2008. 32

[31] H. U. Khan, M. E. Roberts, O. Johnson, R. Förch, W. Knoll, and Z. Bao. **In Situ, Label-Free DNA Detection Using Organic Transistor Sensors**. *Advanced Materials*, **22**(40):4452–4456, 2010. 33, 34

[32] H. U. Khan, M. E. Roberts, O. Johnson, W. Knoll, and Z. Bao. **The effect of pH and DNA concentration on organic thin-film transistor**. *Organic Electronics*, **13**(3):519–524, 2012. 35

[33] J. Liu, M. Agarwal, and K. Varahramyan. **Glucose sensor based on organic thin film transistor using glucose oxidase and conducting polymer**. *Sensors and Actuators B: Chemical*, **135**(1):195–199, 2008. 35, 36

[34] C. Bartic, A. Campitelli K. Baert, J. Suls, and S. Borghs. **Organic-based transducer for low-cost charge detection in aqueous media**. *Electron Devices Meeting, 2000. IEDM '00. Technical Digest. International*, pages 411–414, 2000. 37, 38

[35] C. Bartic, B. Palan, A. Campitelli, and G. Borghs. **Monitoring pH with organic-based field-effect transistors**. *Sensors and Actuators B: Chemical*, **83**(1–3):115–122, 2002. 37, 38

[36] C. Gao, X. Zhu, J.-W. Choi, and C. H. Ahn. **A disposable polymer field effect transistor (FET) for pH measurement**. *TRANSDUCERS, Solid-State Sensors, Actuators and Microsystems, 12th International Conference on*, **2**:1172–1175, 2003. 38, 39

[37] M. W. Shinwari, M. J. Deen, and D. Landheerb. **Study of the electrolyte-insulator-semiconductor field-effect transistor (EISFET) with applications in biosensor design**. *Microelectronics Reliability*, **47**(12):2025–2057, 2007. 39, 116

[38] K. Diallo, M. Lemiti, J. Tardy, F. Bessueille, and N. Jaffrezic-Renault. **Flexible pentacene ion sensitive field effect transistor with a hydrogenated silicon nitride surface treated Parylene top gate insulator**. *Applied Physics Letters*, **93**:183305–1–183305–3, 2008. 39, 40

[39] A. Loi, I. Manunza, and A. Bonfiglio. **Flexible, organic, ion-sensitive field-effect transistor**. *Applied Physics Letters*, **86**:103512–1–103512–3, 2005. 40, 41

[40] C. Bartic, A. Campitelli, and S. Borghs. **Field-effect detection of chemical species with hybrid organic/inorganic transistors**. *Applied Physics Letters*, **82**(3):475–477, 2003. 40, 41

[41] L. Kergoat, B. Piro, M. Berggren, M. Pham, A. Yassar, and G. Horowitz. **DNA detection with a water-gated organic field-effect transistor**. *Organic Electronics*, **13**(1):1–6, 2012. 42, 43

[42] H. S. White, G. P. Kittlesen, and M. S. Wrighton. **Chemical derivatization of an array of three gold microelectrodes with poly-pyrrole: fabrication of a molecule-based transistor**. *Journal of the American Chemical Society*, **106**(18):5375–5377, 1984. 44, 126

[43] E. W. Paul, A. J. Ricco, and M. S. Wrighton. **Resistance of polyani-line films as a function of electrochemical potential and the fabrication of polyaniline-based microelectronic devices**. *The Journal of Physical Chemistry*, **89**(8):1441–1447, 1985. 44

[44] S. Chao and M. S. Wrighton. **Characterization of a solid-state polyaniline-based transistor: water vapor dependent characteristics of a device employing a poly(vinyl alcohol)/phosphoric acid solid-state electrolyte**. *Journal of the American Chemical Society*, **109**(22):6627–6631, 1987. 44

[45] J. W. Thackeray, H. S. White, and M. S. Wrighton. **Poly(3-methylthio-phene)-coated electrodes: optical and electrical properties as a function of redox potential and amplification of electrical and chemical signals using poly(3-methylthiophene)-based microelectrochemical transis-tors**. *The Journal of Physical Chemistry*, **89**(23):5133–5140, 1985. 44

[46] J. W. Thackeray and M. S. Wrighton. **Chemically responsive microelectrochemical devices based on platinized poly(3-methyl-thiophene): variation in conductivity with variation in hydrogen, oxygen, or pH in aqueous solution**. *The Journal of Physical Chemistry*, **90**(25):6674–6679, 1986. 44

[47] D. Nilsson, T. Kugler, P.-O. Svensson, and M. Berggren. **An all-organic sensortransistor based on a novel electrochemical transducer concept printed electrochemical sensors on paper**. *Sensors and Actuators B: Chemical*, **86**(2–3):193–197, 2002. 44, 45

[48] Z.-T. Zhu, J. T. Mabeck, C. Zhu, N. C. Cady, C. A. Battb, and G. G. Malliaras. **A simple poly(3,4-ethylene dioxythiophene)/poly(styrene sulfonic acid) transistor for glucose sensing at neutral pH**. *Chem. Commun*, (13):1556–1557, 2004. 45, 46

[49] M. Nikolou and G. G. Malliaras. **Applications of Poly (3,4-Ethylenedioxythiophene) Doped With Poly(Styrene Sulfonic Acid)Transistors in Chemical and Biological Sensors**. *The Chemical Record*, **8**(1):13–22, 2008. 46

[50] D. J. Macaya, M. Nikolou, S. Takamatsu, J. T. Mabeck, R. M. Owens, and G. G. Malliaras. **Simple glucose sensors with micromolar sensitivity based on organic electrochemical transistors**. *Sensors and Actuators B: Chemical*, **123**(1):374–378, 2006. 46, 47

[51] M. Yamaguchi, M. Mitsumori, and Y. Kano. **Noninvasively measuring blood glucose using saliva**. *The Chemical Record*, **17**(3):59–63, 1998. 47

[52] D. A. Bernards, D. J. Macaya, M. Nikolou, J. A. DeFranco, S. Takamatsu, and G. G. Malliaras. **All-Plastic Electrochemical Transistor for Glucose Sensing Using a Ferrocene Mediator**. *The Chemical Record*, **9**(12):9896–9902, 2009. 47

[53] D. A. Bernards, D. J. Macaya, M. Nikolou, J. A. DeFranco, S. Takamatsu, and G. G. Malliaras. **Enzymatic sensing with organic electrochemical transistors**. *The Chemical Record*, **18**(1):116–120, 2008. 48

[54] S. Y. Yang, J. A. DeFranco, Y. A. Sylvester, T. J. Gobert, D. J. Macaya, R. M.vOwens, and G. G. Malliaras. **Integration of a surface-directed microfluidic system with an organic electrochemical transistor array for multi-analyte biosensors**. *Lab Chip*, **9**(5):704–708, 2009. 47

[55] N. Y. Shim, D. A. Bernards, D. J.vMacaya J. A. DeFranco, M. Nikolou, R. M. Owens, and G. G. Malliaras. **All-Plastic Electrochemical Transistor for Glucose Sensing Using a Ferrocene Mediator**. *Sensors*, **9**(12):9896–9902, 2009. 48, 49

[56] A. Caboni, E. Orgiu, E. Scavetta, M. Barbaro, and A. Bonfiglio. **Organic-based sensor for chemical detection in aqueous solution**. *Applied Physics Letters*, **2**(9):123304–1–123304–3, 2009. 53, 54, 59, 67, 68

[57] A. Caboni, E. Orgiu, M. Barbaro, and A. Bonfiglio. **Flexible Organic Thin-Film Transistors for pH Monitoring**. *Sensors Journal, IEEE*, **9**(2):1963–1970, 2009. 53, 54, 59, 67, 68

[58] J. Jakabovič, J. Kováč, R. Srnánek, J. Kováč, M. Sokolský, J. Cirák, D. Haško, R. Resel, and E. Zojer. **Ultra-low voltage, organic thin film transistors fabricated on plastic substrates by a highly reproducible process**. *Interface Modification of Pentacene OFET Gate Dielectrics*, **129**(5):185–187, 2009. 60

REFERENCES

[59] W. Deng and D. Yang. **Characterization of self-assembled monolayers of thiols on Au(111)**. *SCIENCE CHINA Chemistry*, **39**(3):225–234, 1996. 61

[60] Y.-F. Liu, Y.-C. Yang, and Y.-L. Lee. **Assembly behavior and monolayer characteristics of OH-terminated alkanethiol on Au(111):*in situ* scanning tunneling microscopy and electrochemical studies**. *Nanotechnology*, **19**(6):065609–065618, 2008. 61

[61] J. C. Love, L. A. Estroff, J. K. Kriebel, R. G. Nuzzo, and G. M. Whitesides. **Self-Assembled Monolayers of Thiolates on Metals as a Form of Nanotechnology**. *Chemical Reviews*, **105**(4):1103–1170, 2010. 62, 63, 67

[62] R. K. Shervedani, M. Bagherzadeh, and S. A. Mozaffari. **Determination of dopamine in the presence of high concentration of ascorbic acid by using gold cysteamine self-assembled monolayers as a nanosensor**. *Sensors and Actuators B: Chemical*, **115**(2):614–621, 2006. 72

[63] S. E. Creager and J. Clarke. **Contact-Angle Titrations of Mixed ω -Mercaptoalkanoic Acid/Alkanethiol Monolayers on Gold. Reactive vs Nonreactive Spreading, and Chain Length Effects on Surface pK_a Values**. *Langmuir*, **10**(10):3675–3683, 1994. 72

[64] K. Hu and A. J. Bard. **Use of Atomic Force Microscopy for the Study of Surface Acid-Base Properties of Carboxylic Acid-Terminated Self-Assembled Monolayers**. *Langmuir*, **13**(19):5114–5119, 1997. 72

[65] J. Wang, L. M. Frostman, and M. D. Ward. **Self-assembled thiol monolayers with carboxylic acid functionality: measuring pH-dependent phase transitions with the quartz crystal microbalance**. *The Journal of Physical Chemistry*, **96**(13):5224–5228, 1992. 72

[66] A. Gulino. **Structural and electronic characterization of self-assembled molecular nanoarchitectures by X-ray photoelectron spectroscopy**. *Analytical and Bioanalytical Chemistry*, **405**(5):1479–1495, 2013. 79

[67] A. Cossaro, M. DellAngela, A. Verdini, M. Puppin, G. Kladnik, M. Coreno, M. de Simone, A. Kivimäki, D. Cvetko, M. Canepa, and L. Floreano. **Amine functionalization of gold surfaces : Ultra High Vacuum deposition of Cysteamine on Au (111)**. *The Journal of Physical Chemistry C*, **114**(35):15011–15014, 2010. 79, 80

[68] M. Wirde and U. Gelius. **Self-Assembled monolayers of Cysteamine and Cystamine on gold studied by XPS and voltammetry**. *Langmuir*, **15**(19):6370–6378, 1999. 79, 80

[69] J. Zhang, A. Bilič, J. R. Reimers, N. S. Hush, and J. Ulstrup. **Coexistance of multiple conformations in Cysteamine monolayers on Au (111)**. *The Journal of Physical Chemistry B*, **109**(32):15355–15367, 2005. 79

[70] M. Wirde, U. Gelius, T. Dunbar, and D. L. Allara. **Modification of self-assembled monolayers of alkenthiols on gold by ionizing radiation**. *NIMB*, **131**(1–4):245–251, 1997. 79

[71] *http://en.wikipedia.org/wiki/DNA*. 84

[72] T. M. Herne and M. J. Tarlov. **Characterization of DNA Probes Immobilized on Gold Surfaces**. *Journal of the American Chemical Society*, **119**(38):8916–8920, 1997. 85, 86

[73] D. A. J. Rand and R. Woods. **The nature of adsorbed oxygen on rhodium, palladium and gold electrodes**. *Journal of Electroanalytical Chemistry and Interfacial Electrochemistry*, **31**(1):29–38, 1971. 88

[74] G. Sánchez-Pomales, L. Santiago-Rodr´guez, N. E. Rivera-Vélez, and C. R. Cabrera. **Control of DNA self-assembled monolayers surface coverage by electrochemical desorption**. **611**(1–2):80–86, 2007. 90

[75] A. B. Steel, T. M. Herne, and M. J. Tarlov. **Electrochemical Quantitation of DNA Immobilized on Gold**. *Analytical Chemistry*, **70**(22):4670–4677, 1998. 90, 91

[76] S. K. Park, D. A. Mourey, J.-I. Han, J. E. Anthony, and T. N. Jackson. **Environmental and operational stability of solution-processed 6,13-bis(triisopropyl-silylethynyl) pentacene thin film transistors**. *Organic Electronics*, **10**(3):486–490, 2009. 97

[77] P. Cosseddu, S. Lai, M. Barbaro, and A. Bonfiglio. **Ultra-low voltage, organic thin film transistors fabricated on plastic substrates by a highly reproducible process**. *Applied Physics Letters*, **100**(9):093305–1–093305–5, 2012. 105

[78] D. E. Yates, S. Levine, and T. W. Heal. **Site-binding Model of the Electrical Double Layer at the Oxide/Water Interface**. *J. Chem. Soc., Faraday Trans. 1*, **70**(0):1807–1818, 1974. 115

[79] J. V. Pinto, R. Branquinho, E. Alves R. Martins, and E. Fortunato. **Extended-gate ISFETs based on Sputtered Amorphous Oxides**. *IEEE, Display Technology*, **PP**(99):1–6, 2010. 117

[80] R. Branquinho, J. V. Pinto, T. Busani, P. Barquinha, L. Pereira, P. V. Baptista, R. Martins, and E. Fortunato. **Plastic Compatible Sputtered Ta_2O_5 Sensitive Layer for Oxide Semiconductor TFT Sensors**. *Journal of Display Technology*, **PP**(99):1–6, 2012. 117, 118

[81] H. Shirakawa, E. J. Lewis, A. G. MacDiarmid, C. K. Chiang, and A. J. Heeger. **Synthesis of electrically conducting organic polymers: halogen derivatives of polyacetylene, $(CH)_x$**. *J. Chem. Soc. Chem. Commun.*, **0**(16):578–580, 1977. 125

[82] D. A. Bernards and G. G. Malliaras. **Steady-State and Transient Behavior of Organic Electrochemicalc Transistors**. *Advanced Functional Materials*, **17**(17):3393–3672, 2007. 126, 127, 150

[83] F. Lin and M. C. Lonergan. **Gate electrode processes in an electrolyte-gated transistor:Non-Faradaically versus Faradaically coupled conductivity modulation of a polyacetylene ionomer**. *Applied Physics Letters*, **88**(13):133507–133509, 2006. 130, 131

[84] G. Tarabella, C. Santato, S. Y. Yang, S. Iannotta, G. G. Malliaras, and F. Cicoira. **Effect of the gate electrode on the response of organic electrochemical transistors**. *Applied Physics Letters*, **97**(12):123304–12336, 2010. 132, 133, 138

[85] F. Cicoira, M. Sessolo, O. Yaghmazadeh, J. A. DeFranco, S. Y. Yang, and G. G. Malliaras. **Influence of Device Geometry on Sensor Characteristics of Planar Organic Electrochemical Transistors**. *Advanced Materials*, **22**(9):1012–1016, 2010. 132

[86] L. Basiricò, P. Cosseddu, A. Scidà, B. Fraboni, G. G. Malliaras, and A. Bonfiglio. **Electrical characteristics of ink-jet printed, all-polymer electrochemical transistors**. *Organic Electronics*, **13**(2):244–248, 2012. 134, 138, 140

[87] **Dimatix Materials Printer DMP-2800 Series User Manual**. *FUJIFILM Dimatix*, 2008. 136

[88] L. Basiricò. **Inkjet Printing of Organic Transistor Devices**. *pHD Thesis*, 2012. 138, 139

[89] A. J. Bard and L. R. Faulkner. **Electrochemical Methods**. *John Wiley & Sons*. 139, 173, 174, 177, 178

[90] S. K. M. Jönsson, J. Birgerson, X. Crispin, G. Greczynski, W. Osikowicz, A. W. Denier van der Gon, W. R. Salaneck, and M. Fahlman. **The effects of solvents on the morphology and sheet resistance in poly(3,4-ethylenedioxythiophene)polystyrenesulfonic acid (PEDOTPSS) films**. *Synthetic Metals*, **139**(1):1–10, 2003. 142

[91] J. Ouyang, Q. Xu, C.-W. Chu, Y. Yang, G. Li, and J. Shinar. **On the mechanism of conductivity enhancement in poly(3,4-ethylenedioxythiophene):poly(styrene sulfonate) film through solvent treatment**. *Polymer*, **45**(25):8443–8450, 2004. 143, 146

[92] J. Heinze. **Electrochemistry of conducting polymers**. *Synthetic Metals*, **43**(1–2):2805–2823, 1991. 149

[93] G. L. Duffitt and P. G. Pickup. **Enhanced ionic conductivity of polypyrrole due to incorporation of excess electrolyte during potential cycling**. *J. Chem. Soc., Faraday Trans.*, **88**(10):1417–1423, 1992. 150

[94] F. Beck and M. Dahlhaus. **Evaluation of the first discharge redox process of doped polypyrrole**. *Journal of Electroanalytical Chemistry*, **357**(1–2):289–300, 1993. 150

[95] F. A. Carey. **Organic Chemistry**. *Mc Graw Hill*, 2001. 155

[96] C. D. Dimitrakopoulos and D. J. Mascaro. **The path to ubiquitous and low-cost organic electronic appliances on plastic**. *IBM Corp. Riverton, NJ, USA*, **45**(1):11–27, 2001. 160

[97] A. Moliton and R. Hiorns. **Review of electronic and optical properties of semiconducting π-conjugated polymers: applications in optoelectronics**. *Polymer International*, **53**(10):1397–1412, 2004. 161, 164

[98] H. Bässler. **Charge Transport in Disordered Organic Photoconductors a Monte Carlo Simulation Study**. *Physica Status Solidi (b)*, **175**(1):15–56, 1993. 161

[99] M. C. J. M. Vissenberg and M. Matters. **Theory of the field-effect mobility in amorphous organic transistors**. *Phys. Rev. B*, **57**(20):12964–12967, 1998. 162, 170

[100] H. E. Katz and Z. Bao. **The Physical Chemistry of Organic Field-Effect Transistors**. *The Journal of Physical Chemistry B*, **104**(4):671–678, 2000. 162

[101] G. Horowitz and M. E. Hajlaoui. **Mobility in Polycrystalline Oligothiophene Field-Effect Transistors Dependent on Grain Size**. *Advanced Materials*, **12**(14):1046–1050, 2000. 163

[102] H. Koezuka, A. Tsumura, and T. Ando. **Field-effect transistor with polythiophene thin film**. *Synthetic Metals*, **18**(1-3):699–704, 1987. 163

REFERENCES

[103] M. Shur. **Physics of Semiconductor Devices**. *Englewood Cliffs*, 1990. 163

[104] S. M. Sze. **Physics of semiconductor devices**. *Wiley - New York*. 165, 167

[105] A. Kahn, N. Koch, and W. Gao. **Electronic Structure and Electrical Properties of Interfaces between Metals and π-Conjugated Molecular Films**. *Journal of Polymer Science Part B: Polymer Physics*, **41**(21):2529–2548, 2003. 165, 167

[106] J. Hwang, A. Wan, and A. Kahn. **Energetics of metal-organic interfaces: New experiments and assessment of the field**. *Materials Science and Engineering: R: Reports*, **64**(1–2):1–31, 2009. 165

[107] J. Hwang, A. Wan, and A. Kahn. **Progress in Plastic Electrnics Devices**. *Annual Review of Materials Research*, **36**:199–230, 2006. 165

[108] G. Horowitz, P. Lang, M. Mottaghi, and H. Aubin. **Extracting Parameters from the CurrentVoltage Characteristics of Organic Field-Effect Transistors**. *Advanced Materials*, **14**(11):1069–1074, 2004. 170

[109] J. Wang. **Analytical electrochemistry**. *John Wiley & Sons*, 2001. 175, 176

[110] A. W. Bott and W. R. Heineman. **Chronocoulometry**. 2004. 176, 177

[111] E. Barsoukov and J. Ross Macdonald. **Impedance Spectroscopy Theory, Experiments, and Applications**. *John Wiley & Sons*, 2005. 178

[112] *http://www.chem.agilent.com/*. 179

Acknowledgements

First of all, I would like to thank my advisor Prof. Annalisa Bonfiglio for giving me the chance to do research on such an interesting topic. I will always be grateful to her for believing in me. I would like to thank Dr. Massimo Barbaro for his contribution and I am grateful to Dr. Erika Scavetta for her teaching which introduced me to the incredible world of electrochemistry.

Some of the experimental results reported in this thesis were obtained by means of the collaboration with other groups of research. I would like to thank Prof. Elvira Fortunato, Dr. Joana Pinto and Dr. Rita Branquinho for their contribution to the realization of the LV pH sensor. I am very grateful to Dr. Piero Cosseddu for the AFM measurements, Dr. Nicola Cioffi, Dr. Rosaria Anna Picca and Maria Chiara Sportelli for the XPS analysis. A special thank to Prof. Gian Luca Ferri for his help with the fluorescence detection.

This work would have been harder without the support and friendship of colleagues that I consider the best team to work with. Thanks to Piero, Laura, Giorgio, Alberto, José, Giulia, Andrea and in particular to Stefano whom I started the development of the DNA sensor with. A big thank also to Simona and Silvia who rescued me from bureaucracy.

A special thanks to Giuliana for her friendship and support and for sharing most of the joys and challenges I had to face during this work.

Last but not least thanks to Juri and Dad who are always with me, and to Mum for her love and care which allowed me to become who I am today.